UNIVERSITE ECOLOGIE
BRETAGNE GEOSCIENCES
LOIRE AGRONOMIE ALIMENTATION

UNIVERSITÉ DE NANTES

THESE DE DOCTORAT DE

L'UNIVERSITE DE NANTES
COMUE UNIVERSITE BRETAGNE LOIRE

ECOLE DOCTORALE N° 600
Ecole doctorale Ecologie, Géosciences, Agronomie et Alimentation
Spécialité : *Biochimie, biologie moléculaire et cellulaire*

Par
Kévin VIDOT

Distribution et fonctions des ions métalliques et des composés phénoliques dans les parois de fruits charnus

Modèle pomme et raisin

Thèse présentée et soutenue à Nantes, le 04/10/2019
Unité de recherche : INRA Nantes (unité BIA, équipe PVPP) & ESA Angers (unité GRAPPE)

Rapporteurs avant soutenance :

Carine LE BOURVELLEC	Chargée de recherche (HDR), INRA Avignon - Université Avignon
Géraldine SARRET	Directeur de recherche, Université de Grenoble

Composition du Jury :

Président :	Philippe SIMIER	Professeur des universités, Université de Nantes
Examinateurs :	Thierry ASTRUC	Ingénieur de recherche, Centre INRA Auvergne-Rhône-Alpes
	Azeddine DRIOUICH	Professeur des universités, Université de Rouen
	Laurence GENY-DENIS	Professeur des universités, Université de Bordeaux
Dir. de thèse :	Marc LAHAYE	Directeur de recherche, INRA Nantes
Co-dir. de thèse :	René SIRET	Professeur, ESA Angers
Invité(s) :	Alain LEBAIL	Professeur, Oniris Nantes

"Donne le meilleur de toi-même, et le meilleur viendra"

Madeline Bridge

Remerciements

Ces trois ans de thèse se sont très bien déroulées grâce à toutes les personnes qui m'entourent de manières directe ou indirecte. Merci à vous tous.

Tout d'abord, je tiens à remercier mon directeur de thèse Marc Lahaye qui a toujours été présent, disponible, pédagogue dans ses conseils, son partage de connaissances scientifiques et son expérience, je le remercie pour cela.

Je remercie aussi mon co-directeur de thèse, René Siret de m'avoir accordé sa confiance pour la réalisation de cette thèse. Malgré ses engagements dans d'autres activités chronophages, il a su trouver le temps nécessaire au suivi de ma thèse.

Je tiens à remercier l'ensemble des membres mon comité de thèse : Marie-Pierre Isaure, Cédric Saucier, et en particulier Chantal Maury, Sylvain Guyot, Camille Rivard et Cédric Gaillard, qui par leurs remarques, suggestions et accompagnement ont permis d'améliorer l'orientation et la qualité de mes recherches.

Merci aux membres du jury de soutenance de thèse : Carine Le Bourvellec, Géraldine Sarret, Laurence Gény-Denis, Thierry Astruc, Azeddine Driouich et Philippe Simier, d'avoir accepté d'évaluer mes travaux.

Je remercie la région Pays de la Loire pour le financement de ce programme RFI Food for Tomorrow / Cap Aliment dont cette thèse fait partie.

Je tiens à remercier l'INRA et plus particulièrement BIA pour leur accueil et tous les moyens mis en œuvre pour mener à bien cette thèse.

Je remercie l'ensemble de l'équipe Paroi Végétale et Polysaccharides Pariétaux : Jacqueline, Audrey, Sylviane, Maude et Marie-Jeanne pour votre aide et disponibilité au laboratoire, Estelle pour tes conseils sur les formalités de l'ED, Fabienne, Luc, Mathilde, Axelle, Anne-Laure, Richard, Yves, Mehdi et les autres stagiaires, pour leur collaboration, leur présence et leur sympathie. Merci à Yves pour tes conseils et ton humour ainsi qu'à Medhi compagnon de galère, bon courage pour la fin de thèse.

Je remercie Cédric G. pour avoir passé des heures à m'aider dans le bricolage des microscopes « glacés ». Merci également à Camille A., Laurent H., Sylvie D. et Marie-Françoise D. pour les rudes sessions au synchrotron SOLEIL, où on finissait en « blinds tests » et quiz miss France pour tenir le coup certaines nuits difficiles. Je tiens aussi à remercier les agents de ligne du synchrotron Camille R. et Frederic J pour nous avoir formés, pour leurs investissements, disponibilités et pédagogies lors de nos sessions.

Merci également à l'équipe du GRAPPE à Angers, notamment Dominique L-M. et Vanessa L-V. pour votre aide lors de ma venue au laboratoire, Séverine J. pour les récoltes de raisins, Pierre P. et Chantal M. pour les discussions sur mes résultats.

Je tiens à remercier les doctorants et les membres du groupe Ephem'R du site de Nantes qui pour certains sont devenu bien plus que des collègues. Merci pour l'intégration et m'avoir permis de découvrir la vie dans la belle ville de Nantes de jour comme de nuit. Merci pour les soirées apéros toujours avec modération. Merci également aux étudiants d'Oniris pour les afterworks sportifs et moins sportifs. Un merci tout particulier à Piyush K-J., autre compagnon de galère, notamment pour les discussions scientifiques et volleyistique pendant les pauses café.

Merci à tous les amis, et tout particulièrement François pour me laisser ta voiture à chaque fois que j'en avais besoin, j'aurais fini par te l'acheter au bout d'un moment ; mais également à Claire pour la correction des fautes de grammaires et d'orthographes du manuscrit #mercimaîtresse.
Enfin je remercie les membres de ma famille et surtout ma copine Marie qui m'a toujours soutenu et qui à supporter les week-ends aller-retour entre Nantes et Toulouse pendant plus de 1 an et demi, je vous aime.

Encore un grand merci à tous…

Acronymes

AES : Spectrométrie d'émission atomique
AIM: alcohol-insoluble material
AO: Acridine Orange
ASS : Spectrométrie d'absorption atomique
BIA : Biopolymères Interactions Assemblages
BSA : Bovine serum albumin
C: Cuticle
Ca : Calcium
Cat : (+)-Catéchine
CEMOVIS: Cryo-electron microscopy of vitreous samples
CF : Cabernet Franc
CI: Color Intensity
Cryo-CLEM : Cryo-correlative light transmission electron microscopy
CS : Cabernet Sauvignon
Cu : Cuivre
CW: Cell wall
Cya: Cyanidine
DE: degree of pectin methyl esterification
DISCO : Dichroism, Imaging, mass Spectrometry for Chemistry and biOlogy
DM : Douce Moen (Malus Domestica, Dous moen)
DMACA : p-DiMethyl-AminoCinnamAldehyde
DPBA : 2-AminoethylDiPhenylBorinate
DPPH : 1,1-diphenyl-2-picrylhydrazyl
DUV: Deep UltraViolet
E': Elastic Modulus
EDS : Spectrométrie dispersive en énergie
EELS : Spectroscopie des pertes d'énergie
ESA : Ecole Supérieur d'Agricultures
EXAFS: Extended X-Ray Absorption Fine Structure
FA: Ferulic Acid
Fe : Fer
Flv: Flavonols
GAX: glucuronoarabinoxylan
GR : Grolleau
GRAPPE : Groupe de Recherche en Agroalimentaire sur les Produits et les Procédés
GU : Guillevic (Malus Domestica, Guillevic)
H_2O_2 : Peroxyde d'hydrogène
HC: Hydroxycinnamic acid
HCA : HydroxyCinnamic Acid
HG : Homogalacturonanes
HPF : High Pressure Freezing
HPLC: High Pressure Liquid Chromatography
IC: Ionic Chromatography
IHC : Immunohistochemistry
INRA : Institut National de Recherche Agronomique
J0: Fruit stockés 0 jour
J20: Fruits stockés 20 jours à température ambiante
J30 : Fruits stockés 30 jours à 4°C

K : Potassium
keV : kilo electron Volt
l'EPR : electron paramagnetic resonance
LA-ICP : Ablation Laser couplée a un Plasma a Couplage Inductif
LIBS : Laser Induce Breakdown Spectroscopy
LRW : London Resin White
LSCM: Laser Scanning Confocal Microscopy
LUCIA : Ligne Utilisée pour la Caractérisation par Imagerie et Absorption
MCBL : Microscopie Confocale à Balayage Laser
MEB : Microscopie Electronique à Balayage
MET : Microscopie Electronique en Transmission
Mg : Magnesium
Mn : Manganèse
MS : Spectrométrie de masse
NA: Numerical Aperture
NADPH : Nicotinamide adénine dinucléotide phosphate
OC-1 et 2: Outer Cortex 1 et 2
P: Peel
PBS: phosphate buffer saline
PC: Procyanidin
pCA: para-Coumaric Acid
PCA: Principal Component Analysis
PCs : Composés phénoliques
Pec : Pectine (Hautement méthylé 72 %)
PF : Plunge Freezing
Ph : Groupement phénol
PIXE : Particule Induce X-ray Emission
PPO : Polyphénol oxydase
PVPP: Paroi Végétale et Polysaccharides Pariétaux
RFI: Recherche Formation Innovation
RG I et II : Rhamnogalacturonanes de types I et II
ROS : Reactive Oxygen Species
SEC: Size Exclusion Chromatography
SIMS : Spectrométrie de masse des ions secondaires
SOLEIL : Source Optimisée de Lumière à Energie Intermédiaire du LURE (Laboratoire à Utilisation du Rayonnement Electromagnétique)
S-XRF : Synchrotron X Ray Fluorescence
TMCA : 3-4-5-trimethoxy-trans-cinnamic acid
TPI: Total Polyphenol Index
USDA : United State Department of Agriculture
UUA: non-esterified uronic acid
WD: Working Distance
XANES : X-ray Absorption Near Edge Structure
XAS : Spectrométrie d'absorption des rayons X
XG : Xylogalacturonane
Zn : Zinc

Table des matières

Liste des figures

Liste des tables

Liste des publications

Vidot, K., et al. (2018). "Cryo-laser scanning confocal microscopy of diffusible plant compounds." Plant Methods **14**(1): 89.

Jha, P. K., Vidot, K., et al. (2019). "Benchmarking of techniques used to assess the freeze damage in potatoes." Journal of Food Engineering **262**: 60-74.

Vidot, K., et al. (2019). "Phenolic distribution in apple epidermal and outer cortex tissue by multispectral deep-UV autofluorescence cryo-imaging." Plant Science.

Vidot, K., et al. "Metallic ions distribution in texture and phenolic content contrasted cider apples" (*submitted*).

Introduction

Les fruits charnus sont d'une importance économique majeure dans le milieu agroalimentaire, en particulier la pomme et le raisin qui font partie des premiers fruits produits en Europe. La production annuelle s'élève respectivement à 14 et 23 millions de tonnes pour la pomme et le raisin (Vine 2017, USDA 2018). Environ 60% des pommes et 15% des raisins sont destinés à la consommation directe, alors que 40% des pommes et 85% des raisins produits servent à l'industrie pour la fabrication de produits transformés tels que les jus, cidres, vins, etc.

Dans un contexte de changement climatique associé à l'accroissement de la population, la quantité et la qualité des productions de fruits doivent être adaptées à la demande des consommateurs et de l'industrie de transformation. En particulier ces productions doivent répondre à des rendements maitrisés et faciliter le développement de procédés de transformation durable. Dans un contexte économique toujours plus concurrentiel, les produits issus de la filière fruticole doivent être exemplaires en matière de qualité. Ce terme générique revêt de multiples dimensions déterminantes dans la construction de la satisfaction des consommateurs. Plusieurs composantes sont généralement considérées. On distingue la qualité alimentaire stricto sensu comprenant les dimensions sanitaires, nutritionnelles et organoleptiques, de la qualité d'usage et de service qui regroupe l'aptitude à la transformation, la praticité d'usage et l'aspect économique. Enfin, plus récemment, une dimension environnementale intégrant des notions de durabilité à vue le jour (Bertoluci and Trystram 2013).

La couleur, la fermeté de la chair, la saveur, le parfum ou encore l'aptitude à la conservation, sont les principaux critères de qualité qui déterminent le choix du consommateur et les procédés de transformation. La maitrise de la qualité des fruits charnus est fondamentale pour s'adapter aux goûts des consommateurs ou aux cahiers des charges industrielles de la filière du producteur au transformateur. En ce qui concerne la pomme et le raisin, des fruits plutôt fermes et juteux, aux colorations et arômes intenses, sont souvent recherchés. Pour optimiser les rendements, le transformateur utilisera des variétés de fruits plus résistantes à la fois aux désordres physiologiques et aux maladies. Ces choix sont dictés par un souci de limiter les pertes, d'enrichir les produits transformés en composés d'intérêt nutritionnel, ou encore de limiter les coûts de transformation notamment lors du pressage pour la filière cidricole ou viticole. L'adaptation des productions et des transformations par rapport à ces contraintes requiert une connaissance approfondie des mécanismes sous-jacents aux qualités des productions.

Dans les fruits, les critères de qualité recherchés dépendent de la composition et de la structure des parois cellulaires, ainsi que de la teneur et de la composition en micronutriments tels que les ions métalliques et les composés phénoliques. En effet, la fermeté des fruits serait particulièrement

affectée par les ions métalliques dans le compartiment pariétal et le métabolisme des parois cellulaires. Par ailleurs, les interactions des composés phénoliques intracellulaires vis-à-vis des ions métalliques de transition présents dans la paroi cellulaire et mis en contact lors de la consommation ou de la transformation des fruits restent méconnues. L'impact sensoriel, nutritionnel et technologique des différents produits issus de ces réactions reste à établir. Dans ce contexte, l'objectif de la thèse concerne dans un premier temps l'étude de la distribution et des fonctions des ions métalliques (K, Ca, Mg, Fe, Mn, Cu, Zn) et des composés phénoliques dans les tissus de pomme et de raisin, avant d'initier une étude sur leurs interactions dans un système-modèle mimant les fruits déstructurés.

Ce projet de thèse s'inscrit dans une démarche de meilleure compréhension des aliments de demain, dans le cadre du programme RFI Food for Tomorrow financé par la région Pays de la Loire. Cette thèse a été effectuée au sein de l'équipe Paroi Végétale et Polysaccharides Pariétaux (PVPP) de l'unité Biopolymères Interactions Assemblages (BIA) de l'INRA du Centre Pays de la Loire à Nantes, et au sein de l'équipe du Groupe de Recherche en Agroalimentaire sur les Produits et les Procédés (GRAPPE) de l'Ecole Supérieur d'Agricultures (ESA) à Angers.

Ce manuscrit sera présenté en 7 principaux chapitres. Après une synthèse bibliographique des données de la littérature sur le sujet, cinq chapitres détailleront les travaux effectués. Un dernier chapitre dressera une discussion générale abordant les conclusions et perspectives de ce travail. Des annexes se rapportant aux travaux effectués concluront ce document. Les différents chapitres sur les travaux effectués sont construits sous la forme d'articles rédigés en anglais car ils font ou feront l'objet de publications dans des revues scientifiques.

Chapitre I

I. Etat de l'art

Sommaire

I.1. Les fruits charnus

Le fruit est un organe des plantes à fleurs (angiospermes) issu du développement de l'ovaire, et qui, à maturité, contient les graines. Les fruits charnus se distinguent des fruits secs par un tissu volumineux riche en eau, constituant la pulpe ou la chair. Lorsque la chair provient du développement d'une partie autre que l'ovaire, ce dernier est qualifié de faux-fruit, ou fruit accessoire (fraise, pomme, …). Deux types de fruits charnus sont communément retrouvés, les drupes (fruits à noyau) et les baies (fruits à pépins). Les fruits à pépins (raisin, pomme, groseille, etc.) contiennent généralement plusieurs graines (les pépins) et possèdent un endocarpe mince (Kumar 2009).

Un descriptif de l'histologie des coupes transversales de pomme et de raisin sont décrites dans la **Figure I.1,** présentant, entre autres, les zones communément retrouvées dans les fruits charnus tels que l'endocarpe, le mésocarpe et le péricarpe. Un schéma de l'histologie spécifique à ces deux types de fruits charnus avec une nomenclature des différents tissus et couches cellulaires sera décrit dans le chapitre II.

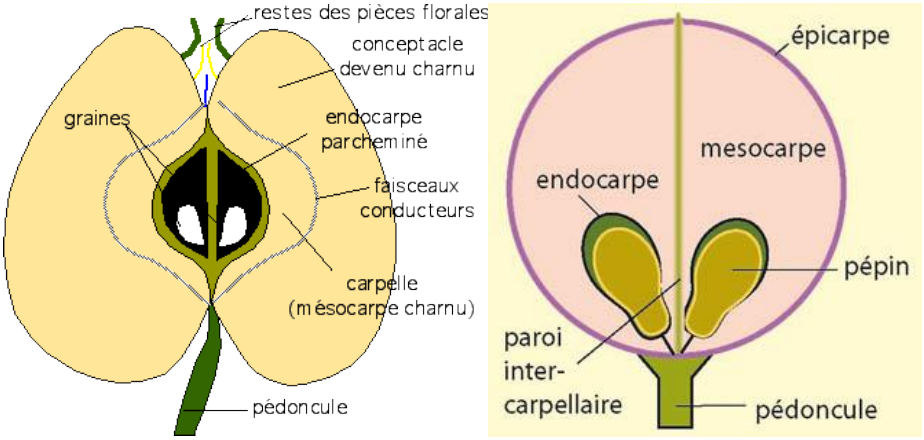

Figure I.1*: Section longitudinale de pomme (à droite) et de raisin (à gauche). Chez la pomme, le conceptacle est aussi appelé péricarpe. L'endocarpe est légèrement lignifié (cartilagineux). (Prat, Mosiniak et al. 2016)*

Au cours de la thèse, le choix des fruits s'est porté sur des variétés cidricoles et viticoles de pomme et de raisin. Les pommes à cidre et en particulier les variétés Douce Moen et Guillevic, ont été choisies pour leur importance économique dans l'industrie cidricole du nord-ouest de la France, mais aussi pour leurs propriétés contrastées en matière de texture et de composition en composés phénoliques. Les cépages Cabernet franc (CF), Cabernet sauvignon (CS) et Grolleau (GR) ont été sélectionnés pour leur production importante en France, en particulier dans la région Val de Loire. Afin de mieux distinguer ces variétés, quelques caractéristiques compositionnelles et mécaniques ont été déterminées au cours de la thèse et seront présentées en annexes et dans le chapitre V.

I.2. Les parois cellulaires

Dans le monde végétal, les parois cellulaires régulent le développement des tissus notamment grâce à leurs propriétés mécaniques et physico-chimiques. Séparant toutes les cellules les unes des autres, elles constituent un milieu de transport hydrophile et assurent les communications intercellulaires.

Dans les fruits charnus, la paroi cellulaire est constituée d'eau, d'ions métalliques, de protéines (enzymes et protéines de structure), de polysaccharides tels que la cellulose, les hémicelluloses et les pectines ainsi que d'autres solutés (sucres, acides, acides aminés…). Les polysaccharides forment une architecture complexe de la paroi telle que représentée dans la **Figure I.2**. La compartimentation de l'eau associée à l'organisation des polysaccharides détermine les propriétés mécaniques de la paroi et la fermeté des fruits charnus. L'assemblage des polysaccharides pariétaux implique des interactions entre les différentes familles de polysaccharides telles que l'hémicellulose et la cellulose sous forme de « hotspots » (Park and Cosgrove 2015) ou entre les pectines via leurs chaines ramifiées et la cellulose (Zykwinska, Ralet et al. 2005). Ces chaines ramifiées des pectines contenant des résidus galactose et arabinose sont également connues pour leurs affinités avec l'eau et pour favoriser la mobilité des molécules dans les parois cellulaires modulant ainsi les propriétés mécaniques de ces parois cellulaires (Ha, Viëtor et al. 2005, Larsen, Byg et al. 2011, Winisdorffer, Musse et al. 2015, Lahaye, Bouin et al. 2018). La composition polysaccharidique des parois cellulaires a notamment été décrite par Voragen, Coenen et al. (2009) et Winisdorffer, Musse et al. (2015) pour la pomme et par Nunan, Sims et al. (1998) et Gao, Fangel et al. (2015) pour le raisin. Au niveau moléculaire, la cellulose est un β-D-glucane linéaire contenant jusqu'à 10000 unités glucose liées en 1-4 (Klemm, Heublein et al. 2005). Aussi avec un squelette β-D-glucane composé d'unité glucose liée en 1-4, les hémicelluloses avec des chaines plus courtes jusqu'à 3000 unités, regroupent plusieurs familles incluant les xyloglucanes (XGs) majoritairement, les xylanes, les glucomannanes et les galactoglucomannanes. Ainsi, les hémicelluloses sont dérivées de plusieurs oses, principalement du xylose mais aussi du mannose, galactose, rhamnose et de l'arabinose (Doco, Williams et al. 2003, Gibson 2012). Les pectines présentent des structures moléculaires légèrement plus complexes mais leurs interactions et réticulations ont souvent été décrites comme déterminantes des propriétés mécaniques des parois cellulaires (Christiaens, Van Buggenhout et al. 2016). Dans les pommes et raisins, les pectines ont un rôle important sur les propriétés mécaniques des parois cellulaires, qui associées aux interactions avec l'eau, participent à la fermeté des tissus. Nous nous concentrerons donc par la suite sur les pectines.

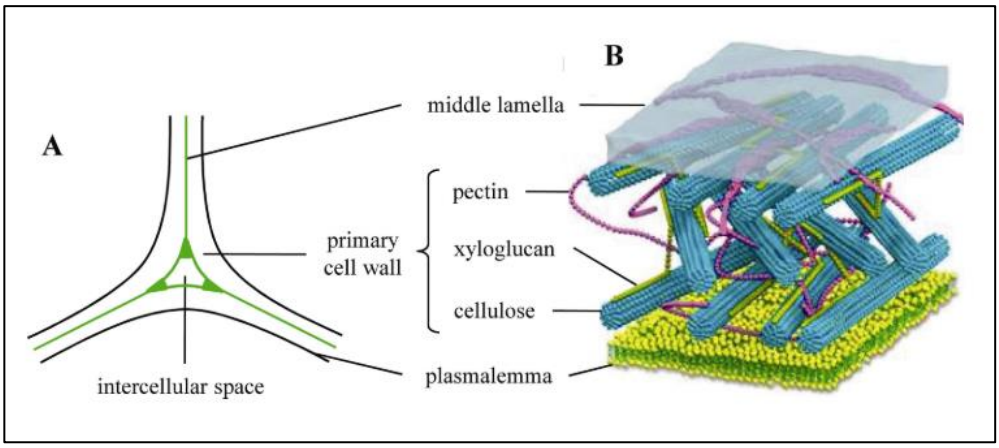

Figure I.2 *: Représentation de la paroi cellulaire des fruits charnus : (A) section de jonction tri-cellulaire, (B) organisation tridimensionnelle des polymères pariétaux (Christiaens, Van Buggenhout et al. 2016)*

I.2.1. Les pectines

Les pectines représentent de 5 à 10 % du poids sec des parois de fruits charnus, en fonction du genre et de la variété (Barnavon, Doco et al. 2000, Thibault and Ralet 2008). La composition et la structure complexe des pectines ont largement été discutées par plusieurs auteurs (Caffall and Mohnen 2009, Voragen, Coenen et al. 2009, Christiaens, Van Buggenhout et al. 2016). Ces polysaccharides sont riches en acides galacturoniques et sont construits à partir de trois principaux blocs structuraux : les homogalacturonanes (HG), les rhamnogalacturonanes de types I et II (RG I et II). Il est généralement accepté que le squelette des pectines est une alternance d'HG et de RG liés de façon covalente, associés à des régions dites « lisses » et « hérissées » tel que représenté dans la **Figure I.3** (Celus, Kyomugasho et al. 2018).

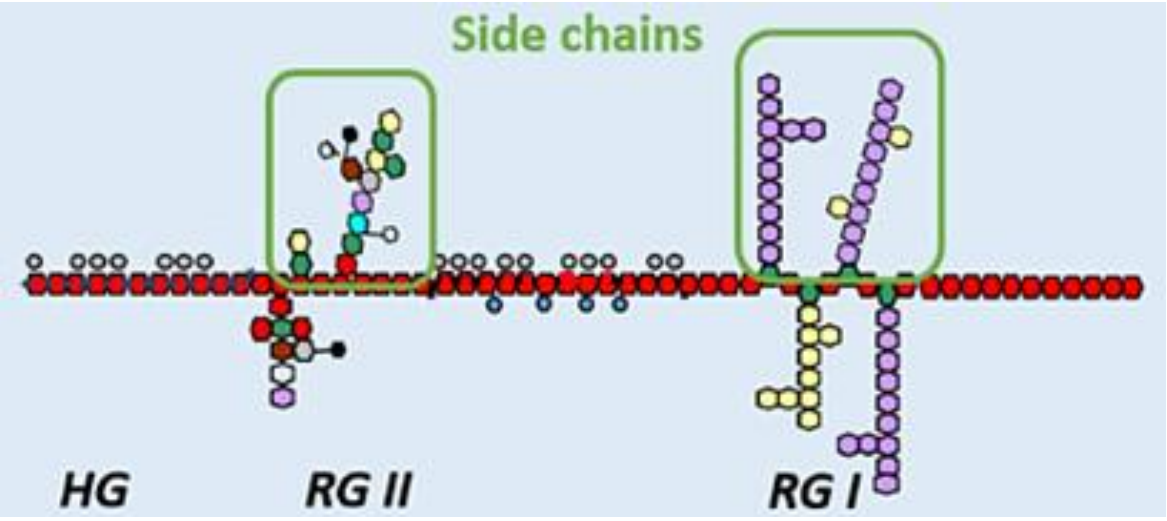

Figure I.3 *: Représentation schématique globale des différents domaines structuraux des pectines selon (Celus, Kyomugasho et al. 2018). HG : homogalacturonanes, RG I et II : rhamnogalacturonanes I et II. Les hexagones rouges : les unités d'acides galacturoniques ; les hexagones d'autres couleurs : les différents oses neutres ; les points gris : les méthyle-esters ; les points bleus : les acétyle-esters.*

I.2.1.1. Les homogalacturonanes

Prédominants, les HG forment le domaine linéaire des pectines, caractérisés par un enchainement d'acides α-D-galacturoniques liés en 1→4. La longueur de ces chaînes peut aller de 70 à 100 résidus d'acide galacturonique dans le citron, la betterave sucrière ou dans la pomme. Des dérivés xylo-(1→4)-α-galacturonanes, correspondant à des HG substitués par des xyloses ou des xylo-oligomères, sont particulièrement présents dans les pectines de pommes (Schols, Bakx et al. 1995). Les acides galacturoniques peuvent être estérifiés par du méthanol ou de l'acide acétique. Le pourcentage d'acide galacturonique estérifié est défini par le degré de méthyle-estérification, paramètre structurel définissant la capacité de complexation des pectines (Thibault and Ralet 2008). En effet, les résidus non méthyles estérifiés d'acides galacturoniques peuvent être sous forme galacturonates lorsque le pH est supérieur à celui du pKa des pectines : compris entre 2,8 et 4,1 (Ralet, Dronnet et al. 2001).

Sans avoir pu le démontrer, Brown et Fry (1993) ont émis l'hypothèse que sous cette forme, les galacturonates peuvent estérifier des groupements alcools environnants et en particulier ceux issus d'autres chaines polysaccharidiques, conduisant à leur réticulation. Outre la formation de ces galacturonoyles, les galacturonates peuvent interagir avec les cations présents dans le milieu. Ainsi, une pectine avec un degré de méthyle estérification faible, présente un nombre important de résidus d'acide galacturonique non méthyle estérifié et donc une capacité d'interaction avec des cations plus élevée. Ces interactions conduisent à la formation de gel pectique qui peut être de différentes natures. En effet, lorsqu'il s'agit de cations métalliques et en particulier le cation divalent du calcium dans le cas des HGs, les blocs non estérifiés s'agrègent pour former des zones de jonction et maintenir le gel pectique (Jarvis, Briggs et al. 2003). Les agrégats peuvent être formés d'au minimum deux ou quatre chaines, et plus, en fonction du taux de calcium. Néanmoins, il a été rapporté que des blocs de 7-20 résidus d'acides galacturoniques libres sont nécessaires pour la complexation des pectines au calcium (Braccini, Grasso et al. 1999). En effet, la gélification des pectines par complexation avec les ions métalliques dépend du degré de méthyle-estérification mais aussi de la distribution des groupements carboxyliques libres dans les chaines polysaccharidiques. Plus le nombre successif de groupements libres est important, et plus la capacité de complexation est élevée (Slavov, Bonnin et al. 2008). La quantification de la distribution de ces groupements carboxyliques libres dans la pectine est définie par le degré de « blockiness » (Löfgren, Guillotin et al. 2005). De travaux récents ont aussi montré la réticulation potentielle des pectines de citron par interaction avec des cations métalliques monovalents tels que le potassium (Wang, Wan et al. 2019). Toutefois, la réticulation des pectines peut faire intervenir d'autres structures polysaccharidiques que les galacturonates, notamment via les RG I et II.

I.2.1.2. Les rhamnogalacturonanes de types I et II

Contrairement aux HG, les RG sont des domaines pectiques fortement ramifiés. Les RG I sont caractérisés par un enchainement de disaccharide → 4)-α-D-acide galacturonique-(1 → 2)-α-L-rhamnose –(1→, présentant différentes chaines ramifiées en C-4 du rhamnose composés d'oses neutres, principalement du D-galactose et L-arabinose (Voragen, Coenen et al. 2009). Les RG I ne possèdent pas de résidus d'acides galacturoniques méthyles estérifiés mais plutôt acétylés en position O2 ou O3. Par contre, les résidus galactose et arabinose de ces RG I peuvent être estérifiés par des acides hydroxycinnamiques, notamment l'acide férulique. Sous leurs formes dimériques, ces esters feruloylés permettent la réticulation des RG I (Voragen, Coenen et al. 2009).

Les RG II, en plus faibles quantités sont composés d'un squelette d'HG d'environ neuf acides α-D-galacturoniques liés en 1→4 avec quatre chaines ramifiées de douze différents glycosides (Caffall and Mohnen 2009). Les résidus d'acide galacturonique peuvent être méthyle estérifiés. Cependant, les RG II complexent aussi le bore formant des esters, notamment via le résidu apiofuranosyle des chaines ramifiées contenant du 2-O-methyl-D-xylose (Ishii, Matsunaga et al. 1999). Les complexes bore-RG II contiennent deux molécules d'acide borique, deux chaines monomères de RG II et aussi deux molécules de calcium (Matoh and Kobayashi 1998). Les RG II ont donc la capacité de se dimériser et de permettre la réticulation de deux molécules de HG (Ishii and Matsunaga 2001).

Les différentes interactions conduisant à la réticulation des pectines sont présentées dans la **Figure I.4**.

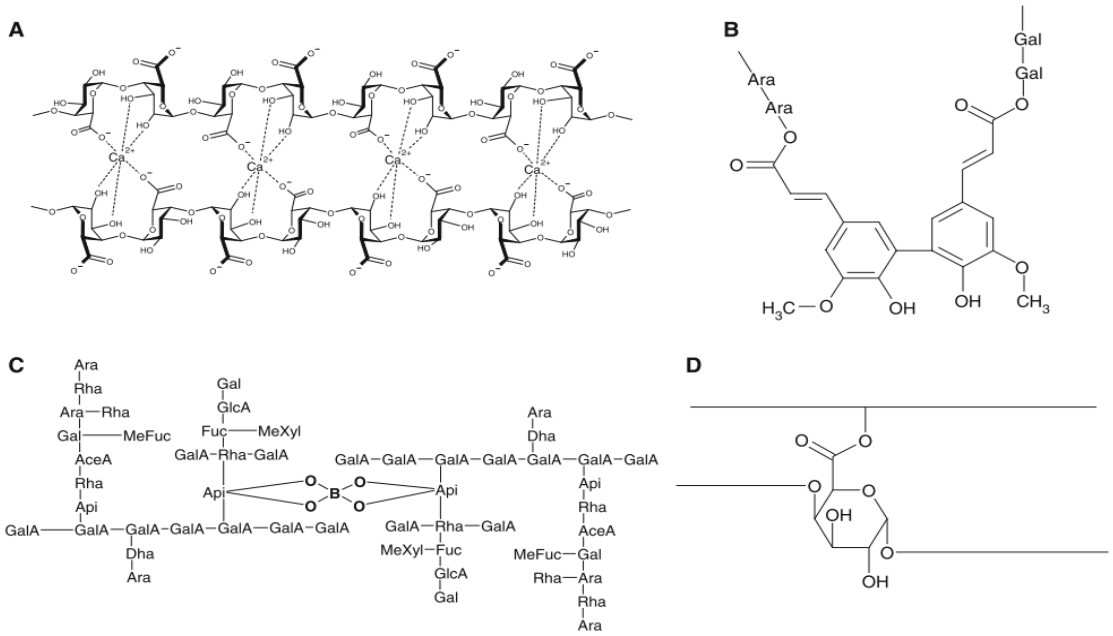

Figure I.4 *: Les mécanismes de réticulation des pectines rapportés par Voragen et al. (2009). A/ Complexe calcium-pectine suivant le modèle « egg-box »; B/ Dimère d'acide férulique lié en C5 estérifié au oses neutres de chaines ramifiés de pectines; C/ Diester de RG II; D/ Hypothétique ester d'uronyl de pectine avec un groupement hydroxyle d'une autre chaine polysaccharidique.*

I.2.2. Les pectines de pomme et de raisin

La composition polysaccharidique, en particulier des pectines issues de pommes et de raisins, a été rapportée par Voragen, Coenen et al. (2009) et est présentée dans la **Table I.1**.

Table I.1 : Proportions des différents éléments structuraux dans la pomme et le raisin (Voragen, Coenen et al. 2009).

	Raisin	*Pomme*
Total polysaccharides (% de matière sèche)	11	20
Substance pectiques (% total polysaccharides)	56	42
Eléments structuraux (% substances pectiques)		
Homogalacturonane (HG)	65	36
Xylogalacturonane (XG)	n.a	4
Rhamnogalacturonane I (RG I)	10	1
Chaines ramifiées neutres	23	47
Rhamnogalacturonane II (RG II)	2	10

Ces données montrent différentes compositions entre les deux types de fruits avec un pourcentage plus élevé de XG, RG II, de chaines ramifiées neutres et de polysaccharides pariétaux pour la pomme. Au contraire, le raisin présente un nombre plus important de substances pectiques associé à un pourcentage plus élevé de HG et de RG I. Cependant, les HG sont des domaines majoritaires pour ces deux fruits, avec des degrés d'estérification élevés à ≈ 70 – 80 % (Klein, Hanzon et al. 1995) pour la pomme et ≈ 50% pour le raisin (Gao, Fangel et al. 2015). Les différentes proportions de ces substances pectiques associées à leur organisation, régulent la façon dont elles peuvent interagir et induire la réticulation de la pectine. Par ailleurs, bien que les aptitudes d'interaction de la pectine avec les cations soient influencées par les différents domaines structuraux, seule l'influence des HG associée à leur degré d'estérification a été étudiée de manière approfondie (Celus, Kyomugasho et al. 2018).

I.3. Les ions métalliques

Les minéraux et les éléments-traces influencent la qualité des fruits. En particulier, la concentration et la distribution des ions métalliques influencent la physiologie, la qualité et la maturation des fruits (Knee 2002).

La présence d'éléments minéraux et en particulier les ions métalliques, est très variable au sein des végétaux en fonction de leur environnement, de leur état physiologique et aussi selon les organes considérés (Lambers, Chapin et al. 2008).

Dans les fruits, le potassium (K) est retrouvé en grande majorité devant le magnésium (Mg) et le calcium (Ca), et les ions métalliques de transition tels que le fer (Fe), le cuivre (Cu), le manganèse (Mn) et le zinc (Zn) sont présents à l'état de traces. Les plages de teneurs rapportées pour ces ions métalliques dans la pomme et le raisin sont détaillés dans la **Table I.2**. Les concentrations de ces ions dans l'apoplaste n'ont pas été décrites pour ces fruits, mais quelques valeurs retrouvées dans le fluide apoplasmique ou dans les parois cellulaires sur d'autres fruits sont aussi rapportées dans la **Table I.2**.

Table I.2 : Teneurs en ions retrouvées dans la littérature (Almeida and Huber 1999, Abadía, López-Millán et al. 2002, Fry, Miller et al. 2002, Özcan, Harmankaya et al. 2012, USDA 2018)

	K	**Ca**	**Mg**	**Fe**	**Cu**	**Mn**	**Zn**
Pomme ($\mu g.g^{-1}$ de fruit sec)	720 – 12000	40 – 1400	30 – 920	0,6 – 35	0,5 – 13	0,2 – 8	0,1 – 35
Raisin ($\mu g.g^{-1}$ de fruit sec)	650 – 13300	980 – 1200	720 – 1400	2 – 32	0,1 – 18	1 – 12	0,8 – 7
Apoplaste (mM)	13 – 37 Tomate	4 – 5 Tomate	8 – 15 Tomate	2,5-5,5 $.10^{-3}$ Betterave	-	-	-
Vacuole (mM)	40-50 Tomate	0,3 Tomate	4-5 Tomate	-	-	-	-
Paroi cellulaire ($\mu g.g^{-1}$ de paroi sec)	-	-	-	-	3-30 Fruit	-	-

I.3.1. Distribution des ions métalliques dans les pommes et raisins

Hautement solubles en solution aqueuse, ces ions métalliques sont absorbés, transportés et distribués dans les différents tissus des fruits via les mouvements d'eau (Finley, Hurst et al. 2018). Dans la pomme et le raisin, ces ions métalliques ont surtout été mesurés à l'échelle du fruit, dans la peau et la chair. Généralement, les teneurs dans la peau et la chair sont assez proches, bien qu'elles aient tendance à être légèrement plus élevées dans la peau, en particulier pour les ions métalliques de

transition. Des travaux anciens sur la distribution du K, Ca et Mg dans des sections de l'ordre du mm pris dans la pomme Cox's Orange Pippin ont montré des teneurs plus élevées dans la peau et le péricarpe (Ferguson and Watkins 1983). Peu d'études ont été réalisées sur la distribution des ions dans les fruits charnus à plus petite échelle. Seuls le Ca et l'azote ont été retrouvés dans les zones de jonctions intercellulaires et les parois cellulaires de pommes (Huxham, Jarvis et al. 1999).

I.3.2. Leurs fonctions connues

Les effets des ions métalliques sur les métabolismes des fruits ont été étudiés aux niveaux biochimique et physiologique. Cependant, au niveau moléculaire les informations sont encore limitées. De façon générale, les ions métalliques permettant le maintien de la turgescence et du pH, agissent sur la perméabilité membranaire et les phénomènes d'oxydation au sein des tissus cellulaires.

I.3.2.1. Le potassium

Le K est l'ion métallique majoritaire dans les fruits sous sa forme cationique monovalente (i.e. K^+) et intervient dans de nombreuses fonctions (Rogiers, Coetzee et al. 2017) telles que décrites en **Figure I.5**. En effet, le K participe à la respiration cellulaire. Il est indispensable pour l'activation de diverses enzymes dans le tissu en complexant l'oxygène des groupements carboxyle et hydroxyle des acides aminés (i.e. acide aspartique, sérine, …) (Mengel 2016). De même, il a été montré que le K serait en partie lié à l'extensine, une protéine impliquée dans le processus de croissance cellulaire comme décrit chez Chara (Boyer 2016). Omniprésent dans les solutions des tissus, le K a un rôle majeur dans l'absorption et le transport des différents ions organiques et inorganiques. Il permet la concentration de composés d'intérêt tels que les ions métalliques, les polyphénols ou les sucres dans les différents compartiments cellulaires. Il a donc une fonction osmotique importante en régulant la turgescence cellulaire et le potentiel électrique des compartiments cellulaires. Pour remplir toutes ces fonctions, cet élément doit être en quantité suffisante dans le tissu cellulaire et il a été montré chez la tomate que malgré une culture sur sols appauvris ou enrichis en potassium, la teneur en potassium reste constante dans le fruit (Mengel 2016).

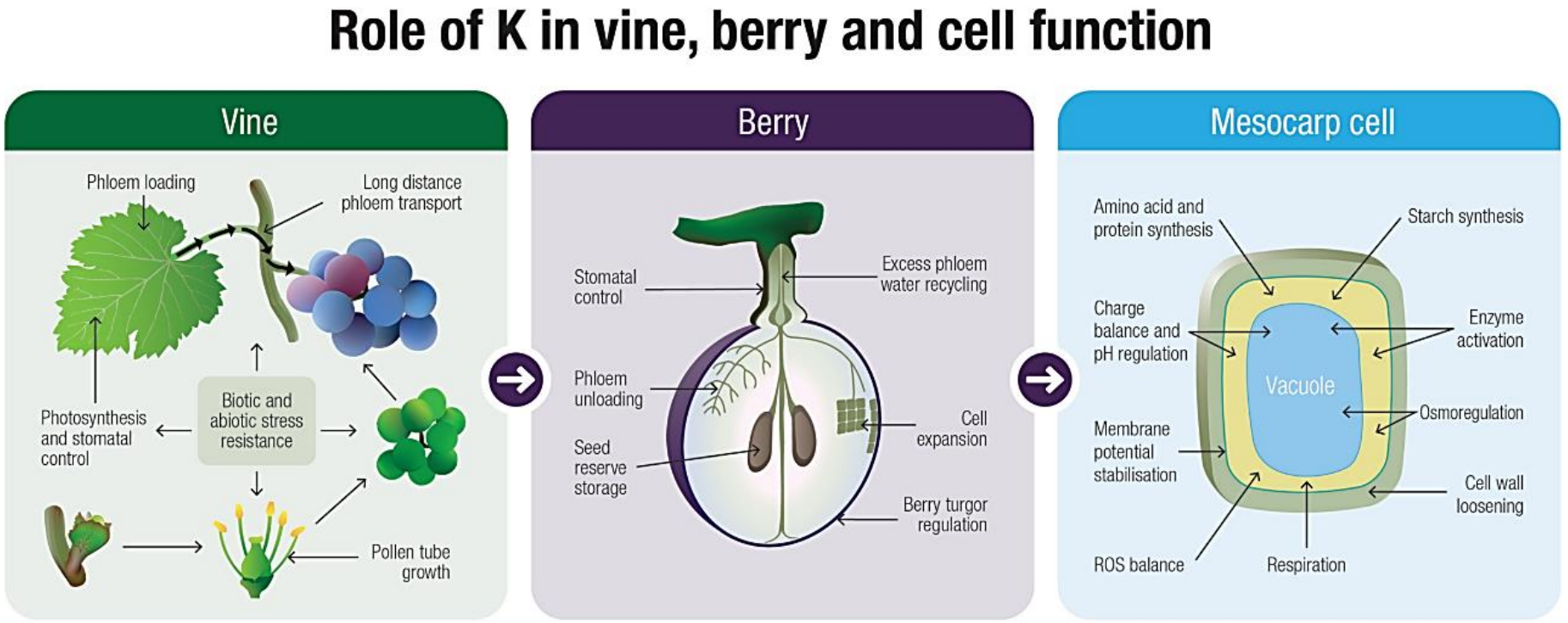

Figure I.5 *: Modèle spéculatif décrivant les fonctions du K^+ dans les raisins de cuves à l'échelle de la plante entière, du fruit et de la cellule. (Rogiers, Coetzee et al. 2017)*

I.3.2.2. Le calcium

Le transport, les fonctions et les interactions du Ca dans les plantes ont largement été étudiés (Pilbeam and Morley 2016), et particulièrement décrits dans les fruits par Hocking, Tyerman et al. (2016) (**Figure I.6**). Le Ca est majoritairement présent sous sa forme Ca^{2+} associée aux anions organiques pour former du malate de calcium, de l'oxaloacetate de calcium et de l'oxalate de calcium (Nakata 2003). Au niveau des parois cellulaires, le Ca a surtout été localisé dans les jonctions tri-cellulaires (Christiaens, Van Buggenhout et al. 2016), en complexant les charges négatives de l'acide galacturonique des pectines **(Figure I.6)**. Outre sa fonction en tant qu'agent réticulant les pectines, le Ca aurait un rôle inhibiteur des enzymes de dégradation des pectines telles que la polygalacturonase (Seling, Wissemeier et al. 2000), limitant ainsi la dégradation de la paroi cellulaire et donc la perte de fermeté du tissu cellulaire et du fruit. Il semble aussi influencer le fonctionnement de l'auxine, une hormone permettant la croissance tissulaire et l'élongation des parois cellulaires (Tonetto De Freitas, Amarante et al. 2016).

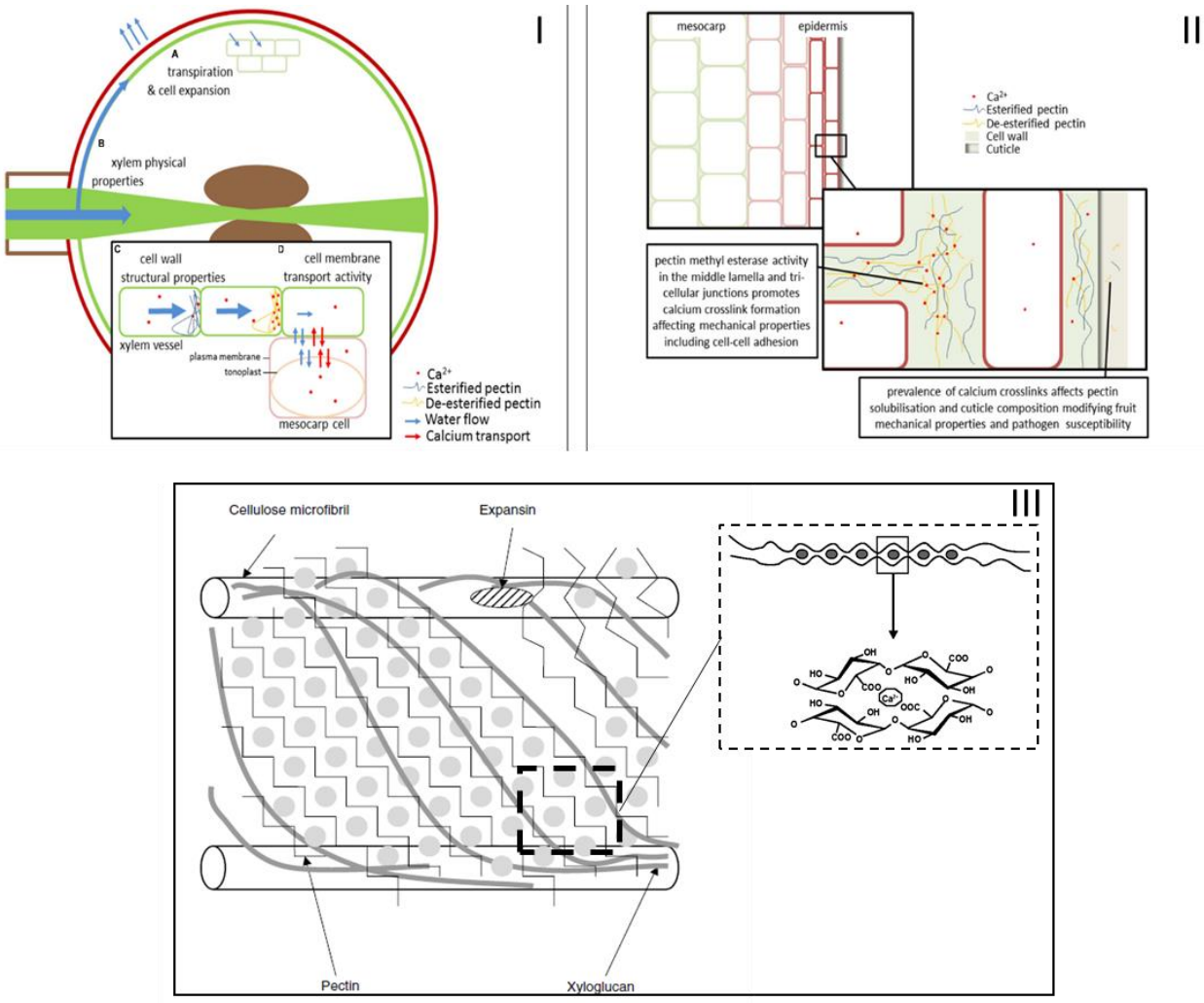

Figure I.6 : *Transport et distribution du calcium dans le fruit (I), sa localisation dans les parois cellulaire (II) et son interaction au niveau moléculaire (III) (Hocking, Tyerman et al. 2016, Pilbeam and Morley 2016).*

I.3.2.3. Le magnésium

Le Mg, majoritaire sous la forme Mg^{2+}, est un élément majeur dans les fruits. Présent dans la structure moléculaire des chlorophylles, le Mg peut aussi être cofacteur de plusieurs enzymes associées à la phosphorylation et à l'hydrolyse de différents composés. 15 à 30% du Mg dans les plantes sont associés à la chlorophylle alors que les autres 70-85% sont associés à sa fonction de cofacteur d'enzymes (Marschner 2011). Au niveau de la physiologie des fruits, il a été montré dans la pomme que les concentrations en Mg étaient inversement corrélées à la couleur contrairement à la concentration en K. Ainsi, la couleur des fruits serait modulée par des variations de concentration en Mg et des autres ions métalliques comme décrit par Fallahi and Simons (1996).

I.3.2.4. Les ions métalliques de transition

Les ions métalliques de transition sont tout aussi importants pour le métabolisme, le développement et la qualité du fruit mais leurs rôles sont encore mal connus. D'autant plus qu'on ne les retrouve qu'en très petites quantités, voire à l'état de traces (**section I.3 ; Table I.2**). Les teneurs dans les plantes sont extrêmement dépendantes de l'environnement, notamment des sols et conditions de culture. Des concentrations élevées dans les tissus peuvent être toxiques pour la plante en altérant divers processus, tel que des activités enzymatiques, l'absorption racinaire, la translocation et l'utilisation d'autres minéraux. Généralement, ils participent à de nombreuses fonctions dans le système enzymatique et les processus biochimiques d'oxydation. La **Table I.3** regroupe les caractéristiques des quatre ions métalliques Fe, Cu, Mn et Zn décrites dans les plantes.

Table I.3 : Quelques caractéristiques des métaux de transition dans les plantes

Métal	Forme majeur	Potentiel redox	Ligands	Références
Fer	Fe^{2+} et Fe^{3+}	Fe^{3+}/ Fe^{2+}: 0,771 Fe^{3+}/Fe : −0,037 Fe^{2+}/Fe : −0,447	- Catalases - Peroxydases - Protéines (complexe type Fer-porphyrine)	(Briat and Lobréaux 1997) (Barrett 1981) (Hether, Olsen et al. 1984) (Römheld and Nikolic 2016)
Cuivre	Cu^{+} ou Cu^{2+}	Cu^{+}/Cu : 0,521 Cu^{2+}/Cu : 0,342 Cu^{2+}/Cu^{+} : 0,153	- Superoxyde dismutase : protéine de défense - Plastocyanine : protéine de transferts d'électrons photosynthétiques - Cofacteur de PPO : peroxydase des composés phénoliques des fruits	(Quartacci, Cosi et al. 2003) (Sautron 2015) (Jukanti 2017) (Kopsell and Kopsell 2016)

			- Complexe les thiols, carbonyles, carboxyles et phénoliques	
Manganèse	Mn^{2+}	Mn^{2+}/Mn : −1.185	- Cofacteur d'enzymes et protéines de photosynthèse - Activateur d'enzymes de la respiration : déshydrogénase, transférases, hydroxylases et décarboxylases	(Humphries, Stangoulis et al. 2016) (Burnell 1988) (Buchanan, Gruissem et al. 2000) (Rengel 2000) (Ducic and Polle 2005, Lei, Korpelainen et al. 2007)
Zinc	Zn^{2+}	Zn^{2+}/Zn : −0.7618	- Complexe les acides organiques - Cofacteur d'enzymes : alcool déshydrogénase, carbone anhydrase	(Kochian 1991) (Vallee and Auld 1990) (Storey 2016)

I.3.2.4.1. Le fer

Accepteur-donneur d'électrons dans le système de respiration, le fer est cofacteur des catalases (réaction A) et peroxydases (réaction B) transformant le peroxyde d'hydrogène en H_2O et O_2:

$$2H_2O_2 \rightarrow 2H_2O + O_2 \text{ (A)}$$

$$H_2O_2 + AH_2 \rightarrow A + 2H_2O \text{ (B)}$$

$$2AH + H_2O_2 \rightarrow A–A + 2H_2O \text{ (C)}$$

- Avec AH_2 un substrat donneur d'électron (souvent des composés phénoliques (Barrett 1981)).

Les catalases ont un rôle majeur dans les réactions de photorespiration, telles que les glycolates oxydases, et elles sont impliquées dans la protection des chloroplastes par les radicaux libres produits lors des réactions de photosynthèse. Les réactions de la peroxydase comme décrites ci-dessus incluent les peroxydases des parois cellulaires et peuvent catalyser la polymérisation des composés phénoliques (réaction C). Le fer libre dans les systèmes biologiques présente une faible solubilité et peut réagir avec l'oxygène pour générer des dérivés réactifs de l'oxygène, incluant les radicaux hydroxyles ; il doit donc être conservé sous une forme « inactive » et soluble. L'apoplaste et les vacuoles sont les deux principaux compartiments impliqués dans cette fonction (Briat and Lobréaux 1997), concentrant le fer sous forme Fe^{2+} (Hether, Olsen et al. 1984, Römheld and Nikolic 2016).

I.3.2.4.2. Le cuivre

Oxydant fort après le fer, le Cu est essentiel pour les plantes comme décrit par Kopsell (2016). Cet élément est principalement associé aux parois cellulaires grâce à son affinité pour les groupements

thiol, carbonyles, carboxyles et phénoliques (Quartacci, Cosi et al. 2003). Le Cu peut aussi être localisé dans les chloroplastes, comme démontré chez *Arabidopsis* à hauteur de 50% du cuivre total de la plante (Sautron 2015). Il y joue le rôle de cofacteur de deux protéines essentielles : la superoxyde dismutase, impliquée dans la défense contre des espèces réactives de l'oxygène au niveau du stroma et la plastocyanine, une protéine du lumen des thylakoïdes, impliquée dans la chaine de transfert des électrons photosynthétiques. Ce métal peut aussi être cofacteur d'enzymes, telles que la polyphénol-oxydase qui est la principale métallo-peroxydase impliquée dans l'oxydation des composés phénoliques dans les fruits (Jukanti 2017).

I.3.2.4.3. Le manganèse

Le Mn a un rôle catalytique et participe à la structure des enzymes et protéines de photosynthèse (Humphries, Stangoulis et al. 2016). Le Mn est un activateur d'enzymes telles que les déshydrogénases, transférases, hydroxylases et décarboxylases impliquées dans la respiration (Burnell 1988). Il est aussi impliqué dans la réaction de Hill conduisant à la formation d'O_2 dans les chloroplastes via la photosynthèse.

Réaction de Hill : $2H_2O + 2A + (\text{lumière, chloroplastes}) \rightarrow 2\,AH_2 + O_2$

➔ Avec A : accepteur d'électron artificiel

Le Mn est en compétition avec l'ion Mg^{2+} et en réduit considérablement son taux d'absorption (Buchanan, Gruissem et al. 2000). A des degrés d'oxydation supérieurs (Mn (III) ou (IV)), il ne peut pas être transporté ou stocké (Rengel 2000).

I.3.2.4.4. Le zinc

Le zinc a un rôle catalytique et structural dans les réactions enzymatiques (Vallee and Auld 1990). Par exemple, il participe à la réduction d'acétaldéhyde en éthanol via l'alcool déshydrogénase et est contenu dans la carbone anhydrase présent dans le cytoplasme et les chloroplastes (Storey 2016).

I.3.3. Génération de ROS

Au-delà de leurs interactions avec les différentes biomolécules présentes dans les tissus cellulaires, les ions métalliques et en particulier les ions de transition conduisent à la formation de dérivés réactifs de l'oxygène plus communément nommés sous le terme anglosaxon « reactive oxygen species » ou ROS. Parmi ces ROS nous retrouvons les formes radicalaires et non radicalaires de l'oxygène comme décrit dans la **Table I.4.**

Table I.4 : Principaux ROS avec leur temps de demi-vie (del Río 2015, Halliwell and Gutteridge 2015)

Radicaux libres	***Demi-vie***	**Non radicalaires**	***Demi-vie***
Peroxyle : $ROO^{\bullet}$	~ *seconde*	Peroxyde d'hydrogène : H_2O_2	~ *minutes*
Superoxyde : $O_2^{\bullet-}$	~ *microseconde*	L'ion peroxynitrite : $ONOO^-$	~ *milliseconde*
Alkoxyle : $RO^{\bullet}$	~ *microseconde*	Oxygène singulet : $^1O_2$	~ *microseconde*
Hydroperoxyle : $HO_2^{\bullet}$	~ *microseconde*	Ozone : O_3	-
Hydroxyle : $HO^{\bullet}$	~ *nanoseconde*	Acide hypochloreux : HOCl	-

Ces ROS peuvent être produits lors de réactions enzymatiques (NADPH, acétyle co-enzyme A, peroxydase, …) ou même par les chloroplastes. En effet, dans les systèmes biologiques en milieu aérobie, les ions métalliques de transition participent à la production de formes radicalaires plus toxiques que les espèces moins réactives, telles que le superoxyde et le peroxyde d'hydrogène issus des voies enzymatiques. La formation de ces radicaux a lieu lors des réactions de Fenton (2) ou d'Haber-Weiss (Kehrer 2000) décrites ci-dessous. Bien que d'autres ions de transition soient capables de catalyser ces réactions, la réaction d'Haber Weiss catalysée par le fer via la réaction de Fenton, est considérée comme le principal mécanisme de formation de ces espèces extrêmement réactives dans les systèmes biologiques (Liochev 1999).

$$Fe^{3+} + O_2^{\bullet-} \rightarrow Fe^{2+} + O_2 \qquad (1)$$

Fenton: $Fe^{2+} + H_2O_2 \rightarrow Fe^{3+} + OH^- + OH^{\cdot}$ (2)

Haber Weiss: $O_2^{\bullet-} + H_2O_2 \xrightarrow{Fe^{2+}/\ Fe^{3+}} O_2 + OH^- + OH^{\cdot}$ (1) + (2)

Les hydroxyles radicalaires sont extrêmement réactifs (temps de demi-vie : 10^{-9} s) et ont donc un taux de diffusion limité. Ainsi, la présence et la concentration des ions métalliques de transition dans différents compartiments cellulaires peuvent déterminer la formation de ces radicaux hydroxyles en générant potentiellement des « hot-spots » avec une action localisée. Par conséquent, les effets destructeurs de ces radicaux seraient donc localisés dans des régions définies de la cellule ou du tissu cellulaire (Desikan, Hancock et al. 2005). Leur présence a aussi été associée à un rôle de signal cellulaire qui serait généré en réponse à un stress primaire biotique ou abiotique (Chen and Schopfer 1999,

Foreman, Demidchik et al. 2003). Ces ROS générés seraient donc nocifs pour les biomolécules environnantes, et induiraient par exemple la déconstruction des pectines de parois cellulaires (Airianah, Vreeburg et al. 2016) ou la structure des composés phénoliques (Gülçin 2012).

I.4. Les composés phénoliques

Encore plus que les ions minéraux, les composés phénoliques interviennent très largement sur l'impact sensoriel des aliments. Ils peuvent agir au niveau du goût, ce qui est le cas des tannins par exemple pour l'astringence et l'amertume des vins, ou encore au niveau de la couleur pour les anthocyanes. Les structures des composés phénoliques se distinguent par leurs squelettes carbonés, leurs degrés de modifications (oxydation, hydratation, méthylation…) et enfin par les liaisons pouvant exister avec d'autres molécules comme des sucres ou d'autres composés phénoliques.

Leurs chimies, structures et biosynthèses dans les végétaux ont largement été décrites dans la littérature (Vermerris and Nicholson 2006, Galanakis 2018). On distingue ainsi une dizaine de grandes classes de composés regroupant des formes simples (acides phénoliques, stilbènes, flavonoïdes, lignanes…) et des phénols condensés issus de la polymérisation des lignanes (lignines) ou de certains flavonoïdes (tannins) **(Figure I.7).** Dans les fruits, les acides hydroxycinnamiques et les flavonoïdes sont donc les principaux composés phénoliques présents.

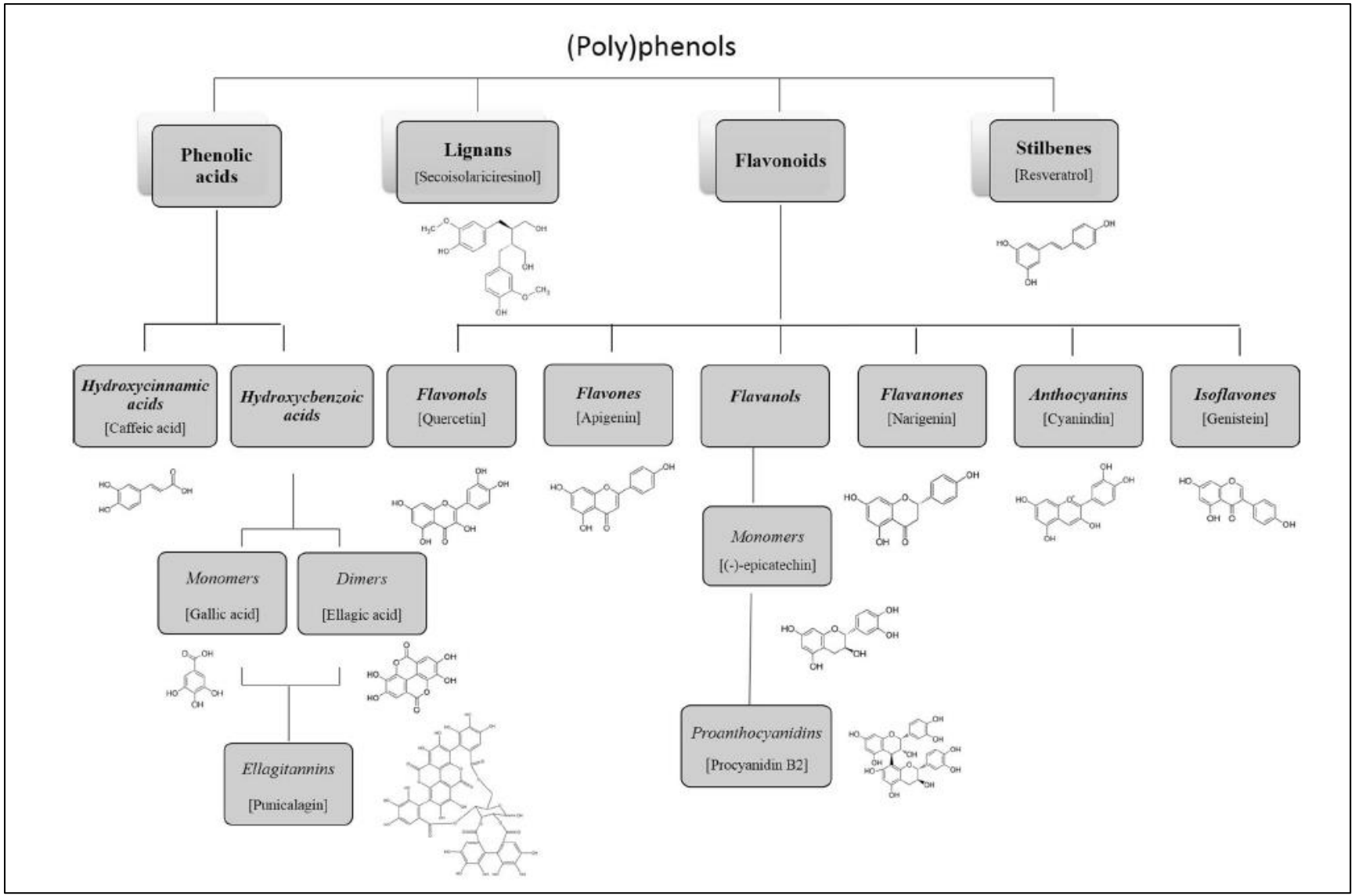

Figure I.7: *Principales classes de (poly)phénols. Les classes sont en gras, les sous-classes en italique-gras et les familles en italiques. La forme aglycone commune est représentée avec son nom respectif entre parenthèses. (Pinto and Santos 2017).*

I.4.1. Les acides hydroxycinnamiques

Dérivés de l'acide cinnamique, ils sont généralement estérifiés, le plus souvent avec l'acide quinique pour la pomme ou l'acide tartrique pour le raisin. L'acide 5'-caféoylquinique, aussi nommé acide chlorogénique, est l'acide majoritaire des pommes, alors que pour le raisin il s'agit de l'acide caféoyltartrique (acide caftarique). Leurs différentes structures sont présentées dans la **Figure I.8**.

Structure chimique	R_1	R_2	R_3	Nom du composé
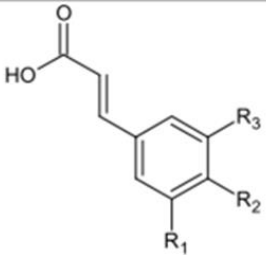	H	H	H	Acide cinnamique
	H	OH	H	Acide p-coumarique
	OH	OH	H	Acide caféique
	OCH_3	OH	H	Acide férulique
	OCH_3	OH	OCH_3	Acide sinapique
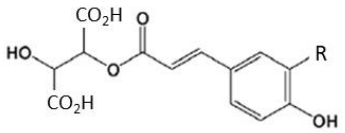	H			Acide p-coumaroyltartrique
	OH			Acide caféoyltartrique (acide caftarique)
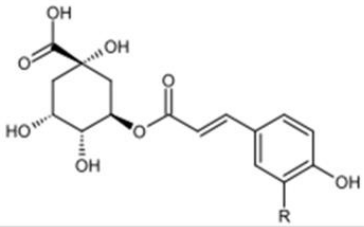	H			Acide 5'-*p*-coumaroylquinique
	OH			Acide 5'-caféoylquinique (acide chlorogénique)

Figure I.8 : *Structure chimique des acides hydroxycinnamiques et leurs esters.*

I.4.2. Les flavonoïdes

Les flavonoïdes ont un squelette formé de deux cycles aromatiques (A et B) et d'un hétérocycle dihydropyrane (C) :

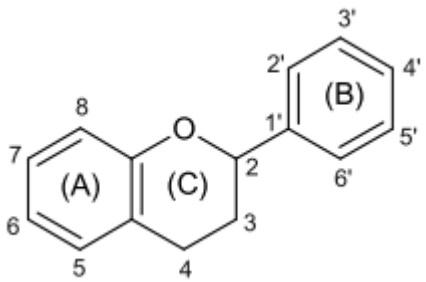

En fonction du degré d'oxydation du cycle (C), on peut distinguer différentes sous-familles de flavonoïdes **(Figure I.9)** : les flavanols, les flavonols, les dihydrochalcones et les anthocyanes.

Flavanols

Structure chimique	R1	R2	Nom du composé
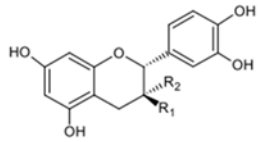	OH	H	(+)-Catéchine
	H	OH	(-)-Epicatéchine

Structure chimique	Nom du composé
épicatéchine-(4β→8)-catéchine	Procyanidine B1
épicatéchine-(4β→8)-épicatéchine	Procyanidine B2
épicatéchine-(4β→6)-catéchine	Procyanidine B5
[épicatéchine-(4β→8)]$_2$-épicatéchine	Procyanidine C1

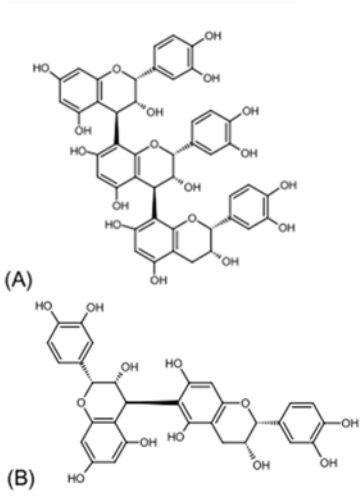

Exemple de structure d'une procyanidine C1 (A) et de la procyanidine B5 (B)

Pomme

Dihydrochalcones

Structure chimique	R	Nom du composé
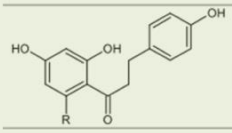	OH	Phlorétine
	O-Glucose	Phloridzine
	O-Glucose-Xylose	2'-*O*-xyloglucoside de phlorétine

Flavonols

Structure chimique	R	Nom du composé
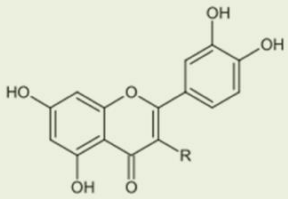	OH	Quercétine
	O-Galactose	Hypérine
	O-Rhamnose	Quercitrine
	O-Glucose	Isoquercitrine
	O-Xylose	Reynoutrine
	O-Arabinose	Avicularine
	O-Rutinose	Rutine

Anthocyanes

Structure chimique	R	Nom du composé
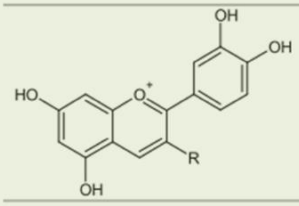	OH	Cyanidine
	O-galactose	Idéaïne

Raisin

Flavonols

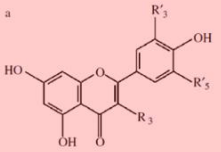

a) flavone (R_3 = H) and flavonol (R_3 = OH)
b) flavanone (R_3 = H) and flavanonol (R_3 = OH)

Anthocyanes

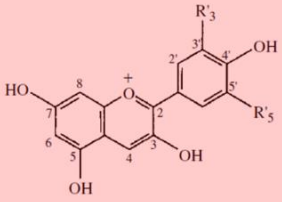

R'_3	R'_5	Name of aglycone
OH	H	Cyanidin
OCH_3	H	Peonidin
OH	OH	Delphinidin
OH	OCH_3	Petunidin
OCH_3	OCH_3	Malvidin

Figure I.9 : *Structure des flavonoïdes retrouvés dans la pomme et le raisin adapté de Ribéreau-Gayon, Glories et al. (2006), Verdu (2013).*

Les flavanols ont le cycle (C) le plus réduit des flavonoïdes. Les principaux monomères chez la pomme et le raisin sont la (+)-catéchine et le stéréo-isomère (-)-épicatéchine. Ces monomères ont la propriété de se polymériser pour donner les procyanidines, aussi appelées tanins condensés. La structure des procyanidines les moins condensées est aujourd'hui bien décrite avec des liaisons en C(4)-C(8) ou C(4)-C(6). Pour les procyanidines plus condensées, la variabilité structurale est plus importante et les données de la littérature ne permettent pas une identification exacte.

Les flavonols ont une fonction carbonyle, une insaturation en position 2,3 et un groupement hydroxyle additionnel sur le cycle (C). Les différents composés de cette sous-famille se distinguent par le degré d'hydroxylation du cycle B (monohydroxylé en 4' pour le kaempférol, dihydroxylé en 3' et 4' pour la quercétine et trihydroxylé en 3', 4' et 5' pour la myricétine) et par la nature des glycosides. Dans la pomme et le raisin, on trouve principalement les dérivés de glycosylés en position 3.

Contrairement aux autres flavonoïdes, les dihydrochalcones n'ont pas subi la cyclisation intramoléculaire conduisant à l'élaboration du cycle pyrane (C). On retrouve deux principaux composés glycosylés dans la pomme dérivée de la phlorétine : la phloridzine et le xyloglucoside de phlorétine.

Les anthocyanes ont le niveau d'oxydation du cycle (C) le plus élevé et sont présentes sous forme cationique en milieu très acide. On distingue là encore les différents anthocyanes en fonction du degré d'hydroxylation de leur cycle (B) et de la nature des sucres associés. Les anthocyanes sont notamment responsables de la coloration rouge des fruits. Plusieurs facteurs peuvent intervenir simultanément pour modifier la couleur des anthocyanes comme la nature même des molécules, leur concentration, le pH ou les interactions avec d'autres molécules du milieu (co-pigments). La couleur d'une solution d'anthocyanes peut ainsi varier du rouge au bleu en passant par toutes les teintes de violet (Macheix, Fleuriet et al. 2017). Dans la pomme, on ne retrouve principalement qu'un dérivé glycosylé de la cyanidine (l'idéaïne) (Khanizadeh, Tsao et al. 2008), alors que dans le raisin ce sont des dérivés glucosidés de la delphinidine, la cyanidine, la petunidine, la peonidine et la malvidine (Mattivi, Guzzon et al. 2006).

I.4.3. Distribution des composés phénoliques dans les pommes et raisins

Les composés phénoliques, comme l'ensemble des métabolites, se répartissent très inégalement en fonction de l'espèce végétale, des variétés, des stades d'évolution physiologique et des organes ou tissus considérés (Macheix, Fleuriet et al. 2017). Abondants dans les fruits, ils influencent largement leurs qualités. Dans la pomme et le raisin, ces composés phénoliques ont surtout été mesurés, à l'échelle du fruit, dans la peau et la chair avec des proportions plus importantes dans la peau (Di Lecce, Arranz et al. 2014, Kschonsek, Wolfram et al. 2018). Peu d'études ont été réalisées sur la localisation des composés phénoliques à plus petite échelle. Des travaux ont montré la

présence de flavanols et tannins condensés au niveau des cellules de l'épiderme, du parenchyme et dans les pépins (Amrani and Mercierz 1994, Lees, Suttill et al. 1995). De même, Hagen, Solhaug et al. (2006) ont montré la localisation des anthocyanes et flavonoïdes dans l'épiderme de pommes. Leur cartographie spécifique au niveau subcellulaire reste méconnue. Cependant, tout comme les autres métabolites (sucres, acides aminés, acides organiques, …), les composés phénoliques sont acheminés et stockés principalement dans la vacuole et la paroi cellulaire, et peuvent également être présents dans le cytosol, le réticulum endoplasmique, les chloroplastes, le noyau, les vésicules golgiennes ou l'espace intercellulaire (Vermerris and Nicholson 2006).

I.5. Interactions pectine - ions métalliques – composés phénoliques

Bien que compartimentés, les ions et les composés phénoliques sont redistribués partiellement lors de la consommation et de la transformation des fruits. La diffusion de ces composés au sein du tissu permet de nouvelles interactions entre ces composés et les autres constituants de la matrice fruit. Par exemple, au niveau de la paroi cellulaire, de nouvelles interactions entre des ions métalliques et composés phénoliques intracellulaires avec les pectines peuvent avoir lieu. L'étude des interactions entre ces trois composés en présence n'a jamais été décrite, bien que quelques travaux aient été réalisés in-vitro sur des mélanges ions-pectine, composés phénoliques-pectine et ions-composés phénoliques.

I.5.1. Ions métalliques et pectine

Le caractère hydrophile et anionique de la pectine permet par ses fonctions carboxyliques non estérifiées la formation de complexes avec les cations. Concernant ces interactions, de nombreuses études ont été réalisées en système modèle dilué par rapport aux conditions réelles du tissu cellulaire de fruit. Un exemple bien connu d'interaction dans les parois cellulaires des fruits est la complexation du Ca^{2+} avec les chaines d'acide galacturonique non estérifié de pectines, telle que décrite précédemment (**section I.3.2.2**). D'autres interactions entre HG avec le K^{+}, Mg^{2+}, Fe^{2+}, Zn^{2+} et le Cu^{2+}, peuvent exister (Celus, Kyomugasho et al. 2018), modulant la réticulation de la pectine et les propriétés mécaniques des parois cellulaires. Par ailleurs, en complexant les ions métalliques de transition, la pectine présente une fonction antioxydante comme démontrée pour des émulsions alimentaires (Xu, Liu et al. 2017), mais sa présence limite l'accessibilité de ces éléments d'un point de vue nutritionnel lors de la consommation humaine (Raes, Knockaert et al. 2014).

Cependant, le pH global mesuré dans les fruits (pommes et raisin) se situe aux environs de 3,0 à 3,5 ; et à ce pH la complexion des ions par la pectine serait plus faible. Ainsi, la présence des ions métalliques de transition libres, en particulier le fer et le cuivre, aurait un effet catalytique sur la formation de ROS au niveau de la paroi cellulaire et induirait notamment une déstructuration des chaines polysaccharidiques, dont les pectines comme décrites par Airianah, Vreeburg et al. (2016). Toutefois, d'autres composés présents dans la paroi cellulaire peuvent potentiellement avoir un rôle antioxydant limitant la dégradation des pectines, tels que les acides organiques (i.e. acide ascorbique (Davey, Montagu et al. 2000)) ou les composés phénoliques (Fry 1998, Galanakis 2018).

I.5.2. Composés phénoliques et pectine

En effet, des acides hydroxycinnamiques estérifiés aux parois cellulaires ont été retrouvés chez les graminées et quelques espèces des dicotylédones (Buanafina 2009). Ces acides

hydroxycinnamiques peuvent piéger les ROS (Abramovič 2015) formés dans les parois cellulaires et ainsi limiter la dégradation des pectines. Cependant, dans les pommes ou les raisins, la présence de ces acides estérifiés aux parois cellulaires n'a pas été montrée.

La protection des parois cellulaires vis-à-vis des ROS par les composés phénoliques n'a pas été décrite, mais des interactions entre composés phénoliques et parois cellulaires sont tout à fait possibles. Ces interactions *in-situ* dans les tissus cellulaires ont été peu étudiées à cause des limites analytiques, et du fait que les interactions sont faibles et ne permettent pas leur quantification. La revue de Jakobek et Matić (2018) décrit que les composés phénoliques tels que les procyanidines majoritairement, les catéchines, la cyanidine-3-glucoside et plus faiblement, les acides phénoliques (acide férulique, acide gallique, acides chlorogéniques, acide tannique) pourraient se condenser sur la cellulose, les hémicelluloses et les pectines via des liaisons hydrogènes, des interactions hydrophobes et de Van der Waals. La grande affinité des procyanidines avec les pectines affecterait l'accessibilité des polyphénols lors des processus de vinification par exemple (Renard, Watrelot et al. 2015). Dans le tissu cellulaire, ces composés phénoliques sont majoritairement situés dans les vacuoles des cellules intactes. Cependant, ces interactions peuvent uniquement avoir lieu lors de la rupture du tissu cellulaire, par exemple lors de traitements thermiques, de broyages ou de mastications (Le Bourvellec and Renard 2012).

I.5.3. Ions métalliques et composés phénoliques

La présence d'ions métalliques catalyse les phénomènes d'oxydation des composés phénoliques comme décrits par Clifford (2000). Plusieurs mécanismes peuvent intervenir tels que l'interaction directe des ions métalliques ou indirecte via leur action catalytique de la formation de ROS et de radicaux.

En effet, les fonctions hydroxyles des composés phénoliques ont une forte capacitée d'interaction avec les ions métalliques divalents, notamment lorsqu'ils se présentent sous la forme ortho-dihydroxyle de type catéchol ou pyrogallol. Des mécanismes de complexation **(Figure I.10**) sont proposés par de Souza, Sussuchi et al. (2003), Esparza, Salinas et al. (2004), Perron and Brumaghim (2009).

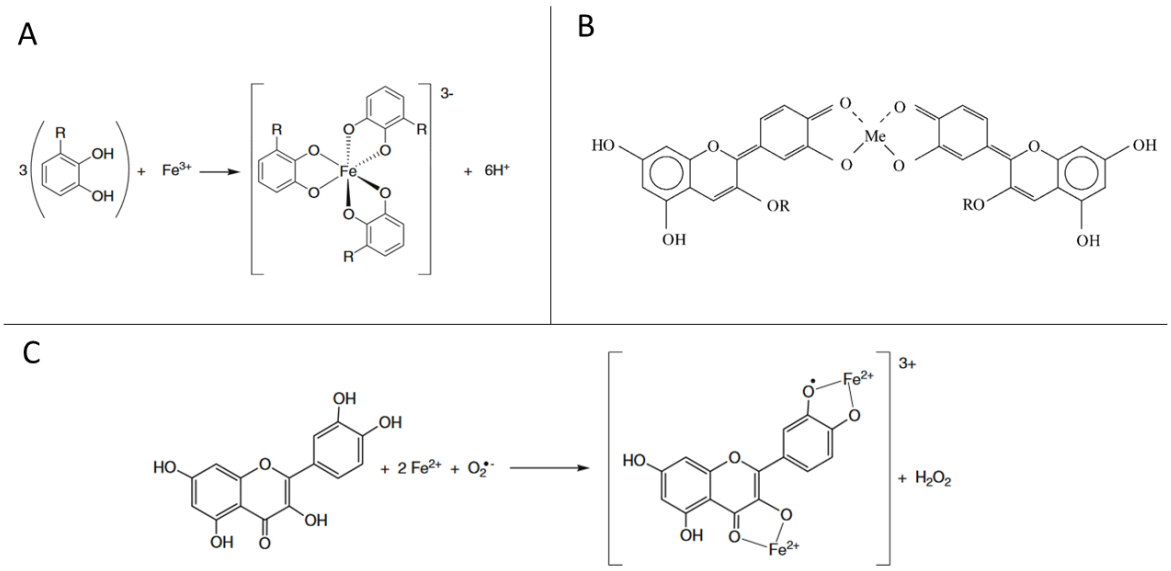

Figure I.10 : *A/Complexe fer-polyphénol (Perron and Brumaghim 2009), B/Structure d'un complexe métal (Me) – cyanidine-3-glucoside (R :glucoside) (Esparza, Salinas et al. 2004), C/ Réaction du complexe Fe^{2+}-quercetine avec le superoxyde (de Souza, Sussuchi et al. 2003).*

Il a été également montré que les ligands polyphénols stabilisent fortement le Fe^{3+} par rapport au Fe^{2+}, alors que les complexes de Fe^{2+}/catecholate (ou gallate) s'oxydent rapidement en présence d'O_2 pour former des complexes de Fe^{3+}/polyphénols, processus généralement renvoyé à l'auto-oxydation (Binbuga, Chambers et al. 2005, Chvátalová, Slaninová et al. 2008). Ainsi, en complexant les ions métalliques, les structures des polyphénols peuvent former des espèces quinones par des réactions d'oxydoréduction telles que décrites par Perron and Brumaghim (2009) dans la **Figure I.11.** Ces espèces quinones sont connues pour être peu stables et peuvent induire des réactions de polymérisation ou de scissions des structures des composés phénoliques (Sinela, Mertz et al. 2017).

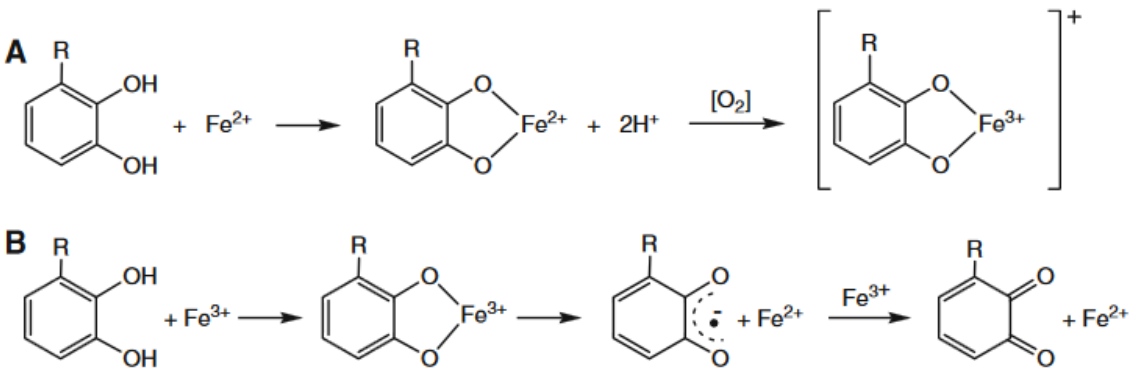

Figure I.11 *: A/ Coordination de Fe^{2+} par les polyphénols et la réaction de transfert d'électron induite en présence d'oxygène. B/ Coordination de Fe^{3+} par les polyphénols conduisant à la réduction du Fer pour former une espèce quinone et du Fe^{2+}. R=H, OH.*

I.5.3.1.1. Interaction avec les ROS

Les ROS formées par réaction des métaux de transition avec l'oxygène et ses dérivés, sont extrêmement réactives avec les structures des composés phénoliques. En effet, au même titre que les ions métalliques, les ROS radicalaires interagissent avec les structures ortho-dihydroxyles des composés phénoliques et forment des intermédiaires phénoxyls radicalaires plus stables (type semi-quinone). L'affinité pour les ROS va aussi dépendre de la structure globale du polyphénol et donc induire des différences de réactivité en fonction du type de composé phénolique (Smirnoff 2005).

I.5.3.1.2. Activité pro-oxydante

Les composés phénoliques peuvent aussi présenter une activité pro-oxydante sous certaines conditions. Cette propriété est due à la forme radicalaire de la semi-quinone qui peut conduire à une seconde réaction de nature pro-oxydante en présence de O_2 produisant du $O_2\bullet^-$, qui peut être ensuite réduit en H_2O_2 par la forme phénolique initiale :

$$Ph–O\bullet^- + O_2 \rightarrow Ph=O + O_2\bullet^-$$

$$Ph–OH + O_2\bullet^- + H^+ \rightarrow Ph–O\bullet^- + H_2O_2$$

De plus, certains composés phénoliques sont sujets à l'auto-oxydation générant des $O_2\bullet^-$, qui donnent des espèces plus réactives H_2O_2 et $\bullet OH$:

$$Ph–OH + O_2 \rightarrow Ph–O\bullet^- + O_2\bullet^- + H^+$$

La combinaison de ces réactions participe à l'activité cyclique d'oxydo-réduction de certains composés phénoliques avec la production concomitante de ROS. Ces activités pro-oxydantes sont souvent démontrées en présence de métaux de transition, en particulier en présence de fer et de cuivre (Cao, Sofic et al. 1997, Sakihama, Cohen et al. 2002).

I.5.3.1.3. Dans les systèmes in-vivo

La compartimentation dans les tissus cellulaires permet la séparation spatiale des composés phénoliques et des sites de production d'agents oxydants dans les chloroplastes et les mitochondries. Mais lorsque les stress oxydants sont élevés et induisent une production accrue de ROS, du H_2O_2 pourrait sortir des organelles et se retrouver dans le cytoplasme, la vacuole et l'apoplaste (Smirnoff 2005). En effet, cet enrichissement cytoplasmique et vacuolaire en peroxyde d'hydrogène (H_2O_2) issu des organelles a été décrite majoritaire lors de la senescence des feuilles associée à la dégradation des chloroplastes (del Río, Pastori et al. 1998). De la même manière, du H_2O_2 pourrait se retrouver dans les différents compartiments tissulaires lors de la maturation des fruits et la transformation des chloroplastes (Heaton and Marangoni 1996). Cependant, les composés phénoliques ne peuvent piéger

directement l'H_2O_2, mais la présence d'agents oxydants tels que les ions métalliques de transition ou des enzymes vacuolaires de type peroxydase permettent l'oxydation de ces composés phénoliques par les dérivés de l'H_2O_2 (Takahama 1989).

Ainsi, le piégeage des ROS et des ions métalliques par les composés phénoliques limite la dégradation des biomolécules environnantes et la formation d'autres ROS, au détriment de la préservation de leur structure. Cependant, les mécanismes de chélation des métaux aux polyphénols et la neutralisation de radicaux, doivent encore être explorés pour comprendre le comportement antioxydant et pro-oxydant des polyphénols dans les fruits frais ou transformés.

I.6. Méthodes d'analyses

I.6.1. Méthodes d'analyses des ions métalliques

Différentes méthodes existent pour l'analyse des ions métalliques mais peu sont adaptées au tissu végétal fortement hydraté ; caractéristique induisant une très forte mobilité de ces ions métalliques en solution.

I.6.1.1. Méthodes quantitatives

Une méthode simple d'analyse des ions métalliques en solution est la chromatographie cationique. Cette méthode présente une limite majeure qu'est la sensibilité vis-à-vis des ions métalliques (env. 50 mg/L) (Weiss 2016). Dans le cas des fruits, cette technique est adaptée pour l'étude du K, Ca et Mg mais pas pour les ions métalliques à l'état de traces. Pour ces derniers (Fe, Mn, Cu et Zn), les méthodes classiques souvent utilisées sont les méthodes de spectrométrie d'absorption atomique (AAS), d'émission atomique (AES) et la spectrométrie de masse (MS), parfois couplée à un plasma inductif (ICP).

Ces analyses quantitatives sont des méthodes destructives et nécessitent souvent la mise en solution de l'échantillon. Elles donnent une mesure globale de la composition de l'échantillon mais ne permettent pas d'avoir des informations sur la distribution spatiale des éléments dans les tissus.

I.6.1.2. Méthodes d'analyses spatiale

L'étude de la distribution élémentaire dans les tissus biologiques est particulièrement difficile. Les principales techniques utilisées pour déterminer la distribution et la localisation des éléments en milieu biologique sont présentées dans la **Table I.5**.

Table I.5 : Principales techniques d'analyse pour l'imagerie et la spéciation des éléments chimiques à l'échelle microscopique (Ortega 2005).

Techniques d'imagerie des éléments chimiques	Limite de détection	Résolution spatiale	Sélectivité	Quantification	Profondeur d'analyse
Spectrométrie dispersive en énergie (EDS)	100 à 1000 µg/g	0,5 µm	Multiélémentaire (Z>6)	Semi-quantitative	0,1 à 1 µm
Spectroscopie des pertes d'énergie (EELS)	1000 µg/g	1nm	Multiélémentaire (Z>6) Formes chimiques	Semi-quantitative	< 50 nm
Microsonde faisceau d'ions	1 à 10 µg/g	0,1-2µm	Multiélémentaire (tous Z)	Quantitative	10 à 100 µm
Microsonde rayonnement synchrotron (XRF)	<0,01 µg/g	0,1-2µm	Multiélémentaire (Z>6)	Semi-quantitative	> 100 µm

Spectrométrie d'absorption des rayons X (XAS)	100 µg/g	1µm	Formes chimiques	Semi-quantitative	> 100 µm
Spectrométrie de masse à plasma induit couplée à l'ablation laser (LA-ICP-MS)	0,001 µg/g	5-15µm	Multiélémentaire Isotopes	Semi-quantitative	200 µm
Spectrométrie de masse des ions secondaires (SIMS)	0,001 µg/g	0,05 µm	Multiélémentaire Isotopes	Semi-quantitative	0,1 µm
Micro Spectrofluorométrie	0,01 µg/g	1µm	Fluorophores (Na, Mg, K, Ca,…)	Quantitative	Cellule

Les méthodes d'imageries les plus communément employées sont celles couplées à la Microscopie Electronique en Transmission (MET) et en Balayage (MEB) telles que la MET-EELS ou la MEB-EDS. La microscopie électronique a souvent été utilisée sur la pomme pour l'analyse structurale des tissus mais peu pour identifier les ions métalliques (Lapsley, Escher, and Hoehn 1992). Seule, la MET-EELS a été utilisée pour obtenir la distribution du Ca et N dans les parois cellulaires de pomme, sur des sections préparées par HPF (High Pressure Freezing)(Huxham et al. 1999). L'avantage principal de ces techniques est la très haute résolution spatiale (ordre du nm) grâce au faisceau d'électrons. Cependant, ces méthodes nécessitent l'usage du vide et donc une préparation d'échantillon adaptée, qui induit une redistribution des éléments non fixés dans les tissus cellulaires.

Parmi les techniques décrites, l'ICP-MS couplée à l'ablation laser a été explorée ces dernières années sur du matériel biologique mais demande encore à être améliorée pour l'analyse sur du tissu végétal très hydraté (Becker, Zoriy et al. 2010). En effet, elle permet l'analyse *in situ* et multiélémentaire de métaux et non-métaux à l'état de trace, avec une bonne résolution quasiment sans préparation d'échantillon et permet l'analyse d'échantillons à grande et petite échelle. Wu et al. (2009) présente un exemple intéressant en l'appliquant pour l'imagerie quantitative des micronutriments (K, Mg, Mn, Cu, P, S, B) sur des feuilles entières (non sectionnées) avec l'utilisation de ^{13}C comme standard interne pour compenser les effets matrices entre les différentes parties analysées. Les temps d'analyses se révèlent cependant assez longs (env. 10 h).

D'autres techniques ont aussi été expérimentées pour l'analyse élémentaire sur du tissu biologique, telles que la PIXE (particule induce X-ray Emission) ou la LIBS (laser induce breakdown spectroscopy). La PIXE consiste à l'analyse des rayons X après l'irradiation de l'échantillon par des particules chargées (proton, ion hélium ou deuton). Cette technique est rapide, non destructive et permet une détection multi-élémentaire (Z>10) d'éléments traces (µg/g), mais nécessite un accélérateur de particules (Bohic, Cotte et al. 2012). La LIBS quant à elle a aussi l'avantage d'être

rapide, ce qui permet le suivi en temps réel, mais l'information récupérée n'est que qualitative, d'autant plus que sa précision est très dépendante de la stabilité de l'énergie d'impulsion du laser et de l'échantillon (de Carvalho, Guerra et al. 2018). L'inconvénient majeur de ces deux techniques est l'état de l'échantillon qui doit être solide.

I.6.1.2.1. La S-XRF

L'analyse par fluorescence X associée au rayonnement synchrotron (S-XRF) a été utilisée sur divers types de tissus végétaux, comme pour le suivi de la localisation des éléments (Ca, K, Fe, Zn, Cu) dans les graines de riz en développement (Iwai, Takahashi et al. 2012), ou encore pour l'étude de la distribution et de l'état d'oxydation du Zn dans des feuilles d' *Arabidopsis thaliana* lyophilisées (Sarret et al. 2009). Dans la même optique, Isaure, Fayard et al. (2006) ont rapporté une étude sur le cadmium et ses différentes formes chimiques par S-XRF dans les racines et feuilles d'*Arabidopsis thaliana*, où une comparaison entre l'analyse sur des échantillons congelés et lyophilisés ne montre pas de différence significative. En revanche, la S-XRF a peu été étudiée pour la cartographie des éléments dans les tissus de fruits charnus comme la pomme ou le raisin, qui sont des tissus très fragiles et aussi très hydratés.

Pourtant, il s'agit d'une méthode d'analyse peu destructive, adaptée à la caractérisation simultanée des éléments (Z>6) avec une très bonne sensibilité et résolution spatiale. Cette technique permet aussi la cartographie de zones assez larges dans des temps raisonnables, ainsi que la caractérisation des états d'oxydation des éléments via les modes spécifiques de type XANES (X-ray Absorption Near Edge Structure) et EXAFS (Extended X-Ray Absorption Fine Structure) (Ortega 2005).

Malgré tout, sans la sensibilité qu'apporte le rayonnement synchrotron, l'analyse du Ca et K dans la pomme à l'aide d'une XRF portative a été possible comme décrite par Kalcsits (2016).

I.6.1.2.2. La microscopie photonique

Les techniques de microscopie photonique, largement étudiées en biologie, offrent un champ de vision plus large de l'échantillon que les autres techniques plus sensibles et résolues comme microscopie électronique ou la S-XRF. En particulier la microscopie confocale à balayage laser (MCBL) présente un large champ de vision et permet l'observation en fluorescence des ions métalliques dans les tissus biologiques moyennant des fluorochromes et lasers d'excitations appropriées. Cependant, ces marqueurs spécifiques des ions métalliques étudiés tels que décrits par Haugland, Gregory et al. (2005), Carter, Young et al. (2014), peuvent faire l'objet de débats quant à leur spécificité. De plus, contrairement à la S-XRF, l'apport de marqueurs fluorescents induit un biais sur la localisation native des ions métalliques.

Outre la localisation des ions métalliques, cette technique permet aussi le contrôle de l'état physique de l'échantillon au niveau microscopique, avant d'y effectuer des analyses plus avancées par les techniques hautement résolues mais avec un champ de vision plus restreint. En effet, les méthodes de préparation des échantillons peuvent notamment affecter la structure cellulaire dans les tissus.

I.6.1.2.3. Méthode de préparation des échantillons

Un facteur important dans l'imagerie de tissus biologiques est la préparation de l'échantillon. Les méthodes d'analyse très résolues et sensibles (microscopie de fluorescence X ou électroniques) opèrent sous vide poussé afin d'éviter la diffusion des particules primaires et secondaires et donc du signal, mais aussi pour éviter l'adsorption de contaminants à la surface de l'échantillon. Cela signifie que les tissus cellulaires vivants, en particulier les fruits, ne peuvent pas être analysés directement puisqu'ils contiennent 80% d'eau. Or l'élimination de l'eau est problématique pour la préparation et la préservation de l'échantillon. De plus, le matériel végétal est extrêmement délicat et hétérogène et il est par conséquent très difficile de le préserver dans son état in-vivo. Les ions métalliques sont très diffusibles et éviter leur redistribution s'avère difficile pendant la préparation de l'échantillon. La technique communément employée est la fixation de l'échantillon soit chimiquement soit par congélation.

La fixation chimique est la méthode de préparation la plus utilisée mais elle modifie de façon drastique le contenu intracellulaire et la distribution *in-vivo* des composés labiles dans les cellules (Grignon et al. 1997). En effet, les différents lavages à l'éthanol et l'inclusion avec l'agent fixateur peuvent induire ces effets de redistribution des composés diffusibles. Cependant, la fixation chimique permet d'obtenir des sections d'échantillons à l'état solide après enrobage dans de la résine. Cette technique a été efficace pour l'analyse de composés très fortement liés comme le Ca au niveau des parois cellulaires des pommes décrit par Huxham, Jarvis et al. (1999).

La fixation par congélation est une alternative développée surtout pour éviter les artefacts causés par l'apport d'agents chimiques externes modifiant l'état natif des tissus biologiques. La congélation permet d'avoir des sections d'échantillon à l'état solide, tout en ayant conservé l'ensemble des composants du tissu, dont l'eau, et de limiter les pertes ou les redistributions de ces composés. Toutefois, il a souvent été décrit que la congélation doit être rapide pour mieux garder l'eau à l'état liquide (surfusion) ou pour limiter la taille des cristaux de glace se formant dans le tissu cellulaire (Moore, Lombi et al. 2012). En effet, la croissance des cristaux de glace à faibles températures négatives (entre 0 et - 20 °C) induit des dommages structuraux et une redistribution des éléments diffusibles. De même, des flux d'eau liés à la modification des pressions osmotiques des différents compartiments cellulaires peuvent avoir lieu lors de ces étapes de congélation. Les méthodes de

congélation rapide généralement décrites sont la « plunge freezing (PF) » et la « high pressure freezing (HFP) ». La PF est beaucoup plus simple et consiste à immerger l'échantillon dans un liquide cryogène, alors que la HFP nécessite des hautes pressions où l'échantillon est congelé par jets de liquide cryogène. Ainsi, la formation de cristaux de glace est limitée grâce à la haute pression utilisée, et la profondeur de vitrification est plus importante (Moore, Lombi et al. 2012). La HFP est la meilleure méthode de préservation d'échantillons biologique actuelle. Cependant, cette méthode nécessite des échantillons de faibles dimensions généralement obtenus par microtomie (taille ≈mm ; épaisseur ≈µm), afin d'avoir une congélation homogène.

I.6.2. Méthodes d'analyse des composés phénoliques

I.6.2.1. Méthodes quantitatives

Ces dernières années, les développements dans l'instrumentation de laboratoire, notamment au niveau des spécificités et sensibilités et d'accessibilités des détecteurs en spectrométrie de masse et d'absorption, ont facilité l'identification et l'analyse des composés phénoliques. Toutefois, la préparation de l'échantillon et l'extraction des composés phénoliques restent les étapes critiques afin d'éviter la dégradation de leurs structures natives, causée par la chaleur, et l'exposition à la lumière et l'oxygène. Plusieurs méthodes ont été répertoriées par Tsao (2010). La quantification des composés phénoliques par les méthodes spectrophotométriques telles que l'absorbance en UV-visible et la colorimétrie, ont été développées et sont toujours utilisées pour la quantification de teneurs globales en composés phénoliques d'extraits. Cependant, l'identification et la quantification spécifique des composés phénoliques sont souvent réalisées par chromatographie liquide en phase inverse couplée à un détecteur à barrette de diode (DAD) et/ou un spectromètre de masse (MS).

I.6.2.2. Méthodes d'analyse spatiale

La localisation *in-situ* des composés phénoliques dans les tissus de pommes et de raisin a rarement été décrite. Quelques travaux ont notamment été conduits en microscopie photonique et électronique.

I.6.2.2.1. La microscopie photonique

La microscopie photonique a été utilisée sur la pomme et le raisin surtout pour localiser les tannins condensés à l'aide du colorant DMACA (p-dimethyl-aminocinnamaldehyde) et du bleu de toluidine (Lees, Suttill et al. 1995, Cadot, Chevalier et al. 2011). Un autre marqueur spécifique des flavonoïdes, le DPBA (2-Aminoethyldiphenylborinate), a été utilisé sur plusieurs tissus cellulaires d'*Arabidopsis thaliana* montrant leur localisation dans les compartiments cytoplasmiques et vacuolaires (Peer, Brown et al. 2001, Poustka, Irani et al. 2007), cependant aucune étude n'a été faite

sur les fruits avec ce marqueur fluorescent. Ces méthodes d'analyse sont assez rapides et faciles à mettre en œuvre mais nécessitent l'apport de marqueurs qui induisent, là encore, une modification de la distribution native des composés dans les tissus cellulaires.

Une alternative à ces méthodes de marquage est l'observation des composés phénoliques dans le tissu cellulaire grâce à leur propriété d'autofluorescence (García-Plazaola, Fernández-Marín et al. 2015). En effet, il a été rapporté que les acides hydroxycinnamiques de même que les lignines présentent une fluorescence dans le bleu après excitation en UV à 375 nm (Harris and Hartley 1976, Rodríguez-Delgado, Malovaná et al. 2001), alors que les anthocyanes et les flavonols sont autofluorescents dans le visible (Drabent, Pliszka et al. 1999). Les flavanols nécessitent cependant une excitation en UV profond à des longueurs d'onde avoisinant 280 nm (Gómez-Alonso, García-Romero et al. 2007, Airado-Rodríguez, Durán-Merás et al. 2011). Ainsi, la localisation de ces différents composés phénoliques de façon simultanée peut être possible avec des approches multispectrales (Corcel, Devaux et al. 2016).

I.6.2.2.2. La microscopie électronique

Pour l'analyse localisée à plus petite échelle, la microscopie électronique à transmission (TEM) a permis la localisation des acides hydroxycinnamiques (Philippe, Tranquet et al. 2007, Tranquet, Saulnier et al. 2009) dans les parois cellulaires des graminées et de quelques dicots, notamment grâce à l'application d'anticorps spécifiques pour marquer ces acides sur des sections d'échantillons fixés et inclus. Ce type de marquage n'a pas été testé sur des fruits charnus. Cependant, sur du tissu hypodermique de raisin préalablement déshydraté, fixé et enrobé, la TEM a permis la localisation des tannins condensés au niveau intracellulaire, par l'ajout d'un colorant spécifique, le Oolong tea (Brillouet, Romieu et al. 2014).

En effet, ces techniques de microscopie électronique nécessitent l'utilisation de marqueurs spécifiques afin de révéler les différents composés phénoliques. Comme pour l'analyse des ions métalliques, la préparation des échantillons pour la microscopie électronique ne permet pas la préservation des composés phénoliques libres dans leur état *in vivo*, mais reste cependant adaptée aux composés fortement fixés dans le tissu.

Cependant, les outils pour identifier la nature et la distribution native des composés phénoliques dans les tissus cellulaires de fruits hautement hydratés, nécessitent encore des développements.

I.7. Objectifs et démarche scientifique

La littérature rapporte de nombreux mécanismes d'interactions possibles entre les ions métalliques, les pectines de parois cellulaires et les composés phénoliques. La grande majorité de ces travaux a été réalisée en solution diluée in-vitro. Cependant, dans les fruits frais tels que la pomme et le raisin, les interactions entre les ions métalliques avec les pectines dans les parois cellulaires et les composés phénoliques ont été très peu décrites. Dans ce contexte, un premier objectif a été d'établir la distribution de ces composés dans les fruits in-vivo et d'établir s'il existait une colocalisation et des interactions associées dans les tissus cellulaires et avec des composés d'intérêt majeur des fruits charnus. Sur la base des résultats issus de ces observations, un deuxième objectif a été ensuite d'aboutir à une meilleure compréhension : des mécanismes physiologiques et physicochimiques associant ces composés *in vivo*, et de la conséquence sur les caractéristiques globales et organoleptiques des fruits et de leurs produits issus de transformation technologique.

Pour répondre à ces différentes questions, la démarche des travaux (et la méthodologie associée) a été dans un premier temps de caractériser les fruits étudiés afin d'identifier leurs différences au niveau de la composition globale en ions, en composés phénoliques et de leurs propriétés mécaniques. Ces échantillons contrastés ont permis d'identifier les composants d'intérêt sur lesquels se concentrent les travaux de la thèse. La première partie du travail, s'est ainsi focalisée sur la mise en place de méthodes « cryo » pour la préparation d'échantillons et ce, pour limiter la redistribution de ces composés hautement diffusibles (**Chapitre II**). Dans un deuxième temps, ces méthodes ont alors été appliquées en utilisant des techniques de fluorescence de marqueurs spécifiques et d'autofluorescence en UV (375 et 275 nm) et par fluorescence X via des rayonnements synchrotrons (**Chapitres II, III, V**). Ces méthodes ont permis ainsi la cartographie des composés phénoliques et des ions métalliques dans les tissus de fruits. Le rapprochement des distributions observées entre les familles de composés a permis d'en faire une sélection qui serait susceptible d'interagir entre eux et avec la paroi cellulaire. Ces résultats ont ouvert la voie à la caractérisation des composés phénoliques estérifiés aux parois cellulaires par des analyses biochimiques au moyen de techniques chromatographiques associées à la spectrométrie de masse et à la spectroscopie UV-visible (**Chapitre IV**). Ils ont également permis de développer un système modèle in vitro pour étudier les interactions potentielles entre composés phénoliques, métaux et polysaccharides pariétaux pouvant avoir des conséquences sur les propriétés organoleptiques des fruits frais et transformés (**Chapitre VI**).

I.8. Références

Abadía, J., A.-F. López-Millán, A. Rombolà and A. Abadía (2002). "Organic acids and Fe deficiency: a review." Plant and Soil **241**(1): 75-86.

Abramovič, H. (2015). Chapter 93 - Antioxidant Properties of Hydroxycinnamic Acid Derivatives: A Focus on Biochemistry, Physicochemical Parameters, Reactive Species, and Biomolecular Interactions. Coffee in Health and Disease Prevention. V. R. Preedy. San Diego, Academic Press**:** 843-852.

Airado-Rodríguez, D., I. Durán-Merás, T. Galeano-Díaz and J. P. Wold (2011). "Front-face fluorescence spectroscopy: A new tool for control in the wine industry." Journal of Food Composition and Analysis **24**(2): 257-264.

Airianah, O. B., R. A. M. Vreeburg and S. C. Fry (2016). "Pectic polysaccharides are attacked by hydroxyl radicals in ripening fruit: evidence from a fluorescent fingerprinting method." Annals of Botany **117**(3): 441-455.

Almeida, D. P. and D. J. Huber (1999). "Apoplastic pH and inorganic ion levels in tomato fruit: a potential means for regulation of cell wall metabolism during ripening." Physiologia Plantarum **105**(3): 506-512.

Amrani, J. and M. Mercierz (1994). "Localisation des tanins dans la pellicule de baie de raisin." Vitis **33**: 133-138.

Barnavon, L., T. Doco, N. Terrier, A. Ageorges, C. Romieu and P. Pellerin (2000). "Analysis of cell wall neutral sugar composition, β-galactosidase activity and a related cDNA clone throughout the development of Vitis vinifera grape berries." Plant Physiology and Biochemistry **38**(4): 289-300.

Barrett, J. (1981). Biochemistry of parasitic helminths, MacMillan Publishers Ltd.

Becker, J. S., M. Zoriy, A. Matusch, B. Wu, D. Salber, C. Palm and J. S. Becker (2010). "Bioimaging of metals by laser ablation inductively coupled plasma mass spectrometry (LA-ICP-MS)." Mass spectrometry reviews **29**(1): 156-175.

Bertoluci, G. and G. Trystram (2013). "Eco-concevoir pour l'industrie alimentaire: quelles spécificités?" Marche et organisations(1): 123-135.

Binbuga, N., K. Chambers, W. P. Henry and T. P. Schultz (2005). "Metal chelation studies relevant to wood preservation. 1. Complexation of propyl gallate with Fe2+." Holzforschung **59**(2): 205-209.

Bohic, S., M. Cotte, M. Salomé, B. Fayard, M. Kuehbacher, P. Cloetens, G. Martinez-Criado, R. Tucoulou and J. Susini (2012). "Biomedical applications of the ESRF synchrotron-based microspectroscopy platform." Journal of Structural Biology **177**(2): 248-258.

Boyer, J. S. (2016). "Enzyme-less growth in Chara and terrestrial plants." Frontiers in plant science **7**: 866.

Braccini, I., R. P. Grasso and S. Pérez (1999). "Conformational and configurational features of acidic polysaccharides and their interactions with calcium ions: a molecular modeling investigation." Carbohydrate Research **317**(1-4): 119-130.

Briat, J.-F. and S. Lobréaux (1997). "Iron transport and storage in plants." Trends in Plant Science **2**(5): 187-193.

Brillouet, J.-M., C. Romieu, M. Lartaud, E. Jublanc, L. Torregrosa and C. Cazevieille (2014). "Formation of vacuolar tannin deposits in the chlorophyllous organs of Tracheophyta: from shuttles to accretions." Protoplasma **251**(6): 1387-1393.

Brown, J. A. and S. C. Fry (1993). "Novel OD-galacturonoyl esters in the pectic polysaccharides of suspension-cultured plant cells." Plant Physiology **103**(3): 993-999.

Buanafina, M. M. d. O. (2009). "Feruloylation in Grasses: Current and Future Perspectives." Molecular Plant **2**(5): 861-872.

Buchanan, B., W. Gruissem and R. Jones (2000). Biochemistry&Molecular Biology of Plants. American Society of Plant Physiologists. Drake Int. Services, Oxford.

Burnell, J. N. (1988). The biochemistry of manganese in plants. Manganese in soils and plants, Springer**:** 125-137.

Cadot, Y., M. Chevalier and G. Barbeau (2011). "Evolution of the localisation and composition of phenolics in grape skin between veraison and maturity in relation to water availability and some climatic conditions." Journal of the Science of Food and Agriculture **91**(11): 1963-1976.

Caffall, K. H. and D. Mohnen (2009). "The structure, function, and biosynthesis of plant cell wall pectic polysaccharides." Carbohydrate research **344**(14): 1879-1900.

Cao, G., E. Sofic and R. L. Prior (1997). "Antioxidant and prooxidant behavior of flavonoids: structure-activity relationships." Free Radical Biology and Medicine **22**(5): 749-760.

Carter, K. P., A. M. Young and A. E. Palmer (2014). "Fluorescent Sensors for Measuring Metal Ions in Living Systems." Chemical Reviews **114**(8): 4564-4601.

Celus, M., C. Kyomugasho, A. M. Loey, T. Grauwet and M. E. Hendrickx (2018). "Influence of Pectin Structural Properties on Interactions with Divalent Cations and Its Associated Functionalities." Comprehensive Reviews in Food Science and Food Safety **17**(6): 1576-1594.

Chen, S. x. and P. Schopfer (1999). "Hydroxyl-radical production in physiological reactions." The FEBS Journal **260**(3): 726-735.

Christiaens, S., S. Van Buggenhout, K. Houben, Z. Jamsazzadeh Kermani, K. R. N. Moelants, E. D. Ngouémazong, A. Van Loey and M. E. G. Hendrickx (2016). "Process–Structure–Function Relations of Pectin in Food." Critical Reviews in Food Science and Nutrition **56**(6): 1021-1042.

Chvátalová, K., I. Slaninová, L. Březinová and J. Slanina (2008). "Influence of dietary phenolic acids on redox status of iron: Ferrous iron autoxidation and ferric iron reduction." Food Chemistry **106**(2): 650-660.

Clifford, M. N. (2000). "Anthocyanins–nature, occurrence and dietary burden." Journal of the Science of Food and Agriculture **80**(7): 1063-1072.

Corcel, M., M.-F. Devaux, F. Guillon and C. Barron (2016). "Comparison of UV and visible autofluorescence of wheat grain tissues in macroscopic images of cross-sections and particles." Computers and Electronics in Agriculture **127**: 281-288.

Davey, M. W., M. v. Montagu, D. Inze, M. Sanmartin, A. Kanellis, N. Smirnoff, I. J. J. Benzie, J. J. Strain, D. Favell and J. Fletcher (2000). "Plant L-ascorbic acid: chemistry, function, metabolism, bioavailability and effects of processing." Journal of the Science of Food and Agriculture **80**(7): 825-860.

de Carvalho, G. G. A., M. B. B. Guerra, A. Adame, C. S. Nomura, P. V. Oliveira, H. W. P. de Carvalho, D. Santos, L. C. Nunes and F. J. Krug (2018). "Recent advances in LIBS and XRF for the analysis of plants." Journal of Analytical Atomic Spectrometry **33**(6): 919-944.

de Souza, R. F., E. M. Sussuchi and W. F. De Giovani (2003). "Synthesis, electrochemical, spectral, and antioxidant properties of complexes of flavonoids with metal ions." Synthesis and reactivity in inorganic and metal-organic chemistry **33**(7): 1125-1144.

del Río, L. A. (2015). "ROS and RNS in plant physiology: an overview." Journal of Experimental Botany **66**(10): 2827-2837.

del Río, L. A., G. M. Pastori, J. M. Palma, L. M. Sandalio, F. Sevilla, F. J. Corpas, A. Jiménez, E. López-Huertas and J. A. Hernández (1998). "The Activated Oxygen Role of Peroxisomes in Senescence." Plant Physiology **116**(4): 1195-1200.

Desikan, R., J. Hancock and S. Neill (2005). Reactive oxygen species as signalling molecules. Antioxidants and Reactive Oxygen Species in Plants**:** 169-196.

Di Lecce, G., S. Arranz, O. Jáuregui, A. Tresserra-Rimbau, P. Quifer-Rada and R. M. Lamuela-Raventós (2014). "Phenolic profiling of the skin, pulp and seeds of Albariño grapes using hybrid quadrupole time-of-flight and triple-quadrupole mass spectrometry." Food Chemistry **145**: 874-882.

Doco, T., P. Williams, M. Pauly, M. A. O'Neill and P. Pellerin (2003). "Polysaccharides from grape berry cell walls. Part II. Structural characterization of the xyloglucan polysaccharides." Carbohydrate Polymers **53**(3): 253-261.

Drabent, R., B. Pliszka and T. Olszewska (1999). "Fluorescence properties of plant anthocyanin pigments. I. Fluorescence of anthocyanins in Brassica oleracea L. extracts." Journal of Photochemistry and Photobiology B: Biology **50**(1): 53-58.

Ducic, T. and A. Polle (2005). "Transport and detoxification of manganese and copper in plants." Brazilian Journal of Plant Physiology **17**(1): 103-112.

Esparza, I., I. Salinas, I. Caballero, C. Santamaría, I. Calvo, J. M. García-Mina and J. M. Fernández (2004). "Evolution of metal and polyphenol content over a 1-year period of vinification: sample fractionation and correlation between metals and anthocyanins." Analytica Chimica Acta **524**(1): 215-224.

Fallahi, E. and B. R. Simons (1996). "Interrelations among leaf and fruit mineral nutrients and fruit quality in'Delicious' apples." Journal of Tree Fruit Production **1**(1): 15-25.

Ferguson, I. B. and C. B. Watkins (1983). "Cation distribution and balance in apple fruit in relation to calcium treatments for bitter pit." Scientia Horticulturae **19**(3): 301-310.

Finley, J. W., W. J. Hurst and C. Y. Lee (2018). Principles of food chemistry, Springer.

Foreman, J., V. Demidchik, J. H. Bothwell, P. Mylona, H. Miedema, M. A. Torres, P. Linstead, S. Costa, C. Brownlee and J. D. Jones (2003). "Reactive oxygen species produced by NADPH oxidase regulate plant cell growth." Nature **422**(6930): 442.

Fry, S. (1998). "Oxidative scission of plant cell wall polysaccharides by ascorbate-induced hydroxyl radicals." Biochemical Journal **332**(Pt 2): 507.

Fry, S. C., J. G. Miller and J. C. Dumville (2002). "A proposed role for copper ions in cell wall loosening." Plant and Soil **247**(1): 57-67.

Galanakis, C. M. (2018). Polyphenols: Properties, Recovery, and Applications, Woodhead Publishing.

Gao, Y., J. U. Fangel, W. G. T. Willats, M. A. Vivier and J. P. Moore (2015). "Dissecting the polysaccharide-rich grape cell wall changes during winemaking using combined high-throughput and fractionation methods." Carbohydrate Polymers **133**: 567-577.

García-Plazaola, J. I., B. Fernández-Marín, S. O. Duke, A. Hernández, F. López-Arbeloa and J. M. Becerril (2015). "Autofluorescence: Biological functions and technical applications." Plant Science **236**: 136-145.

Gibson, L. J. (2012). "The hierarchical structure and mechanics of plant materials." Journal of The Royal Society Interface **9**(76): 2749-2766.

Gómez-Alonso, S., E. García-Romero and I. Hermosín-Gutiérrez (2007). "HPLC analysis of diverse grape and wine phenolics using direct injection and multidetection by DAD and fluorescence." Journal of Food Composition and Analysis **20**(7): 618-626.

Gülçin, İ. (2012). "Antioxidant activity of food constituents: an overview." Archives of Toxicology **86**(3): 345-391.

Ha, M.-A., R. J. Viëtor, G. D. Jardine, D. C. Apperley and M. C. Jarvis (2005). "Conformation and mobility of the arabinan and galactan side-chains of pectin." Phytochemistry **66**(15): 1817-1824.

Hagen, S. F., K. A. Solhaug, G. B. Bengtsson, G. I. A. Borge and W. Bilger (2006). "Chlorophyll fluorescence as a tool for non-destructive estimation of anthocyanins and total flavonoids in apples." Postharvest Biology and Technology **41**(2): 156-163.

Halliwell, B. and J. M. Gutteridge (2015). Free radicals in biology and medicine, Oxford University Press, USA.

Harris, P. and R. Hartley (1976). "Detection of bound ferulic acid in cell walls of the Gramineae by ultraviolet fluorescence microscopy." Nature **259**(5543): 508.

Haugland, R. P., J. Gregory, M. T. Z. Spence and I. D. Johnson (2005). Handbook of fluorescent probes and research products, Molecular Probes.

Heaton, J. W. and A. G. Marangoni (1996). "Chlorophyll degradation in processed foods and senescent plant tissues." Trends in Food Science & Technology **7**(1): 8-15.

Hether, N., R. Olsen and L. Jackson (1984). "Chemical identification of iron reductants exuded by plant roots." Journal of Plant Nutrition **7**(1-5): 667-676.

Hocking, B., S. D. Tyerman, R. A. Burton and M. Gilliham (2016). "Fruit calcium: transport and physiology." Frontiers in plant science **7**: 569.

Humphries, J. M., J. C. R. Stangoulis and R. D. Graham (2016). Manganese. Handbook of Plant Nutrition**:** 351-366.

Huxham, I. M., M. C. Jarvis, L. Shakespeare, C. J. Dover, D. Johnson, J. P. Knox and G. B. Seymour (1999). "Electron-energy-loss spectroscopic imaging of calcium and nitrogen in the cell walls of apple fruits." Planta **208**(3): 438-443.

Isaure, M.-P., B. Fayard, G. Sarret, S. Pairis and J. Bourguignon (2006). "Localization and chemical forms of cadmium in plant samples by combining analytical electron microscopy and X-ray spectromicroscopy." Spectrochimica Acta Part B: Atomic Spectroscopy **61**(12): 1242-1252.

Ishii, T. and T. Matsunaga (2001). "Pectic polysaccharide rhamnogalacturonan II is covalently linked to homogalacturonan." Phytochemistry **57**(6): 969-974.

Ishii, T., T. Matsunaga, P. Pellerin, M. A. O'Neill, A. Darvill and P. Albersheim (1999). "The plant cell wall polysaccharide rhamnogalacturonan II self-assembles into a covalently cross-linked dimer." Journal of Biological chemistry **274**(19): 13098-13104.

Iwai, T., M. Takahashi, K. Oda, Y. Terada and K. T. Yoshida (2012). "Dynamic changes in the distribution of minerals in relation to phytic acid accumulation during rice seed development." Plant physiology **160**(4): 2007-2014.

Jakobek, L. and P. Matić (2018). "Non-covalent dietary fiber-polyphenol interactions and their influence on polyphenol bioaccessibility." Trends in food science & technology.

Jarvis, M., S. Briggs and J. Knox (2003). "Intercellular adhesion and cell separation in plants." Plant, Cell & Environment **26**(7): 977-989.

Jukanti, A. (2017). Function (s)/Role (s) of Polyphenol Oxidases. Polyphenol Oxidases (PPOs) in Plants, Springer**:** 73-92.

Kalcsits, L. A. (2016). "Non-destructive Measurement of Calcium and Potassium in Apple and Pear Using Handheld X-ray Fluorescence." Frontiers in Plant Science **7**(442).

Kehrer, J. P. (2000). "The Haber–Weiss reaction and mechanisms of toxicity." Toxicology **149**(1): 43-50.

Khanizadeh, S., R. Tsao, D. Rekika, R. Yang, M. T. Charles and H. P. Vasantha Rupasinghe (2008). "Polyphenol composition and total antioxidant capacity of selected apple genotypes for processing." Journal of Food Composition and Analysis **21**(5): 396-401.

Klein, J. D., J. Hanzon, P. L. Irwin, N. B. Shalom and S. Luria (1995). "Pectin esterase activity and pectin methyl esterification in heated golden delicious apples." Phytochemistry **39**(3): 491-494.

Klemm, D., B. Heublein, H. P. Fink and A. Bohn (2005). "Cellulose: Fascinating Biopolymer and Sustainable Raw Material." Angewandte Chemie International Edition **44**(22): 3358-3393.

Knee, M. (2002). Fruit quality and its biological basis, CRC Press.

Kochian, L. V. (1991). "Mechanisms of micronutrient uptake and translocation in plants." Micronutrients in agriculture(micronutrientsi2): 229-296.

Kopsell, D. and D. Kopsell (2016). Copper. Handbook of Plant Nutrition**:** 293-323.

Kschonsek, J., T. Wolfram, A. Stöckl and V. Böhm (2018). "Polyphenolic Compounds Analysis of Old and New Apple Cultivars and Contribution of Polyphenolic Profile to the In Vitro Antioxidant Capacity." Antioxidants **7**(1): 20.

Kumar, A. (2009). A Text Book Of Practical Botany 2, Rastogi Publications.

Lahaye, M., C. Bouin, A. Barbacci, S. Le Gall and L. Foucat (2018). "Water and cell wall contributions to apple mechanical properties." Food Chemistry **268**: 386-394.

Lambers, H., F. S. Chapin and T. L. Pons (2008). Mineral Nutrition. Plant Physiological Ecology. New York, NY, Springer New York**:** 255-320.

Larsen, F. H., I. Byg, I. Damager, J. Diaz, S. B. Engelsen and P. Ulvskov (2011). "Residue specific hydration of primary cell wall potato pectin identified by solid-state 13C single-pulse MAS and CP/MAS NMR spectroscopy." Biomacromolecules **12**(5): 1844-1850.

Le Bourvellec, C. and C. M. G. C. Renard (2012). "Interactions between Polyphenols and Macromolecules: Quantification Methods and Mechanisms." Critical Reviews in Food Science and Nutrition **52**(3): 213-248.

Lees, G. L., N. H. Suttill, K. M. Wall and T. H. Beveridge (1995). "Localization of condensed tannins in apple fruit peel, pulp, and seeds." Canadian Journal of Botany **73**(12): 1897-1904.

Lei, Y., H. Korpelainen and C. Li (2007). "Physiological and biochemical responses to high Mn concentrations in two contrasting Populus cathayana populations." Chemosphere **68**(4): 686-694.

Liochev, S. I. (1999). The mechanism of "Fenton-like" reactions and their importance for biological systems. A biologist's view. Metal ions in biological systems, Routledge**:** 1-39.

Löfgren, C., S. Guillotin, H. Evenbratt, H. Schols and A.-M. Hermansson (2005). "Effects of calcium, pH, and blockiness on kinetic rheological behavior and microstructure of HM pectin gels." Biomacromolecules **6**(2): 646-652.

Macheix, J.-J., A. Fleuriet and J. Billot (2017). Fruit Phenolics, CRC press.

Marschner, H. (2011). Marschner's mineral nutrition of higher plants, Academic press.

Matoh, T. and M. Kobayashi (1998). "Boron and calcium, essential inorganic constituents of pectic polysaccharides in higher plant cell walls." Journal of Plant Research **111**(1): 179-190.

Mattivi, F., R. Guzzon, U. Vrhovsek, M. Stefanini and R. Velasco (2006). "Metabolite profiling of grape: flavonols and anthocyanins." Journal of agricultural and food chemistry **54**(20): 7692-7702.

Mengel, K. (2016). Potassium. Handbook of plant nutrition, CRC Press**:** 107-136.

Moore, K. L., E. Lombi, F.-J. Zhao and C. R. M. Grovenor (2012). "Elemental imaging at the nanoscale: NanoSIMS and complementary techniques for element localisation in plants." Analytical and Bioanalytical Chemistry **402**(10): 3263-3273.

Nakata, P. A. (2003). "Advances in our understanding of calcium oxalate crystal formation and function in plants." Plant Science **164**(6): 901-909.

Nunan, K. J., I. M. Sims, A. Bacic, S. P. Robinson and G. B. Fincher (1998). "Changes in cell wall composition during ripening of grape berries." Plant physiology **118**(3): 783-792.

Ortega, R. (2005). "Imagerie des elements chimiques. Analyse par faisceau d'ions et rayonnement synchrotron X." Spectra analyse **34**(246): 36.

Özcan, M. M., M. Harmankaya and S. Gezgin (2012). "Mineral and heavy metal contents of the outer and inner tissues of commonly used fruits." Environmental monitoring and assessment **184**(1): 313-320.

Park, Y. B. and D. J. Cosgrove (2015). "Xyloglucan and its interactions with other components of the growing cell wall." Plant and Cell Physiology: pcu204.

Peer, W. A., D. E. Brown, B. W. Tague, G. K. Muday, L. Taiz and A. S. Murphy (2001). "Flavonoid accumulation patterns of transparent testa mutants of Arabidopsis." Plant Physiology **126**(2): 536-548.

Perron, N. R. and J. L. Brumaghim (2009). "A review of the antioxidant mechanisms of polyphenol compounds related to iron binding." Cell biochemistry and biophysics **53**(2): 75-100.

Philippe, S., O. Tranquet, J.-P. Utille, L. Saulnier and F. Guillon (2007). "Investigation of ferulate deposition in endosperm cell walls of mature and developing wheat grains by using a polyclonal antibody." Planta **225**(5): 1287-1299.

Pilbeam, D. J. and P. S. Morley (2016). Calcium. Handbook of Plant Nutrition**:** 121-140.

Pinto, P. and C. N. Santos (2017). "Worldwide (poly) phenol intake: assessment methods and identified gaps." European journal of nutrition **56**(4): 1393-1408.

Poustka, F., N. G. Irani, A. Feller, Y. Lu, L. Pourcel, K. Frame and E. Grotewold (2007). "A trafficking pathway for anthocyanins overlaps with the endoplasmic reticulum-to-vacuole protein-sorting route in Arabidopsis and contributes to the formation of vacuolar inclusions." Plant physiology **145**(4): 1323-1335.

Prat, R., M. Mosiniak and J.-C. Roland. (2016). "La Pomme : un fruit complexe." 2019, from http://www.snv.jussieu.fr/bmedia/Fruits/pomme.htm.

Quartacci, M. F., E. Cosi, S. Meneguzzo, C. Sgherri and F. Navari-Izzo (2003). "Uptake and translocation of copper in Brassicaceae." Journal of plant nutrition **26**(5): 1065-1083.

Raes, K., D. Knockaert, K. Struijs and J. Van Camp (2014). "Role of processing on bioaccessibility of minerals: Influence of localization of minerals and anti-nutritional factors in the plant." Trends in food science & technology **37**(1): 32-41.

Ralet, M.-C., V. Dronnet, H. C. Buchholt and J.-F. Thibault (2001). "Enzymatically and chemically de-esterified lime pectins: characterisation, polyelectrolyte behaviour and calcium binding properties." Carbohydrate research **336**(2): 117-125.

Renard, C. M. G. C., A. A. Watrelot and C. Le Bourvellec (2015). "Interactions between polyphenols and polysaccharides: mechanisms and consequences in food processing and digestion." Trends in Food Science & Technology.

Rengel, Z. (2000). "Uptake and transport of manganese in plants." Metal Ions in Biological Systems. Marcel Dekker, New York: 57-87.

Ribéreau-Gayon, P., Y. Glories, A. Maujean and D. Dubourdieu (2006). Handbook of Enology, Volume 2: The Chemistry of Wine-Stabilization and Treatments, John Wiley & Sons.

Rodríguez-Delgado, M. A., S. Malovaná, J. P. Pérez, T. Borges and F. J. García Montelongo (2001). "Separation of phenolic compounds by high-performance liquid chromatography with absorbance and fluorimetric detection." Journal of Chromatography A **912**(2): 249-257.

Rogiers, S. Y., Z. A. Coetzee, R. R. Walker, A. Deloire and S. D. Tyerman (2017). "Potassium in the Grape (Vitis vinifera L.) Berry: Transport and Function." Frontiers in Plant Science **8**: 1629.

Römheld, V. and M. Nikolic (2016). Iron. Handbook of Plant Nutrition**:** 329-345.

Sakihama, Y., M. F. Cohen, S. C. Grace and H. Yamasaki (2002). "Plant phenolic antioxidant and prooxidant activities: phenolics-induced oxidative damage mediated by metals in plants." Toxicology **177**(1): 67-80.

Sautron, E. (2015). Homéostasie du cuivre dans le chloroplaste : étude comparée de deux transporteurs de la famille des ATPases de type PIB.

Schols, H. A., E. J. Bakx, D. Schipper and A. G. J. Voragen (1995). "A xylogalacturonan subunit present in the modified hairy regions of apple pectin." Carbohydrate Research **279**: 265-279.

Seling, S., A. H. Wissemeier, P. Cambier and P. Van Cutsem (2000). "Calcium deficiency in potato (Solanum tuberosum ssp. tuberosum) leaves and its effects on the pectic composition of the apoplastic fluid." Physiologia Plantarum **109**(1): 44-50.

Sinela, A. M., C. Mertz, N. Achir, N. Rawat, K. Vidot, H. Fulcrand and M. Dornier (2017). "Exploration of reaction mechanisms of anthocyanin degradation in a roselle extract through kinetic studies on formulated model media." Food Chemistry **235**: 67-75.

Slavov, A., E. Bonnin, C. Garnier, M.-J. Crépeau, S. Durand and J.-F. Thibault (2008). "Enzymatic modification of pectin in ca-pectic gels/A." Slavov, E. Bonnin, C. Garnier, MJ. Crepeau, S. Durand, JF. Thibault//Bulgaria scientific papers **36**(5): 75-82.

Smirnoff, N. (2005). Antioxidants and reactive oxygen species in plants, Wiley Online Library.

Storey, B. J. (2016). Zinc. Handbook of Plant Nutrition 411-430.

Takahama, U. (1989). "A Role of Hydrogen Peroxide in the Metabolism of Phenolics in Mesophyll Cells of Viciafaba L." Plant and cell physiology **30**(2): 295-301.

Thibault, J.-F. and M.-C. Ralet (2008). "32 Pectins, their Origin, Structure and Functions." Advanced dietary fibre technology: 369-378.

Tonetto De Freitas, S., C. d. Amarante and E. Mitcham (2016). Calcium Deficiency Disorders in Plants, Postharvest ripening physiology of crops. CRC Press.

Tranquet, O., L. Saulnier, J.-P. Utille, J. Ralph and F. Guillon (2009). "Monoclonal antibodies to p-coumarate." Phytochemistry **70**(11-12): 1366-1373.

Tsao, R. (2010). "Chemistry and Biochemistry of Dietary Polyphenols." Nutrients **2**(12): 1231-1246.

USDA (2018). National Nutrient Database for Standard Reference.

USDA, U. (2018). "Fresh deciduous Fruit: World markets and trade (apples, grapes, & pears)."

Vallee, B. L. and D. S. Auld (1990). "Zinc coordination, function, and structure of zinc enzymes and other proteins." Biochemistry **29**(24): 5647-5659.

Verdu, C. (2013). "Cartographie génétique des composés phénoliques de la pomme."

Vermerris, W. and R. Nicholson (2006). Phenolic compounds biochemistry, Springer.

Vine, I. O. o. (2017). 2017 world vitiviniculture situation, OIV Statistical Report on World Viniculture.

Voragen, A. G. J., G.-J. Coenen, R. P. Verhoef and H. A. Schols (2009). "Pectin, a versatile polysaccharide present in plant cell walls." Structural Chemistry **20**(2): 263.

Wang, H., L. Wan, D. Chen, X. Guo, F. Liu and S. Pan (2019). "Unexpected gelation behavior of citrus pectin induced by monovalent cations under alkaline conditions." Carbohydrate polymers **212**: 51-58.

Weiss, J. (2016). Handbook of Ion Chromatography, 3 Volume Set, John Wiley & Sons.

Winisdorffer, G., M. Musse, S. Quellec, A. Barbacci, S. Le Gall, F. Mariette and M. Lahaye (2015). "Analysis of the dynamic mechanical properties of apple tissue and relationships with the intracellular water status, gas distribution, histological properties and chemical composition." Postharvest Biology and Technology **104**: 1-16.

Xu, X., W. Liu, L. Luo, C. Liu and D. J. McClements (2017). "Influence of anionic polysaccharides on the physical and oxidative stability of hydrolyzed rice glutelin emulsions: Impact of polysaccharide type and pH." Food hydrocolloids **72**: 185-194.

Zykwinska, A. W., M.-C. J. Ralet, C. D. Garnier and J.-F. J. Thibault (2005). "Evidence for in vitro binding of pectin side chains to cellulose." Plant physiology **139**(1): 397-407.

Chapitre II

II. Cryo-laser scanning confocal microscopy of diffusible plant compounds

Introduction

Après étude de la littérature, l'utilisation de la cryo-fixation pour préserver la distribution des ions métalliques dans des sections de fruits charnus s'avère être fondamentale. Une première étude décrite, dans ce deuxième chapitre, concerne les travaux sur le développement de méthodes cryo adaptées à la microscopie confocale pour l'observation de composés hautement diffusibles dans les tissus de fruits charnus. Ce travail a fait l'objet d'une publication dans « Plant Method » référencée ci-dessous et dont le PDF est présenté en **annexe 1-A**.

Vidot, K., et al. (2018). "Cryo-laser scanning confocal microscopy of diffusible plant compounds." Plant Methods 14(1): 89.

La méthode développée a aussi permis des études parallèles sur de la pomme de terre réalisées dans le cadre de la thèse de Piyush Kumar Jha « Étude de l'effet des radiations électromagnétiques pendant la congélation sur la structure de glace et la qualité des tissus des fruits et légumes ». Les travaux ont été publiés dans « Journal of Food Engineering » référencé ci-dessous et dont le PDF est en **annexe 1-B**.

Jha, P. K., Vidot, K., et al. (2019). "Benchmarking of techniques used to assess the freeze damage in potatoes." Journal of Food Engineering 262: 60-74.

Sommaire

II.1. Abstract

Background: The *in vivo* observation of diffusible components, such as ions and small phenolic compounds, remains a challenge in turgid plant organs. The analytical techniques used to localize such components in water-rich tissue with a large field of view are lacking. It remains an issue to limit compound diffusion during sample preparation and observation processes.

Results: An experimental setup involving the infusion staining of plant tissue and the cryo-fixation and cryo-sectioning of tissue samples followed by fluorescence cryo-observation by laser scanning confocal microscopy (LSCM) was developed. This setup was successfully applied to investigate the structure of the apple fruit cortex and table grape berry and was shown to be relevant for localizing calcium, potassium and flavonoid compounds.

Conclusion: The cryo-approach was well adapted and opens new opportunities for imaging other diffusible components in hydrated tissues.

Keys words: cryogenic fixation, cryo-confocal microscopy, metallic ions, phenolics, apple, grape

II.2. Background

Plant growth involves intricate relations between cell water compartmentalization and cell wall mechanical properties [1]. These relations involve cations for osmotic regulation and cell wall polysaccharide interactions, remodelling or deconstruction [2-7], but detailed knowledge on cation roles and interactions is impeded by their high mobility and/or low abundance in turgid tissue. Analytical methods for cation localization with a high spatial resolution are thus required. Due to the high water content of growing plant tissue, restraining the diffusion of mobile ions and preserving tissue integrity remain a challenge [8-10].

Specific chemical or physical fixation methods of plant tissue structures for microscopic observations exist [11]. Cryo-techniques coupled to cryo-observation in large fields of view using fluorescent techniques are particularly suited to localize metallic cations and diffusible compounds at low concentrations. The cryogenic fixation of plant tissues for light microscopy, called cryo-observation, has been described [12] but has been rarely used in the fluorescent mode [13]. This scarcity is most likely due to the difficulty in keeping the cold chain intact between sample cryo-fixation, cryo-sectioning and sample observation in frozen conditions. To that end, a method of fluorescence staining followed by cryo-fixation and cryo-observation by laser scanning confocal microscopy (LSCM) was developed and applied to the apple fruit cortex and table grape berry as models of turgid plant organs.

II.3. Results

II.3.1. Staining approaches

Staining of the sample with aqueous dye solutions must be completed prior to cryo-fixation. In the present case, it was achieved by the infusion or perfusion (**Figure II.1)** of fresh samples using acridine orange (AO), a fluorescent dye for the cell walls and anionic sites of cell organelles, DNA and RNA [14-16]. Compared to the direct staining of fresh sample sections, AO infusion was efficient, while perfusion showed limited dye diffusion in the vicinity of the capillary and required an increase of the laser intensity to reveal probe fluorescence. Although less efficient, the latter method may be useful to study specific tissue locations with limited operation artefacts. Due to its efficiency and simplicity, infusion staining was chosen in the following study. Such a staining method that is used prior to fixation and cutting a section has already been reported to successfully stain potassium in leaves [17].

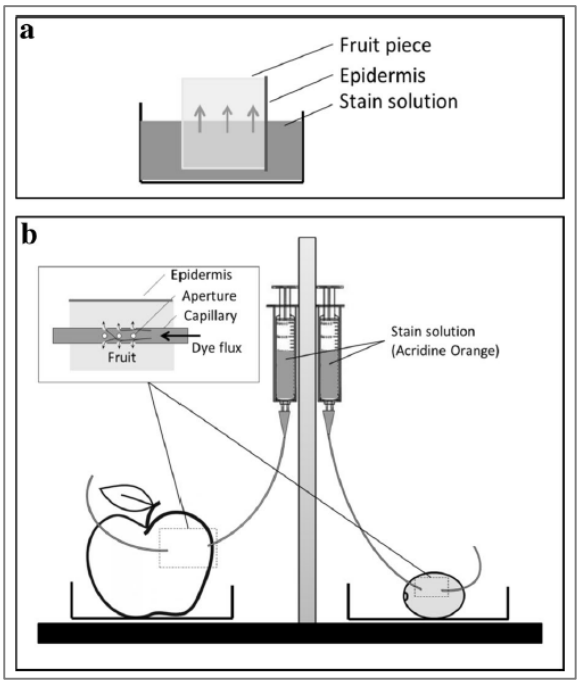

Figure II.12 *: Staining methods by* ***a*** *infusion and* ***b*** *perfusion*

II.3.2. Cryo-fixation

The freezing process impacts turgid tissue structure due to ice crystal formation. The different cryo-fixation methods of AO infused samples were compared with regard to the apparent integrity of cell walls (**Figure II.2**).

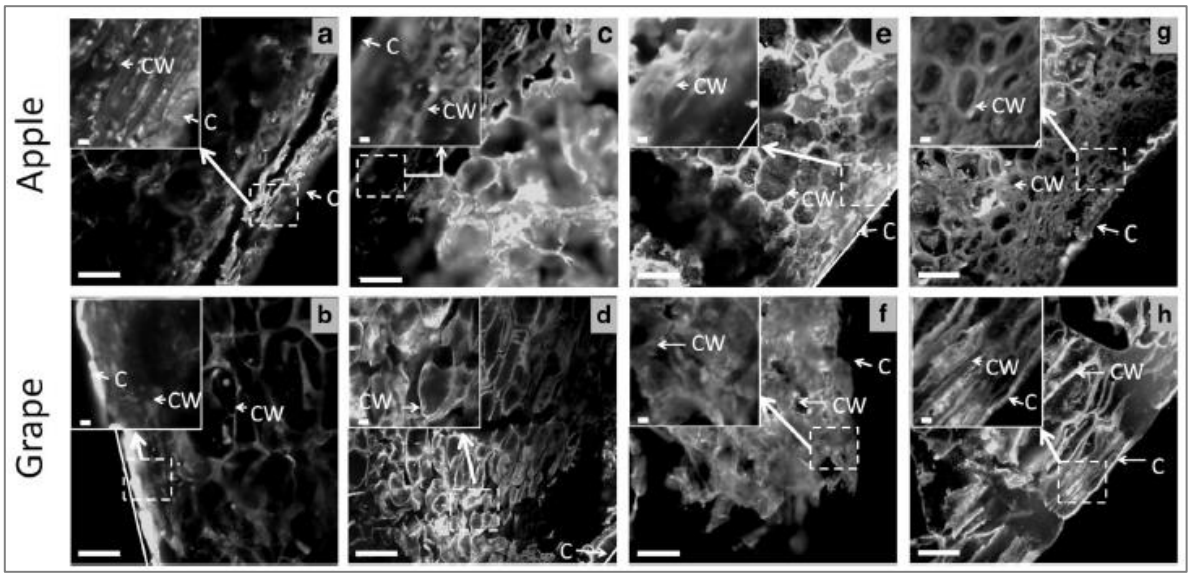

Figure II.13 *: Effect of cryo-fixation methods on the apple cortex and grape berry tissue structure:* ***a-b*** *frozen samples at -20°C;* ***c-d*** *fast-frozen samples in liquid nitrogen;* ***e-f*** *fast-frozen samples in cooled isopentane; and* ***g-h*** *frozen samples at -30°C under microwaves. All sections were prepared from apples (****a,c,e,g****) or grapes (****b,d,f,h****) and stained by infusion with Acridine Orange. CW: Cell wall; C: Cuticle. Scale bar: 100 and 10 µm in insert.*

Observations at approximately -25 °C revealed that slow freezing at -20 °C **(Figure II.2 a-b)**, fast freezing in liquid nitrogen **(Figure II.2 c-d)**, and fast freezing in cold isopentane **(Figure II.2 e-f)** impacted the

overall tissue structure from most to least. These results agree with the impact of the rate of ice nucleation: the faster the freezing technique is, the less ice nucleation is present, and the better that structures are preserved. Slow-freezing under microwaves was also tested as an alternative to fast-freezing. Applying low-power microwaves during freezing drastically reduced the growth of ice nuclei and limited cell damage due to ice expansion [18]. The fruit tissue cryo-fixed by this technique yielded remarkable results with regard to the preservation of its cell integrity (**Figure II.2 g-h**). This was particularly the case for the grape berry, for which tissue integrity was the most difficult to preserve. However, this promising technique still needs development to optimize its parameters, such as microwave power, freezing temperature and processing time. The preservation of inner cells in apple and grape tissues was more efficient using cooled isopentane freezing (**Figure II.2 e-f**) than using microwave freezing (**Figure II.2 g-h**). This may be explained by the short processing time of isopentane freezing (60 sec) compared to that of 3 h for the microwave technique due to the air blast freezer used. Furthermore, by avoiding the Leidenfrost effect, isopentane freezing was preferred over liquid nitrogen freezing. However, the measurement of cell wall thickness as a function of freezing conditions revealed an impact of the cooling rate on cell wall thickness **(Figure II.3)**. Congo Red-stained apple cell walls at approximately 200 µm from the cuticle were 2.5-fold thicker in tissue frozen by cold isopentane than in fresh tissue (room temperature), while tissue frozen at -20 °C or by liquid nitrogen gave an intermediate average thickness.

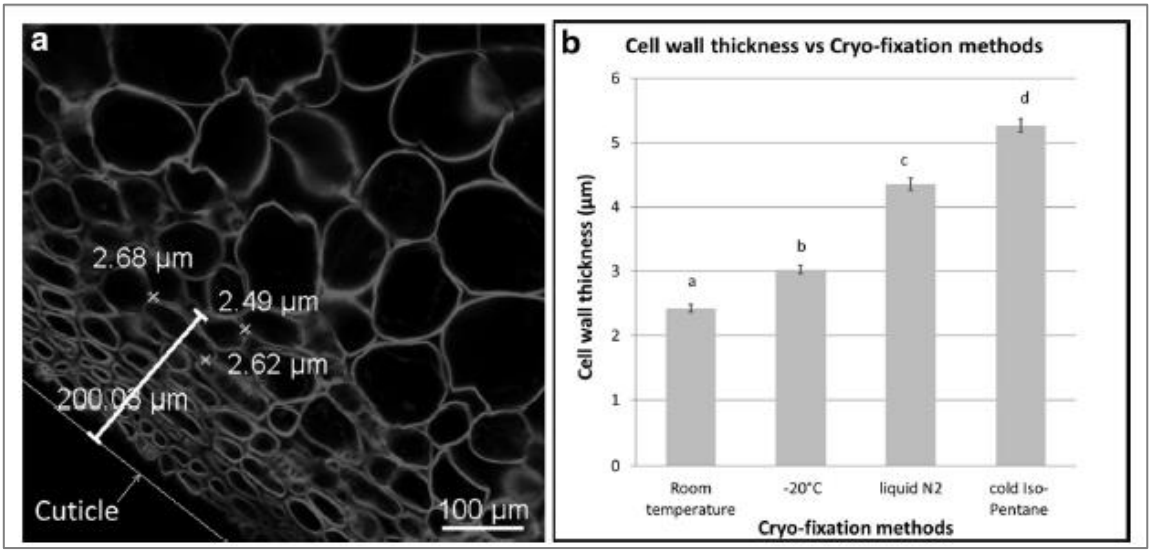

***Figure II.14** : A) Cell wall measurement on fresh apple tissue stained with Congo Red; B) cell wall thickness according to different cryo-fixation methods. Bars: standard error of the mean (n=80 for each condition).*

II.3.3. Observation of diffusible compounds

As an application of the entire process on turgid plant organs, calcium, potassium and flavonoid compounds were localized in apple fruit and table grape berry tissue. Samples were independently infused with the calcium probe Fluo-3, potassium probe PBFI, and flavonoid probe DPBA. The samples

were then fast-frozen in cold isopentane, cryo-sectioned and observed by cryo-LCSM **(Figure II.4 a-f).** The results showed diffuse calcium staining in the cell wall, while fluorescence spots were observed within cells (**Figure II.4 a-b**). Potassium and flavonoids were distributed in the entire fruit tissue **(Figure II.4 c-f),** and specific locations appeared in the cytosol next to the cell walls **(Figure II.4 e-f)**. As a comparison, the direct staining of fresh sections yielded weaker labelling mainly due to the absence of intracellular staining (**Figure II.4 g-l)**. These observations may be attributed to low compound concentrations resulting from their diffusion during staining and loss during washes as well as from the higher diffusion of quenchers inducing faster fluorescence bleaching at room temperature [19, 20].

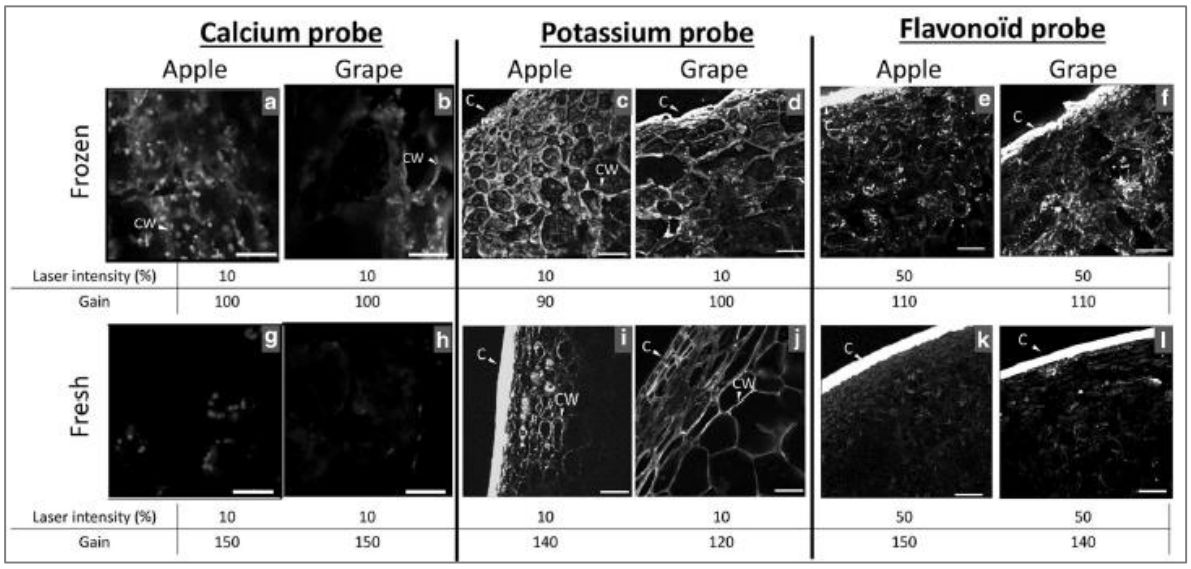

Figure II.15 : Cryo-observation of apple (a, c, e) and grape (b, d, f) tissues infused by Fluo-3 (calcium), PBFI (potassium), DPBA (flavonoid) dyes and cryo-fixed in cooled isopentane. Fluorescence observations in fresh apple fruit (g, i, k) and grape berry (h, j, l) sections directly stained by Fluo-3, PBFI and DPBA. C: Cuticle, CW: Cell Wall. Scale bar: 50 µm for calcium probe and 100 µm for potassium and flavonoid probes. Laser excitation and gain are indicated to stress the difference in fluorescence intensity recovered between fresh and frozen samples. The applied fluorescence intensity of the cuticle is due in part to autofluorescence related to the presence of phenolic compounds.

II.4. Discussion

The experimental setup presented here was developed to image metallic cations and phenolic compound distributions in *in vivo*-like fleshy fruit by fluorescence confocal microscopy. Particular care was paid to the issues related to the low concentration and highly diffusible properties of these components. The fruit region of interest was established at the epidermal areas of grape and apple fruit. To allow full cell observation (range of cell diameter i.e., 10-100 µm) [21], section thicknesses needed to be adapted according to the tissue. Despite the particular physicochemical and mechanical characteristics of samples, sections with thicknesses of 100 µm were achieved but required dexterity for their handling, particularly for grape tissue. In addition, the physical state of the sample is essential when studying diffusible components [22]. For turgid plant organs such as fleshy fruit, water, which

amounts to 80-85% of their weight, determines the morphological, physiological and physical properties of tissues at room temperature or in frozen solid states. Cryo-fixation limits the diffusion and redistribution of highly diffusible components [22, 23] but has several drawbacks. First, it requires that the sample be stained before freezing, and second, it faces the issue of structural damage by ice crystals [24, 25]. We found that fresh tissue infusion remains the most efficient and user-friendly method. It is well adapted to turgid plant tissue due to its porosity and exchange properties. Applied to apple and grape tissues, labelling was observed up to the fifth or sixth cell layer from the exposed area (approximately 100 µm for each layer) after two hours of staining. To reduce tissue destruction by ice crystals, cryogenic techniques have been developed. Plunge freezing [26], jet freezing, or slam freezing in cryogenic fluid or high pressure freezing (HPF) transform liquid water to a vitreous solid phase [27]. Currently, HPF is recognized as the method of choice for cryopreservation and is well adapted for ultramicrotome sections. This fast freezing process (≈ 0.5 ms) allows cell preservation up to 600 µm in thickness [28] and is optimal for investigating small cells and objects by the cryo-electron microscopy of vitreous samples (CEMOVIS) [29], cryo-correlative light transmission electron microscopy (cryo-CLEM) [30] or cryo-correlative light scanning electron microscopy [31]. These techniques are suited for preparing samples for cryo-transmission electron microscopy (cryo-TEM), which has a field of view of smaller than 100 μm^2 and is thus not suitable for large sample sizes when a field of view of more than 500 μm^2 is required. In that context, hand freezing at atmospheric pressure remains the simplest, fastest and most repeatable method of cryo-fixation, as samples are dipped in a cryogen, such as cold isopentane. The hand freezing method used here was inspired by the freezing step involved in the Tokuyasu method, with no sucrose infiltration, as fruit tissues are naturally rich in osmolytes that logically act as natural cryoprotectants [32]. Cryo-observation in light microscopy has already been developed [12], but to our knowledge, only a few commercial or homemade fluorescence microscopes equipped with a cryo-chamber cooled by liquid nitrogen are available. They are specifically used to observe vitrified ultrathin sections by fluorescence microscopy as a preliminary step prior to observation by cryo-TEM. In available cryo-fluorescence microscopy setups, dry lenses with relatively long working distances (WDs) and limited numerical apertures (NAs) are used [30]. Recently, a prototype of a LSCM stage and objective lens were described for the high-resolution cryo-observation of sub-cellular localization of animal proteins [20]. In our setup, the inverted optic of the LSCM possesses a short WD that maximizes the NA. These are key factors determining the fluorescence sensitivity and spatial resolution required to localize compounds at low concentrations, such as metallic cations or phenolic compounds in fruit tissue, with a large field of view.

The freezing of water-rich biological materials has been reported to affect cell contraction and the swelling of cell walls [33]. In the present study, the cell wall thickness was observed to vary

according to the apple cryo-fixation temperature. As postulated [33], the extracellular water medium freezes first and provokes an outward water flux from the cells to osmotically equilibrate intracellular and extracellular media. Water in biomaterials is also known to expand by almost 9% during freezing and develops transient stress when the material is frozen from all sides [34]. The cell wall swelling observed in relation to the freezing rate and temperature may be related to these mechanisms, but further studies are required to understand the water behaviour in the fruit cell wall during cryo-fixation. Although water flux and osmolyte redistribution may have occurred during sample cryo-fixation, which impacted the diffusible component distribution, these artefacts may have been limited. Indeed, the two types of calcium labelling distribution observed in both apple and grape tissues showing diffuse staining in cell walls and intense fluorescence spots in cells (**Figure II.4 a-b**) were in agreement with their reported presence in nuclei, vesicles and plant cell walls [22, 35]. Furthermore, the observation of potassium labelling in the apoplast and cell wall of fresh tissue (**Figure II.4 i-j**) and in cells (**Figure II.4 c-d**) of frozen tissue was in agreement with its apoplastic, cytosolic and vacuolar location in fleshy fruit cells [36]. In the literature, calcium and potassium were measured directly on isolated cells and organelles using a fluorescent probe. Lastly, flavonoid distribution mainly observed in the cytosol close to the cell wall supports their putative sites of synthesis. Conversely, their proposed accumulation in the vacuole was not dominant in the present observations in apple and grape, but such localization remains a matter of debate **(Figure II.4 e-f)** [37]. The cellular localization of these different diffusible compounds in the two fleshy fruit parenchymal tissues demonstrated the benefit of the cryo-method.

II.5. Conclusion

The localization of highly diffusible and low concentrated components such as metallic cations and flavonoids was achieved in fluorescence mode by LSCM. The reduction of component mobility was realized by keeping samples in a frozen state during the entire preparation process and by the design and adaptation of a cryo-LSCM setup for the observation of frozen sections. The successful localization of calcium, potassium and flavonoids in apple and grape fruits as a model of turgid tissue illustrated the benefits of the cryo-approach. The results indicated that the freezing temperature and cooling rate remain key parameters in the preservation of hydrated tissue integrity and require further studies to better control the associated osmotic-related structural rearrangements. The extension of this approach to other highly diffusible compounds will benefit from the development of specific and sensitive diffusible fluorescent markers. This approach opens new opportunities for studies of small metabolites and ions in the plant sciences.

II.6. Materials and methods

II.6.1. Plant Material

The fruit tissue nomenclature used in this study is shown in **Figure II.5**. Gala apples and Italia white table grapes were obtained from a local retail store. Regions of interest corresponding to the apple cortex and grape berry with epidermis were sampled as cubes of approximately 0.125 cm^3 using a razor blade (**Figure II.5)**.

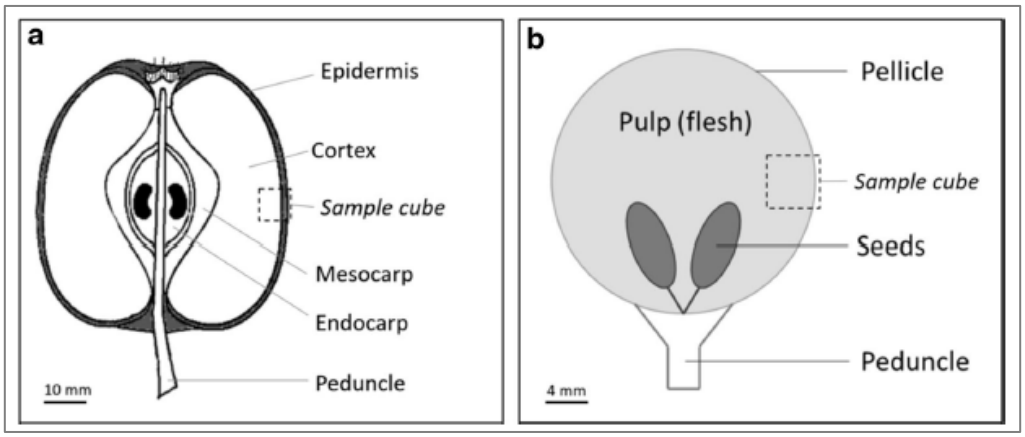

Figure II.16: *Apple A) and grape berry B) sampling and nomenclature.*

II.6.2. Sample preparation for microscopy

Samples were stained by infusion or perfusion before freezing according to different paths followed by cryo-sectioning and cryo-observation. For comparison, samples were also stained by a conventional method and observed in an unfrozen state.

II.6.2.1. Staining

- *Fluorescence stains:* Acridine orange (AO hydrochloride salt; MERCK Calbiochem, France) was prepared as a *0.02% w/v solution in 0.01 M PBS buffer (pH 7).* Congo Red stain (Congo Red powder, FLUKA, Switzerland) was prepared as a 0.1 mg/mL solution in deionized water at pH 5. Fluo-3 calcium probe (Fluo-3 pentapotassium salt, Thermo Fisher Scientific, France) and PBFI potassium probe (PBFI, tetraammonium salt, Thermo Fisher Scientific, France) were prepared as a 0.1 mg/mL solution in MES (25 mM) + Tris (10 mM) buffer (pH 6.0) [17] and kept as a stock solution in an amber flask at 4 °C. The phenolic probe DPBA (2-Aminoethyl diphenylborinate, Sigma-Aldrich, UK) was prepared by dissolving 20 mg in 5 mL of ethanol and 15 ml of phosphate buffer solution 0.01 M (pH 7).

- *The conventional staining of fruit sections (see below for sectioning details) was performed by applying* 2 mL of staining solution onto the sections for 5-10 min at room temperature. Sections were then rinsed 3 times with buffer for approximately 5 min each.
- Staining by infusion of fruit samples: Cubes of *apple and grape were bathed in staining solutions for 2 h at 5 °C* **(Figure II.1-A***).*

- *Staining by perfusion* of entire fruit*: Staining solution was introduced in specific areas of the entire fruit using a syringe (5 mL) filled with 2 mL of staining solution connected to 10 cm of capillary tubing (inner diam. 1 mm) inserted in the fruit. The tubing was perforated at the contact zone in the fruit,* with a 10-mm length and a 0.8-mm pore size (approximately 10 apertures) *to* allow for the diffusion of the stain*. To ensure the flow of the stain in the fruit, the syringe outlet was set 10 cm above the capillary outlet. The flow rate was approximately 125 µL/h. Diffusion was applied overnight at 5 °C* ***(Figure II.1-B)****.*

II.6.2.2. Cryo-fixation

Cryo-fixation was achieved following several methods to obtain different cooling rates:

- The slow freezing of samples at -20 °C was conducted for at least 24 h in a conventional freezer.

- Two fast-freezing methods were tested using the cryogen: for the first one, the sample was directly plunged in liquid nitrogen, whereas for the second one, it was plunged in isopentane (2-methylbutan anhydrous >99%, SIGMA) cooled by liquid nitrogen. In both cases, the freezing duration was 60 sec.

- Freezing under microwave [38] was conducted with the following parameters: microwave equipment (SAIREM, France) operated at a frequency of 2450 MHz, the microwave chamber stabilization time was 30 min at 5 °C, a temperature of -30 °C was set using an air blaster (ACFRI, France), the microwave power was 5 ± 0.1 W, and the duration of freezing was 3 h.

II.6.2.3. Sectioning

- Fresh specimens were sectioned at room temperature using a vibrating blade microtome (Vibratome HM 650V, MICROM, France), stained by a conventional method and collected between 60 x 24 mm glass cover slips (#1) (Thermo Fisher Scientific, Germany) separated by a 250-µm-thick spacer (Gene Frame, 25 µL, 1 x 1 cm^2, Thermo Fisher Scientific, UK). The

sectioning parameters used were a section frequency of 60 Hz, a vibration amplitude of 1.0 mm, and a cutting speed of 1.0 mm/sec. Sections were cut to a thickness of 100 µm.

- Frozen specimens were cryo-sectioned using a cryotome (microtome cryostat HM 500 OM, MICROM, France) operated at -20 °C. The sample cube was fixed on the support section using a water droplet free of cryo-protectant. The cryotome steel blade was a type C profile (16 cm length). The cutting speed was fixed at 1 mm/sec, and the thickness of the sections was 100 µm. Sections were picked up and placed between two 22 x 22 mm #1 glass cover slips (Thermo Fisher Scientific, Germany), which were sealed by frozen water microdroplets.

In all cases, sectioning was performed on the stained sample contact area. The transfer of cold sections within cover slips to the confocal microscope was conducted rapidly over liquid nitrogen.

II.6.3. Laser Scanning Confocal Microscopy (LSCM) observations

LSCM (Eclipse Ti inverted microscope, NIKON Inc. Japan) was used both in bright field and fluorescence modes. Observations were made using a 20x magnification objective lens and, if needed, a numerical zoom of 3x. The laser excitation and fluorescence emission wavelengths were 488 nm for acridine orange, 500-530 nm for Fluo-3 and DPBA dyes, 488 nm and 600 nm for Congo Red dye, and 375 nm and 500-530 nm for PBFI dye. Laser intensity and gain were adjusted visually for sample fluorescence.

II.6.4. Cryo-observation by LSCM

The critical points to manage for LSCM cryo-observation were sample section warming induced by environmental factors and by the laser during observation as well as frost formation on the sample slide. The sample slide was placed onto a Peltier stage (PE100, Linkam Scientific, Epsom UK) under which an adaptable flexible rubber seal was fixed between the objective lens and the stage (**Figure II.6**). This closed space between the lens and the stage was flushed by a cooled nitrogen gas flux to prevent frost formation on the sample slide. A glass container filled with dry ice was placed on top of the sample slide. The measured temperature of the Peltier stage was approximately -25 °C. The container transparency allowed the microscope optical condenser to observe the sample in a bright field.

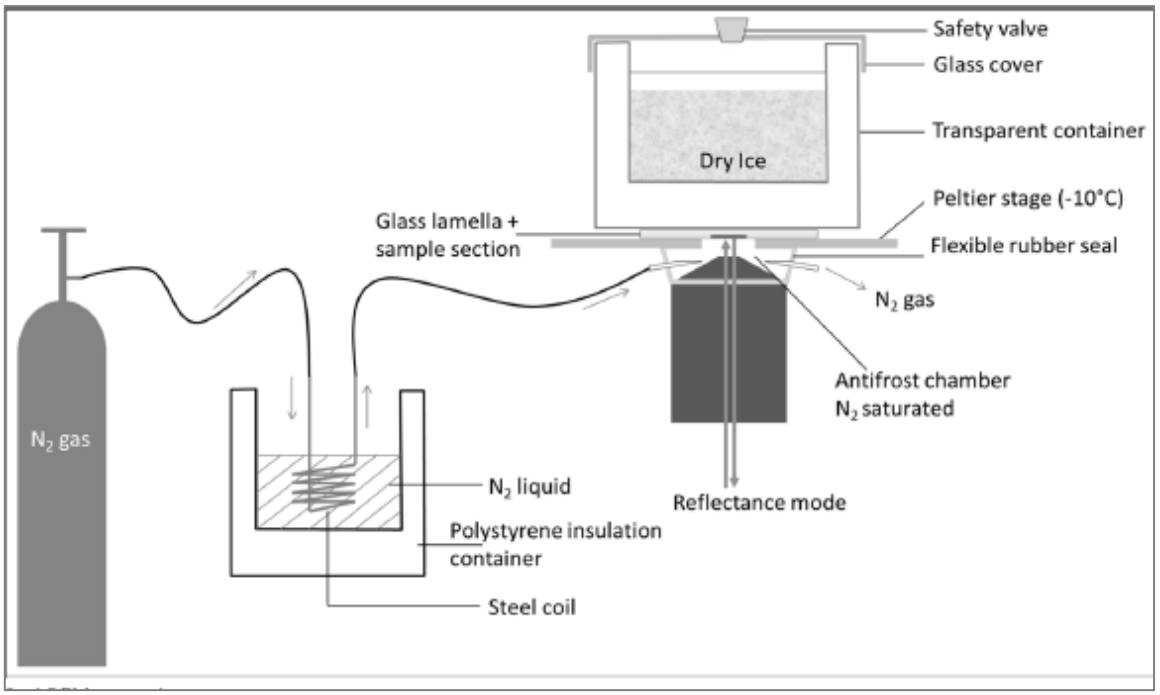

***Figure II.17** : Setup for LSCM cryo-observation.*

II.6.5. Cell wall thickness measurement

Cell wall thickness was specifically evaluated on four apple fruit samples after staining with Congo Red (a cell wall specific dye) and observed at room temperature after slow freezing at -20 °C and after fast freezing by liquid nitrogen and by isopentane. Four sections per sample were recovered, and five cell wall measurements (a total of 80 measurements) were performed on the cell layer at approximately 200 µm from the cuticle using NIS Analysis software (Nikon).

II.7. Acknowledgements

Prof. Alain Lebail and Piyush-Kumar Jha, Ph.D., of the GEPEA team, ONIRIS (Nantes, France), are thanked for their discussions on microwave freezing, making their microwave equipment available and helping with its operation.

II.8. References

1. Hamant O, Traas J: **The mechanics behind plant development**. *New Phytol* 2010, **185**(2):369-385.
2. Jarvis MC, Briggs SPH, Knox JP: **Intercellular adhesion and cell separation in plants**. *Plant Cell Environ* 2003, **26**:977-989.
3. White PJ, Broadley MR: **Calcium in plants**. *Ann Bot* 2003, **92**(4):487-511.
4. Dumville JC, Fry SC: Solubilisation of tomato fruit pectins by ascorbate: a possible non-enzymatic mechanism of fruit softening. *Planta* 2003, 217:951-961.
5. Francoz E, Ranocha P, Nguyen-Kim H, Jamet E, Burlat V, Dunand C: **Roles of cell wall peroxidases in plant development**. *Phytochemistry* 2015, **112**(0):15-21.
6. Rice RW: **The physiological role of minerals in the plant**. In: *Mineral Nutrition and Plant Disease.* Edited by Datnoff LE, Elmer WH, Huber DM. St Paul, USA: APS Press; 2007: 9-29.
7. Sattelmacher B: The apoplast and its significance for plant mineral nutrition. *New Phytol* 2000, 149:167-192.
8. Mentré P: Preservation of the diffusible cations for SIMS microscopy. I. A problem related to the state of water in the cell. *Biology of the Cell* 1992, 74(1):19-30.
9. Chandra S, Morrison GH: Sample preparation of animal tissues and cell cultures for secondary ion mass spectrometry (SIMS) microscopy. *Biology of the Cell* 1992, 74(1):31-42.
10. Moore KL, Chen Y, van de Meene AM, Hughes L, Liu W, Geraki T, Mosselmans F, McGrath SP, Grovenor C, Zhao FJ: Combined NanoSIMS and synchrotron X-ray fluorescence reveal distinct cellular and subcellular distribution patterns of trace elements in rice tissues. *New Phytol* 2014, 201(1):104-115.
11. Palin R, Geitmann A: **The role of pectin in plant morphogenesis**. *Biosystems* 2012, **109**(3):397-402.
12. Echlin P: **Low-temperature microscopy and analysis**: Springer Science & Business Media; 1992.
13. Kitin P, Voelker SL, Meinzer FC, Beeckman H, Strauss SH, Lachenbruch B: Tyloses and phenolic deposits in xylem vessels impede water transport in low-lignin transgenic poplars: a study by cryo-fluorescence microscopy. *Plant Physiol* 2010, 154(2):887-898.
14. Widholm JM: The use of fluorescein diacetate and phenosafranine for determining viability of cultured plant cells. *Stain Technology* 1972, 47(4):189-194.
15. Houtman CJ, Kitin P, Houtman JCD, Hammel KE, Hunt CG: **Acridine orange indicates early oxidation of wood cell walls by fungi**. *PLOS ONE* 2016, **11**(7):e0159715.
16. Nafisi S, Saboury AA, Keramat N, Neault J-F, Tajmir-Riahi H-A: **Stability and structural features of DNA intercalation with ethidium bromide, acridine orange and methylene blue**. *Journal of Molecular Structure* 2007, **827**(1-3):35-43.
17. Mühling KH, Sattelmacher B: Determination of apoplastic K+ in intact leaves by ratio imaging of PBFI fluorescence. *J Exp Bot* 1997, 48(8):1609-1614.
18. Xanthakis E, Le-Bail A, Ramaswamy H: **Development of an innovative microwave assisted food freezing process**. *Innovative Food Science & Emerging Technologies* 2014, **26**:176-181.
19. Lakowicz JR: **Principles of Fluorescence Spectroscopy**, 3rd Edition edn. New York: Springer; 2006.
20. Nahmani M, Lanahan C, DeRosier D, Turrigiano GG: High-numerical-aperture cryogenic light microscopy for increased precision of superresolution reconstructions. *Proc Natl Acad Sci U S A* 2017, 114(15):3832-3836.
21. Bain JM, Robertson RN: The physiology of growth in apple fruits. I. Cell size, cell number, and fruit development. *Aust J Sci Res B* 1951, 4(2):75-107.
22. Hare DJ, New EJ, de Jonge MD, McColl G: Imaging metals in biology: balancing sensitivity, selectivity and spatial resolution. *Chem Soc Rev* 2015, 44(17):5941-5958.
23. McRae R, Bagchi P, Sumalekshmy S, Fahrni CJ: **In Situ Imaging of Metals in Cells and Tissues**. *Chemical Reviews* 2009, **109**(10):4780-4827.

24. Moor H: **Theory and practice of high pressure freezing**. In: *Cryotechniques in biological electron microscopy.* Edited by Steinbrecht RA, Zierold K: Springer Science & Business Media; 1987: 175-191.
25. Dahl R, Staehelin LA: High-pressure freezing for the preservation of biological structure: Theory and practice. *J Elec Mic Tech* 1989, 13(3):165-174.
26. Ryan PR, Newman IA, Arif I: **Rapid calcium exchange for protons and potassium in cell walls of Chara**. *Plant, Cell & Environment* 1992, **15**(6):675-683.
27. Kanno H, Speedy RJ, Angell CA: **Supercooling of water to -92°c under pressure**. *Science* 1975, **189**:880-881.
28. Moore KL, Lombi E, Zhao F-J, Grovenor CRM: Elemental imaging at the nanoscale: NanoSIMS and complementary techniques for element localisation in plants. *Analytical and Bioanalytical Chemistry* 2012, 402(10):3263-3273.
29. Al-Amoudi A, Chang JJ, Leforestier A, McDowall A, Salamin LM, Norlén LP, Richter K, Blanc NS, Studer D, Dubochet J: **Cryo-electron microscopy of vitreous sections**. *The EMBO Journal* 2004, **23**:3583-3588.
30. Schorb M, Briggs JA: Correlated cryo-fluorescence and cryo-electron microscopy with high spatial precision and improved sensitivity. *Ultramicroscopy* 2014, 143:24-32.
31. Strnad M, Elsterova J, Schrenkova J, Vancova M, Rego RO, Grubhoffer L, Nebesarova J: Correlative cryo-fluorescence and cryo-scanning electron microscopy as a straightforward tool to study host-pathogen interactions. *Sci Rep* 2015, 5:18029.
32. Tokuyasu KT: **A technique for ultracryotomy of cell suspensions and tissues**. *The Journal of Cell Biology* 1973, **57**(2):551-565.
33. Floury J, Le Bail A, Pham QT: A three-dimensional numerical simulation of the osmotic dehydration of mango and effect of freezing on the mass transfer rates. *J Food Engin* 2008, 85(1):1-11.
34. Ishii T, Matsunaga T, Pellerin P, O'Neill MA, Darvill A, Albersheim P: **The plant cell wall polysaccharide rhamnogalacturonan II self-assembles into a covalently cross-linked dimer**. *J Biol Chem* 1999, **274**(19):13098-13104.
35. Bush DS: **Calcium regulation in plant cells and its role in signaling**. *Annual review of plant biology* 1995, **46**(1):95-122.
36. Rogiers SY, Coetzee ZA, Walker RR, Deloire A, Tyerman SD: **Potassium in the Grape (Vitis vinifera L.) Berry: Transport and Function**. *Front Plant Sci* 2017, **8**:1629.
37. Kitamura S: Transport of flavonoids: from cytosolic synthesis to vacuolar accumulation. In: *The science of flavonoids.* Springer; 2006: 123-146.
38. Hanyu Y, Ichikawa M, Matsumoto G: An improved cryofixation method: cryoquenching of small tissue blocks during microwave irradiation. *J Microsc* 1992, 165(2):255-271.

Chapitre III

III. Phenolic distribution in apple epidermal and outer cortex tissue by multispectral deep-UV autofluorescence cryo-imaging

Introduction

Ce chapitre reprend la méthodologie développée dans le chapitre II afin de faire la cartographie des composés phénoliques par fluorescence en UV profond via une source synchrotron. Le montage a été adapté au microscope d'épi-fluorescence de la ligne DISCO du synchrotron SOLEIL. Les images de fluorescences obtenues ont été corrigées et traitées pour accéder aux profils de distribution des composés phénoliques dans le tissu grâce aux différents scripts suivants :

- **Annexe 2** : Les scripts de correction des images réalisés sur MatLab.
- **Annexe 3** : Le script « R » d'analyse en composantes principales des images pour distinguer les filtres d'émission de fluorescence d'intérêt.
- **Annexe 4** : Le script « ImageJ » pour récupérer les intensités de fluorescence par lignes de pixels en fonction de la forme de l'échantillon.
- **Annexe 5** : Le script « R » pour récupérer les profils de gradient lissés.

Ce travail a aussi fait l'objet d'une publication dans « Plant Science » référencée ci-dessous et dont le PDF est présenté en **annexe 1-C**.

Vidot, K., et al. (2019). "Phenolic distribution in apple epidermal and outer cortex tissue by multispectral deep-UV autofluorescence cryo-imaging." Plant Science.

Sommaire

III.1. Abstract

Phenolic compounds in fruit are involved in responses to biotic and abiotic stress and are responsible for organoleptic properties. To establish the distribution of these secondary metabolites at the tissue and sub-cellular scales, mapping of fluorescence in apple epidermis and outer cortex tissue in cryogenic condition was performed after deep-UV excitation at 275 nm. Douce Moën and Guillevic cider apple varieties were sampled and frozen after harvest, after 30 days at 4 °C and after 20 days at room temperature. Image analysis of fluorescence emission images acquired between 300 and 650 nm allowed the assignment of fluorescence signals to phenolic compound families based on reference molecules. Emission attributed to monomeric and/or condensed flavanol was localized in whole tissue with major fluorescence in the cuticle region. Hydroxycinnamic acids were found predominantly in the outer cortex and appeared in the cell wall. Fluorescent pigments were mostly found in the epidermis. The distribution of flavanols in the sub-cuticle and phenolic acids in the outer cortex distinguished apple varieties. Storage conditions had no impact on phenolic distribution. The proposed fluorescent imaging and analysis approach enables studies on phenolic distribution in relation to fruit development, biotic/abiotic stress resistance and quality.

Key words: Malus domestica, phenolic compounds, autofluorescence, multispectral imaging, deep-UV synchrotron light, cryo-microscopy.

III.2. Introduction

Phenolic compounds are common plant secondary metabolites that have been grouped into three classes: flavonoids, phenolic acids and stilbenes [1]. The flavonoids encompass flavanols that are also found as oligomers and polymers (i.e., proanthocyanidins and condensed tannins), anthocyanins and flavonols, while phenolic acids comprise hydroxybenzoic acids and hydroxycinnamic acids (**Figure III.1**).

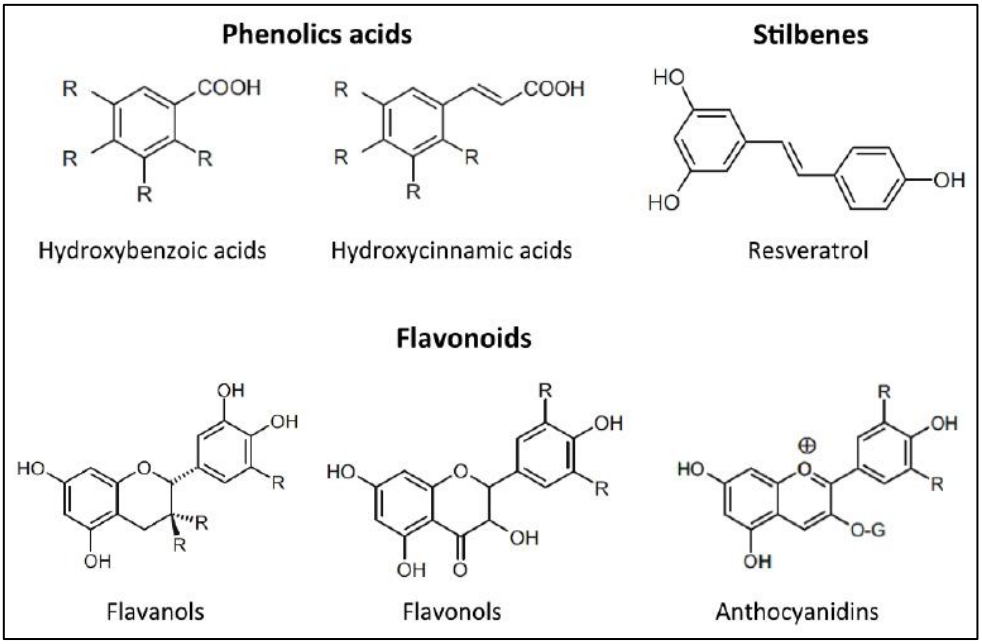

Figure III.18 *: Generic phenolic compound structures. -R may correspond to -H, -OH or -OCH3 and –X may correspond to –H in monomeric form or other flavanol units in polymeric form Vermerris and Nicholson (2006).*

Except for flavanols and hydroxybenzoic acids, which are mainly present in their free form, most phenolic compounds are glycosylated and/or acylated derivatives. Their ultraviolet absorption capacity limits light- induced damage to tissues while they are part of plant defence mechanisms against external biotic stress [2, 3]. In fleshy fruit, phenolic compounds are known for their antioxidant contribution to foods and organoleptic properties, such as colour, astringency or bitterness [4-6]. Various studies in apple and grape have shown important differences in phenolic content between varieties according to fruit development and tissue [7]. Phenolic compounds are commonly characterized by biochemical techniques on whole fruit, skin, flesh, seed or juice extracts. However, there are few reports on the distribution of specific phenolic compounds at the tissue and sub-cellular scales under in-vivo-like conditions. Flavanols and condensed tannins were determined to be localized in the epidermis, parenchyma and seeds by microscopy of fresh or chemically fixed apple [8], grape [9, 10] and other fruits [11-14]. Flavanols were localized by DMACA staining (4-dimethyl-aminocinnamaldehyde) [14-16] while flavonols were highlighted by fluorescence microscopy using the specific dye DPBA (diphenylboric acid-2-aminoethyl ester) [17, 18]. However, chemical preparation

damage to fleshy fruit tissue integrity affects the cellular localization of diffusible compounds [19], and dyes are limited by their specificities.

To address these issues, mapping phenolic compounds through their autofluorescence characteristics appears to be a good alternative as no specific stain is required. Hydroxycinnamic acids express a blue fluorescence when excited at the UV wavelength of approximately 350 nm [20, 21] while anthocyanins and flavonols are autofluorescent at visible wavelengths [22]. Monomeric and condensed tannin ((+)-catechin, (-)epi-catechin, procyanidins) fluorescence requires deep-UV wavelength excitation at approximately 280 nm [23] [24]. The use of different bandpass filters to select specific ranges of fluorescence emissions offers the opportunity to localize different compounds within the same sample through a multispectral approach [25]. However, data on the fluorescence emission of specific phenolic compounds are scarce due to the high number of entities that constitute this metabolite family and because access to pure reference phenolic compounds is limited.

To avoid artefacts related to small compound diffusion and loss during sample preparation, cryo-fixation, cryo-microtomy and fluorescence cryo-observation of biological samples have seen recent developments. Cryo-confocal observations at high resolutions were introduced with the realization of specific microscope stages and immersion objective lens prototypes [26, 27]. A simpler and readily accessible setup was developed to observe fleshy fruit tissue by cryo-laser scanning confocal microscopy (LSCM) [18]. Among the advantages of cryo-observations is the lower fluorescence bleaching compared to that during room temperature observations and thus the recovery of higher fluorescence intensity [26, 28].

Preliminary tests of fresh fruit auto-fluorescence responses after excitation at 375 nm were performed on apple and grape. The latter revealed promising autofluorescence signals, while a lower excitation wavelength was found necessary to assess flavanol localization. The objective of the present work was to map phenolic compounds in cryo-fixed outer tissues of apple. The mapping was performed at a large field of view by multispectral autofluorescence imaging after deep-UV excitation at 275 nm using the setup developed for fleshy fruit cryo-observation. Two cider apple varieties stored in three different conditions were studied to evaluate the genetic and physiological impacts on phenolic compound distribution. Fluorescence excitation and emission characteristics of reference phenolic compounds were recorded to help identify fruit tissue phenolics.

III.3. Materials and methods

III.3.1. Materials

III.3.1.1. Chemicals

Phenolic compounds used for reference fluorescence spectra were from the laboratory collections of ESA-GRAPPE (Angers, France) and BIA-PRP (Rennes, France). Formic acid was purchased from Sigma-Aldrich (UK) and methanol was purchased from CarloErba (Italy).

III.3.1.2. Fruits

Apple (Malus domestica, Royal Gala) and grape (Vitis vinifera, Red Italian) for preliminary fluorescence analysis after 375 nm UV excitation were from a local retail store. These fruits were used without further storage. For the fluorescence mapping following excitation at 275 nm, two cider apple varieties, Douce Moën (M. domestica, Douce Moën) and Guillevic (M. domestica, Guillevic), were provided by IFPC (Le Rheu, France). Fruits were harvested on October 2017 in orchards at Surzur (Morbihan, France). Nine fruits of each variety were subjected to three different storage conditions: three were immediately sampled, three were stored at 4 °C for 30 days and three were stored at room temperature for 20 days before sampling.

III.3.2. Methods

III.3.2.1. Spectrofluorometry

Phenolic references were dissolved at 2 mg mL-1 in 2 mL of H2O:MeOH (1:1 in volume) + 1% formic acid (in volume). Quartz cuvettes (10 x 4 mm, 114F-QS, Suprasil HELLMA Analytics, France) were filled with 500 µL of standard solution and observed by spectrofluorimetry (F-4500, HITACHI, Japan). Emission and excitation spectra for each compound were recorded between 200 nm and 600 nm.

III.3.2.2. Laser scanning confocal microscopy (LSCM)

Cubes of 5 x 5 x 5 mm3 were sampled from the epidermal region of equatorial fruit slices of commercial apple and grape. Sections of 100 µm thickness were cut from fresh cubes with a vibrating blade microtome (HM 650V, MICROM, France) and immediately observed or dipped in standard buffer solution pH 10 (HI 70010C, NIST standard, HANNA INSTRUMENTS, Hungary) followed by H2O milliQ wash prior to LSCM observations at room temperature. LSCM (A1 Eclipse Ti inverted microscope, NIKON Inc., Japan) was configured with laser diode excitation at 375 nm. Fluorescence emission was acquired at 20× magnification with a resolution of 0.63 µm pixel-1 and image size of 512 x 512 pixels2 (16-bit). Four bandpass emission filters were used to map fluorescence: 400-450 nm, 500-530 nm, 560-

600 nm and 630-700 nm. These form sets of multispectral images of four channels with spectral controlled excitation and emission parameters.

III.3.2.3. Synchrotron deep-UV wide-field fluorescence microscopy (DUV)

One 5 x 5 x 5 mm3 cube was randomly sampled from the epidermal region of a cider apple fruit equatorial slice. The cube was frozen in liquid nitrogen-cooled isopentane and stored at -20 °C prior to analysis. Sections (60 µm thick) were cut from frozen cubes using a cryostat microtome (HM 500 OM, MICROM, France) at -20 °C. The section was placed between quartz lamella (R52-5000, ESCO Optics, USA) glued together by frozen water droplets. Synchrotron UV microscopy was performed at the DISCO (Dichroism, Imaging, mass Spectrometry for Chemistry and biOlogy) beamline at the SOLEIL (Source Optimisée de Lumière à Energie Intermédiaire du LURE (Laboratoire à Utilisation du Rayonnement Electromagnétique)) synchrotron radiation facility [29] (Gif-sur-Yvette, Saint-Aubin, France) on the inverted epi-fluorescence TELEMOS microscope [30]. Observation was realized under cryogenic conditions using a handmade setup composed of a Peltier stage (PE100, LINKAM Scientifics, UK) cooled by dry ice as described in [18]. The wide-field microscope TELEMOS modified by the DISCO beamline staff was a Zeiss Axio Observer Z-1 designed to observe samples after deep-UV (DUV) excitation. The microscope was equipped with a motorized sample plate (MS-2000 XY, Applied Scientific Instrument, USA) to move the sample along the X and Y axes. Sample movement along the Z axis was controlled by the inverted microscope. The setup used the 10× magnification Zeiss Ultrafluar lens (N.A 0.2, WD 7.4) and a sharp 300 nm dichroic mirror “DM” (Omega Optical), which reflected the 280 nm excitation and transmitted emission light above 300 nm. Multispectral fluorescence emission was recorded using six different emission bandpass filters: 300-306 nm, 327-353 nm, 352-388 nm, 412-438 nm, 420-480 nm and 600-650 nm (Semrock, Rochester, USA). In the text, filters are referred to by their low wavelength limit. A back-illuminated CCD camera (Pixis BUV, Princeton Instrument, USA) recorded the images (1024 x 1024 pixels; 1 x 1 µm² per pixel; grey level coded in 16 bit). Acquisition times were 12.5 s for the 300 nm filter, 5 s for the 327, 352, 412 and 420 nm filters, and 7.5 s for the 600 nm filter. Acquisition was performed from the sample cuticle to approximately one mm inside the tissue. With three biological repetitions and three different storage modalities, a total of nine images were registered per variety.

The beamline intensity, which was focused at the centre of the observation field, led to raw images that required corrections to homogenize illumination. In addition, the camera provided a non-null background without illumination. Both inhomogeneous illumination and background corrections were realized according to the following formula:

$$\mathbf{I_c = (I - Dark) / (White - Dark)}$$

where **Ic** is the corrected image; **I** is the raw image; **Dark** is the background and **White** is the flat field.

For this purpose, nine different "dark" images were recorded without sample and without any illumination, one for each of the six emission filters. The "White" images were acquired using a frame (1.0 x 1.0 cm2, AB-0576, Gene Frame, THERMOSCIENTIFIC, UK) displaying a homogeneous autofluorescent signal. Thresholding was also required to define the sample image from the camera noise. Image pretreatments were performed using MATLAB® 2017b.

The corrected images were cropped to 300 x 400 µm² size to fit within a pertinent sample image area. To take into account out-of-plane sample sections, several acquisitions were recorded for the same sample area with a maximum of six focal planes. As this method was not confocal imaging, a clear image was reconstructed by combining the different focal plane views with the extended focus software HeliconFocus6® (version 6.8.0) using the pyramidal method.

III.3.2.3.1. Multispectral analysis of DUV fluorescence images

DUV fluorescence emission was valued based on the grey scale intensity of pixels in cropped images. Principal component analysis was applied separately on each multispectral image, and fluorescence profiles were extracted from selected emission filters.

III.3.2.3.2. Image Analysis

Individual emission images were unfolded to form one vector [31]. The image vectors were combined into one table per sample containing six columns corresponding to the six filters and n rows corresponding to the n pixels of the image. Principal component analysis (PCA) was applied to the resulting data table, and correlation circles were drawn from the PCA loadings. Principal component images were obtained by refolding scores [31]. Component images were filtered to keep 99% of pixels closer to the median value and to remove eventual aberrant pixel values prior to normalization of grey levels between 0 and 255. PCA reconstructed colour images were created from components 1, 2 and 3 identified in the blue, red and green channels, respectively.

Localization of phenolic compounds in samples was also analysed by computing fluorescence intensity profiles from the cuticle to the inner tissue. This "image distance" analysis was realized using FIJI/ImageJ® software [32] and the mathematical morphology plugin process/erode (3D) [33]. Thresholding was first applied to create a binary mask of the sample. Distance from the cuticle was obtained by the following procedure: one-pixel erosion (pixel size = 1 x 1 µm2) was applied to the sample mask and the resulting binary image was subtracted from the initial sample binary image. This step was iteratively applied until the last image column was reached. The mean profile was smoothed

to reduce intensity variations due to the presence of cell lumens with low fluorescence and cell walls with high fluorescence. This was realized by applying local regression (LOESS) with a degree of smoothing of 0.4. Normalization between 0 and 1 was realized on the maximum smoothed mean value to allow profiles comparison between samples. Examples of raw and smoothed profiles are shown for Douce Moën at harvest in **Supplementary Figures III.1 and III.2**. The smoothed profiles from the three biological replicates per storage modality were averaged and the mean profile per modality was plotted with its 95% confident interval (**Supplementary Figure III.3**).

III.3.2.4. Statistical analyses

The effect of storage was evaluated by Student's t-tests of the smoothed mean pixel values of three biological replicates per pixel distance. As no significant differences were found between storage modalities, Student's t-test for variety effect was performed on the nine replicates.

Principal component analysis, LOESS smoothing and Student's t-tests were performed in R [34].

III.4. Results

III.4.1. Fluorescence properties of reference phenolic compound

Excitation and emission fluorescence spectra were registered from standard phenolic compounds (**Supplementary figure III.4**) and the maximum wavelength responses recorded (**Table III.1**). If associating specific compounds with peculiar emission wavelengths is difficult due to the width of spectra with large overlaps, distinguishing families of compounds, such as flavanols (including condensed tannins), phenolic acids, anthocyanins and flavonols remains possible. For example, phenolic acids, such as p-coumaric acid, ferulic acid and caffeic acid have a maximum emission at approximately 420 nm, while flavanols such as (+) catechin, (-) epi-catechin and procyanidin share maximum emission at approximately 320 nm. In fact, due to their large excitation spectra, most phenolic compounds will fluoresce under excitation at 275 nm. Among the tested reference compounds, only phloridzin, rutin and arbutin will not fluoresce after deep-UV excitation.

Table III.6: Fluorescence excitation/emission maxima of phenolic compounds registered by spectrofluorometry: regular case: literature, **bold case**: this study.

Compounds	$\lambda_{max\ excitation}$ (nm)	$\lambda_{max\ emission}$ (nm)		Compounds	$\lambda_{max\ excitation}$ (nm)	$\lambda_{max\ emission}$ (nm)
Emission range (<350 nm)				**Emission range (400-500nm)**		
Protein group				*Phenolic acids group*		
Phenylalanin[70]	258	285		**Ferulic acid**	**310/370**	**420**
Tyrosin [70]	276	302		**p-Coumaric acid**	**350**	**420**
Emission range (300-400 nm)				**Caffeic acid**	**270/360**	**440**
Flavanols group				**Chlorogenic acid**	**360**	**460**
(-) Epicatechin	**290**	**320**		*Others compounds*		
(+) Catechin	**290**	**320**		Kaempferol[21]	268	422
Procyanidin B1	**285**	**320**		**Rutin**	**300**	**460**
Procyanidin B2	**295**	**320**		**Emission range (500-600nm)**		
Epigallocatechin	**275**	**320**		*Flavonols group*		
Others compounds				Anthocyanins[22]	300/410	360/420/530
Tryptophan [22]	280	357		**Cyanidin hydrate**	**278**	**550**
2,5-Dihydroxybenzaldehyde[21]	278	360		**Quercetin-3-O-glucoside**	**260/410**	**510**
Syringic acid	**310**	**360**		**Quercetin**	**420**	**520**
Vanillic acid[21]	278	360		**Quercetin galactoside**	**295**	**600**
Gallic acid	**320**	**370**		*Others compounds*		
Myricetin[21]	268	370		**Arbutin**	**420**	**530**
Resveratrol	**310/360**	**390**		**Phloridzin**	**250/330**	**540**
				Chlorophyll/chloroplast[37]	360	680

III.4.2. Preliminary analysis of autofluorescence observed after excitation at 375 nm

In a preliminary study, autofluorescence observations of fleshy fruit were realized with a laboratory confocal laser scanning microscope using a UV diode laser at 375 nm **(Figure III.2)**. This test was performed to check the pertinence of autofluorescence analysis on two types of fleshy fruits: Royal Gala apple and Italian Red grape. In all cases, the cuticle presented bright and intense fluorescence as previously observed [35]. Red spots were observed within the cells of both fruit but particularly in grape, while light yellow fluorescence was observed in vacuole-like compartments only in apple. Red fluorescence could correspond to chlorophyll residues while yellow emission could be related to compounds of the flavonol class, such as quercetin derivatives [36] [37]. A weak blue emission was also observed in the cell wall at native pH and was found to increase at pH 10, as reported for ferulic

or coumaric acids [20]. These emission variations after UV excitation at 375 nm provided support for the mapping of phenolic compounds using multispectral autofluorescence imaging. However, a lower excitation wavelength was sought to access compounds in the flavanol family.

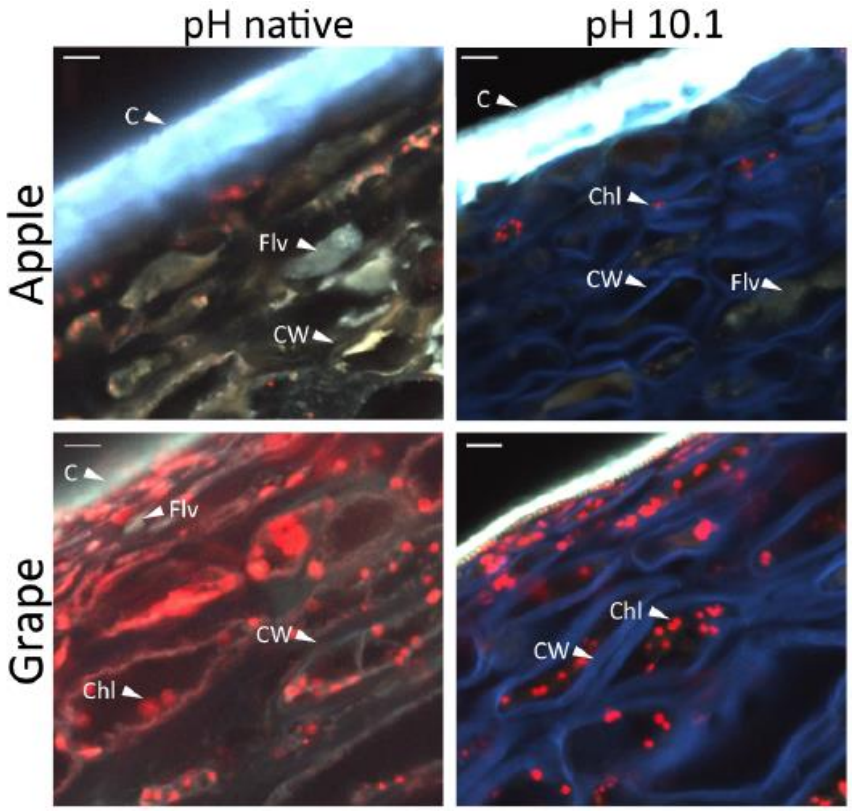

Figure III.19*: Local retail store fresh apple and grape autofluorescence at natural pH and at pH=10.1 after excitation at 375 nm. The fluorescence emissions recorded are 400-450 nm (blue), 500-530 nm (green), 560-600 nm (yellow), and 630-700 nm (red). C: cuticle, CW: cell wall, Chl: chlorophyll residues, Flv: flavonols. Scale bar: 20 µm.*

III.4.3. Autofluorescence after excitation at 275 nm

The autofluorescence of flavanols in fleshy fruit tissue requires excitation at a low UV wavelength, which is yet inaccessible with a common microscopy laser beam. The synchrotron beamline at DISCO allows for exciting samples in the 200-350 nm range. To limit the diffusion of phenolic compounds, apple tissue was first cryo-fixed prior to cryo-observation of multispectral fluorescence from 300 nm to 650 nm (**Figure III.3**). Outer-cortex parenchyma fluorescence was distinguished from that of epidermal tissue, which encompasses cuticle and sub-cuticular cell layers (**Figure III.3**). Between 327 and 388 nm, sub-cuticular cell layer fluorescence was more intense and disappeared at higher bandpass wavelength filters except, for the 600 nm filter. Intense fluorescent spots were observed inside the cell mainly with 300 and 327 nm filters, but in all cases, cells walls showed a more intense signal than cells.

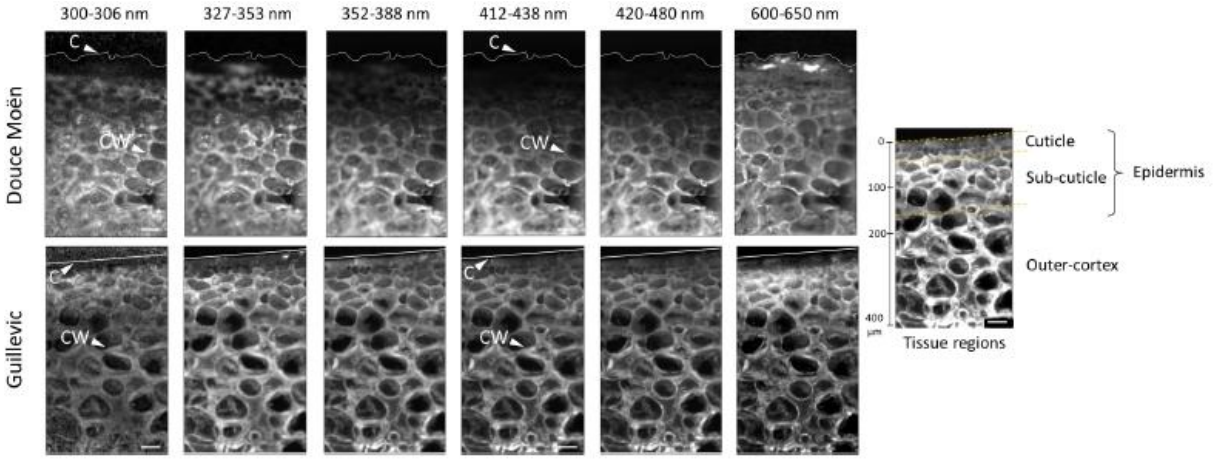

***Figure III.20**: Frozen apple autofluorescence for one replicate of Douce Moën and Guillevic at harvest after excitation at 275 nm. Tissue regions are drawn on the right image resulting from a combination of whole Guillevic filter emission images. C: cuticle, CW: cell wall, Scale bar: 40 µm.*

To better distinguish differences in sample fluorescence, principal component analysis was applied to the collection of images obtained with the different bandpass filters. All principal component analyses performed on the three modalities presented similar loadings. For example, the loading and component images are shown in **Figure III.4** for representative samples of Douce Moën and Guillevic apple varieties at harvest. Fluorescence through 300, 327, 352, 412, 420 and 600 nm filters contributed mainly to components 1 and 2 and fluorescence at 300, 327 and 600 nm contributed more weakly to components 3 and 4. Most filters contributed to component 1, which corresponded to the general variations of fluorescence intensity and explained 65.8% and 61.7% of the total variance for Douce Moën and Guillevic, respectively. The component images showed that the highest overall fluorescence intensity was mainly localized in the walls of outer-cortical cells. The second component, expressing the contribution of the 300 and 327 nm filters (positive side) in opposition to the emission filters 412 and 420 nm (negative side), contrasted the sub-cuticular cell layers. Filters 352 and 600 nm were inversely related to this second component for the two varieties. The third component pointed out the cuticle region with a relatively higher fluorescence measured using the 327 nm emission filter (in red) compared to the 300 and 600 nm filters (in blue), showing the rest of the sample. The fourth component showed a higher level of noise and a relatively higher fluorescence level associated with the 300 nm filter (in blue) in the epidermal region as well as in the cell walls of sub-cuticular cells and outer cortical cells. Thus, fluorescence distinguished three areas: the cuticle region with a relatively higher fluorescence emission using the 327 nm filter, the sub-cuticular cell layers with the 300 nm and 600 nm filters, and the walls of outer-cortical cells with the 352, 412 and 420 nm filters. The three first component images of the representative samples were combined in an RGB image to better visualize the tissue regions according to fluorescence (**Figure III.4**). To objectivize differences observed in fluorescence distribution, normalized intensity profiles for all images of the two varieties at the different storage conditions were measured.

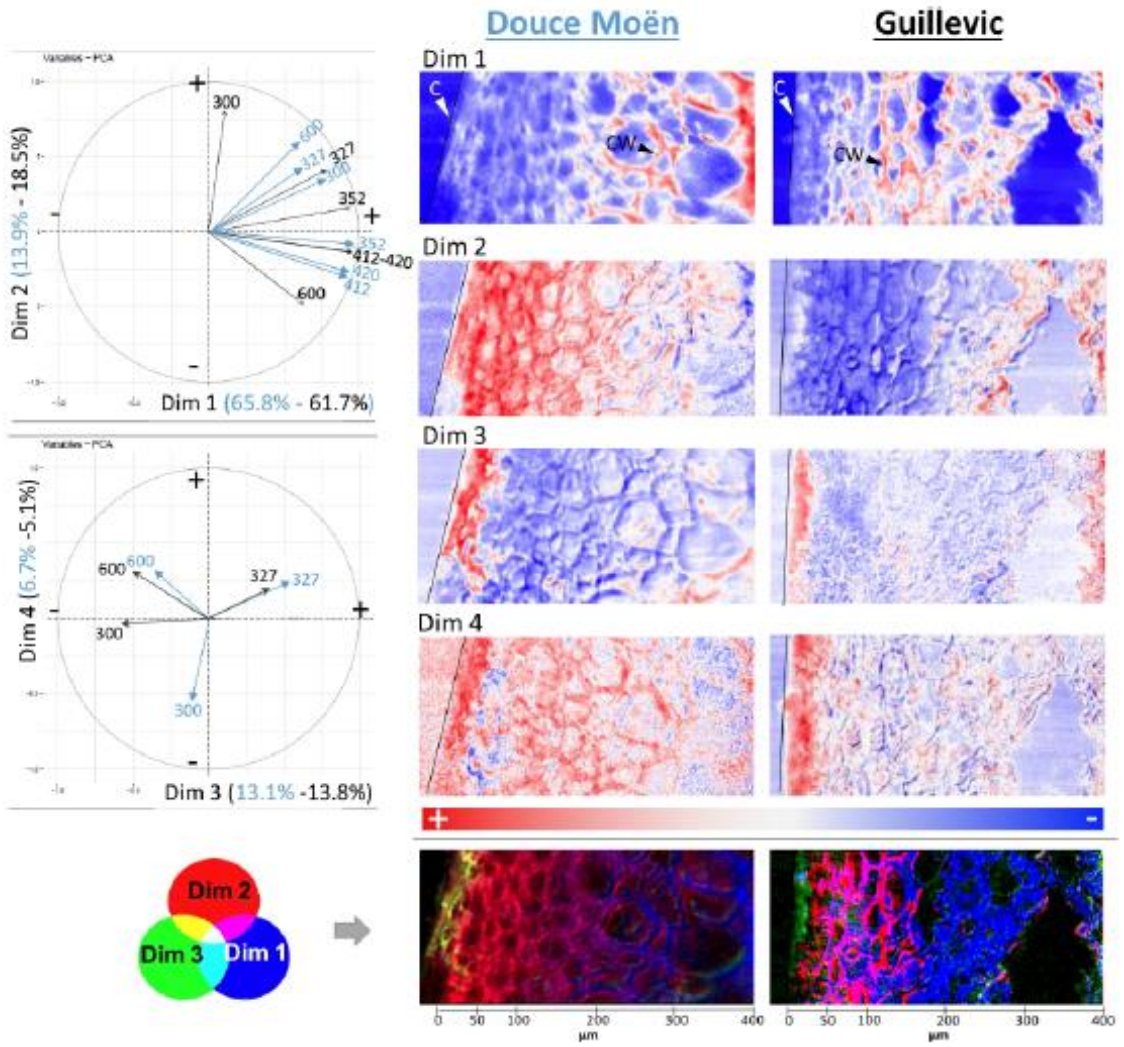

Figure III.21*: Principal component analysis on the six emission filter images for one replicate of Douce Moën (blue character and arrows) and Guillevic (black character and arrows) at harvest and the PCA images of the four components. On the component images, blue and red pixels represent negative and positive contributions of the emission filters to the component. RGB reconstructed images from PCA components were built from dimension 1 (blue), dimension 2 (red) and dimension 3 (green). C: cuticle, CW: cell wall*

Intensity profiles from the cuticular to the outer cortical tissue were obtained for the four bandpass filters discriminating the most apple tissues: 300, 327, 420 and 600 nm. As cell lumen and cell walls showed marked differences in fluorescence intensities, smoothing of each profile was realized by local regression (LOESS) at the expense of fine structures contributing to fluorescence (cells, cell walls, sub-cellular structures). The smoothed and normalized curves allowed comparison of trends in fluorescence variations along the first 400 µm under the cuticle. Examples of raw and smoothed profiles are shown for the Douce Moën variety at harvest in **Supplementary Figures III.1 and III.2**. Considering close fruit calibres within varieties, Student's t-test at each distance point per filter showed that storage modalities had no effect on fluorescence profiles (p-value > 0.05; **Supplementary Figure**

III.3). Thus, all biological replicates (n= 9) were used to evaluate the effect of apple varieties on fluorescence intensity profiles (**Figure III.5**).

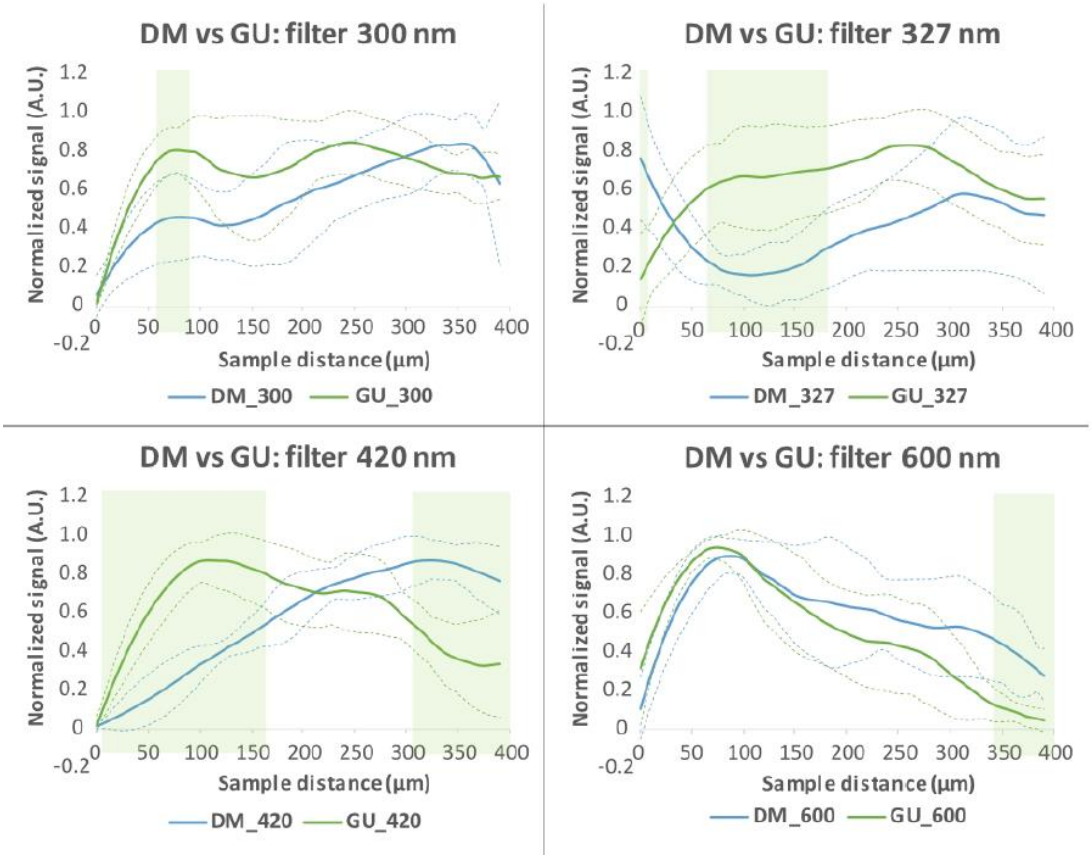

***Figure III.22**: Smoothed (LOESS method: α = 0.4) and normalized average plot profiles of Douce Moën (DM) and Guillevic (GU) signal acquisition for emission filters 300 nm, 327 nm, 420 nm and 600 nm after excitation at 275 nm. The dotted lines represent the 95% confidence interval. The coloured areas correspond to significant differences between DM and GU with a p-value < 0.01 by Student's test (n = 9).*

Significant differences were particularly noted with the 327 nm and 420 nm filters (**Figure III.5**). For the 327 filter, an inverse gradient was observed between the two varieties with a rupture point at approximately 100 µm from the cuticle. Douce Moën showed higher fluorescence intensity than Guillevic, particularly in the first 10 µm under the cuticle but was lower than that of Guillevic 60 µm away from the cuticle. The 420 nm filter also presented two significantly different areas, first in the epidermis where the Guillevic signal was higher than that of Douce Moën and opposite to the 327 nm filter profile and second in the outer cortex (300 to the 400 µm limit of the images) where Guillevic fluorescence was lower. A maximum was observed at approximately 100 µm for Guillevic, while for Douce Moën, it was at approximately 330 µm from the cuticle. Weak significant differences were observed between Guillevic and Douce Moën in the sub-cuticular cell layers for the 300 nm filter and in the outer cortex for the 600 nm filter. These two profiles also showed similar ruptures at approximately 75-100 µm from the cuticle. The mean smoothed plot profiles (**Figure III.5**) showed

good agreement with the fluorescence distribution observed in the representative PCA reconstructed images (**Figure III.4**). The three regions observed may be approximately delimited from these results (**Figure III.6**) for Douce Moën to range from approximately 0 to 50 µm, 50 to 200 µm and 200 µm to 400 µm while for Guillevic, to range from approximately 0 to 60 µm, 60 to 150 µm and 150 to 400 µm. These regions may correspond to the cuticle and the sub-cuticle forming the epidermis and the outer cortex as depicted in **Figure III.3**.

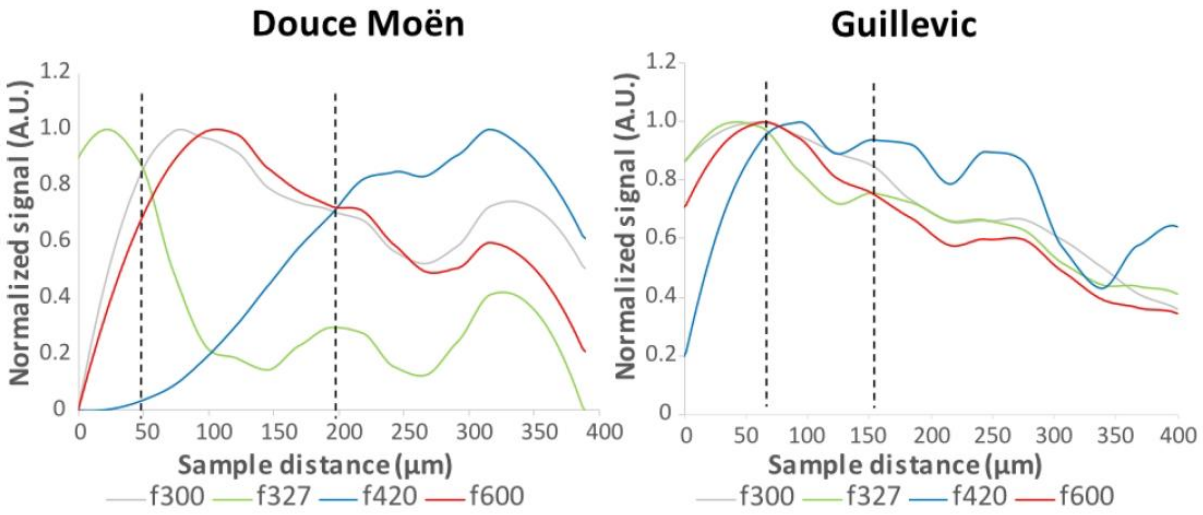

***Figure 23**: Superposed smoothed (LOESS method: α = 0.4) and normalized average plot profiles of Douce Moën and Guillevic signal acquisition for emission filters 300 nm (grey line), 327 nm (green line), 420 nm (blue line) and 600 nm (red line) after excitation at 275 nm. The profiles were plotted along the sample section distance from the outer cuticle to 400 µm deep inside the tissue.*

The fluorescence emission of reference phenolic compounds allowed us to propose the possible nature of chemicals in the different tissues (**Table III.1**). Fluorescence observed with the 300 nm filter was more likely due to proteins as this range of emission is related to the amino-acids tyrosine and phenylalanine [38]. Fluorescence through the 327 nm filter may have corresponded to the tryptophan and most likely to catechins that are predominant in apple fruit tissue. Since these compounds are flavanol monomers and oligomers, by extension such fluorescence would also reveal condensed tannins. Likewise, fluorescence at 420 nm would represent the phenolic acid family, such as hydroxycinnamic acids, while the fluorescence at 600 nm would be pigments, such as anthocyanin or chlorophyll. According to these propositions, pigments would be particularly localized in the sub-cuticular cell layers of both varieties, while flavanols including condensed tannins would be present in the epidermis and outer cortex of both varieties, though with higher intensity in the sub-cuticular cell layers of Guillevic. The distribution of phenolic acids differed markedly between the two varieties. In Douce Moën, they were present mainly in the outer cortex, while in Guillevic they were also present in the sub-cuticular cell layers. Storage conditions did not appear to affect these distributions.

III.5. Discussion

The results showed that multispectral observation of auto-fluorescence provides a convenient alternative for localizing phenolic compound families in fleshy fruit tissue with limited sample preparation and artefact introduction compared to classical resin embedding and staining methods. Adaptation of the cryogenic procedures developed for cryo-LSCM [18] to the wide-field TELEMOS microscope of the DISCO beamline at the SOLEIL synchrotron facility allowed observation of fluorescence from 275 nm, which excited flavanols and condensed tannins together with other phenolic compounds in well-preserved apple tissue with limited metabolite diffusion. The obtained images confirmed the efficiency of the cryogenic process as intracellular content appeared filled, though of lower fluorescence intensity compared to cell walls. Cryo-observation also improved fluorescence intensity [26], likely by reducing fluorescent bleaching due to the temperature dependency of quencher diffusion [28]. This phenomenon was particularly helpful in establishing the qualitative distribution of fluorescent compounds in fruit tissue.

Fluorescence tended to indicate phenolic compounds within cell walls. However, most phenolics are localized within cell organelles, vacuoles or the cytoplasm [39, 40] with fewer in cell walls. In apple, phenolic compounds have not been described as part of the cell wall polysaccharide composition [41] [42]. Some authors [43] suggested that tannin accumulation takes place in the vacuole, but their polymerization appeared near the cell walls. As apple fruit cells are highly hydrated, ice crystals formed during cryo-fixation of the water-filled vacuoles [44] may have pushed fluorescent organelles and cytoplasmic materials close to the cell walls. As a consequence, part of the cell wall fluorescence observed with the 10× magnification lens (resolution: 1.24 µm / pixel) may have resulted from nearby intracellular fluorescent compounds/organelles. However, the blue emission observed by LSCM in the cell wall of fresh apple and grape tissue and its increased fluorescence at basic pH supported the presence of hydroxycinnamic acids in cell walls. This observation was realized at higher magnification (20×, resolution of 0.63 µm / pixel) than that of the TELEMOS setup and excluded the potential of ice crystal effects on cell wall fluorescence. Hydroxycinnamic acids have already been reported in apple fruit mostly in vacuoles due to their characterization in the juice [45] [46, 47], but they are also known to be present in plant cell walls [48]. Their low concentration in apple cell walls likely prevented their detection by classic analytical techniques. However, further work is needed to assess the nature of these compounds and whether they are esters of cell wall polysaccharides, as reported for other plants [20] [49, 50].

The cuticle was the most fluorescent zone of apple and grape fruit tissues observed by LSCM (**Figure III.2**). The observation of cuticle autofluorescence was already reported in several fruits, including apples and grapes and may be related to high concentrations of proteins and phenolic acids

[35] [51]. Though anthocyanins, flavonols, flavanols (including condensed tannins), hydroxycinnamic acids and proteins were essentially reported in the epidermis region [52-54], they were more rarely localized in sub-cuticular cell layers [8, 10, 14]. The high concentration of phenolic compounds in the sub-cuticular cell layers is probably related to defence against pathogens [55] or light damage to tissues. The firmer mechanical resistance of grape and apple skins compared to their flesh [56, 57] may also be associated to the important presence of phenolic compounds in the skin. Indeed, phenolic compounds and, in particular, flavonoids were proposed to increase the rigidity of the cutin matrix in the cuticle of ripe tomato [58]. Comparatively, excitation with DUV at 275 nm revealed a lower cuticle autofluorescence. Although flavonoids and phenolic acids, the main cuticle phenolic compounds, have large excitation and emission spectra (**Supplementary Figure III.4**), 275 nm excitation was not optimal to yield high autofluorescence intensities. Though such a wavelength was beneficial for exciting flavanols and proteins fluorescence, it appears that flavanols are in low concentration - if any- within the cuticle but are present in the first cell layers underneath (**Figure III.3**).

The red-skinned Douce Moën and the yellow-skinned Guillevic cider apples were used as model fruits to help distinguish phenolic compound locations by their autofluorescence. Douce Moën is known to be richer in hydroxycinnamic acids and in monomeric tannins, such as (+) catechin, (-) epicatechin and procyanidin with lower tannin degrees of polymerization compared to Guillevic [59]. Anthocyanins were not characterized in the two varieties, but the more colourful Douce Moën skin evidenced higher anthocyanin and/or pigment contents than that of Guillevic. Based on distinct fluorescent emissions of reference compounds after 275 nm excitation, autofluorescence in Douce Moën and Guillevic cryo-sections allowed the detection of pigments in the sub-cuticular cell layers in agreement with the known flavanols, anthocyanins and chlorophyll concentrations in apple skin [60, 61]. The main distribution of tannins in the sub-cuticular area together with that of phenolic acids in the outer cortex parenchyma may be related to the ratio reported for procyanidin (PC) and hydroxycinnamic acid (HC) concentrations in the fresh peel (HC/PC: 0.14) and parenchyma (HC/PC: 0.27)[62]. This different distribution was not reported in the literature for grape in which flavanols were mainly localized in the epidermis and in the seeds although hydroxycinnamic acid content was higher in skin than in pulp [16, 54, 63].

Changes in phenolic compounds distribution were not observed with storage modalities that were aimed at impacting apple ripening. This result is at odds with studies showing phenolic compound variations during ripening of fruit [7], such as apple [52, 64] and grape [10, 65]. The lack of autofluorescence discrimination between ripening stages may be related to the small tissue area observed. Instead, the present study evidenced a variation in phenolic distribution between apple varieties. This may be related to different tissue thicknesses as for both varieties, different rupture

points in phenolic distributions were observed along distance profiles from the cuticle. These ruptures could correspond to different cell layers in the epidermis and the outer cortex. In particular, a rupture was discernible in fluorescence profiles at an approximately 100 µm depth from the skin samples. Apple histology studies have shown changes from smaller cells in the epidermis to larger cells in the outer cortex parenchyma tissue at an approximately 100-µm depth from the surface of mature fruit [66-68]. Thus, differences in phenolic compound distribution between the two varieties could reveal genetically distinct thicknesses of epidermal cell layers as well as different secondary metabolism in these tissues.

III.6. Conclusion

The cryo-method used here could benefit from further developments in sample preparation and means of cryo-multispectral fluorescence observations. Applying microwaves during cryo-fixation [69] to avoid ice crystal growth combined with the use of confocal microscope stages and lenses for high-resolution cryo-observations [26, 27] is expected to improve the localization of phenolic compounds in the cell and cell wall. Nevertheless, multispectral fluorescence cryo-imaging at 275 nm excitation allowed the distinction of three major classes of phenolic compounds in tissue under in-vivo-like conditions without any specific dyes. The detection of hydroxycinnamic acids in apple and grape cell walls requires their identification and linkage in the walls. Coupling multispectral analysis based on LSCM observations in the UV-visible wavelength and synchrotron deep-UV analysis could provide a convenient way to extend the range of accessible autofluorescent phenolic compound distributions in the same sample tissue section. These observations will enable other studies on the mechanical behaviour resulting from the presence of these compounds in fruit tissues in the context of fruit development, quality and processing.

III.7. Acknowledgements

Part of this work was realized and supported under the proposal number 20170043 at synchrotron SOLEIL. This work was also supported in part by the Food for Tomorrow programme from the Region Pays de la Loire.

III.8. Supplementary figures

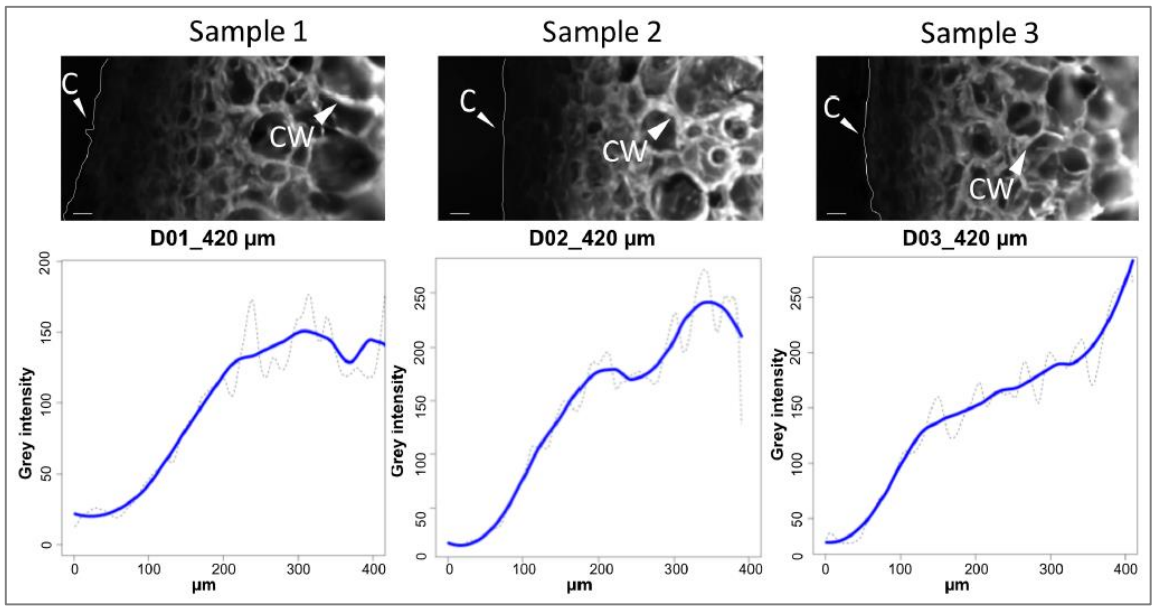

Supplementary figure III.24 *: Example of the three biological replicate acquisitions for Douce Moen at harvest. Pictures represent the three samples emission with the 420 nm filter. The dotted lines correspond to the plot profiles of samples images in grey scale value and the plain blue lines are after smoothing by the LOESS method with α = 0.4. C:Cuticle, CW: Cell Wall, Scale bar: 30 µm.*

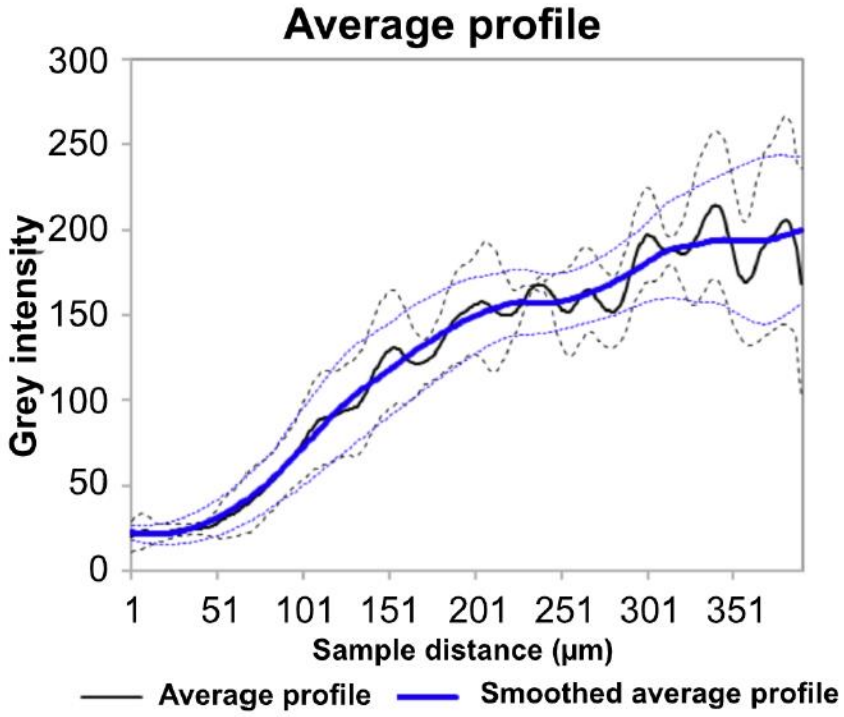

Supplementary figure III.25 *: Average of the three replicates for Douce Moen at harvest. The black line represents the average of the three samples profiles replicates for Douce Moen at harvest. The plain blue line corresponds to the smoothed average obtained by LOESS method with α = 0.4. The broken and dotted lines represent the standard deviation at 95 % confidence interval.*

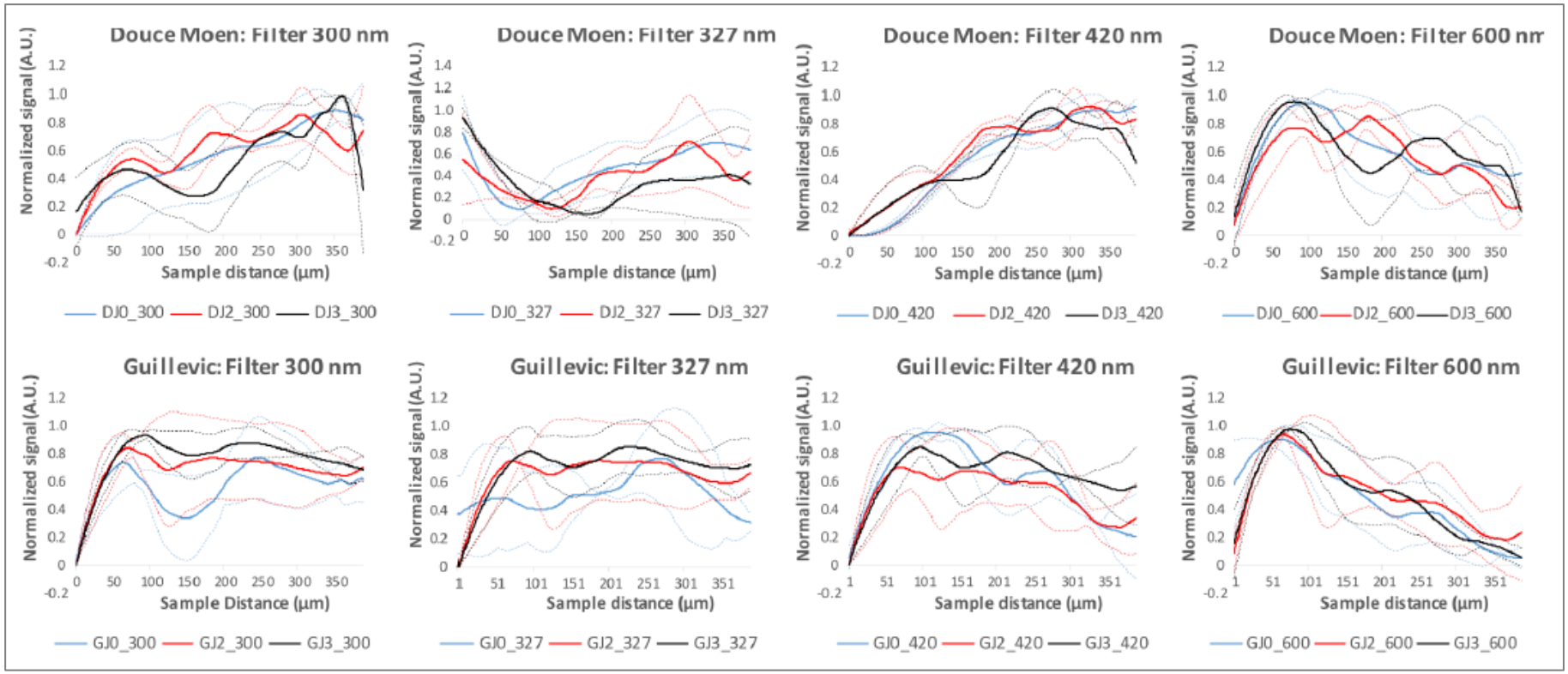

Supplementary figure III.26*: Comparison of the smoothed (LOESS method, α = 0.4) and normalized average profiles between the three storage modalities for the two apple varieties: haverst: J0 (blue), 20 days at room temperature: J2 (red), 30 days at 4°C: J30 (black). The broken lines represent the 95 % confidence interval. A Student t-test between the three modalities revealed no significant differences with a* p *value > 0.05 (n = 3).*

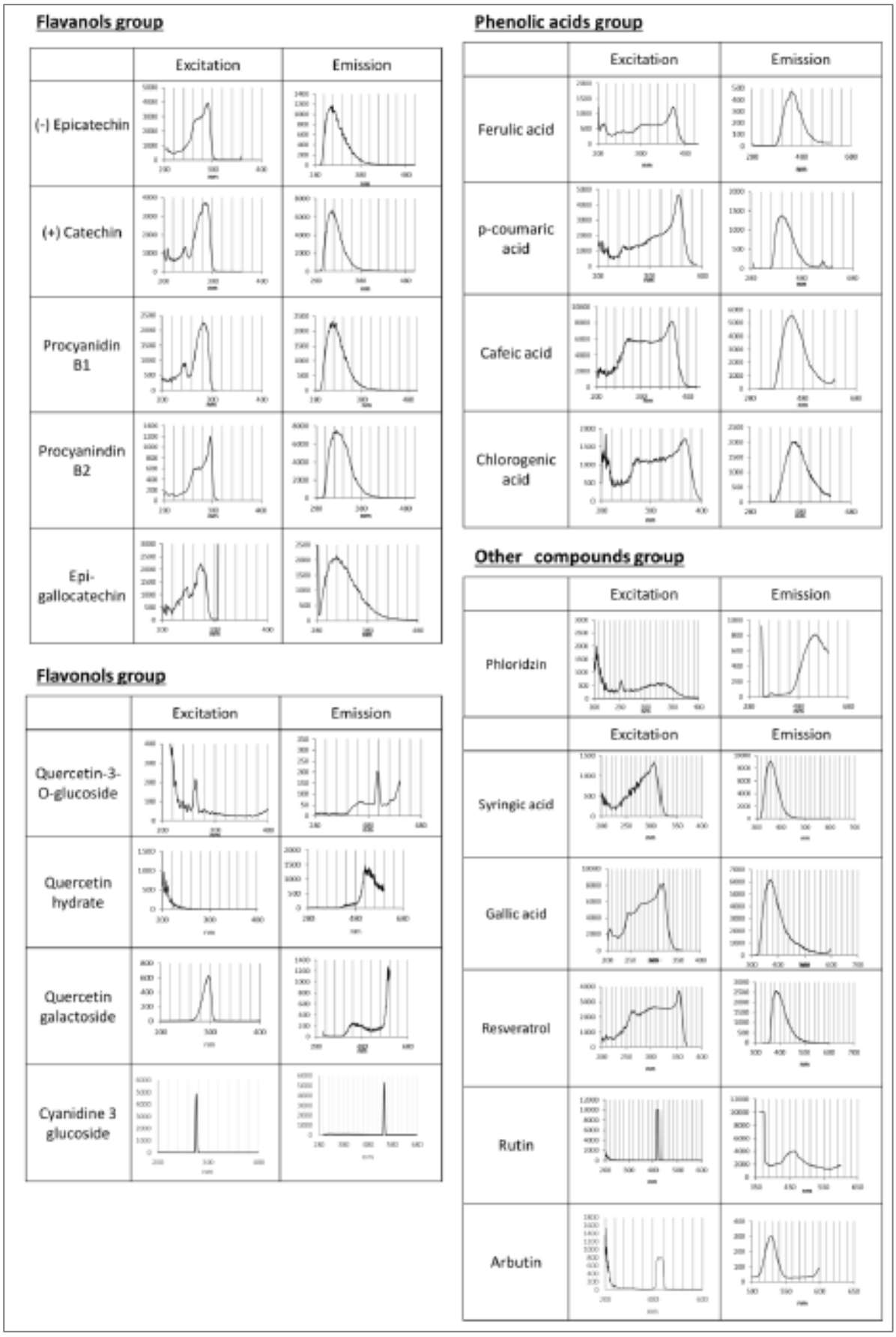

Supplementary figure 27 *: Fluorescence excitation and emission spectra of reference phenolic compounds.*

III.9. References

[1] W. Vermerris, R. Nicholson, Phenolic compound biochemistry, Springer, Dordrecht, The Netherlands, 2006.

[2] A. Solovchenko, M. Merzlyak, Optical properties and contribution of cuticle to UV protection in plants: experiments with apple fruit, Photoch Photobio Sci, 2 (2003) 861-866.

[3] A. Edreva, The importance of non-photosynthetic pigments and cinnamic acid derivatives in photoprotection, Agriculture, ecosystems & environment, 106 (2005) 135-146.

[4] G. Williamson, The role of polyphenols in modern nutrition, Nutr Bull, 42 (2017) 226-235.

[5] J.W. Finley, W.J. Hurst, C.Y. Lee, Principles of food chemistry, 4th edition ed., Springer, 2018.

[6] J. Kschonsek, T. Wolfram, A. Stockl, V. Bohm, Polyphenolic compounds analysis of old and new apple cultivars and contribution of polyphenolic profile to the in vitro antioxidant capacity, Antioxidants (Basel), 7 (2018).

[7] J.-J. Macheix, Fruit Phenolics, CRC press, 2018.

[8] G.L. Lees, N.H. Suttill, K.M. Wall, T.H. Beveridge, Localization of condensed tannins in apple fruit peel, pulp, and seeds, Can. J. Bot., 73 (1995) 1897-1904.

[9] K. Amrani Joutei, Y. Glories, M. Mercier, Localisation des tanins dans la pellicule de baie de raisin, VITIS, 33 (1994) 133-138.

[10] Y. Cadot, M. Chevalier, G. Barbeau, Evolution of the localisation and composition of phenolics in grape skin between veraison and maturity in relation to water availability and some climatic conditions, J. Sci. Food Agric., 91 (2011) 1963-1976.

[11] F.B. Essig, A Systematic histological study of palm fruits. I. The Ptychosperma Alliance, Systematic Botany, 2 (1977) 151-168.

[12] K. Yonemori, M. Oshida, A. Sugiura, Fine structure of tannin cells in fruit and callus tissues of persimmon, Acta Hort., 436 (1997) 403-416.

[13] L. Raymond, B. Schaffer, J.K. Brecht, J.H. Crane, Internal breakdown in mango fruit: symptomology and histology of jelly seed, soft nose and stem-end cavity, Postharvest Biol. Technol., 13 (1998) 59-70.

[14] H. Hammouda, C. Alvarado, B. Bouchet, J. Kalthoum-Chérif, M. Trabelsi-Ayadi, S. Guyot, Tissue and cellular localization of tannins in tunisian dates (Phoenix dactylifera l.) by light and transmission electron microscopy, J. Agric. Food Chem., 62 (2014) 6650-6654.

[15] U. Mayr, S. Michalek, D. Treutter, W. Feucht, Phenolic compounds of apple and their relationship to scab resistance, J Phytopathol, 145 (1997) 69-75.

[16] Y. Cadot, M.T. Miñana Castelló, M. Chevalier, Flavan-3-ol compositional changes in grape berries (Vitis vinifera L. cv Cabernet Franc) before veraison, using two complementary analytical approaches, HPLC reversed phase and histochemistry, Analytica Chimica Acta, 563 (2006) 65-75.

[17] W.A. Peer, D.E. Brown, B.W. Tague, G.K. Muday, L. Taiz, A.S. Murphy, Flavonoid accumulation patterns of transparent testa mutants of Arabidopsis, Plant Physiol., 126 (2001) 536-548.

[18] K. Vidot, C. Gaillard, C. Rivard, R. Siret, M. Lahaye, Cryo-laser scanning confocal microscopy of diffusible plant compounds, Plant Methods, 14 (2018) 89.

[19] K.L. Moore, Y. Chen, A.M. van de Meene, L. Hughes, W. Liu, T. Geraki, F. Mosselmans, S.P. McGrath, C. Grovenor, F.J. Zhao, Combined NanoSIMS and synchrotron X-ray fluorescence reveal distinct cellular and subcellular distribution patterns of trace elements in rice tissues, New Phytol, 201 (2014) 104-115.

[20] P.J. Harris, R.D. Hartley, Detection of bound ferulic acid in cell walls of the Gramineae by ultraviolet fluorescence microscopy, Nature, 259 (1976) 508.

[21] M.A. Rodríguez-Delgado, S. Malovaná, J.P. Pérez, T. Borges, F.J. García Montelongo, Separation of phenolic compounds by high-performance liquid chromatography with absorbance and fluorimetric detection, J. Chromato. A, 912 (2001) 249-257.

[22] R. Drabent, B. Pliszka, T. Olszewska, Fluorescence properties of plant anthocyanin pigments. I. Fluorescence of anthocyanins in Brassica oleracea L. extracts, Journal of Photochemistry and Photobiology B: Biology, 50 (1999) 53-58.

[23] S. Gómez-Alonso, E. García-Romero, I. Hermosín-Gutiérrez, HPLC analysis of diverse grape and wine phenolics using direct injection and multidetection by DAD and fluorescence, Journal of Food Composition and Analysis, 20 (2007) 618-626.

[24] D. Airado-Rodríguez, I. Durán-Merás, T. Galeano-Díaz, J.P. Wold, Front-face fluorescence spectroscopy: A new tool for control in the wine industry, Journal of Food Composition and Analysis, 24 (2011) 257-264.

[25] M. Corcel, M.-F. Devaux, F. Guillon, C. Barron, Comparison of UV and visible autofluorescence of wheat grain tissues in macroscopic images of cross-sections and particles, Computers and Electronics in Agriculture, 127 (2016) 281-288.

[26] M. Nahmani, C. Lanahan, D. DeRosier, G.G. Turrigiano, High-numerical-aperture cryogenic light microscopy for increased precision of superresolution reconstructions, Proc Natl Acad Sci U S A, 114 (2017) 3832-3836.

[27] R. Faoro, M. Bassu, Y.X. Mejia, T. Stephan, N. Dudani, C. Boeker, S. Jakobs, T.P. Burg, Aberration-corrected cryoimmersion light microscopy, Proc Natl Acad Sci U S A, 115 (2018) 1204-1209.

[28] J.R. Lakowicz, Principles of Fluorescence Spectroscopy, 3rd Edition ed., Springer, New York, 2006.

[29] A. Giuliani, F. Jamme, V. Rouam, F. Wien, J.-L. Giorgetta, B. Lagarde, O. Chubar, S. Bac, I. Yao, S. Rey, DISCO: a low-energy multipurpose beamline at synchrotron SOLEIL, Journal of Synchrotron Radiation, 16 (2009) 835-841.

[30] F. Jamme, S. Kascakova, S. Villette, F. Allouche, S. Pallu, V. Rouam, M. Refregiers, Deep UV autofluorescence microscopy for cell biology and tissue histology, Biol Cell, 105 (2013) 277-288.

[31] H. Grahn, P. Geladi, K. Esbensen, Multivariate and hyperspectral image analysis, in: Encyclopedia of Analytical Chemistry, John Willey & Sons, 2016.

[32] C.A. Schneider, W.S. Rasband, K.W. Eliceiri, NIH Image to ImageJ: 25 years of Image Analysis, Nature methods, 9 (2012) 671-675.

[33] A.A. Neves, E.J. Silva, J.M. Roter, F.G. Belladona, H.D. Alves, R.T. Lopes, S. Paciornik, G.A. De-Deus, Exploiting the potential of free software to evaluate root canal biomechanical preparation outcomes through micro-CT images, International Endodontic Journal, 48 (2015) 1033-1042.

[34] R Core Team, R: A language and environment for statistical computing, in, R Foundation for Statistical Computing, http://www.R-project.org, Vienna, Austria, 2014.

[35] J.A. Considine, R.B. Knox, Development and histochemistry of the cells, cell-walls, and cuticle of the dermal system of fruit of the grape, Vitis-vinifera L, Protoplasma, 99 (1979) 347-365.

[36] P. Hutzler, R. Fischbach, W. Heller, T.P. Jungblut, S. Reuber, R. Schmitz, M. Veit, G. Weissenböck, J.-P. Schnitzler, Tissue localization of phenolic compounds in plants by confocal laser scanning microscopy, J. Exp. Bot., 49 (1998) 953-965.

[37] J.I. García-Plazaola, B. Fernández-Marín, S.O. Duke, A. Hernández, F. López-Arbeloa, J.M. Becerril, Autofluorescence: Biological functions and technical applications, Plant Sci., 236 (2015) 136-145.

[38] F.W.J. Teale, G. Weber, Ultraviolet fluorescence of the aromatic amino acids, Biochem. J., 65 (1957) 476-482.

[39] A.H. Moskowitz, G. Hrazdina, Vacuolar contents of fruit subepidermal cells from Vitis species, Plant Physiol., 68 (1981) 686-692.

[40] S. Kitamura, Transport of flavonoids: from cytosolic synthesis to vacuolar accumulation, in: E. Grotewold (Ed.) The science of flavonoids, Springer, 2006, pp. 123-146.

[41] C. Le Bourvellec, K. Bouzerzour, C. Ginies, S. Regis, Y. Ple, C.M.G.C. Renard, Phenolic and polysaccharidic composition of applesauce is close to that of apple flesh, Journal of Food Composition and Analysis, 24 (2011) 537-547.

[42] C.M.G.C. Renard, A.A. Watrelot, C. Le Bourvellec, Interactions between polyphenols and polysaccharides: Mechanisms and consequences in food processing and digestion, Trends in Food Science & Technology, 60 (2017) 43-51.

[43] S. Gagné, C. Saucier, L. Gény, Composition and cellular localization of tannins in cabernet sauvignon skins during growth, J. Agric. Food Chem., 54 (2006) 9465-9471.

[44] S. Chassagne-Berces, C. Poirier, M.F. Devaux, C. Fonseca, M. Lahaye, G. Pigorini, C. Girault, M. Marin, F. Guillon, Changes in texture, cellular structure and cell wall composition in apple tissue as a result of freezing, Food Res. Int., 42 (2009) 788-797.

[45] S. Guyot, N. Marnet, P. Sanoner, J. Drilleau, Variability of the polyphenolic composition of cider apple (Malus domestica) fruits and juices, J Agric Food Chem, 51 (2003) 6240 - 6247.

[46] P. Mattila, J. Hellström, R. Törrönen, Phenolic acids in berries, fruits, and beverages, J. Agric. Food Chem., 54 (2006) 7193-7199.

[47] J. Lee, B.L. Chan, A.E. Mitchell, Identification/quantification of free and bound phenolic acids in peel and pulp of apples (Malus domestica) using high resolution mass spectrometry (HRMS), Food Chem, 215 (2017) 301-310.

[48] P. Albersheim, A. Darvill, K. Roberts, R. Sederoff, A. Staehelin, Plant cell walls, Garland Sciences, New York, 2011.

[49] S.C. Fry, Phenolic components of the primary cell wall. Feruloylated disaccharides of D-galactose and L-arabinose from spinach polysaccharides, Biochem. J., 203 (1982) 493-504.

[50] L. Saulnier, J.F. Thibault, Ferulic acid and diferulic acids as components of sugar-beet pectins and maize bran heteroxylans, J. Sci. Food Agric., 79 (1999) 396-402.

[51] S. Fernández, S. Osorio, A. Heredia, Monitoring and visualising plant cuticles by confocal laser scanning microscopy, Plant Physiol. Biochem., 37 (1999) 789-794.

[52] M. Awad, A. de Jager, L. van der Plas, A. van der Krol, Flavonoid and chlorogenic acid changes in skin of Elstar and Jonagold apples during development and ripening, Scientia Hort, 90 (2001) 69 - 83.

[53] S. Khanizadeh, R. Tsao, D. Rekika, R. Yang, M.T. Charles, H.P. Vasantha Rupasinghe, Polyphenol composition and total antioxidant capacity of selected apple genotypes for processing, Journal of Food Composition and Analysis, 21 (2008) 396-401.

[54] G. Di Lecce, S. Arranz, O. Jáuregui, A. Tresserra-Rimbau, P. Quifer-Rada, R.M. Lamuela-Raventós, Phenolic profiling of the skin, pulp and seeds of Albariño grapes using hybrid quadrupole time-of-flight and triple-quadrupole mass spectrometry, Food Chem., 145 (2014) 874-882.

[55] R.M. Bostock, S.M. Wilcox, G. Wang, J.E. Adaskaveg, Suppression of Monilinia fructicola cutinase production by peach fruit surface phenolic acids, Physiol. Mol. Plant Pathol., 54 (1999) 37-50.

[56] M. Grotte, F. Duprat, D. Loonis, E. Pietri, Mechanical properties of the skin and the flesh of apples, International Journal of Food Properties, 4 (2001) 149-161.

[57] H. Bargel, K. Koch, Z. Cerman, C. Neinhuis, Evans Review No. 3: Structure–function relationships of the plant cuticle and cuticular waxes — a smart material?, Functional Plant Biology, 33 (2006) 893.

[58] B.P. Khanal, M. Knoche, Mechanical properties of cuticles and their primary determinants, J. Exp. Bot., 68 (2017) 5351-5367.

[59] P. Sanoner, S. Guyot, N. Marnet, D. Molle, J.F. Drilleau, Polyphenol profiles of french cider apple varieties (Malus domestica sp.), J. Agric. Food Chem., 47 (1999) 4847-4853.

[60] E.A. Veraverbeke, N. Van Bruaene, P. Van Oostveldt, B.M. Nicolai, Non destructive analysis of the wax layer of apple (Malus domestica Borkh.) by means of confocal laser scanning microscopy, Planta, 213 (2001) 525-533.

[61] R.-N. Bae, K.-W. Kim, T.-C. Kim, S.-K. Lee, Anatomical observations of anthocyanin rich cells in apple skins, Hortscience, 41 (2006) 733-736.

[62] S. Guyot, N. Marnet, D. Laraba, P. Sanoner, J.-F. Drilleau, Reversed-Phase HPLC following thiolysis for quantitative estimation and characterization of the four main classes of phenolic compounds in different tissue zones of a french cider apple variety (Malus domestica Var. Kermerrien), J. Agric. Food Chem., 46 (1998) 1698-1705.

[63] Y. Cadot, M.T. Miñana-Castelló, M. Chevalier, Anatomical, histological, and histochemical changes in grape seeds from Vitis vinifera L. cv cabernet franc during fruit development, J. Agric. Food Chem., 54 (2006) 9206-9215.

[64] M. Murata, M. Tsurutani, M. Tomita, S. Homma, K. Kaneko, Relationship between apple ripening and browning: changes in polyphenol content and polyphenol oxidase, J. Agric. Food Chem., 43 (1995) 1115-1121.

[65] R. Delgado, P. Martín, M. del Álamo, M.R. González, Changes in the phenolic composition of grape berries during ripening in relation to vineyard nitrogen and potassium fertilisation rates, J. Sci. Food Agric., 84 (2004) 623-630.

[66] H.P. Bell, The protective layers of the apple, Canadian Journal of Research, 15c (1937) 391-402.

[67] H.B. Tukey, J.O. Young, Gross morphology and histology of developing fruit of the apple, Botanical Gazette, 104 (1942) 3 - 25.

[68] B.P. Khanal, M. Knoche, Mechanical properties of apple skin are determined by epidermis and hypodermis, J. Am. Soc. Hortic. Sci., 139 (2014) 139-147.

[69] E. Xanthakis, A. Le-Bail, H. Ramaswamy, Development of an innovative microwave assisted food freezing process, Innovative Food Science & Emerging Technologies, 26 (2014) 176-181.

[70] J. Christensen, L. Nørgaard, R. Bro, S.B. Engelsen, Multivariate autofluorescence of intact food systems, Chemical Reviews, 106 (2006) 1979-1994.

Chapitre IV

IV. Hydroxycinnamic acid esters in cell walls of apple and grape

Introduction

Ce chapitre IV a été initié suite à l'observation de l'auto-fluorescence en bleu après excitation UV des parois cellulaires dans le chapitre III. Il s'agissait de reprendre et d'adapter les méthodes classiques de dosages HPLC des acides hydroxycinnamiques pariétaux de graminées, à nos fruits charnus pommes et raisins. L'idée étant de confirmer et d'identifier leur présence sous formes estérifiées aux parois cellulaires.

Sommaire

IV.1. Abstract

Esters of hydroxycinnamic acids (HCAs) in the cell walls of wine grape (Cabernet franc) and cider apples (Douce Moen, Guillevic) were studied. Caffeic acid, *p*-Coumaric acid (pCA) and ferulic acid (FA) monomers were identified by HPLC and MS. Means of limiting oxidative degradation during cell wall preparation were assessed on the yield of HCA recovered after alkaline extraction. Following the optimum cell wall preparation, pCA content varied between 2.3 to 32.5 µg g^{-1} of dry cell wall and that of FA between 0.3-17.2 µg g^{-1} of dry cell wall. Higher HCA quantities were found in the peel compared to the flesh, and in apples compared to grape. Douce Moen apple was richer in HCA than Guillevic. pCA was localized in the cell wall by TEM after labelling with INRA-COU1 antibody recognizing pCA linked to O-5 of arabinose. The anti-FerAra antibody targeting FA on O-5 of arabinose failed to locate FA esters in apple and grape cell wall. The results are discussed with regard to possible origin and function of these HCAs in apple and grape cell wall in connection with fresh and processed fruit quality.

Key words: Cell wall, hydroxycinnamic esters, p-coumaric acid, ferulic acid, wine grape, cider apple, Cabernet franc, Guillevic, Douce Moen

IV.2. Introduction

In fleshy fruit, particularly in cider apples, the hydroxycinnamic acids (HCAs) are mostly chlorogenic acid (i.e. cafeoylquinic acid) and p-coumaroylquinic acid, and have been reported from the cortex of Douce Moen and Guillevic apples at 1.06 mg g^{-1} and 0.60 mg g^{-1} of fresh matter (Sanoner, Guyot et al. 1999), respectively. For grape, HCAs are caffeoyl tartrate, p-coumaroyl tartrate and coutaric acid, with content reported at 223, 62, and 48 µg g^{-1} of fresh fruit (Moskowitz and Hrazdina 1981, Alonso Borbalán, Zorro et al. 2003, Mattivi, Guzzon et al. 2006). However, in these fruits, there is no report on esterified HCAs in their cell wall. Esters of ferulic (FA) and *p*-coumaric acids (pCA) on the cell wall polysaccharides have been reported of monocot (Parr, Waldron et al. 1996, Saulnier and Thibault 1999, Buanafina 2009, Bento-Silva, Vaz Patto et al. 2018, Schäfer, Sattler et al. 2019) and dicot plants (Hartley and Harris 1981, Eraso and Hartley 1990, Parr, Ng et al. 1997, Christiaens, Van Buggenhout et al. 2016) though in lower amounts compared to monocots. For example, FA esters represent up to 3% of the dry weight of graminaceous cell walls, about 0.9% dry weight of rice endosperm cell walls and 3.1% in maize bran (Buanafina 2009), whereas it is found much lower in dicot as for sugar beet and carrot reported at 0.08% and 0.002% of dry weight cell walls (Saulnier and Thibault 1999).

In monocots, FA and pCA esters are found on O-5 of arabinose in arabinoxylan (Bunzel, Funk et al. 2004, Vismeh, Lu et al. 2013) while in dicot cell walls, such as sugar beet, they are reported esterified on O-3, O-2 of arabinose and O-6 galactose residues in the pectin side-chains within the cell wall (Fry 1982, Ishii 1997). The location of feruloyl and *p*-coumaroyl esters in cell walls has been revealed in cereal by labelling with antibodies recognizing FA and pCA esterified on O-5 of arabinose. The immunolabelling is particularly concentrated in the cell walls of the aleurone layer of wheat grain, in the epidermis of cereal straw, and in the exoderm of wheat root (Philippe, Tranquet et al. 2007, Tranquet, Saulnier et al. 2009). The function of these esters is still not fully understood, though for FA, they cross-link cell wall polysaccharides through their condensed dimeric forms (Ralph, Quideau et al. 1994, Vismeh, Lu et al. 2013). As a result, these cross-links contribute to strengthening the plant cell walls and enhance the mechanical properties of plant tissue (Antoine, Peyron et al. 2003, Waldron, Parker et al. 2003). In addition, the presence of the feruloyl esters in cell wall increases plant resistance to biotic stress (Reem, Pogorelko et al. 2016).

HCA esters are commonly identified and quantified from alkaline extracts of cell wall material by chromatography techniques. In most cases, cell wall preparations are performed with limited precautions to prevent oxidation (Parker, Ng et al. 2005). In polyphenol rich plants, such as in fleshy fruit, HCAs are often highly concentrated in the vacuoles. After damaging of the tissues, these acids under hydroxycinnamate forms and, in particular, those having a catechol moiety are prone to

oxidation by enzymes, such as with polyphenol oxidase (PPO) (Jukanti 2017), or non-enzymatic reactions (Pierpoint 1966, Clifford 1999, Guyot, Bernillon et al. 2008). The oxidation produced quinone or semi-quinone forms that can interact with protein (Le Bourvellec and Renard 2012) and may bind to both cellulose and pectin (Padayachee, Netzel et al. 2012). Thus, if oxidation is not prevented during the different cell wall extraction and saponification steps, the quantification of the HCA extracted may be overestimated, as described the schema in **Figure IV.1**.

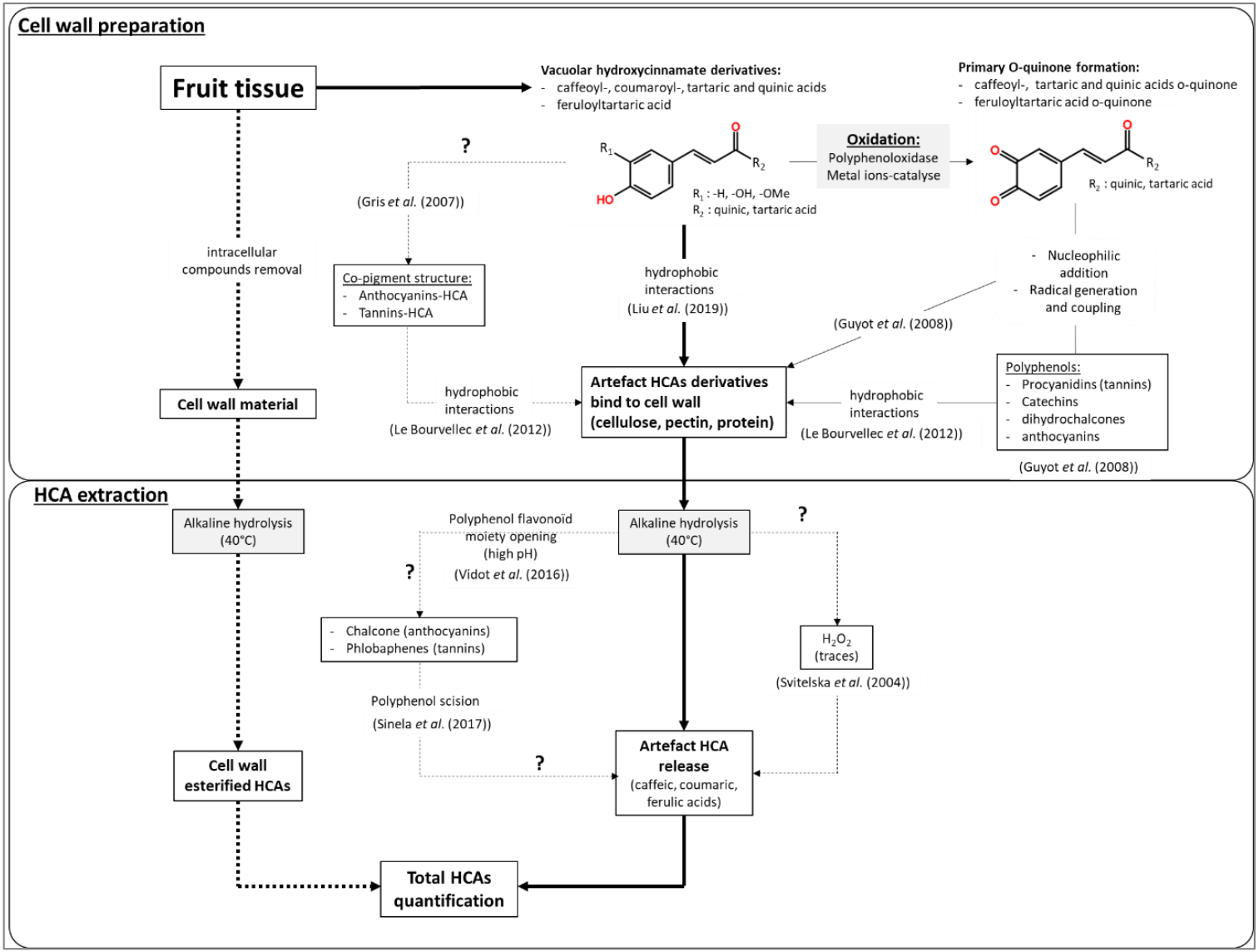

***Figure IV.28**: Schemes of the different reactions that may happen during fleshy fruit cell wall preparation leading to an over quantification of esterified HCAs. Bold dotted lines: standard cell wall HCA esters extraction; Bold lines: main artefact reaction; Plain lines: intracellular compound oxidative reactions; Dotted lines: hypothetic pathways.*

Both pCA and FA have already been reported as free or bound forms in extracts from the peel, flesh and seeds of apple and grape (Di Lecce, Arranz et al. 2014, Lee, Chan et al. 2017), while their specific presence within cell wall has never been reported. However, in these fruits, a blue autofluorescence was observed in the cell walls after UV excitation at 375 nm (Vidot, Devaux et al. 2019). At this excitation wavelength, aromatic amino acids do not fluoresce contrarily to HCAs and lignin that are commonly described as sources of plant cell wall fluorescence (Lichtenthaler and Schweiger 1998, Talamond, Verdeil et al. 2015, Vidot, Devaux et al. 2019).

In the present study, HCAs were identified in a saponified fraction of the cell wall of apple and grape. Three methods of cell wall preparations using different levels of precaution to limit oxidation were compared and applied to quantify pCA and FA in the flesh and peel of Cabernet franc grape, Douce Moen and Guillevic cider apples. Cabernet franc was selected as it is the major wine grape of the Val de Loire region while both cider apples are economically important to the cider industry in North West of France. Moreover, these apples were selected as they are texture- and phenolic content-contrasted, with Guillevic being firmer and richer in condensed tannins than DM (Sanoner, Guyot et al. 1999).

IV.3. Materials and methods

IV.3.1. Materials

IV.3.1.1. Chemicals

Paraformaldehyde ($(CH_2O)_n$), sodium phosphate, London Resin White (LRW) acrylic resin, bovine serum albumin (BSA), sodium fluoride, sodium dodecyl sulphate, sodium chloride, sodium hydroxide, 3-4-5-trimethoxy-trans-cinnamic acid (TMCA), trans-ferulic acid (FA), para-coumaric acid (pCA), hydrochloric acid (HCl, 37%), formic acid (95%), sodium acetate trihydrate, acetic acid, acetone, diethyl ether, ethanol absolute, methanol (MeOH) and acetonitrile were from Sigma-Aldrich, UK. Glutaraldehyde 25% (R1012), carbon coated nickel TEM grid and uranyl acetate were from Agar Oxford Instruments, UK. Unless otherwise stated, all chemicals were of far UV quality HPLC grade purity.

IV.3.1.2. Fruits

Cabernet franc (CF) wine grapes fruit harvested on September 2016, 2017 and 2018 were provided by ESA-GRAPPE, Angers-France.

Douce Moen (DM) and Guillevic (GU) apples were harvested on October 2017 and 2018 from a commercial orchard (IFPC, Sees, France).

IV.3.1.3. Antibodies

INRA-COU1 monoclonal antibody specific to para-coumaric acid esterified on O-5 of arabinose (Tranquet, Saulnier et al. 2009) and polyclonal anti-FerAra specific to ferulic acid esterified on O-5 of arabinose (Philippe, Tranquet et al. 2007) were from the laboratory collection (INRA-BIA-PVPP, France).

IV.3.2. Methods

IV.3.2.1. Immunohistochemistry (IHC)

IHC was performed on Douce Moen apple harvested on 2018. The cubes of 1 mm^3 were sampled from the epidermis of equatorial apple sections. Tissue fixation followed the method of Guillon, Tranquet et al. (2004) (Guillon, Tranquet et al. 2004). It was done in a mixture of 3% of paraformaldehyde and 0.5% of glutaraldehyde in a 0.1 M phosphate buffer saline (PBS, pH 7.2) for 4 h at 4 °C. After washing, samples were dehydrated in a graded aqueous ethanol series, progressively infiltrated with LRW acrylic resin and then embedded in gelatine capsules. The resin was polymerized for 4 days at 55 °C without accelerator. Ultrathin sections of 80 nm thickness were prepared and mounted on a carbon-coated nickel grids. Sections were stained with aqueous uranyl acetate (1%). Immunolabelling was carried out on transverse ultrathin sections treated as follows: 30 min in the blocking solution PBS-1% BSA, incubated with primary antibodies (diluted to 1:1500 and 1:3 for anti-FerAra and INRA-COU1, respectively) in PBS-0.3% BSA for 1 h followed by incubation with a second goat anti-rabbit (anti-FerAra sections) or anti mouse (INRA-COU1 sections) antibodies (at 1:20 dilution) conjugated to 10 nm gold particles (Aurion, Wageningen, NL). Sections were counterstained with aqueous uranyl acetate (1%) and examined by transmission electron microscopy (JEOL 100S).

IV.3.2.2. Cell wall preparations

Different methods were used to prepare apple and grape cell wall materials **(Supplementary figure IV.1**). The methods differed by their potential to limit the oxidation of phenolic compounds during cell wall preparations. Inspired from Lichtenthaler and Schweiger (1998), the basic process consisted of removing apple core and grape seeds prior to separating the peel and the flesh. The two fruit parts were mashed and cell walls were prepared through elimination of ethanol (70%) soluble compounds. Afterward, the insoluble residues were washed with water, aqueous sodium dodecyl sulphate (3%), aqueous sodium chloride (1 M) and acetone, prior to drying overnight at 40 °C. In a first experiment, the whole preparation was done at ambient air (method A). For the method B, fruit parts were first dipped in aqueous sodium fluoride (1%) to inhibit oxidative enzymes (Février, Le Quéré et al. 2017) before proceeding to the method A that was realized in a glove box filled with nitrogen gas.

For the last method (method C), prior to sampling following method B, fruits were placed in a desiccator in a glove box and air in fruit was removed by vacuum aspiration and nitrogen purge. This gas exchange was only realized on apples. In this method, a first extraction of water-soluble compounds was done prior to ethanol (70%) extraction for both apple and grape. Method A was realized only on CF grape fruit and method B and C were applied on CF, DM and GU. Fruits were separated in pools of 300 g for CF and 500 g for apples. Method A and B were performed on three pools and method C on four pools.

IV.3.2.3. Saponification of phenolic esters from cell wall

Saponification of phenolic acid esters was inspired from the method described by Antoine, Peyron et al. (2003) with some adaptations **(Supplementary figure IV.1)**. Dry cell wall material (500 mg) was submitted to alkaline hydrolysis for 30 min at 40 °C in NaOH (2 M, 150 mL) in order to remove the esterified phenolic compound of cell wall. Internal standard (IS, TMCA; 1 mg mL^{-1}, 15 mL) was then added to the suspension prior to filtration under vacuum on fritted glass filter (Borosilicate Glass n°1, Pyrex™, ThermoFisher Scientific, France). The alkaline filtrate was slowly acidified in an ice bath to pH < 1 by HCl. Acidification provoked a changed of the filtrate colour from dark-red to orange. The acidified solution was extracted at least three times with diethyl ether (≈ 50 mL). The pooled ether phases were then evaporated to dryness and the dry residue were solubilized by a solution of MeOH-(H_2O, formic acid 1%) (1:1). A standard solution was prepared by dissolving *p*CA, FA and TMCA at 0.1 mg mL^{-1} in the MeOH-(H_2O, formic acid 1%) (1:1). The extract and standard solution were then filtered through PTFE (UPTIDISC Filters PTFE, 4 mm, 0.45µm, PP HOUSING Interchrom, France) and transferred in amber vials prior to chromatographic analysis.

IV.3.2.4. Chromatography analysis

Phenolic compounds were identified by HPLC-UV coupled to mass spectrometry (MS). As described in Malec, Le Quere et al. (2014).

Analysis was carried out using a system composed of a thermostated autosampler (model Surveyor, Thermo Finnigan, San Jose, CA, USA), a binary high-pressure pump (model 1100, Agilent Technologies, Palo Alto, CA, USA), a UV−vis diode array detector (model UV6000 LP, Thermo Finnigan), and an ion trap mass spectrometer equipped with an electrospray source (model LCQ Deca, Thermo Finnigan). The column was a Purospher® STAR RP-18 end-capped (3µm) Hibar® HR (Merck, 2.1 x 150 mm) equipped with a precolumn Eclipse XDB-C8 (Agilent Technologies, 2.1 x 12.5 mm, 5 µm) and thermostated at 30 °C. Solvents were (A) acidified pure water (0.1% formic acid) and (B) acidified acetonitrile (0.1% formic acid), both degassed with a SCM1000 vacuum membrane degasser (Thermo

Fisher Scientific Inc). The flow rate was set at 0.2 mL min^{-1} and the elution gradient were: 0 min (97% A; 3% B), 3 min (93% A; 7% B), 21 min (87% A; 13% B), 27 min (87% A; 13% B), 41 min (80% A; 20% B), 51 min (55% A; 45% B), 53 min (10% A, 90% B), 56 min (10% A, 90% B), 58 min (97% A; 3% B) and 76 min (97% A; 3% B). The UV−vis detection was set at 320 nm and mass detection was realised by electrospray ionisation in the negative ion mode by deprotonation. Data were collected and processed by XCalibur software (version 1.2, Thermo Finnigan). An example of chromatogram and mass spectra is presented in **Figure IV.2**.

Inspired from the method described by Antoine, Peyron et al. (2003), the identified HCAs were quantified by HPLC-UV using a C18 reverse phase column (Vision HT C18 HL 5µl, 250mm x 4.6mm, Grace, Germany) thermostated at 25 °C and eluted by acetonitrile (solvent A) and acetate buffer (solvent B: 4.5 g sodium acetate trihydrate dissolved in 1 L of distilled water containing 2.2 mL acetic acid). Solvent mixing was done by binary pump (Dionex UltiMate 3000 pump, Thermo Scientific, USA) during elution at a flow-rate of 1 mL min^{-1}. Elution was realized by 15% solvent A and 85% solvent B for 5 min that was then increased to 25% solvent A and 75% solvent B by a linear gradient over 15 min, and hold for a further 5 min at the last solvent condition. Detection was realized by a diode array detector (Dionex UltiMate 3000, Thermo Scientific, USA). Peak area at 320 nm was used for quantification and compared to IS (TMCA) and known amounts of phenolic acids in a standard solution used for calibration. Data were collected and processed by Chromeleon software® (version 6.8, Thermo Scientific, USA).

IV.3.2.5. Statistics

Statistical evaluation of means was realized by Student's t-test with Microsoft Excel® software (2016). Statistically significant difference was taken at p value ≤ 0.05.

IV.4. Results

The phenolic esters found in the saponified fraction of the peel and flesh cell wall of CF, DM and GU were identified by HPLC coupled to mass spectrometry. The results showed the presence of caffeic acid, pCA and FA eluting at 19.8, 28.5 and 31.2 min on the HPLC chromatogram. These HCAs were identified by comparing their elution time with that of reference compounds and by the molecular weight at 164 and 194 Da measured by MS for pCA and FA (**Figure IV.2)**. Other peaks that did not correspond to common phenolic standards were also present on the HPLC chromatogram and were in too low amounts to be identified by mass spectrometry. None had retention times of known FA dimers.

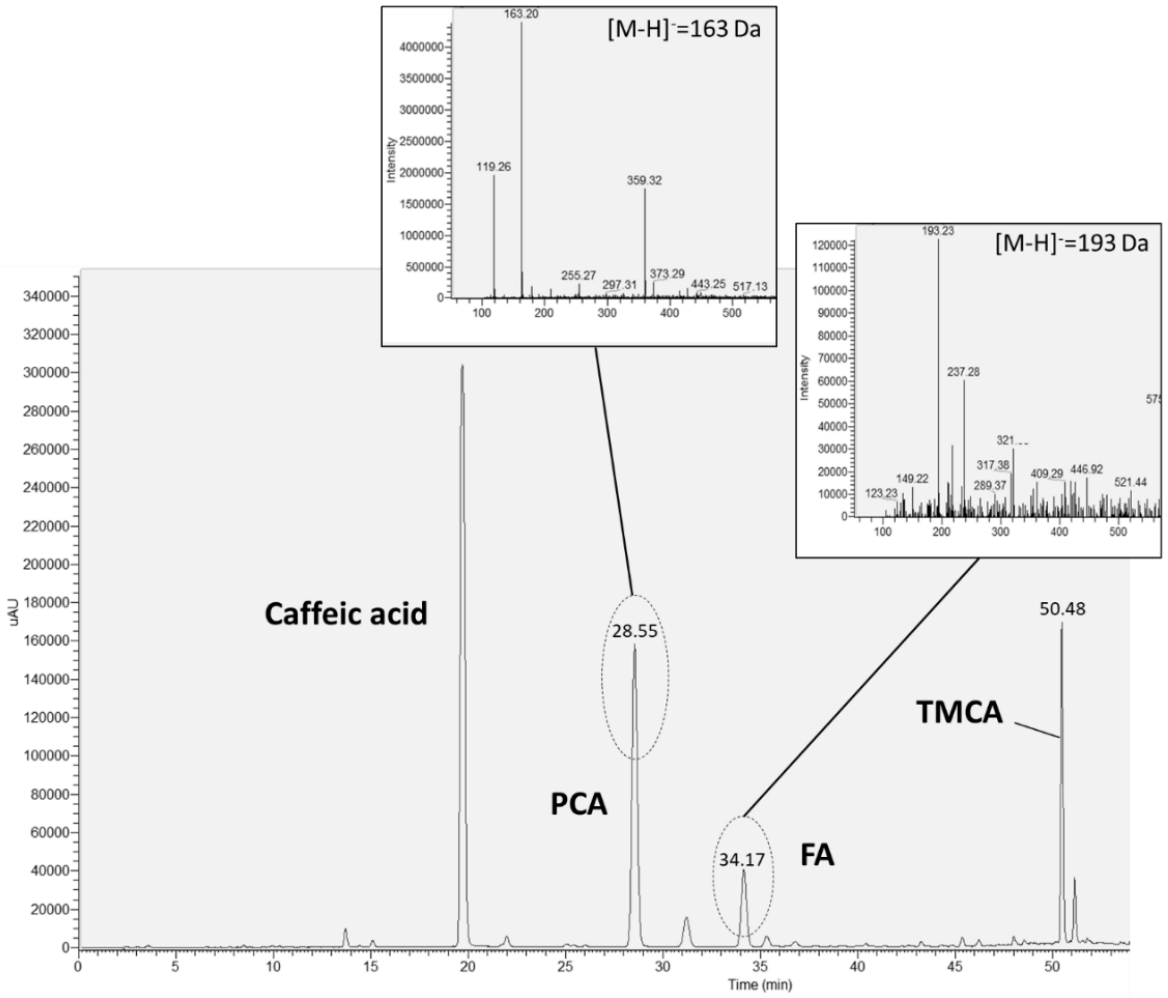

***Figure IV.29**: Example of HPLC-UV profile at 320 nm of phenolic esters apple and grape cell wall: Douce Moen. The mass spectra (inserts) of the two major peaks eluting at 28.55 min and 34.17 min correspond to pCA and FA, respectively. The internal standard TMCA eluted at 50.48 min. pCA: p-Coumaric acid; FA: Ferulic acid; TMCA: 3-4-5-trimethoxy-trans-cinnamic acid*

Among identified HCAs, the study focused on pCA and FA as they have been reported esterified in other plant cell walls (Parr, Ng et al. 1997, Buanafina 2009), contrary to caffeic acid, which was considered as resulting from phenolic compounds contaminating the cell wall preparation (see below). The quantification of pCA and FA was performed following the three cell wall preparation methods (A, B and C) for Cabernet franc grape (CF) and the two methods B and C for Douce Moen (DM) and Guillevic (GU) apples. The sum of pCA and FA contents showed important variations according to the cell wall preparation method (**Figure IV.3**). This value reached 1.532 mg g^{-1} in CF cell walls when the oxidation was not prevented (method A). It was drastically reduced to 0.136 mg g^{-1} when oxidation by ambient oxygen and oxidative enzyme activities were limited (method B). Moreover, removing water-soluble component (method C) further reduced significantly the amount of extracted pCA and FA to 29 µg g^{-1}. For DM apple, removing air from intercellular spaces and water-soluble components (method C) reduced significantly the amount of extracted pCA and FA from 97 µg g^{-1} (method B) to 62 µg g^{-1}. The efficiency of method C over the method B was more obvious for CF and DM than for GU, as for the

latter, both methods yielded around 41-42 µg g^{-1} of the two esters **(Figure IV.3)**. Assuming that method C allowed measuring HCAs content in the saponified fraction of the cell wall with limited oxidation artefacts, the content of pCA and FA ranked from the highest to the lowest: Douce Moen > Guillevic > Cabernet franc (**Figure 30**).

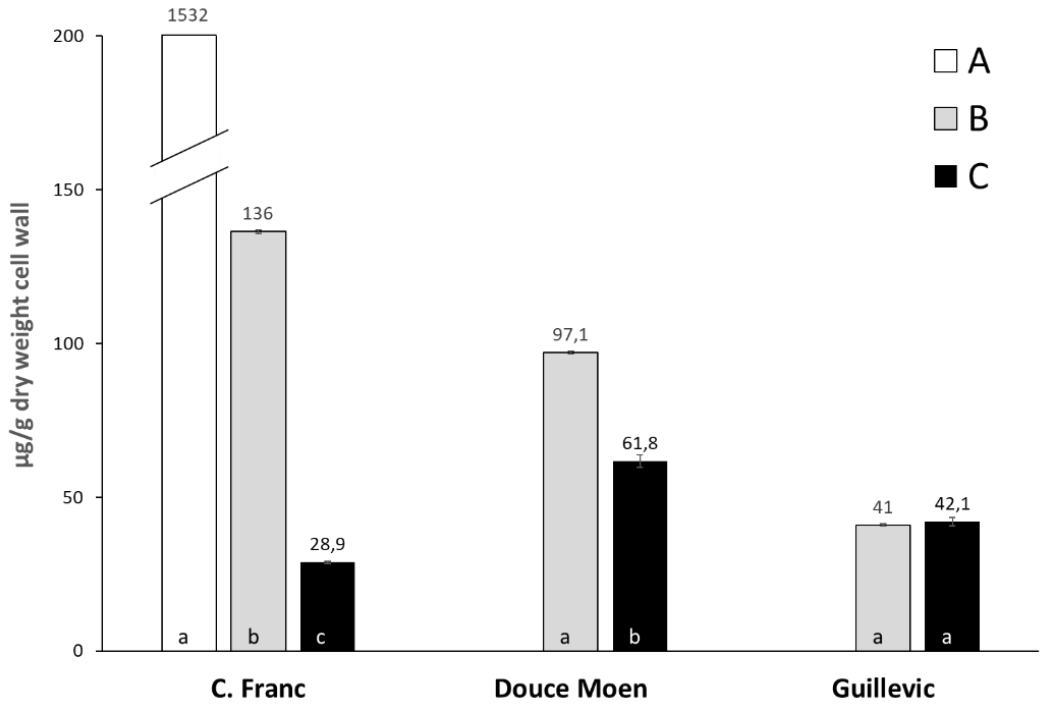

Figure IV.30: *Sum of pCA and FA content in the saponified fraction of cell wall (µg g^{-1} of dry weight cell wall) in Cabernet franc (C.franc) grape and Douce Moen and Guillevic apples according to the method of cell wall preparation (A, B and C). Different letters present significant differences (p-value < 0.05; n ≥ 3).*

The mean pCA and FA contents in the saponified fraction of the cell wall of peel and flesh of grape and apple prepared according to the method C are presented in **Figure IV.4**. For the three fruits, the content of the two HCAs was significantly higher in the cell wall from the peel and showed significantly higher proportion of pCA compare to FA. The pCA content in the peel of Douce Moen was significantly higher than that of Guillevic, while the difference in FA content between the two apple varieties was not significant. In the flesh, the higher amount of pCA and FA in Douce Moen compared to Guillevic was significant. In agreement with results shown in **Figure IV.3**, the content of the two HCAs in the peel of Cabernet franc grape was significantly lower than that of the two apple varieties. However, in the saponified fraction of the cell wall from the flesh of Cabernet franc, the pCA and FA contents were close to those of Douce Moen with approximately 10 µg g^{-1} for pCA and 2.4 µg g^{-1} for FA. These contents were significantly higher than those found for Guillevic.

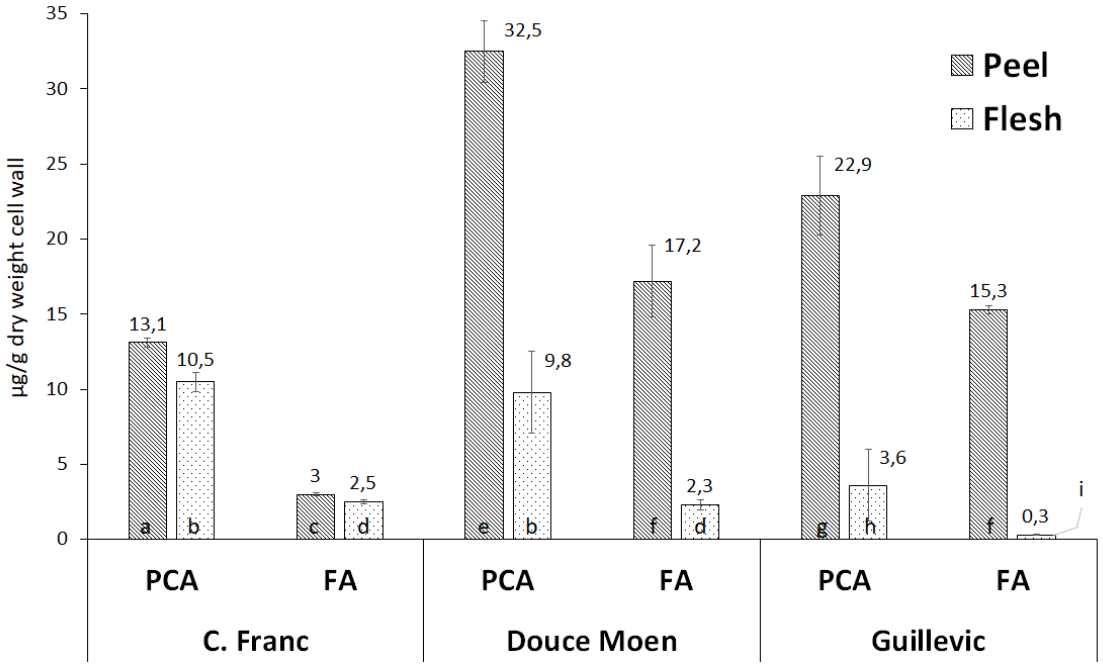

***Figure IV.31**: Mean content (± SD; n=4) of pCA and FA, in the saponified fraction of cell wall prepared according to the method C from the peel and flesh of Cabernet franc grape, Douce Moen and Guillevic cider apples. Different letters present significant differences (p-value < 0.05).*

pCA and FA were searched in the cuticle, the sub-cuticle and the parenchyma tissue of Douce Moen by transmission electron microscopy following labelling by INRA-COU1 and anti-FerAra antibodies recognizing pCA and FA linked to O-5 of arabinose. pCA labelling was low and distributed in the cell wall of the cuticle and the sub-cuticle areas without specific localization **(Figure IV.5)**. Labelling by anti-FerAra was too faint to identify the presence of FA linked to O-5 of arabinose in apple cell wall, contrary to that observe on graminaceous by Philippe, Tranquet et al. (2007). Immunostaining was not realized in Guillevic apple or Cabernet franc grape due to limitations in antibody available.

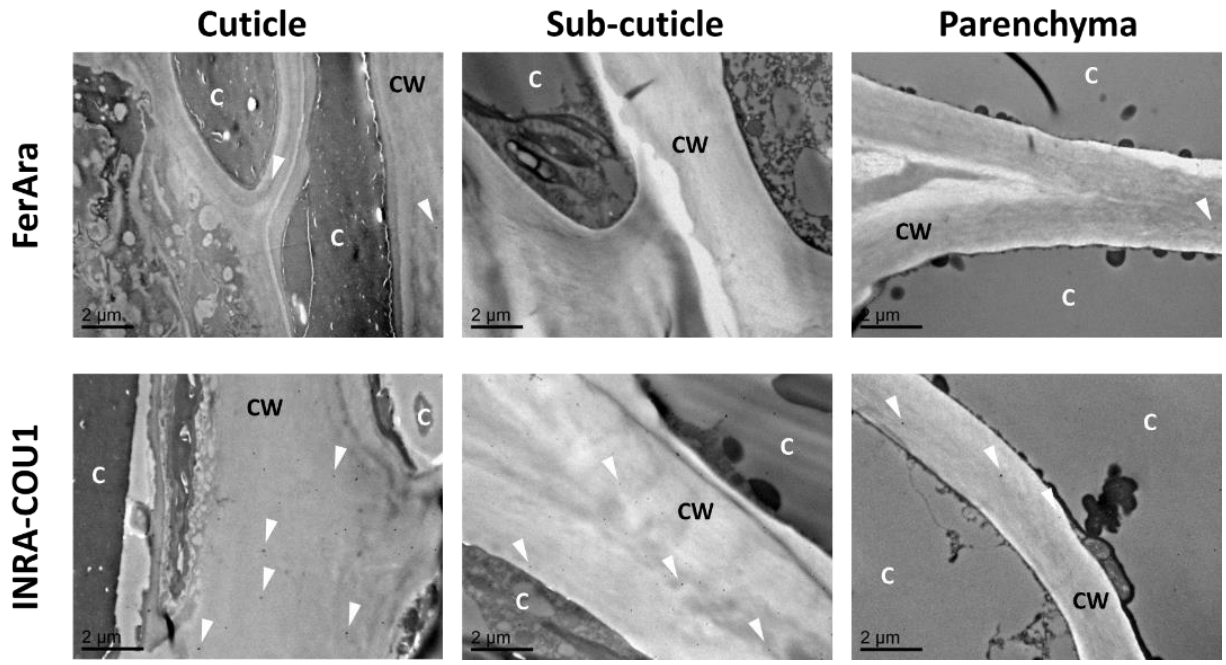

Figure IV.32*: Transmission electron micrographs of Douce Moen apple tissue after labelling by INRA- COU1 and anti-FerAra antibodies. White arrows show labelled black spots. C: Cell, CW: Cell Walls.*

IV.5. Discussion

Cell wall autofluorescence of apple and grape observed by epifluorescence and confocal microscopies after UV excitation suggested the presence of HCAs (Vidot, Devaux et al. 2019). The present study aimed at identifying and quantifying these HCAs through saponification of the cell wall as commonly described in literature for other plant species. Results have shown that the major HCA found in the saponified fraction of cell wall was caffeic acid next to low amounts of pCA and FA. In fact, pCA and FA contents amounted to 0.003% and 0.004 – 0.006% of the cell wall dry weight of grape and apples, respectively, compared to sugar beet (0.08%), which is itself low with regard to cereals (1.5%) (Saulnier and Thibault 1999). The low values of pCA and FA leave doubts on their origin.

IV.5.1. Potential artefacts in HCAs quantification

The results pointed to the extreme care that is needed to avoid over-quantification of these HCA during quantitative analysis. Beside diffusion and creation of artefactual interactions of phenolic compounds with cell wall components during sample preparation (cutting, crushing…), the risk of artefacts increases due to oxidative mechanisms and to drastic hydrolysis conditions **(Figure IV.1)**. In fact, caffeic acid is the main artefact HCA that can be expected due to the high content of chlorogenic acid in apple and caffeoyltartaric acid in grape among other hydroxycinnamate derivatives (ie caffeoylquinic acids, coumaroylquinic acids, caffeoyltartaric acids, coumaroyl- and feruloyltartaric acids….). At least chlorogenic and caffeoyltartaric acids fluoresce under UV excitation (Vidot, Devaux et al. 2019) but they are normally present, as other hydroxycinamate derivatives, in the vacuole

(Moskowitz and Hrazdina 1981, Sanoner, Guyot et al. 1999). Other potential sources of caffeic acid are the vacuolar caffeic acid-anthocyanin co-pigments and tannins (Gris, Ferreira et al. 2007). The presence in the cell wall of these cellular phenolic compounds is favored by their ability to bind to cell wall polysaccharides through hydrophobic or hydrogen bonds as described for chlorogenic acid, (-)-epicatechin, phloridzin and tannins (Le Bourvellec and Renard 2012, Liu, Lopez-Sanchez et al. 2019) (**Figure IV.1**).

Caffeic acids, FA and pCA can thus originate from the hydrolysis and oxidative degradation of different phenolic compounds (**Figure IV.1**). Oxidation of hydroxycinnamate derivatives by peroxidase enzymes or by non-enzymatic reactions with the phenolic group can lead to other HCA derivatives that bind cell wall polysaccharides. During alkaline hydrolysis, the drastic conditions used would release the hydroxycinnamate derivatives interacting with the cell wall and saponify them, to release the HCAs. Moreover, the presence of trace hydrogen peroxide (H_2O_2) in the fruit matrix and under alkaline conditions, may also promote the hydroxycinnamates released from cell wall as shown by Svitelska, Gallios et al. (2004).

Method C was developed to remove intracellular compounds and limit oxidation during the cell wall preparation. Such method succeeded in reducing the HCA content of the saponified fraction of cell wall and was particularly efficient on Cabernet franc grape and Douce Moen apple, both known to be rich in HCA in contrast to Guillevic apple. It was expected that, the hydroxycinnamate derivatives and their oxidized products would have been removed by the numerous washings of the cell walls prior to the alkaline extraction. Nevertheless, even after careful preparation of cell walls (method C), the dark-red color of the extracts obtained after saponification was likely an indicator of degradation of cell wall bound tannins to phlobaphenes. These reddish-colored phenolic substances of complex chemical composition are synthesized by non-enzymatic oxidation of flavan-4-ol monomers or polymers and during hydrolysis of condensed tannins (Lachman, Martinek et al. 2017). Thus, as a hypothesis, alkaline degradation of cell wall bound tannins may produce phlobaphenes and free HCAs, among which would be caffeic acid (**Figure IV.1**). Furthermore, in the case of tannins containing anthocyanin aglycon structures, alkaline hydrolysis combined to thermal degradation may have released HCAs (**Figure IV.1**), through scission of the chalcon form as described for others phenolics acids (Sun, Bai et al. 2011, Sinela, Mertz et al. 2017). The phenolic compounds released by saponification were then extracted by diethyl ether which low polarity was able to recover caffeic acid, FA and pCA, but left other compounds, such as phlobaphenes in the aqueous phase. Thus, the HCAs measured were likely originating from esters released from cell wall polysaccharides combined with hydroxycinnamates derivatives and/or tannins that were made to strongly interact with the cell walls during their preparation and resisted to the different washing steps.

IV.5.2. p-Coumaric acid esterifies cell wall polysaccharides

The immunolabelling of pCA coupled to transmission electron microscopy observation of the cell walls of Douce Moen apple not only confirmed HCA presence in the cell wall, but also indicated that a part of pCA likely occurs as ester on O-5 of arabinose. In apple, cell walls are rich in pectin and contain trace amounts of glucuronoarabinoxylan (GAX) (Ray, Vigouroux et al. 2014). The antibody INRA-COU1 recognizes pCA esters of arabinoxylan in monocot cell walls (cereals) and not pCA bound to pectin in dicots (Tranquet, Saulnier et al. 2009). Thus, pCA esterified to pectin would not be recognized and the faintly pCA labelling in **Figure IV.5** may correspond to pCA esterified on GAX. No clear labelling was observed for FA likely due to its trace amount in the cell wall, to different linkages on cell wall polysaccharides or to its different origin.

IV.5.3. HCAs content in alkaline extracts of cell wall varies between grape and apple and between fruit tissues

Although the cell wall origin of HCAs may partly be due to artefacts, the focus on pCA and FA contents was related to their esters reported in other plant cell walls (Parr, Ng et al. 1997, Saulnier and Thibault 1999, Buanafina 2009). The content in these HCAs varied in the saponified fraction of cell wall according to genera (Vitis and Malus), varieties (Douce Moen and Guillevic) and tissues (peel and flesh) (**Figure IV.4**). The low contents of pCA and FA measured in the alkaline extract of cell wall GU compared to DM followed the total vacuolar polyphenols content reported in the cortex of each variety (Sanoner, Guyot et al. 1999). In addition, higher pCA and FA contents in peel compared to flesh of DM and GU showed similar trends as reported in four table apple varieties (Lee, Chan et al. 2017). These authors measured from 30.1 to 60.5 µg g^{-1} dw for pCA and from 3.3 to 31.6 µg g^{-1} dw for FA in the peel extracts and from 6.1 to 26.1 µg g^{-1} dw for pCA and from 0.8 to 3.1 µg g^{-1} for FA dw in flesh.

IV.6. Conclusion

If the precise origin of pCA and FA in the saponified fraction of Cabernet franc grape, Douce Moen and Guillevic apples cell walls remains to be established, due to their low amount, they may have a limited contribution to the crosslinking of cell wall polysaccharides and, by consequence, to the mechanical properties of the flesh. However, in the light of the higher concentration of pCA and FA in the peel compared to the flesh of apple and grape, their contribution to cutin crosslinks need to be established if the higher mechanical properties reported for the cuticle compared to the flesh of various fleshy fruit is considered (Domínguez, Cuartero et al. 2011).

Due to the known antioxidant ability of phenolic compounds (Abramovič 2015, Galanakis 2018), it would be worth testing the existence of a relation between cell wall bound hydroxycinnamic derivatives/tannin/HCA esters and the extent of pectin oxidative cleavage during fruit processing and the consequences on the rheology of the products. Further work on the relation between cell wall HCA esters and bound flavonoids in processed fruit matrices content would help designing fruit-based food with controlled organoleptic and nutritional characteristics related to these phenolic compounds. However, further knowledge on that subject would need to improve fruit cell wall preparation to avoid ambiguity about the origin of HCAs in the saponified fraction of cell wall and to clearly establish the origin of the blue autofluorescence in apple and grape cell walls.

IV.7. Acknowledgements

This work was supported in part by Cap Aliment Food for Tomorrow program funding by Région Pays de la Loire. The HPLC-MS analysis was performed at the P2M2 analytical platform (Metabolic Profiling and Metabolomic Platform, INRA, Rennes – Le Rheu). The authors thank Dr JM Le Quere (INRA BIA, Rennes) for fruitful suggestion, H Sotin (INRA, BIA Rennes) for carrying out HPLC-MS analyses, C Alvarado (INRA, BIA Nantes) for microscopy analysis and D Le Meurlay for technical support (ESA, Angers). Part of this work was realized on the platforms BIBS (INRA, BIA Nantes).

IV.8. Supplementary figures

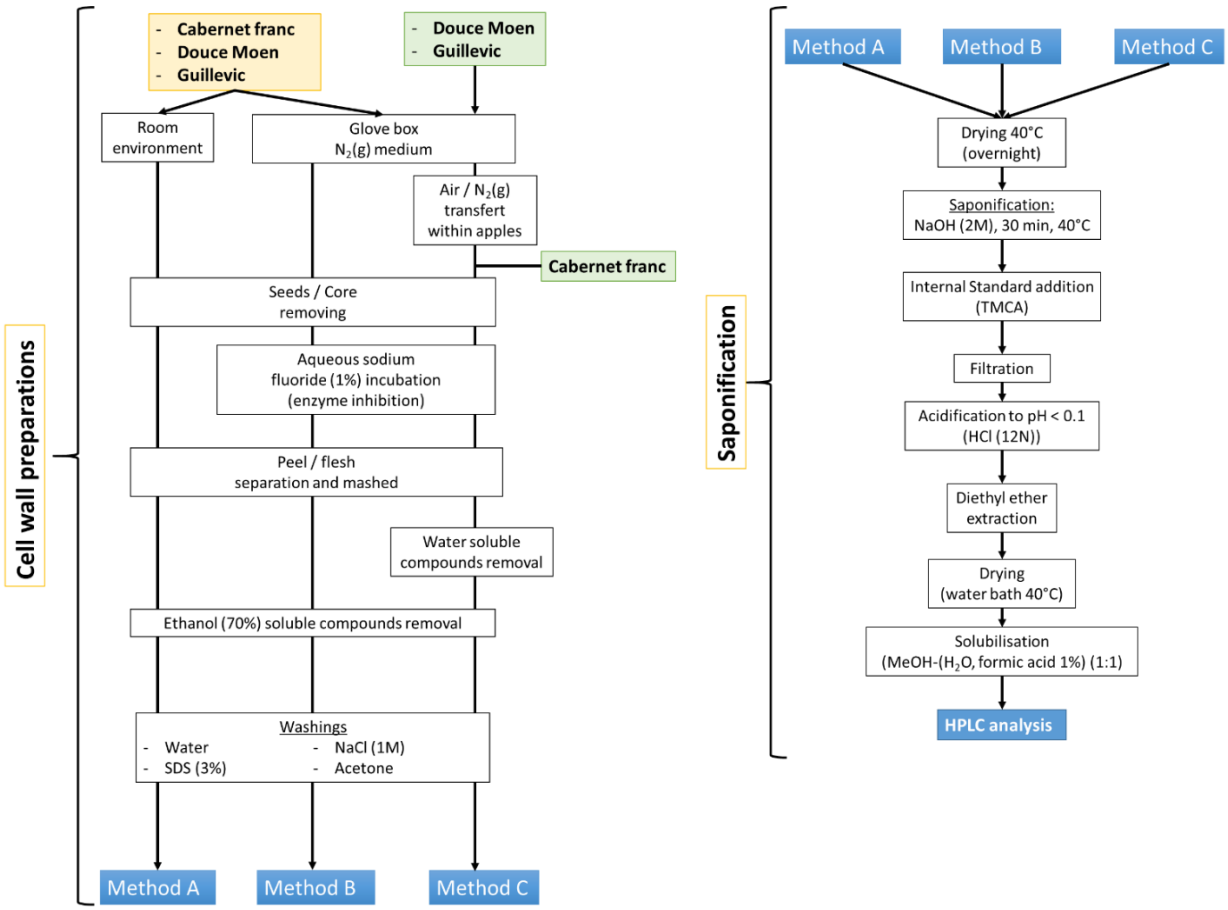

Supplementary figure IV.33: *Work flow of fruit cell wall preparation and cell wall phenolic compound extraction.*

IV.9. References

Abramovič, H. (2015). Chapter 93 - Antioxidant Properties of Hydroxycinnamic Acid Derivatives: A Focus on Biochemistry, Physicochemical Parameters, Reactive Species, and Biomolecular Interactions. Coffee in Health and Disease Prevention. V. R. Preedy. San Diego, Academic Press**:** 843-852.

Alonso Borbalán, Á. M., L. Zorro, D. A. Guillén and C. García Barroso (2003). "Study of the polyphenol content of red and white grape varieties by liquid chromatography–mass spectrometry and its relationship to antioxidant power." Journal of Chromatography A **1012**(1): 31-38.

Antoine, C., S. Peyron, F. Mabille, C. Lapierre, B. Bouchet, J. Abecassis and X. Rouau (2003). "Individual contribution of grain outer layers and their cell wall structure to the mechanical properties of wheat bran." Journal of Agricultural and Food Chemistry **51**(7): 2026-2033.

Bento-Silva, A., M. C. Vaz Patto and M. do Rosário Bronze (2018). "Relevance, structure and analysis of ferulic acid in maize cell walls." Food Chemistry **246**: 360-378.

Buanafina, M. M. d. O. (2009). "Feruloylation in Grasses: Current and Future Perspectives." Molecular Plant **2**(5): 861-872.

Bunzel, M., C. Funk and H. Steinhart (2004). "Semipreparative isolation of dehydrodiferulic and dehydrotriferulic acids as standard substances from maize bran." Journal of Separation Science **27**(13): 1080-1086.

Christiaens, S., S. Van Buggenhout, K. Houben, Z. Jamsazzadeh Kermani, K. R. N. Moelants, E. D. Ngouémazong, A. Van Loey and M. E. G. Hendrickx (2016). "Process–Structure–Function Relations of Pectin in Food." Critical Reviews in Food Science and Nutrition **56**(6): 1021-1042.

Clifford, M. N. (1999). "Chlorogenic acids and other cinnamates – nature, occurrence and dietary burden." Journal of the Science of Food and Agriculture **79**(3): 362-372.

Di Lecce, G., S. Arranz, O. Jáuregui, A. Tresserra-Rimbau, P. Quifer-Rada and R. M. Lamuela-Raventós (2014). "Phenolic profiling of the skin, pulp and seeds of Albariño grapes using hybrid quadrupole time-of-flight and triple-quadrupole mass spectrometry." Food Chemistry **145**: 874-882.

Domínguez, E., J. Cuartero and A. Heredia (2011). "An overview on plant cuticle biomechanics." Plant Science **181**(2): 77-84.

Eraso, F. and R. D. Hartley (1990). "Monomeric and dimeric phenolic constituents of plant cell walls—possible factors influencing wall biodegradability." Journal of the Science of Food and Agriculture **51**(2): 163-170.

Février, H., J.-M. Le Quéré, G. Le Bail and S. Guyot (2017). "Polyphenol profile, PPO activity and pH variation in relation to colour changes in a series of red-fleshed apple juices." LWT - Food Science and Technology **85**: 353-362.

Fry, S. (1982). "Phenolic components of the primary cell wall. Feruloylated disaccharides of D-galactose and L-arabinose from spinach polysaccharide." Biochemical Journal **203**(2): 493-504.

Galanakis, C. M. (2018). Polyphenols: Properties, Recovery, and Applications, Woodhead Publishing.

Gris, E. F., E. A. Ferreira, L. D. Falcão and M. T. Bordignon-Luiz (2007). "Caffeic acid copigmentation of anthocyanins from Cabernet Sauvignon grape extracts in model systems." Food Chemistry **100**(3): 1289-1296.

Guillon, F., O. Tranquet, L. Quillien, J.-P. Utille, J. J. Ordaz Ortiz and L. Saulnier (2004). "Generation of polyclonal and monoclonal antibodies against arabinoxylans and their use for immunocytochemical location of arabinoxylans in cell walls of endosperm of wheat." Journal of Cereal Science **40**(2): 167-182.

Guyot, S., S. Bernillon, P. Poupard and C. Renard (2008). "Multiplicity of phenolic oxidation products in apple juices and ciders, from synthetic medium to commercial products." Recent advances in polyphenol research **1**: 27.

Hartley, R. D. and P. J. Harris (1981). "Phenolic Constituents of the cell walls of dicotyledons." Biochemical Systematics and Ecology **9**(2): 189-203.

Ishii, T. (1997). "Structure and functions of feruloylated polysaccharides." Plant Science **127**(2): 111-127.

Jukanti, A. (2017). Function (s)/Role (s) of Polyphenol Oxidases. Polyphenol Oxidases (PPOs) in Plants, Springer**:** 73-92.

Lachman, J., P. Martinek, Z. Kotíková, M. Orsák and M. Šulc (2017). "Genetics and chemistry of pigments in wheat grain – A review." Journal of Cereal Science **74**: 145-154.

Le Bourvellec, C. and C. M. G. C. Renard (2012). "Interactions between Polyphenols and Macromolecules: Quantification Methods and Mechanisms." Critical Reviews in Food Science and Nutrition **52**(3): 213-248.

Lee, J., B. L. S. Chan and A. E. Mitchell (2017). "Identification/quantification of free and bound phenolic acids in peel and pulp of apples (Malus domestica) using high resolution mass spectrometry (HRMS)." Food Chemistry **215**: 301-310.

Lichtenthaler, H. K. and J. Schweiger (1998). "Cell wall bound ferulic acid, the major substance of the blue-green fluorescence emission of plants." Journal of Plant Physiology **152**(2): 272-282.

Liu, D., P. Lopez-Sanchez, M. Martinez-Sanz, E. P. Gilbert and M. J. Gidley (2019). "Adsorption isotherm studies on the interaction between polyphenols and apple cell walls: Effects of variety, heating and drying." Food chemistry **282**: 58-66.

Malec, M., J.-M. Le Quere, H. Sotin, K. Kolodziejczyk, R. Bauduin and S. Guyot (2014). "Polyphenol profiling of a red-fleshed apple cultivar and evaluation of the color extractability and stability in the juice." Journal of agricultural and food chemistry **62**(29): 6944-6954.

Mattivi, F., R. Guzzon, U. Vrhovsek, M. Stefanini and R. Velasco (2006). "Metabolite profiling of grape: flavonols and anthocyanins." Journal of agricultural and food chemistry **54**(20): 7692-7702.

Moskowitz, A. H. and G. Hrazdina (1981). "Vacuolar contents of fruit subepidermal cells from *Vitis* species." Plant Physiology **68**(3): 686-692.

Padayachee, A., G. Netzel, M. Netzel, L. Day, D. Zabaras, D. Mikkelsen and M. J. Gidley (2012). "Binding of polyphenols to plant cell wall analogues – Part 2: Phenolic acids." Food Chemistry **135**(4): 2287-2292.

Parker, M. L., A. Ng and K. W. Waldron (2005). "The phenolic acid and polysaccharide composition of cell walls of bran layers of mature wheat (Triticum aestivum L. cv. Avalon) grains." Journal of the Science of Food and Agriculture **85**(15): 2539-2547.

Parr, A. J., A. Ng and K. W. Waldron (1997). "Ester-linked phenolic components of carrot cell walls." Journal of agricultural and food chemistry **45**(7): 2468-2471.

Parr, A. J., K. W. Waldron, A. Ng and M. L. Parker (1996). "The wall-bound phenolics of Chinese water chestnut (Eleocharis dulcis)." Journal of the Science of Food and Agriculture **71**(4): 501-507.

Philippe, S., O. Tranquet, J.-P. Utille, L. Saulnier and F. Guillon (2007). "Investigation of ferulate deposition in endosperm cell walls of mature and developing wheat grains by using a polyclonal antibody." Planta **225**(5): 1287-1299.

Pierpoint, W. (1966). "The enzymic oxidation of chlorogenic acid and some reactions of the quinone produced." Biochemical Journal **98**(2): 567.

Ralph, J., S. Quideau, J. H. Grabber and R. D. Hatfield (1994). "Identification and synthesis of new ferulic acid dehydrodimers present in grass cell walls." Journal of the Chemical Society, Perkin Transactions 1(23): 3485-3498.

Ray, S., J. Vigouroux, B. Quémener, E. Bonnin and M. Lahaye (2014). "Novel and diverse fine structures in LiCl–DMSO extracted apple hemicelluloses." Carbohydrate Polymers **108**: 46-57.

Reem, N. T., G. Pogorelko, V. Lionetti, L. Chambers, M. A. Held, D. Bellincampi and O. A. Zabotina (2016). "Decreased polysaccharide feruloylation compromises plant cell wall integrity and increases susceptibility to necrotrophic fungal pathogens." Frontiers in plant science **7**.

Sanoner, P., S. Guyot, N. Marnet, D. Molle and J. F. Drilleau (1999). "Polyphenol Profiles of French Cider Apple Varieties (Malus domestica sp.)." Journal of Agricultural and Food Chemistry **47**(12): 4847-4853.

Saulnier, L. and J. F. Thibault (1999). "Ferulic acid and diferulic acids as components of sugar-beet pectins and maize bran heteroxylans." Journal of the Science of Food and Agriculture **79**(3): 396-402.

Schäfer, J., M. Sattler, Y. Iqbal, I. Lewandowski and M. Bunzel (2019). "Characterization of Miscanthus cell wall polymers." GCB Bioenergy **11**(1): 191-205.

Sinela, A. M., C. Mertz, N. Achir, N. Rawat, K. Vidot, H. Fulcrand and M. Dornier (2017). "Exploration of reaction mechanisms of anthocyanin degradation in a roselle extract through kinetic studies on formulated model media." Food Chemistry **235**: 67-75.

Sun, J., W. Bai, Y. Zhang, X. Liao and X. Hu (2011). "Identification of degradation pathways and products of cyanidin-3-sophoroside exposed to pulsed electric field." Food Chemistry **126**(3): 1203-1210.

Svitelska, G. V., G. P. Gallios and A. I. Zouboulis (2004). "Sonochemical decomposition of natural polyphenolic compound (condensed tannin)." Chemosphere **56**(10): 981-987.

Talamond, P., J.-L. Verdeil and G. Conéjéro (2015). "Secondary metabolite localization by autofluorescence in living plant cells." Molecules **20**(3): 5024-5037.

Tranquet, O., L. Saulnier, J.-P. Utille, J. Ralph and F. Guillon (2009). "Monoclonal antibodies to p-coumarate." Phytochemistry **70**(11-12): 1366-1373.

Vidot, K., M.-F. Devaux, C. Alvarado, S. Guyot, F. Jamme, C. Gaillard, R. Siret and M. Lahaye (2019). "Phenolic distribution in apple epidermal and outer cortex tissue by multispectral deep-UV autofluorescence cryo-imaging." Plant Science.

Vismeh, R., F. Lu, S. P. Chundawat, J. F. Humpula, A. Azarpira, V. Balan, B. E. Dale, J. Ralph and A. D. Jones (2013). "Profiling of diferulates (plant cell wall cross-linkers) using ultrahigh-performance liquid chromatography-tandem mass spectrometry." Analyst **138**(21): 6683-6692.

Waldron, K. W., M. Parker and A. C. Smith (2003). "Plant cell walls and food quality." Comprehensive Reviews in Food Science and Food Safety **2**(4): 128-146.

Chapitre V

V. Metallic ions distribution in texture and phenolic content contrasted cider apples

Introduction

Ce chapitre concerne un deuxième volet de la thèse sur la distribution des ions métalliques dans les tissus de fruits charnus. Les images brutes de fluorescences X obtenues pour les deux variétés de pommes aux différents temps de stockages décrites dans ce chapitre sont présentées en **annexe 6**. De même, les images représentant les cartographies en profondeur dans le tissu sont présentées en **annexe 7**. A partir de ces images de fluorescence X, un traitement d'images similaire à celui des images de fluorescence en UV profond a été réalisé afin d'obtenir les profils de distribution. Les scripts sont présentés en **annexe 8 et 5**.

L'objectif initial étant de faire la corrélation avec les propriétés physicochimiques des fruits, leur caractérisation notamment les compositions osidiques et l'histologie des tissus cellulaires pour la pomme sont présentées en **annexes 9 et 10**. Pour le raisin, les teneurs globales en ions métalliques et les fermetés globales sont décrites en **annexes 11 et 12**. Cependant, comme pour le chapitre III, les travaux ont été réalisés sur la pomme par manque de temps au synchrotron, bien que quelques essais aient donné les cartographies des ions métalliques dans le raisin (Cabernet Franc) présentées en **annexe 13**.

Ce chapitre est en cours de soumission.

Sommaire

V.1. Abstract

Metallic ions were quantified and mapped at the tissue and the cell scales in two texture and phenolic content contrasted cider apples by atomic absorption spectroscopy, ion chromatography and synchrotron cryo X-ray fluorescence imaging. The content of non-esterified uronic acid (UUA) in the cell wall pectin was also measured and found higher than the total metallic ions in the two varieties. Metallic ions content and gradient distribution from the cuticle to the inner tissue significantly varied between years of harvest. The results are discussed with regard to the co-location of metallic ions with the phenolic compounds which questions their role in oxidative mechanisms during fruit development and processing, affecting particularly the colour and taste of fruit products.

Keywords: Metal ions; Cider apples; Multi-scales; Synchrotron cryo-XRF; Image analysis; Atomic absorption spectroscopy; Pectin; Firmness

V.2. Introduction

Mineral elements are important components affecting development, quality and postharvest storage of fleshy fruit[1-2]. Among them, metallic ions play important roles in the regulation of cell turgor, cell electric potential, membrane permeability, and through ionic interactions with cell wall polysaccharides, they contribute to tissue and cell mechanical properties. Calcium (Ca) is particularly studied due to its role in cell wall pectin cross-links affecting fruit texture and preservation of quality. Together with potassium (K) and magnesium (Mg), the Ca content is also responsible for the occurrence of physiological disorders in apples[3]. The major ion, K, has also a key role in fruit quality with the regulation of osmotic pressure, cell expansion and transport of molecules, such as polyphenolic compounds that affect fruit organoleptic characteristics[4]. Among other metallic ions, Mg in the chlorophyll is associated with the green pigmentation of tissue[5], whereas the trace transition metals iron (Fe), copper (Cu), manganese (Mn), and zinc (Zn)[6] are often involved in oxidative biochemical processes[7] through the Fenton and Haber–Weiss chemistry[8]. The reactive oxygen species (ROS) produced are highly reactive toward biomolecules, as they cleave cell wall pectin, degrade phenolic compounds and genetic material[9]. These transition metals are also cofactors of metalloproteins involved in oxidative metabolisms[10] and have been described to affect fruit quality, such as fruit size, color, firmness, and phenolic compounds chemistry[11-12]. In most case, the precise mechanisms of action of metallic ions remain unknown and the localization and quantification of the metallic ions would help in the understanding of their roles in fundamental processes and metabolisms of plant organs, such as during fruit development and postharvest storage but also during elaboration of organoleptic characteristics of fruit and fruit products.

In the present work, the metallic ions distribution in two cider apple varieties, Douce Moen (DM; Malus domestica Borkh. Dous Moen) and Guillevic (GU; Malus domestica Borkh. Guillevic) harvested over two consecutive years is reported at the fruit, tissue and cell scales. These two varieties were chosen as they are contrasted for their phenolic compounds content[13] and firmness. The analysis at the fruit scale was done by atomic absorption spectroscopy (AAS) and ionic chromatography (IC) while at the tissue and cell scales, synchrotron cryo-X-ray fluorescence (S-cryo-XRF) was used. The metallic ions content was compared with the cell wall pectin sites available for ionic interactions and discussed with respect to fruit texture.

V.3. Methods

V.3.1. Fruits

Douce Moen (DM) and Guillevic (GU) apples were harvested on October 2017 and 2018 from a commercial orchard (courtesy of Institut Français des Production Cidricoles, Le Rheu, France).

V.3.2. Viscoelastic analysis

Five fruits of both varieties harvested in 2017 were analysed. Four cylinders (8 x 8 mm, height x diameter) were sampled per fruit at approximately 3 to 5 mm from the cuticle in a 1.5 cm thick equatorial section. The elastic modulus (E') was measured by dynamic mechanical analysis using a Bose ElectroForce 3100 (Bose Corporation, Eden Prairie, MI, USA) according to the method described in Winisdorffer et al. (2015)[14]. The elastic modulus is almost equal to the usual elastic Young's modulus for apple flesh material with low damping[15].

V.3.3. Cell wall analysis

Cell wall was prepared from equatorial sections used to sampling material for the viscoelastic analysis of the fruits harvested in 2017. Samples were freeze-dried and cell walls were obtained as alcohol-insoluble material (AIM)[14].

Uronic acids were quantified using the metahydroxydiphenyl colorimetric method[16] after acid hydrolysis of the AIM for sugar analysis[14].

The methanol quantity in cell wall pectin was measured by HPLC (High Pressure Liquid Chromatography)[17]. The degree of pectin methyl esterification (DE) was calculated as moles of methanol per 100 moles of uronic acid, subsequently the moles of non-esterified uronic acids (UUA) were calculated from DE.

V.3.4. Sample preparation for metallic ions analysis

V.3.4.1. Atomic absorption spectrometry (AAS) and Ionic chromatographic (IC)

Five GU and ten DM apples were slow-frozen at -20 °C at harvest and freeze-dried. A two cm thick slice was sampled at the equator from each dried fruit. Each slice was further sampled in three regions: Peel (P; ≈ 1 mm thick), Outer Cortex 1 (OC-1; ≈ 5 mm thick for DM and 1 cm for GU) and Outer Cortex 2 (OC-2; ≈ 5 mm thick for DM and 1 cm for GU) as shown in **Supplementary Figure V.1**. All cuttings were realized with a ceramic knife. Each region sampled was pooled and ground into a fine

powder using a FastPrep-24 instrument (MP Biochemicals) and ceramic balls at a speed of 5 m s^{-1} for 5 min.

Metal analysis was realized after calcination of the samples using an electrical furnace (Thermolyne type F62700, Thermo scientific) followed by acid dissolution of ashes. Eight mL glass vials were used. Before use, new vials were calcinated 6 h at 450 °C then filled with deionised water (>= 15 MΩcm) containing 0.45% (v/v) HNO_3 66% (Fisher analytical grade) and placed in an ultrasonic bath (Fisher brand FB150 046) for 30 min. They were checked for contaminating Zn by atomic spectrometry and polluted vial were discarded. Vials were dried 1 h at 130 °C before being used. Between 50 and 150 mg of freeze-dried apple powder were added in each vial (triplicate) and weighed precisely (sample weight was adjusted depending on metal concentrations). The 3 vials with a blank were placed in the oven for 6 h at 450 °C. Then, after cooling, they were filled with 8 mL of deionised water containing 0.45% (v/v) HNO_3 66% and ultrasonicated for 30 min. Samples were diluted according to standard concentrations range prior to IC and AAS analyses.

V.3.4.2. Synchrotron cryo-X-rays fluorescence microscopy (S-cryo-XRF)

Nine and three apples per variety harvested in 2017 and 2018, respectively, were studied. Cubes of 5 x 5 x 5 mm^3 were sampled in the epidermis taken from equatorial slices. In addition, the distribution of metallic ions from the peel to the core of apples was analysed in one DM (diam. ≈ 40 mm) and one GU (diam. ≈ 65 mm) fruits harvested in 2018. Three and five adjacent successive cubes of 5 x 5 x 5 mm^3 were sampled for DM and GU, respectively (**Supplementary Figure V.1**).

All samplings of fresh apple were fast-frozen in liquid nitrogen-cooled isopentane and stored at -20 °C prior to analysis. Sections of 60 µm were cut from frozen cubes at -20 °C using a cryostat microtome (Shandon Cryotome FSE Cryostats, Thermo Fisher Scientific, US). Sections were mounted in sandwich between two layers of Ultralene® films and clipped on copper plates that were screwed on copper holders.

V.3.5. Atomic Absorption Spectroscopy (AAS)

Metals were measured with Perkin Elmer AAnalyst 600 atomic spectrometer equipped with an electric graphite furnace and an AS800 auto-sampler. Spectrometer was controlled by Winlab32 software which included a temperature program for each metal. Multi elements (Fe, Zn, Cu, Mn) and mono element (Mg) lamps were used. Multi elements Perkin Elmer standards solution was used for quantification. Measurements were repeated three times for each sample of the triplicate and the value retained was the mean of the nine values. Blank was used to check for the absence of pollution.

V.3.6. Ionic chromatography (IC)

K^+ and Ca^{2+} concentrations were measured by cationic chromatography with a Dionex ICS1100 equipped with a CS16 column and a CG16 guard heated at 40 °C. H_2SO_4 17 mM was used as eluent at a flow rate of 1.2 mL min^{-1}, internal SRS (Self Regeneration Suppressor) at 120 mA. Quantification was done with ionic standards (CPAchem Voisins-le-Bretonneux, France). The value retained for K^+ and Ca^{2+} was the mean of the triplicate.

V.3.7. Synchrotron cryo-X-ray fluorescence microscopy (S-cryo-XRF)

Metallic ion distributions in fruit tissue were collected by S-cryo-XRF at LUCIA (Ligne Utilisée pour la Caractérisation par Imagerie et Absorption) beamline[18] at SOLEIL (Source Optimisée de Lumière à Energie Intermédiaire du LURE (Laboratoire à Utilisation du Rayonnement Electromagnétique)) synchrotron radiation facility (Gif-sur-Yvette, Saint-Aubin, France). The X-ray beam was monochromatized at 7.2 keV to collect Fe, Mn, Ca, and K maps and 2.1 keV to collect Mg maps using a fixed exit double-crystal Si (111) monochromator. The beam was focused to 3 × 3 (v × h) μm^2 by means of a Kirkpatrick-Baez mirror arrangement. The XRF signal was collected using a 60 mm^2 Bruker SDD. The experimental chamber was operated under vacuum to minimize absorption and scattering by air. It was equipped with a cryostat filled with liquid nitrogen and connected to the sample holder by a copper braid; the temperature on the sample holder was -140 °C. The thin sections were transferred under N_2 vapour into the experimental chamber to maintain the cold chain. Cryogenic conditions were used to limit the redistribution of highly diffusible metallic ions.

XRF maps were collected using a pixel size of 3 × 3 μm^2 with an integration time of 500 ms per pixel in continuous FlyScan mode. Scans were performed on 60 µm thick frozen sections prepared from the cubes of 5 x 5 x 5 mm^3. Scan dimensions for epidermis sections were 250 µm in height and 600 µm in width by steps of 3 µm. Scan dimensions for the analysis of metallic ions distribution in fruit sections (from the peel to the core of the fruit) were 100 µm in height and 1500 or 3000 µm in width as described in **Supplementary figure V.1**. For DM, acquisition started from the skin to 1500 µm deep (Zone 1) that included the peel and a part of the OC. A second acquisition of 1500 µm in length was realized at approximately 5 mm from skin (Zone 2) and a third one of 3000 µm in length at approximately 12 mm from skin (Zone 3) included the carpellary bundles before the air space in the apple core. For GU, due to its bigger size, four sections of 1500 µm were scanned from the skin to 16.5 mm deep into the fruit with a gap of 3.5 mm between zones (Zones 1, 2, 3 and 4). A longer scan of 3000 µm was registered 22 mm deep in the fruit (Zone 5), which included the fruit core tissue and carpellary bundles.

V.3.7.1. Data treatments

An XRF spectrum was recorded for each pixel of the map. Spectra were fitted using PyMCA[19] based on the different elements detected. Elements detected at 7.2 keV excitation were Fe, Mn, Cr, V, Ti, Ca, K, Cl, S, P, Si, Al, Mg and Na; while at 2.1 keV excitation they were Cu, Ni, P, Si, Al, Mg and C. Among them, elements of interest were K, Ca, Fe, Mn and Mg. An example of XRF spectrum (black trace) with its fittings (green trace) and corresponding extracted maps of Fe, Mn, Ca, K and Mg are shown in the **Supplementary Figure V.2.** Copper detection in fruit was hampered by the nature of the sample holder, which are made of copper and the relatively high excitation energy (2.1 keV), in comparison to Cu L_3-edge (0.9 keV).

The count number of the XRF signal was normalized by the count number of the incoming beam signal and corrected by the XRF detector dead time. Afterward, the XRF maps were processed as described in **Supplementary Figure V.3** for potassium in DM harvested in 2017, to produce the smoothed distribution profile of each element. These treatments consisted firstly, in the removal of pixels in the XRF maps with null or quasi null signals due to the absence of matter within the sample. Thus, pixels in the Compton scattering signal with value lower than 0.1 count were removed and the same pixels were also removed from the XRF maps of the elements analysed. Secondly, XRF maps were normalized by the Compton scattering signal to allow comparing the relative amount of each element between samples[20]. This normalization reduced errors due to possible thickness differences between sections and allowed considering the variable density of cell walls in sections. Then, analysis of XRF maps was realized by computing XRF intensity profiles per element from the cuticle to the inner tissue using the ImageJ software[21] and the mathematical morphology plugin Process/erode (3D)[22]. The whole data processing used was that of Vidot et al. (2019)[23]. Briefly, thresholding was first applied to create a binary mask of the sample that distinguished the sample from empty space (**Supplementary Figure V.3)**. Distance-image was obtained by applying one-pixel erosion to the sample mask starting from the cuticle followed by the subtraction of the resulting mask from the initial sample mask. This step was iteratively applied until the last pixel column of the initial mask was reached. The masks obtained were applied to the elemental maps to compute the average profile intensity per element. The profiles from the biological replicates were averaged and plotted with standard deviation. To obtain the trend of elements distribution, smoothing of the mean profile was achieved by local regression (LOESS) with a degree of smoothing of 0.3 (**Supplementary Figure V.3)**. The mean profiles are presented with their standard deviations (2017: n = 9; 2018: n = 3).

For both fruit and epidermis profiling, the smoothed normalized counts for the different metallic ions were averaged to compare their global proportion within each map.

V.3.8. Statistics

Statistical evaluation of means was realized by Student's t-test with Microsoft Excel® software (2016). Statistically significant difference was taken at p value ≤ 0.05.

V.4. Results and Discussion

V.4.1. Metal ions and pectin contents distinguish firm from soft apples

The elastic modulus (E'), the cell wall pectin content as uronic acids, the degree of methyl esterification (DE) and the mole number of non-esterified uronic acids (UUA) are reported in **Table V.1**. GU firmness (E') was more than twice that of DM. The content in pectin was close between varieties while the DE of GU pectin was significantly lower compared to DM and the opposite was observed for UUA.

Table V.7: Elastic modulus (E'), amount of uronic acids in cell wall, degree of methyl esterification of pectin (DE), molar proportion of non-esterified uronic acids (UUA). Unless otherwise stated by ǂ, differences are significant (p value < 0.05, n ≥ 3).

	Douce Moen	Guillevic
E' (MPa)	1.9 *±0.1*	4.2 *±0.2*
Uronic acids (% cw dw)	28 *±4.5* ǂ	26 *±5.3* ǂ
DE (%)	80.7 *±7.4*	67.0 *±3.8*
UUA (10^{-2} mol g^{-1} cw)	3.1 *±0.2*	4.9 *±0.2*

The average content in metallic ions measured by IC and AAS in the peel (P, ≈ 1 mm thick) and in the two outer-cortex regions (OC1 ≈ 1.1 cm deep and OC2≈ 2.1 cm deep; Supplementary Figure 1), which are areas of sampling for determining the flesh viscoelastic characteristics and pectin chemistry, is reported according to the year of harvest (**Table V.2**). K was the major element (from 7600 to 9800 µg g^{-1}) followed by Mg and Ca, respectively. Transition metals were present at trace levels amounting from 1.2 to 10 µg g^{-1}. Fe was the main trace element (6.4 to 10.0 µg g^{-1}) while Mn, Cu and Zn contents were close and ranged from 1.2 to 5.8 µg g^{-1}. The content in metallic ions was within values of table apples [12, 24-25]. It showed significant variations between year of harvest and varieties (**Figure V.1**) as also reported for table apples [24-26], which indicate combinations of genetic and environmental factors controlling ion uptake and metabolism during fruit development. The year of harvest had more impact on the content of metallic ions in DM, which showed the highest variation range (from -32 % to 294%) compared to GU (from -59 to 32%) **(Table V.2)**. The most affected metallic ions in DM were Zn and Cu and to a lesser extent Fe while for GU they were Ca and to lesser extents Zn and Fe. The potassium content was the least affected between years of harvest among metallic ions (**Figure V.1 and Table V.2**). As a major component of osmotic regulation and cell transport[27], K is likely involved in robust

mechanisms of regulations to preserve basic cell functioning under different environmental conditions.

Table V.8: Content in metallic ions (µg g^{-1} dry weight) in lyophilised Douce Moen and Guillevic apples harvested in 2017 and 2018 measured by IC and AAS and percentage of variation between harvest years (Years Var.). The molar ratio of non-esterified uronic acid in apples cell wall and calcium, magnesium, potassium and the sum of these ions are also presented for the 2017 harvest. Unless otherwise stated by similar letters, differences are significant (*p* value < 0.05, n = 4).

	Douce Moen			Guillevic		
	2017	**2018**	**Years Var. (%)**	**2017**	**2018**	**Years Var. (%)**
K	7645 *±49*	8512 *±11*	11	9821 *±85* [a]	9701 *±74* [a]	-1
Mg	349 *±4* [b]	237 *±2*	-32	357 *±5* [b]	295 *±13* [c]	-17
Ca	268 *±8*	308 *±1* [c]	14	108 *±2*	44 *±8*	-59
Fe	6.42 *±0.1*	10.03 *±0.14*	55	9.62 *±0.08*	6.68 *±0.13*	-30
Mn	1.64 *±0.01* [d]	1.28 *±0.01* [e]	-22	1.58 *±0.01*	1.34 *±0.01*	-15
Cu	1.84 *±0.03*	5.79 *±0.08*	215	2.51 *±0.03*	2.80 *±0.01*	11
Zn	1.23 *±0.06* [e]	4.85 *±0.19*	294	1.25 *±0.04* [e]	1.65 *±0.04* [d]	32
UUA/2Ca	$2.3\ 10^3$			$9.1\ 10^3$		
UUA/2Mg	$1.1\ 10^3$			$1.7\ 10^3$		
UUA/K	$1.6\ 10^2$			$1.9\ 10^2$		
UUA/(2Ca + 2Mg + K)	$1.3\ 10^2$			$1.7\ 10^2$		

The content of potassium increased from the peel to the OC in GU while in DM the gradient varied with years of harvest. The content of the other metal ions was higher in peel than in the other tissue regions, except for: Ca and Cu in GU, and Cu in DM harvested in 2017 (**Figure V.1**). Moreover, OC regions of GU were significantly richer in Fe and Cu than DM. This enrichment could be related with mechanisms of polymerisation of phenolic compounds since the degree of polymerisation of tannin is higher in GU cortex than in DM[13].

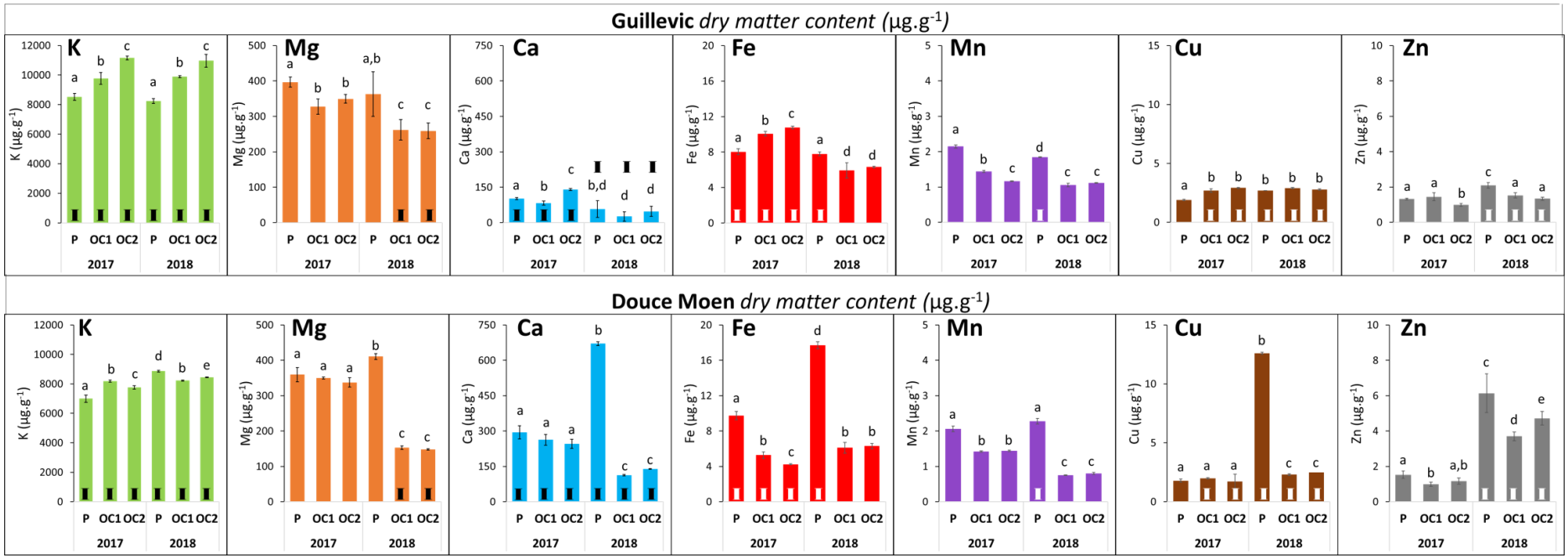

Figure V.34: Mean (± sd, n=4) of K, Mg, Ca, Fe, Mn, Cu and Zn contents (µg g-1 dry weight) in the peel "P", outer cortex 1 "OC-1" and 2 "OC-2" regions of freeze-dried Guillevic and Douce Moen apples harvested in 2017 and 2018. Different letters represent significant differences (p value < 0.05) between ions, regions and years while I indicate significant differences between varieties.

The molar ratio of UUA and the major metallic ions for the two apple varieties are also presented in **Table V.2** for fruit harvested in 2017. The ratio of the molar proportion of UUA to that of metallic ions was significantly higher for GU than for DM. These ratios evidenced a large excess of UUA in the cell wall regarding the total Ca and other major metallic ions potentially availiable within cell wall. In fact, besides metallic ions bound to acidic pectin in the cell walls, a part of them is in the cytoplasm and cellular organelles[28-29]. Thus, considering the total content of the major metallic ions in the tissue of the two apples varieties (**Table V.2**), part of the UUA in pectin occurs under the protonated form or in complex with other apoplastic organic cations (amino acids, peptides, polyamine…).

Among metallic ions, cell wall bound Ca likely contributes to tissue mechanical properties through the formation of pectin ionic cross-links[30]. However, since the soft DM had higher Ca content and higher DE compared to the firm GU, other mechanisms besides pectin calcium cross-links are most likely involved in fruit firmness. Mg, the second most quantitatively important divalent ion, is not able to cross-link pectin in dilute solution[31]. In the cell walls, it may contribute to the compensation of the negative charge of acidic pectin and regulate cell wall swelling, but due to the high pectin concentration, it may also participate to a limited number of weak cross-links[32]. Of interest is the observation that the firmer GU fruits were the richest in the major metallic ion K. Potassium, as a major solute in the regulation of cell turgor pressure, may modulate fruit firmness according to its cellular and apoplastic distribution. In the acidic GU cell wall, due to a higher number of non-esterified pectin, K may act as a charge compensating ion and, through a Donnan effect, may contribute to create a cell wall osmotic pressure and swelling that would add to turgor pressure to yield firm fruits. In addition, the ability of K to cross-link pectin in alkaline conditions [33] supports a structural role of this ion in the cell wall that would add to water compartmentation, cell wall composition and structure, cell wall thickness and histological factors[14-15, 34-35] to modulate cell wall and tissue mechanical properties.

V.4.2. S-cryo-XRF mapping reveals distinct gradient distributions of metal ions in the fruit

Beside quantification, mapping of metallic ions at the cell scale across apple tissue was realized by S-cryo-XRF (**Figure V.2**). An example of cryo-XRF spectrum at 7.2 keV excitation showed that the highest signal was measured for K, followed by Ca, Fe, and Mn **(Supplementary Figure V.2)**. Low counts were measured in cells compared to cell walls (**Supplementary Figure V.3**). Despite the fast plunge-freezing method used in this study, ice formation may have occurred in the vacuole and pushed solutes and organelles close to the cell wall area where higher counts were registered as previously observed for phenolic compounds[23]. The signal intensity for the different metallic ions in fruit regions showed variations **(Figure V.2)** in agreement with contents measured by the AAS and IC **(Figure V.1)**.

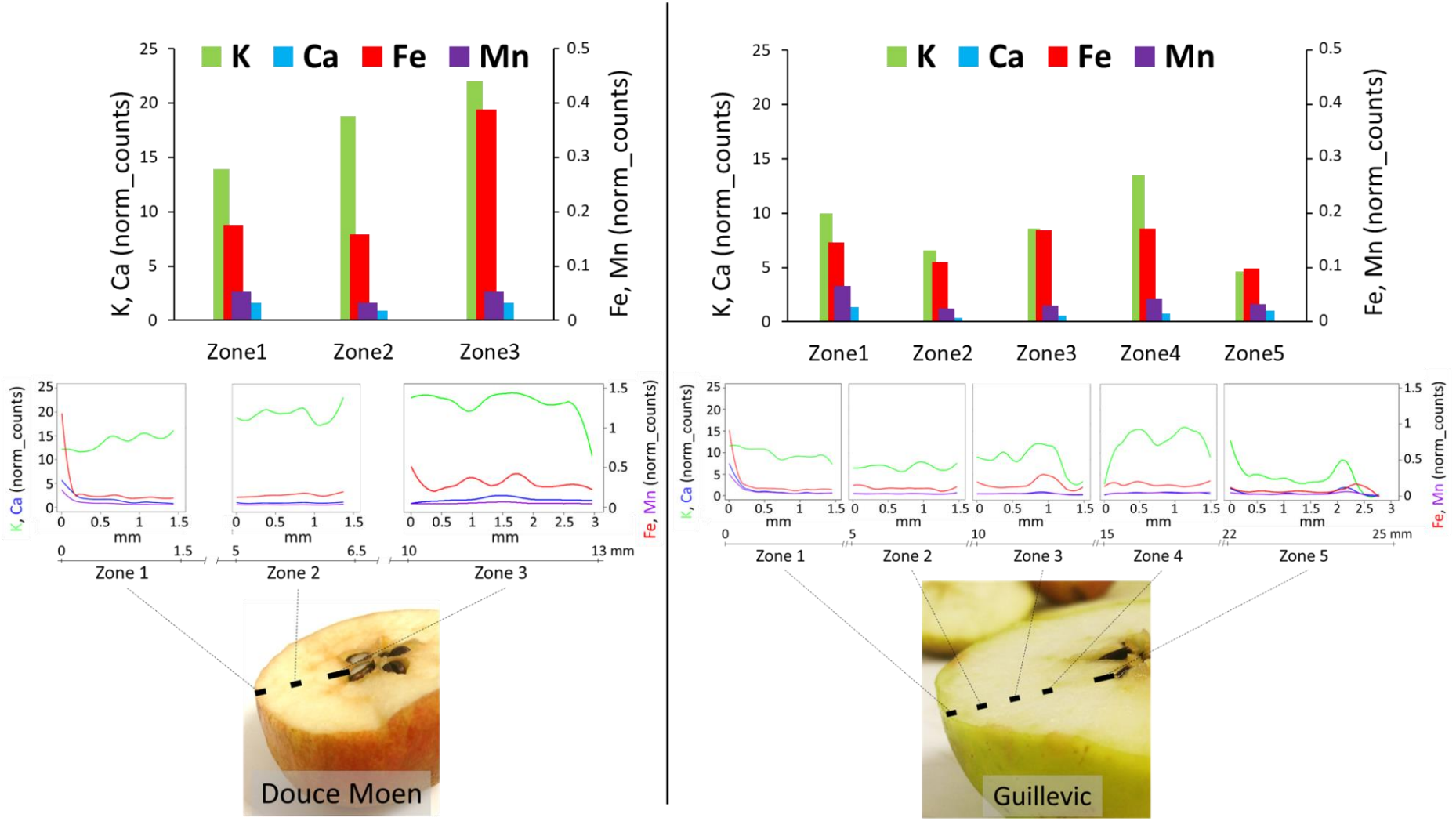

Figure V.35: Distribution of K, Ca, Fe and Mn extracted from XRF maps in sections of Guillevic and Douce Moen apples (n=1) harvested in 2018. Top: sum of K, Ca, Fe, Mn counts per zone; bottom: profile of ions per zone. The left y-axis plots for K (green) and Ca (blue) counts, while the right y-axis plots for Fe (red) and Mn (purple).

An increase of the K signal intensity in the inner fruit regions was observed. Ca and Mn signal intensities were close in all fruit zones (**Supplementary Figure V.1**) though they appeared higher in zone 1 including the peel and to lesser extent, in inner zones. Similar trend in Ca content variation has already been reported in table apple [36]. Higher signals were measured for Fe in internal tissue zones, which included part of the core tissue (zone 3 for DM; zones 3-4 for GU). Furthermore, as previously reported in Cox's Orange Pippin apple[36], there was a trend for a decrease in K signal intensity from the cuticle until 0.5 mm deep for DM and 1.5 mm for GU, prior to an increase until a maximum reached in the outer part of the core tissue where fewer K counts were then measured in GU in comparison to DM. Ca, Fe and Mn distribution followed close trends with higher counts in the cuticle area (0-50 µm) that decreased to low counts in inner tissues. However, areas rich in Ca and Fe appeared as "bumps" on gradient profiles past 11 mm deep tissue. These variations likely corresponded to specific tissues, such as floral tube, sepal bundles or core line[37]. The DM fruit analysed showed a higher metallic cation counts compared to GU.

A focus on K, Ca, Fe, Mn and Mg in the epidermis region, from the cuticle to 550 µm deep inside the tissue, was carried out, as AAS and IC analyses and literature data[24-25, 36] evidenced that apple peel concentrates metallic ions. The distributions of these ions in the epidermis are presented in **Figure V.3** for fruit harvested in 2017 and 2018, except Mg that was only mapped in 2018. The 50 – 150 µm deep tissue regions were delimited by stippled lines in **Figure V.3** as they could correspond to the cuticle, sub-cuticle and outer-cortex cell layers delimitation proposed for these fruits[23]. The distribution of the metallic ions showed significant variations between the two harvests (**Figure V.3**).

K showed the highest signal intensity at approximately 80 µm followed by a slight decrease going deeper into the tissue. The low K amount in the cuticle and its increase in the inner fruit tissue may be related to osmotic regulation. Gradient of small metabolites, such as organic acids and sugars in apple could compete with K in the maintenance of cell osmotic pressure. K would be limited in the peel cell layers due to the concentration of organic metabolites in this region[38].

Ca and Mg showed the highest count at approximately 60 µm from the cuticle and then steeply decreased further inside the tissue (**Figure V.3**). These sub-cuticle cell layers play the role of a barrier to water and gas exchange, and in pathogen defence[39]. This barrier is under tension stress that requires specific mechanical properties to which Ca-pectin complex may locally participate. The contribution of Mg to pectin crosslinks may be limited[32] but its presence in the sub-cuticle cell layers may be related in part with intracellular organelles, such as plasts arising from ripening-modified chloroplasts with chlorophyll remains that are pushed close to the wall.

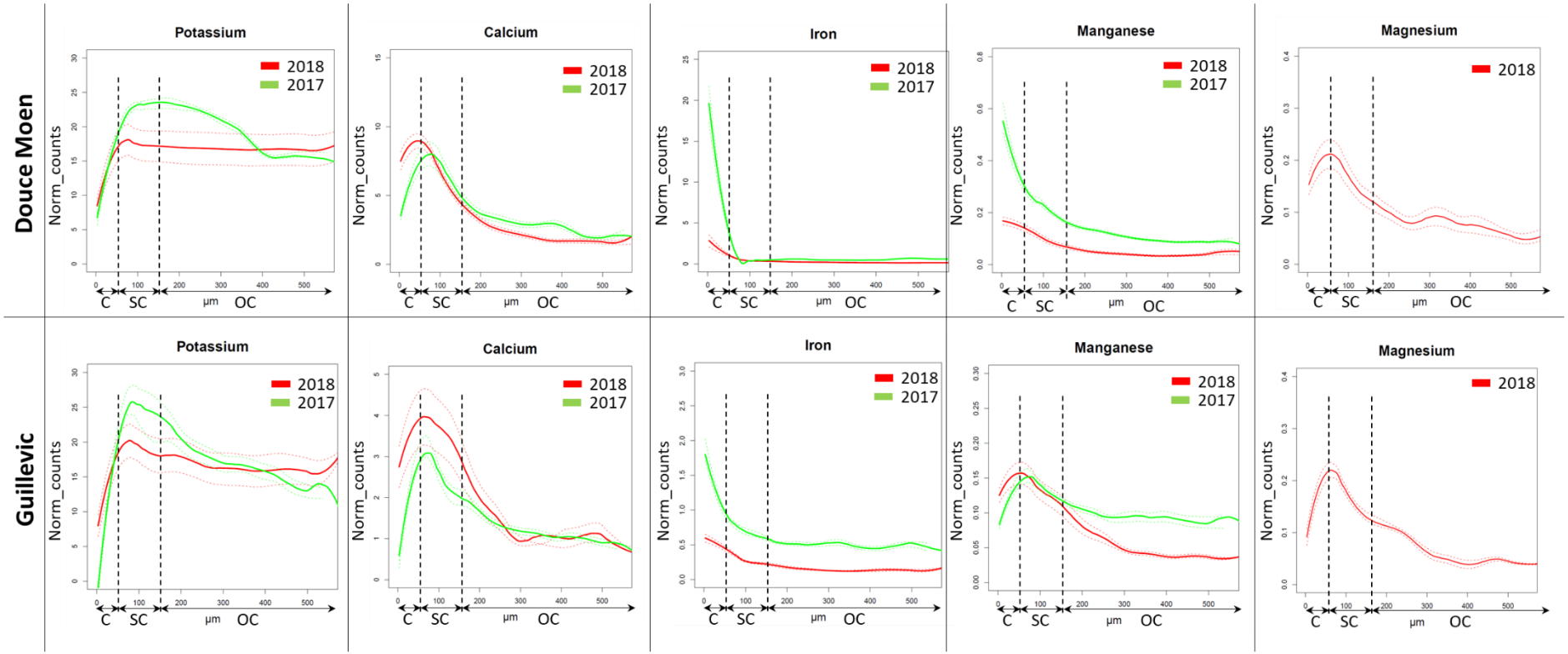

Figure V.36: Smoothed distribution of K, Ca, Fe, Mn and Mg in the epidermis (550 µm deep) of Douce Moen and Guillevic harvested in 2017 (green) and 2018 (red). Dotted lines represent the standard deviation (n = 9 for 2017; n = 3 for 2018). Vertical dashed lines separate the cuticle (C), sub-cuticle (SC) and the outer-cortex (OC) cell layer.

Fe and Mn counts peaked in the cuticle, a region that is also known to be enriched in phenolic compounds[23], and then decreased close to zero past 80 µm into apple tissue (**Figure V.3**). As fruit are particularly exposed to a large range of biotic and abiotic stress, the high concentration of transition metals may be associated with phenolic compounds in oxidative mechanisms of defence[40]. Indeed, based on previous works on phenolic compounds distribution[23], these results evidenced tissue co-location of metallic ions and flavonoids that may act in concert in oxidative mechanisms during fruit development and processing. In fact, these transition metals are known cofactors of metalloproteins such as polyphenol oxidase, malic decarboxylase, peptidases, etc.[38]. In that context, it would have been interesting to map Cu in apple tissue as this metal is part of polyphenol oxidase which is an enzyme involved in the browning of apple flesh exposed to air[10]. Unfortunately, its X-ray fluorescence would have required a higher excitation energy and a copper-free sample handling set-up that were not available on the synchrotron beam line. Fe, Mn, Cu and Zn could also form complexes with pigments known to be present in cell layers under the cuticle[23]. Thus, the lower counts in Fe and Mn in the epidermis of GU compared to DM (**Figure V.3**) may be related with the different skin colour of theses varieties.

This study pointed to the benefit of S-cryo-XRF imaging for the observation of several metallic ions distribution within sections of apple tissue in one experiment. Quantification was realized by classical approaches (AAS, IC) as proper calibrated matrices for measuring metallic ion content by S-cryo-XRF are still lacking. These quantifications allowed highlighting the high content of non-esterified galacturonic acid in cell wall pectin with regard to the total metallic ions measured. This result challenges the mechanisms by which charges in cell wall polysaccharides are controlled and the consequences on pectin interactions, cell wall swelling and the mechanical properties. To that end, further work by S-cryo-XRF at the nanoscale and by cryo-X-ray Absorption Near Edge Structure spectroscopy would help in distinguishing the location of specific metallic ions in cell compartments and cell wall, with regard to their presence as complexes with polysaccharides, enzymes, or polyphenols. In fact, the distribution of metal ions observed in this study and that of phenolic compounds in the same varieties of cider apples[23] open the way for a better understanding of their mutual roles in the development of organoleptic properties in fresh or transformed apple fruit.

V.5. Acknowledgements

We acknowledge Ms C. Alvarado, Ms S. Durand, Mr L. Helary and Mr C. Gaillard (INRA BIA) for participation in samples preparation and data acquisition during synchrotron XRF experiments. The authors thank Ms L. Lavenant (INRA BIA) for technical assistance during IC and AAS measurements. This work was supported in part by Cap Aliment Food for Tomorrow program funding by Région Pays de la Loire. Synchrotron analyses were conducted and supported under the proposal 20170043 at synchrotron SOLEIL on LUCIA beamline.

V.6. Supplementary figures

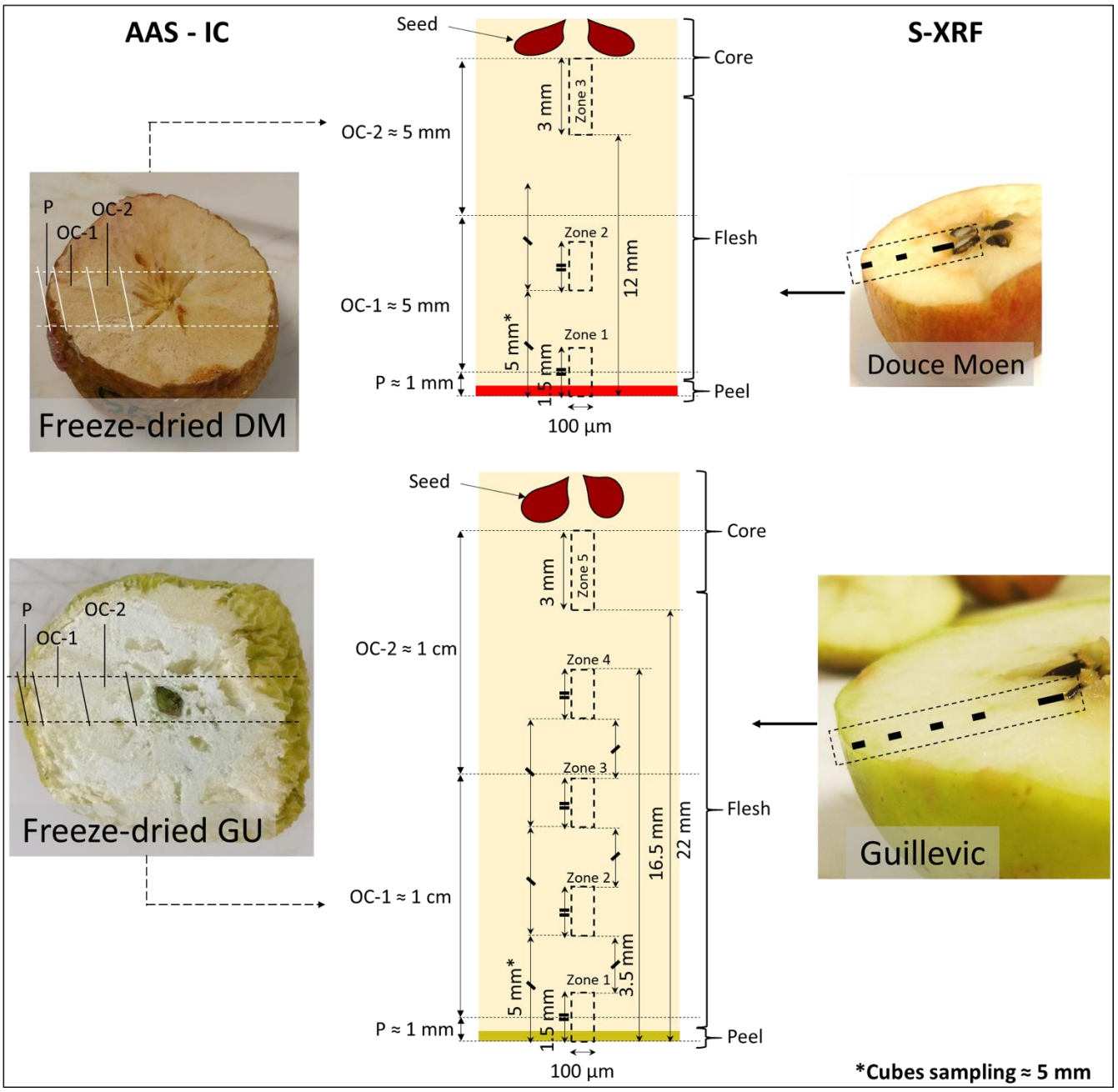

***Supplementary Figure V.37**: Sampling of freeze-dried Douce Moen (DM) and Guillevic (GU) apples for AAS and IC analyses (P: peel; OC-1, OC-2: outer-cortex region 1 and 2). From the 5 x 5 x 5 mm³ sampled frozen cubes, the XRF analysed zones and dimensions within 60 µm thick sections, were described with black thick lines in dashed rectangles.*

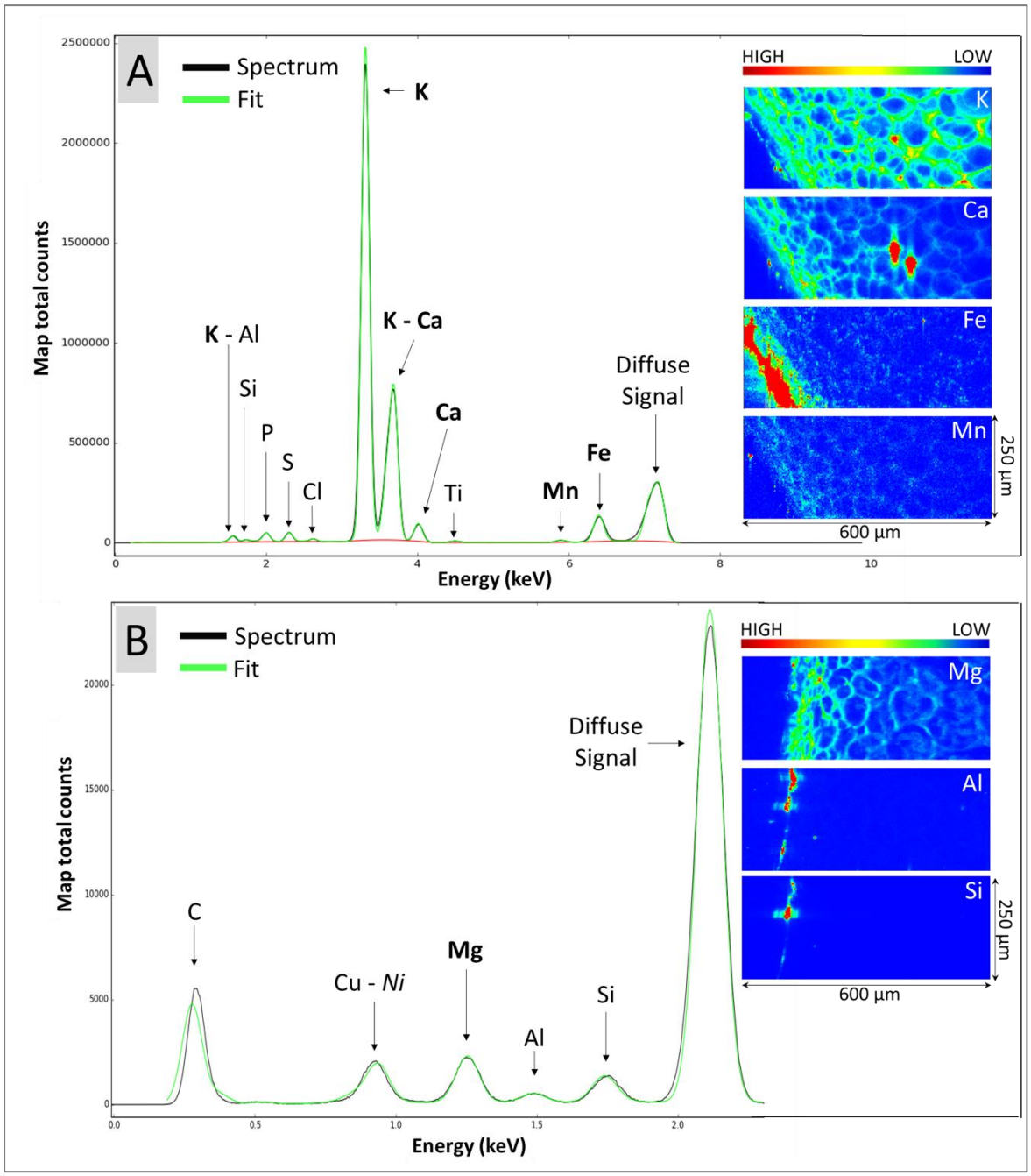

Supplementary Figure V.38: *Example of X-ray fluorescence spectrum (raw: black trace and fitted: green trace) of Douce Moen apple* ***(A)*** *with 7.2 keV excitation and* ***(B)*** *with 2.1 keV excitation. On the right, maps of K, Ca, Fe, Mn, Mg, Al and Si counts.*

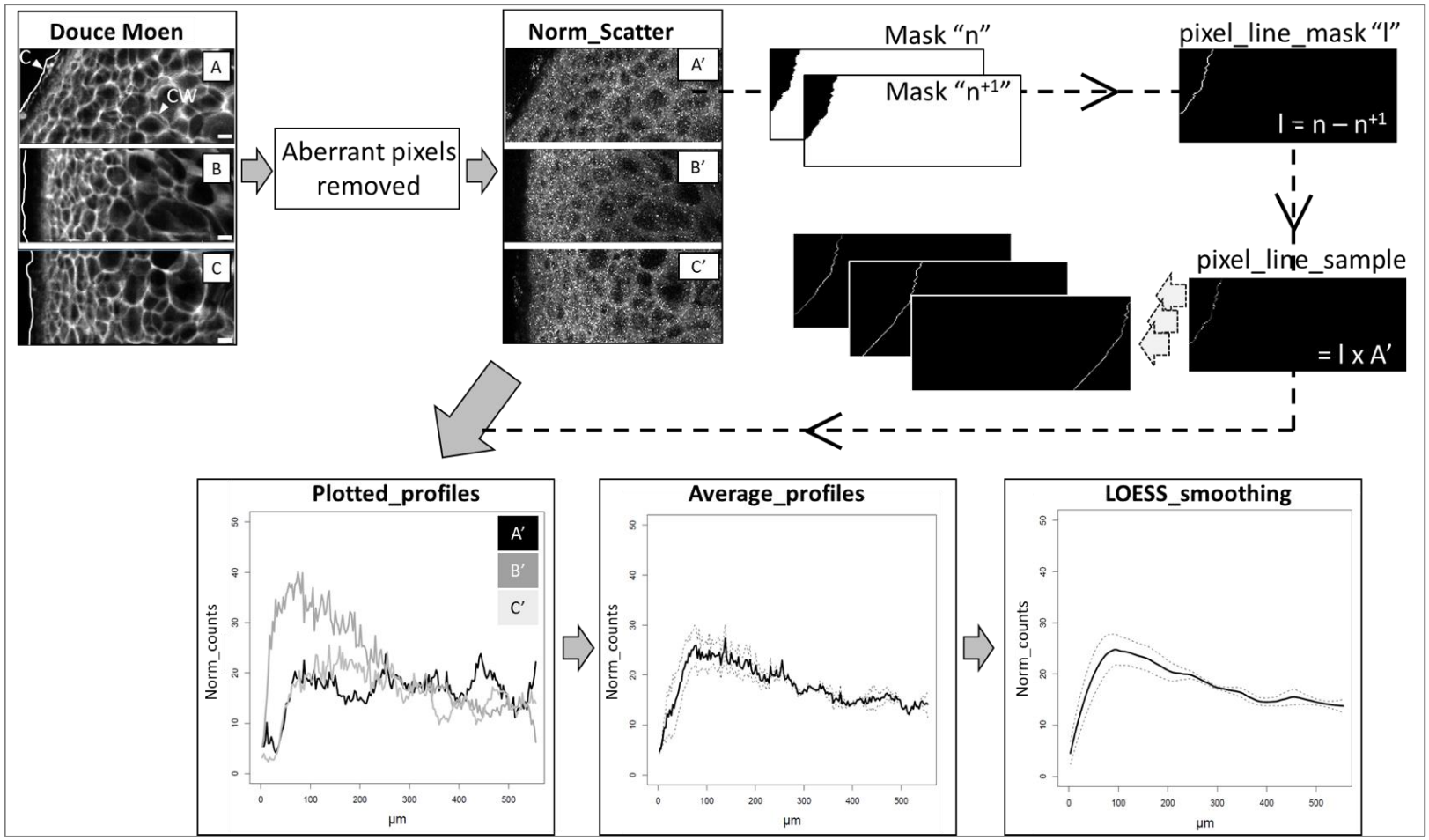

***Supplementary Figure V.39**: Example of image treatment to obtain metallic ions mean distribution profile: on the top left are three replicate XRF maps of potassium of Douce Moen harvested in 2017 (A, B, and C). First, the pixels with value lower than 0.1 count within Compton scattering signal, corresponding to area without signal or extremely low signal, were removed on XRF and Compton scattering maps to avoid division by zero and artefact values in the ratio. XRF maps are then normalized by Compton scatter signal (A', B' and C'). Masks of pixels line (l, l^{+1},…,l^{+n}) are calculated from 3x 3 µm² pixels erosion of samples masks (n, n^{+1},…, n^{+n}). On masks, black and white pixels correspond to value 0 and 1 respectively. These masks of lines lead to pixels lines of samples after multiplication with "Norm_Scatter" maps. The curves on the left (Plotted profiles) correspond to the plots of the average value of positive pixels in each "pixel_line_sample" maps, giving the distribution of the element from the peel. These curves represent the distribution of potassium counts normalized by the Compton scattering in the three replicates. These curves are then averaged (Average profile) and smoothed by the LOESS method with α = 0.3 (LOESS smoothing). C: Cuticle ≈ Peel, CW: Cell Wall, Scale bar: 40 µm.*

V.7. References

1. Finley, J. W.; Hurst, W. J.; Lee, C. Y., *Principles of food chemistry*. Springer: 2018.
2. Ferguson, I. B.; Boyd, L. M., Inorganic nutrients and fruit quality. In *Fruit Quality and its Biological Basis*, Knee, M., Ed. Sheffield Academic Press Ltd.: Sheffield, UK, 2002; pp 17-45.
3. Jemrić, T.; Fruk, I.; Fruk, M.; Radman, S.; Sinkovič, L.; Fruk, G., Bitter pit in apples: pre-and postharvest factors: A review. *Spanish journal of agricultural research* **2017,** *14* (4), 08-01.
4. Mengel, K., Potassium. In *Handbook of plant nutrition*, CRC Press: 2016; pp 107-136.
5. Pareek, S.; Sagar, N. A.; Sharma, S.; Kumar, V.; Agarwal, T.; González-Aguilar, G. A.; Yahia, E. M., Chlorophylls: Chemistry and Biological Functions. *Fruit and Vegetable Phytochemicals: Chemistry and Human Health, 2 Volumes* **2017**, 269.
6. Broadley, M.; Brown, P.; Cakmak, I.; Rengel, Z.; Zhao, F., Function of Nutrients: Micronutrients. In *Marschner's Mineral Nutrition of Higher Plants (Third Edition)*, Marschner, P., Ed. Academic Press: San Diego, 2012; pp 191-248.
7. Pons, T.; Lambers, H.; Chapin, F., Plant physiological ecology. Springer, New York: 1998.
8. Kehrer, J. P., The Haber–Weiss reaction and mechanisms of toxicity. *Toxicology* **2000,** *149* (1), 43-50.
9. Airianah, O. B.; Vreeburg, R. A. M.; Fry, S. C., Pectic polysaccharides are attacked by hydroxyl radicals in ripening fruit: evidence from a fluorescent fingerprinting method. *Annals of Botany* **2016,** *117* (3), 441-455.
10. Jukanti, A., Function (s)/Role (s) of Polyphenol Oxidases. In *Polyphenol Oxidases (PPOs) in Plants*, Springer: 2017; pp 73-92.
11. Àlvarez-Fernàndez, A.; Abadía, J.; Abadía, A., Iron Deficiency, Fruit Yield and Fruit Quality. In *Iron Nutrition in Plants and Rhizospheric Microorganisms*, Barton, L. L.; Abadia, J., Eds. Springer Netherlands: Dordrecht, 2006; pp 85-101.
12. Brunetto, G.; Wellington Bastos De Melo, G.; Toselli, M.; Quartieri, M.; Tagliavini, M., The role of mineral nutrition on yields and fruit quality in grapevine, pear and apple. *Revista Brasileira de Fruticultura* **2015,** *37* (4), 1089-1104.
13. Sanoner, P.; Guyot, S.; Marnet, N.; Molle, D.; Drilleau, J. F., Polyphenol Profiles of French Cider Apple Varieties (Malus domestica sp.). *Journal of Agricultural and Food Chemistry* **1999,** *47* (12), 4847-4853.
14. Winisdorffer, G.; Musse, M.; Quellec, S.; Barbacci, A.; Le Gall, S.; Mariette, F.; Lahaye, M., Analysis of the dynamic mechanical properties of apple tissue and relationships with the intracellular water status, gas distribution, histological properties and chemical composition. *Postharvest Biology and Technology* **2015,** *104*, 1-16.
15. Videcoq, P.; Barbacci, A.; Assor, C.; Magnenet, V.; Arnould, O.; Le Gall, S.; Lahaye, M., Examining the contribution of cell wall polysaccharides to the mechanical properties of apple parenchyma tissue using exogenous enzymes. *Journal of experimental botany* **2017,** *68* (18), 5137-5146.
16. Blumenkrantz, N.; Asboe-Hansen, G., New method for quantitative determination of uronic acids. *Analytical biochemistry* **1973,** *54* (2), 484-489.
17. Levigne, S.; Thomas, M.; Ralet, M.-C.; Quemener, B.; Thibault, J.-F., Determination of the degrees of methylation and acetylation of pectins using a C18 column and internal standards. *Food Hydrocolloids* **2002,** *16* (6), 547-550.
18. Vantelon, D.; Trcera, N.; Roy, D.; Moreno, T.; Mailly, D.; Guilet, S.; Metchalkov, E.; Delmotte, F.; Lassalle, B.; Lagarde, P.; Flank, A.-M., The LUCIA beamline at SOLEIL. *Journal of Synchrotron Radiation* **2016,** *23* (2), 635-640.
19. Solé, V. A.; Papillon, E.; Cotte, M.; Walter, P.; Susini, J., A multiplatform code for the analysis of energy-dispersive X-ray fluorescence spectra. *Spectrochimica Acta Part B: Atomic Spectroscopy* **2007,** *62* (1), 63-68.

20. Shackley, M. S., X-Ray Fluorescence Spectrometry in Twenty-First Century Archaeology. In *X-Ray Fluorescence Spectrometry (XRF) in Geoarchaeology*, Shackley, M. S., Ed. Springer New York: New York, NY, 2011; pp 1-6.
21. Schneider, C. A.; Rasband, W. S.; Eliceiri, K. W., NIH Image to ImageJ: 25 years of Image Analysis. *Nature methods* **2012,** *9* (7), 671-675.
22. Neves, A. A.; Silva, E. J.; Roter, J. M.; Belladona, F. G.; Alves, H. D.; Lopes, R. T.; Paciornik, S.; De-Deus, G. A., Exploiting the potential of free software to evaluate root canal biomechanical preparation outcomes through micro-CT images. *International Endodontic Journal* **2015,** *48* (11), 1033-1042.
23. Vidot, K.; Devaux, M.-F.; Alvarado, C.; Guyot, S.; Jamme, F.; Gaillard, C.; Siret, R.; Lahaye, M., Phenolic distribution in apple epidermal and outer cortex tissue by multispectral deep-UV autofluorescence cryo-imaging. *Plant Science* **2019**.
24. Özcan, M. M.; Harmankaya, M.; Gezgin, S., Mineral and heavy metal contents of the outer and inner tissues of commonly used fruits. *Environmental monitoring and assessment* **2012,** *184* (1), 313-320.
25. USDA USDA National Nutrient Database for Standard Reference, Release 27. http://www.ars.usda.gov/ba/bhnrc/ndl.
26. Manzoor, M.; Anwar, F.; Saari, N.; Ashraf, M., Variations of antioxidant characteristics and mineral contents in pulp and peel of different Apple (Malus domestica Borkh.) cultivars from Pakistan. *Molecules* **2012,** *17* (1), 390-407.
27. Morgan, J. M., Osmoregulation and Water Stress in Higher Plants. *Annual Review of Plant Physiology* **1984,** *35* (1), 299-319.
28. Tonetto De Freitas, S.; Amarante, C. d.; Mitcham, E., Calcium Deficiency Disorders in Plants. Postharvest ripening physiology of crops. CRC Press: 2016.
29. Vidot, K.; Gaillard, C.; Rivard, C.; Siret, R.; Lahaye, M., Cryo-laser scanning confocal microscopy of diffusible plant compounds. *Plant Methods* **2018,** *14* (1), 89.
30. Jarvis, M.; Briggs, S.; Knox, J., Intercellular adhesion and cell separation in plants. *Plant, Cell & Environment* **2003,** *26* (7), 977-989.
31. Malovíková, A.; Rinaudo, M.; Milas, M., Comparative interactions of magnesium and calcium counterions with polygalacturonic acid. *Biopolymers: Original Research on Biomolecules* **1994,** *34* (8), 1059-1064.
32. Morris, V.; Ring, S.; MacDougall, A.; Wilson, R., Biophysical characterization of plant cell walls. *Annual Plant Reviews, The Plant Cell Wall* **2003**, 55-65.
33. Wang, H.; Wan, L.; Chen, D.; Guo, X.; Liu, F.; Pan, S., Unexpected gelation behavior of citrus pectin induced by monovalent cations under alkaline conditions. *Carbohydr Polym* **2019,** *212*, 51-58.
34. Lahaye, M.; Bouin, C.; Barbacci, A.; Le Gall, S.; Foucat, L., Water and cell wall contributions to apple mechanical properties. *Food Chemistry* **2018,** *268*, 386-394.
35. Ting, V. J.; Silcock, P.; Bremer, P. J.; Biasioli, F., X-ray micro-computer tomographic method to visualize the microstructure of different apple cultivars. *Journal of food science* **2013,** *78* (11), E1735-E1742.
36. Ferguson, I. B.; Watkins, C. B., Cation distribution and balance in apple fruit in relation to calcium treatments for bitter pit. *Scientia Horticulturae* **1983,** *19* (3), 301-310.
37. Herremans, E.; Verboven, P.; Hertog, M.; Cantre, D.; van Dael, M.; De Schryver, T.; Van Hoorebeke, L.; Nicolai, B., Spatial development of transport structures in apple (Malus × domestica Borkh.) fruit. *Frontiers in Plant Science* **2015,** *6* (679).
38. Hulme, A. C., The biochemistry of fruits and their products. Vol. 2. *The biochemistry of fruits and their products. Vol. 2.* **1971**.
39. Khanal, B. P.; Knoche, M., Mechanical properties of cuticles and their primary determinants. *Journal of Experimental Botany* **2017,** *68* (19), 5351-5367.
40. Perron, N. R.; Brumaghim, J. L., A review of the antioxidant mechanisms of polyphenol compounds related to iron binding. *Cell biochemistry and biophysics* **2009,** *53* (2), 75-100.

Chapitre VI

VI. Pectin, metal ions and phenolic compounds comportments in an oxidant system model

Introduction

Ce dernier chapitre reprend les distributions obtenues dans les chapitres précédents, afin d'évaluer l'impact de telles distributions sur les fruits déstructurés. L'objectif étant de comprendre notamment les interactions et mécanismes réactionnels potentiels associés à leur proximité dans le fruit, qui impacteraient leurs propriétés organoleptiques. Ces travaux ne sont que les prémices des futures études nécessaires pour mieux comprendre ces interactions potentielles à partir des distributions des différents composés.

Sommaire

VI.1. Abstract

During fruit consumption and processing, metallic cations, cell wall pectin and vacuolar phenolic components are made to come into contact. This mixing is at the origin of new interactions and reactions catalysed in particular by reactive oxygen species (ROS) arising from fruit metabolism or the presence of transition metal cations. As consequences, these reactions will modify the fruit product organoleptic properties, such as texture, color and taste.

A system model mimicking fruit matrix rich in phenolic compounds, such as found in apple and grape, was used to study the impact of (+)-catechin (Cat), p-coumaric acid (pCA), cyanidin (Cya), calcium, iron and hydrogen peroxide on pectin molecular weight. Pectin molecular weight was analysed by size exclusion chromatography, and the phenolic components were followed by the total polyphenol index (TPI) and the color intensity (CI) in model solutions.

Results showed that boosted oxidative conditions are required to depolymerize pectin while phenolic compounds acted as antioxidants limiting pectin degradation. However, at low iron concentration (+)-catechin was revealed to act as a pro-oxidant. The results are discussed with regard to possible mechanisms involving the redox potential of iron and H_2O_2 and interactions between pectin, phenolic compounds and iron.

VI.2. Introduction

Cell walls, phenolic components and metallic cations are often linked to the organoleptic properties, such as texture, astringency, color and taste of raw and processed fleshy fruits (Broadley, Brown et al. 2012, Galanakis 2018). These properties depend on the reactive oxygen species (ROS) produced during fruit metabolism. Among them is H_2O_2 that originates as an intermediary product from several sources, such as from enzymatic reactions (NADPH, AcCoA, cell wall peroxidase, etc.) or chloroplast for examples (Chen and Schopfer 1999, del Río 2015). Together with oxygen and a catalyst, such as ascorbic acid or transition metals and particularly iron through the Fenton and Haber-Weiss reactions (Briat 2002), H_2O_2 decomposes in other ROS among which are hydroxyl and oxygen radicals that are extremely reactive (Inze and Van Montagu 2002). These ROS damage nearby molecules, such as pectin in the cell walls (Fry, Miller et al. 2001) or phenolic compounds responsible for fruit organoleptic properties (Robards, Prenzler et al. 1999, Gülçin 2012).

Pectin in cell walls are polysaccharide of which the partially methyl-esterified 1,4-linked α-D-galacturonic acids in homogalacturonan structural domains play an important role in fruit texture (Videcoq, Barbacci et al. 2017). Fruit softening often involves pectin degradation by enzymatic or oxidative mechanisms which cleaves the (1-4)-linkages (Airianah, Vreeburg et al. 2016).

Among the phenolic compounds, catechins and anthocyanidins condensation or polymerisation formed in the presence of ROS catalysed by iron (Perron and Brumaghim 2009) play major roles in organoleptic characteristics of fruit product (Macheix, Fleuriet et al. 2017). Hydroxycinnamic acids, particularly ferulic and p-coumaric acid, predominantly found in the cells of fruit (Gómez-Alonso, García-Romero et al. 2007, Lee, Chan et al. 2017) and at trace levels in the cell walls (Parr, Ng et al. 1997, Saulnier and Thibault 1999), could take part in the regulation of oxidative stress by scavenging ROS (Abramovič 2015). Phenolic components have been widely described as antioxidants and more rarely as pro-oxidants (Lambert and Elias 2010, Eghbaliferiz and Iranshahi 2016). The anti-oxidative activity of (+)-catechin is higher than that of cyanidin followed by p-coumaric acid (Luís, Duarte et al. 2018). Together p-coumaric and cyanidin were described to have synergic anti-oxidative effects while (+)-catechin has an antagonist effect on p-coumaric acid and cyanidin (Sekher Pannala, Chan et al. 2001, Luís, Duarte et al. 2018). Instead, the hydrogen or hydrophobic binding of (+)-catechin and related condensed polymers complexes on pectin formed during cell breakdown or fruit processing (Renard, Baron et al. 2001, Le Bourvellec and Renard 2012) limit their anti-oxidative activity.

Pectin amounts to approximately 0.5 – 3 mg g^{-1} of the fresh fruit weight (Thibault and Ralet 2008) while the phenolic compounds as flavanols, hydroxycinnamic acids and anthocyanidins range from 0.1 mg g^{-1} to 3 mg g^{-1}, from 0.04 to 0.6 mg g^{-1} and from 0.008 to 0.6 mg g^{-1} of the fresh fruit

weight, respectively (Harnly, Doherty et al. 2006, Mattivi, Guzzon et al. 2006, Di Lecce, Arranz et al. 2014, Lee, Chan et al. 2017). Metallic ions among which iron and calcium have been reported in fruit from 0.06 to 3.5 µg g^{-1} and 4 to 140 µg g^{-1} of fresh fruit weight, respectively (Özcan, Harmankaya et al. 2012, USDA 2018). Iron and calcium have been localised in apple tissues specifically within cuticle and sub-cuticle cell layers, respectively (Vidot, Rivard et al. 2019). These tissues layers were shown to be also rich in phenolic compounds as flavanols particularly concentrated in the cuticle, and a mix of hydroxycinnamic acids and pigments together with flavanols was described for inner cell layers (Vidot, Devaux et al. 2019). During fruit consumption and processing, the compartmentalized phenolic compounds and transition metals in the cells are mixed together with the cell wall to form a very complex medium where new interactions are induced. These interactions modify the initial structural characteristics, physicochemical properties and chemical reactivity of all components which change the organoleptic properties of the processed fruit. To study these changes in fruit matrix, models systems are commonly realized (Sinela, Mertz et al. 2017).

However, if models have been used to mimic plant apoplast in studies aiming at assessing the reactivity and modifications of cell wall polysaccharides in the presence of metallic cation under oxidative conditions (Fry 1998, Fry, Miller et al. 2001, Dumville and Fry 2003), none included phenolic compounds. The aim of the present study described in this chapter was to follow pectin and phenolic compounds interactions with metal cations under oxidative conditions that may happen in fruit matrix rich in phenolic compounds, such as in crushed or pressed apples or grapes. The model system uses hydrogen peroxide to boost ROS in an attempt to mimic ROS production from various sources in real fruit matrix. Besides these purposes, since iron was found as the main transition metal in apple and grape (Vidot, Rivard et al. 2019), an excess of iron concentration was tested to better evaluate its impact. Pectin degradation was followed through size exclusion chromatography while the phenolic component structural changes were estimated from the UV-vis absorption variation through the total polyphenol index (TPI) and the color intensity (CI) of the model solutions.

VI.3. Materials

(+) Catechin hydrate (Cat), para-coumaric acid (pCA), cyanidin chloride (Cya), hydrogen peroxide (H_2O_2, 30%), $FeCl_2$ tetra hydrate (Fe), $CaCl_2$ anhydrous (Ca) and sodium nitrate ($NaNO_3$) were from Sigma-Aldrich, UK. Pectin (Pec) with a degree of methylation of 72% (UNIPECTINE QC 100, HM PECTIN E440i, batch 09518MHMPA 2018) was from Cargill, France. Unless otherwise stated, all chemicals were of far UV quality HPLC grade purity.

VI.4. Methods

VI.4.1. Model solutions

Stock solutions of the individual compounds were prepared in H_2O milliQ. These were Pec: 12 mg mL^{-1}, Fe: 3 mg mL^{-1} and 0.15 mg mL^{-1}, H_2O_2: 6 mg mL^{-1}, Ca: 6 mg mL^{-1}, Cat: 4 mg mL^{-1}, pCA: 2 mg mL^{-1} and Cya: 0.4 mg mL^{-1}. Model solutions of 1 mL were prepared by diluting the stock solutions in H_2O to reach the final concentrations of the different components: Pec: 3 mg mL^{-1}, Fe: 0.3 mg mL^{-1} (300 ppm) or 0.015 mg mL^{-1} (15 ppm), H_2O_2: 0.1 mg mL^{-1}, Ca: 0.3 mg mL^{-1}, Cat: 1 mg mL^{-1}, pCA: 0.1 mg mL^{-1} and Cya: 0.02 mg mL^{-1}. The different components were added in the following order: Pec, Fe, H_2O_2, Ca, Cat, pCA and Cya, respectively. Mix PCs corresponded to the mixture of the three phenolic components Cat, pCA and Cya. The pH of the solutions was constant at pH = 3.0. The model solutions were immediately analysed after addition of each components. The mole number of each compound in model solution together with the equivalent according to both iron content was calculated as shown in **Table VI.1**. The pectin used for the experiment is 72% methyl esterify, though the pectin was presented by it un-esterified uronic acid moles in the **Table VI.1**.

Table VI.9: Systems model stoichiometry following iron concentration at 0.3 and 0.015 mg mL^{-1}

Compounds	Fe^{2+}	H_2O_2	UA	Cat	pCA	Cya
Conc. (mg/mL)	0.3	0.1	0.84	1	0.1	0.02
Mol (10^{-3})	5.4	2.9	4.8	3.4	0.6	0.1
Equivalent	1	0.54	0.9	0.6	0.1	0.02
Conc. (mg/mL)	0.015	0.1	0.84	1	0.1	0.02
Mol (10^{-3})	0.2	2.9	4.8	3.4	0.6	0.1
Equivalent	1	14.5	24	17	3	0.5

H_2O_2: hydrogen peroxide, UA: un-esterified galacturonic acid of pectin, Cat: (+)-catechin, pCA: p-Coumaric acid, Cya: Cyanidin

VI.4.2. Size-exclusion chromatography (SEC) analysis

Model solutions (1 mL) were filtered (PVDF 0.45 µm, 13 mm, AIT France) prior to SEC analysis. The autosampler (Waters 717 plus, WATERS, France) injected 50 µL of the model solutions on a Shodex 804 column (SB-804-HQ, 250 mm, OHpak, AIT, France) thermostated at 25 °C. Elution was with $NaNO_3$ 50 mM in H_2O at a flow-rate of 0.6 mL min^{-1} (Waters 590 HPLC pump). Detection was realized by a refractive index detector (Waters 2414 Refractive Index detector). Data were collected and processed by Chromeleon software® (version 6.8, Thermo Scientific, USA).

UV detection (SpectroMonitor® 3000, LDC Milton Roy, France) was at 280 nm and was coupled to the refractive index detection for the model solutions composed of Pec, Fe at 300 ppm or 15 ppm, H_2O_2 and Cat.

VI.4.3. Spectrophotometric analysis

The model solutions (500 µL) were transferred to Quartz cuvettes (10 x 4 mm, 114F-QS, Suprasil Hellma Analytics, France) and spectra registered between 200 nm to 800 nm with a UV-1600PC Scanning Spectrophotometer (VWR®, Belgium). Absorbances at 280, 420, 520 and 620 nm were extracted using the UV-Analyst software (version 5.44). The total polyphenol index (TPI) was taken as the absorbance at 280 nm and the color intensity (CI) was the sum of absorbance at 420, 520 and 620 nm as described Wirth, Morel-Salmi et al. (2010).

VI.4.4. Statistics

Each model solution was realised in triplicate and statistical evaluation of means was achieved by Student's t-test with Microsoft Excel® software (2016). Statistically significant difference was taken at p value ≤ 0.05.

VI.5. Results

Pectin molecular weight was taken as a mean to follow oxidative degradation of cell wall polysaccharides in the presence of solutes likely to be present in fleshy fruit during processing. The sequential addition of the solutes was aimed at identifying their respective contribution to the oxidative degradation or to its prevention. Pectin was not directly affected by the different components independently as shown in **Figure VI.1-A**. In fact, the Pec alone (black trace) or mixed with 300 ppm Fe (blue trace), H_2O_2 (orange trace), Ca (dark-blue trace), Cat (red trace), pCA (purple trace), or Cya (green trace), did not alter pectin elution time between 8.5 to 16 min. The variations of Pec elution were not significant and peaks eluting at 17.8 and 18.3 min corresponded to phenolic compounds and metallic ions, respectively (**Figure VI.1-A**). In contrast, when individual components were added to a solution of Pec and Fe at 300 ppm (blue trace, **Figure VI.1-B**), only H_2O_2 led to a significant increase in the elution time of Pec (orange trace; max 14 min), while Ca (dark-blue trace) or phenolic components (Cat, red trace; pCA, purple trace; Cya, green trace) had no effect (**Figure VI.1-B**). Thus, Pec degradation in the combined presence of Fe (300 ppm) and H_2O_2 was taken as a model solution to test for the impact of other solutes (Ca and phenolic compounds) in the oxidative degradations of pectin in fruit cell walls.

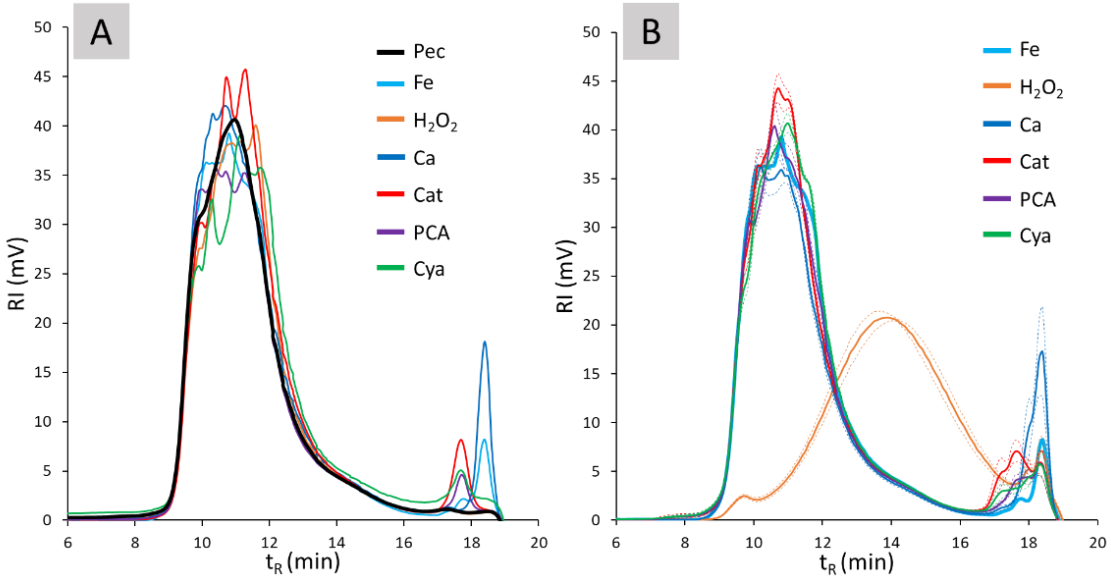

***Figure VI.40**: A/ Size-exclusion chromatograms of pectin (Pec) solutions mixed with iron at 300 µg g^{-1} (Fe), hydrogen peroxide (H_2O_2), calcium (Ca), (+)-catechin (Cat), p-coumaric acid (PCA) or cyanidin (Cya). B/ SEC Chromatograms of pectin-iron (Fe at 300 µg g^{-1}, blue trace "Fe") solutions mixed with the above components. t_R: retention time, RI: refractive index. Dotted lines: standard deviations (n = 3).*

Ca addition did not prevent Pec oxidative degradation (dark-blue trace, **Figure VI.2-A**). Instead, the addition of the three combined phenolic components to the oxidative model solution limited degradation of Pec but not totally (Mix PCs, green trace; elution between 8.5 and 16.5 min, max 11.8 min; **Figure VI.2-A**). Using a model solution with 15 ppm Fe instead of 300 ppm, which is more realistic

with regard to Fe content in fruit (Vidot, Rivard et al. 2019), pectin was still degraded in the presence of H_2O_2 (H_2O_2, orange trace; max 11.7 min; **Figure VI.2-B**), though to a lesser extent (H_2O_2, orange trace; max 14 min; **Figure VI.2-A**). The addition of the pool of phenolic compounds to this 15 ppm Fe oxidative model solution (Mix PCs, green trace; **Figure VI.2-B**) presented an opposite effect compared to that of the 300 ppm Fe solution with an increase pectin elution time (Mix PCs, green trace; max 12.8 min instead of 12 min with 300 ppm Fe; **Figure VI.2-A**). Thus at 15 ppm Fe, the pool of phenolic compounds promoted pectin degradation instead of limiting it.

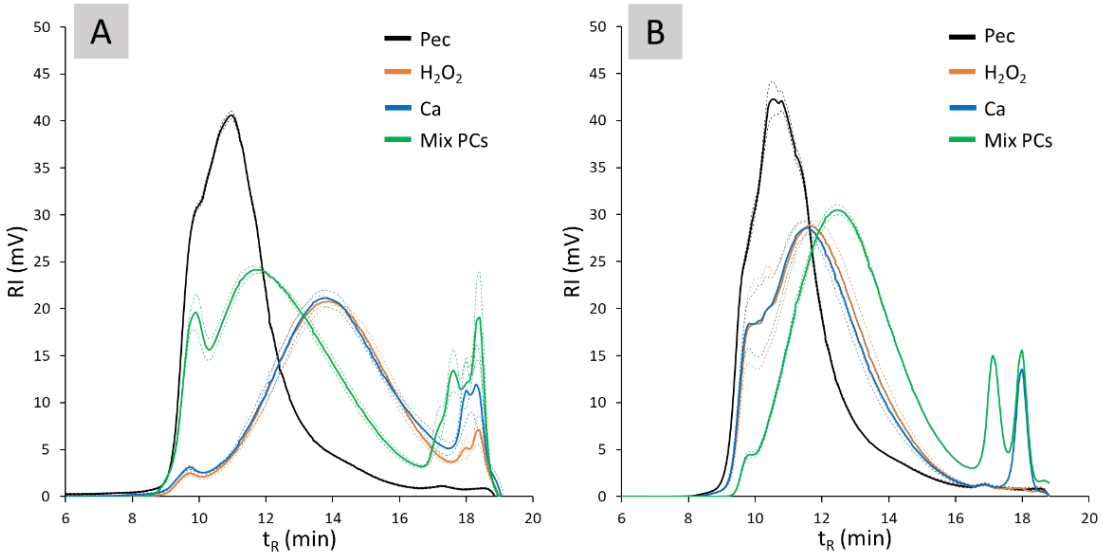

***Figure VI.41**: Size exclusion chromatograms of a solution of pectin (Pec), pectin mixed with iron and hydrogen peroxide (H_2O_2), pectin mixed with iron, hydrogen peroxide and calcium (Ca), and pectin mixed with iron, hydrogen peroxide, calcium and a pool of phenolic compounds (Mix PCs that are (+) catechin, p-coumaric acid and cyanidin). Iron concentration was fixed at 300 µg g^{-1} in A/ and at 15 µg g^{-1} in B/.RI: refractive index; t_R: retention time. Dotted lines: standard deviations (n = 3).*

To better appreciate the role of the different phenolic compounds on the degradation of pectin, each phenolic component was added individually to oxidative model solutions at Fe 300 ppm (**Figure VI.3-A**) and at 15 ppm (**Figure VI.3-B**). Compared to pectin in the oxidative model alone (Pec, orange trace, max: 14 min), pectin degradation was particularly limited in the presence of (+)-catechin in the oxidative solution containing 300 ppm Fe (Cat, red trace, max= 11.8 min), and to a lesser extent by p-coumaric acid (pCA, purple trace, max = 13.1 min) and cyanidin (Cya, green trace, max = 13.6 min), respectively (**Figure VI.3-A**). Contrariwise, the 15 ppm Fe oxidative solution showed that (+)-catechin promoted pectin degradation (Cat, red trace, max = 12.7 min) while p-coumaric acid partially limited it (pCA, purple trace, max = 11.4 min; (**Figure VI.3-B**)). Cyanidin had no significant impact (Cya, green trace, max =11.9 min) compared to the reference solution (H_2O_2, orange trace, max =11.7 min). Thus, (+)-catechin was the phenolic component that affected the most pectin degradation according to Fe content.

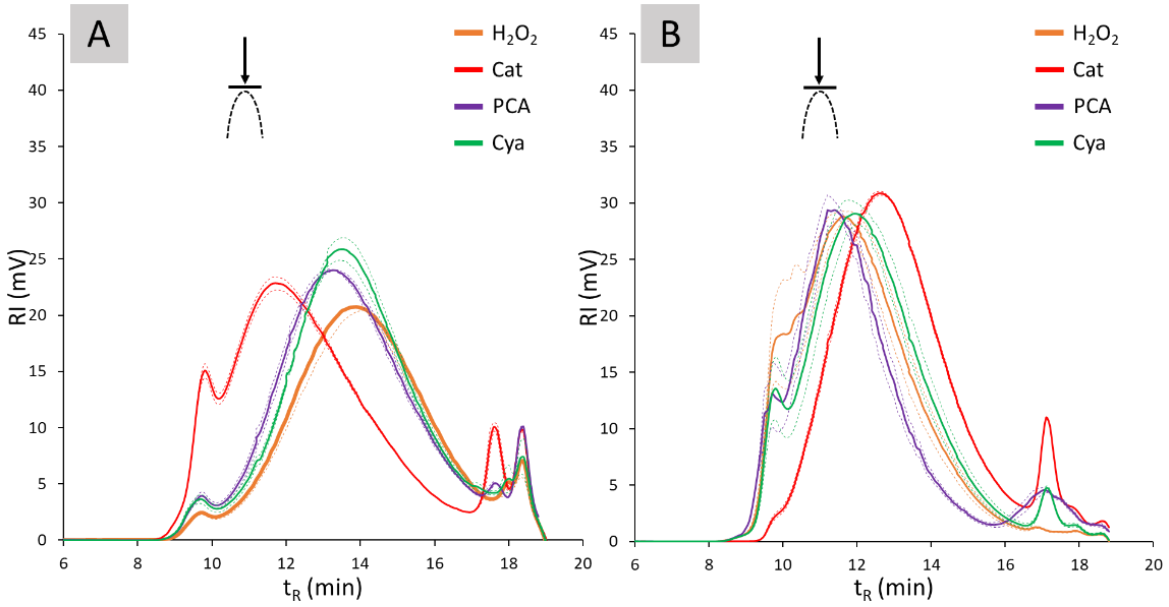

***Figure VI.42**: Size exclusion chromatograms of solutions mixture of pectin, iron and hydrogen peroxide (H_2O_2), with addition of (+) catechin (Cat), p-coumaric acid (PCA) or cyanidin (Cya). Iron concentration was fixed at 300 µg g^{-1} in A/ and at 15 µg g^{-1} in B/. RI: refractive index, t_R: retention time, Dotted lines: standard deviations (n = 3), arrow trace: maximum of initial pectin peak.*

Going further in the understanding of the interaction between (+)-catechin and pectin under oxidative conditions, the model solutions with the two Fe concentrations and containing only Cat as phenolic component was analysed by size exclusion chromatography coupled to RI and UV detectors (**Figure VI.4**). The UV trace was recorded at 280 nm, which is the maximum absorption wavelength of (+)-catechin. The results confirmed the higher pectin degradation in the presence of Cat at low Fe versus high Fe content (solid trace: max= 13.8 min for 15 ppm Fe and 12.2 min for 300 ppm Fe; **Figure VI.4-A and VI.4-B**). The UV chromatogram (dotted line) of the model solution containing 300 ppm Fe revealed three components eluting at 10.2, 17.8 and 18.3 min that absorbed at 280 nm. In contrast, with 15 ppm Fe, only a minor peak at 10.2 min and a major component eluting at 17.8 min and corresponding to Cat were observed (i.e. **Figure VI.1**). UV absorbing components eluting at 10.2 min was interpreted as a complex between (+)-catechin and pectin or as polymerized tannins while the peak at 18.3 min was interpreted as arising from the complex of Fe and Cat. Thus, oxidative conditions can induce pectin degradation as well as (+)-catechin structural modifications.

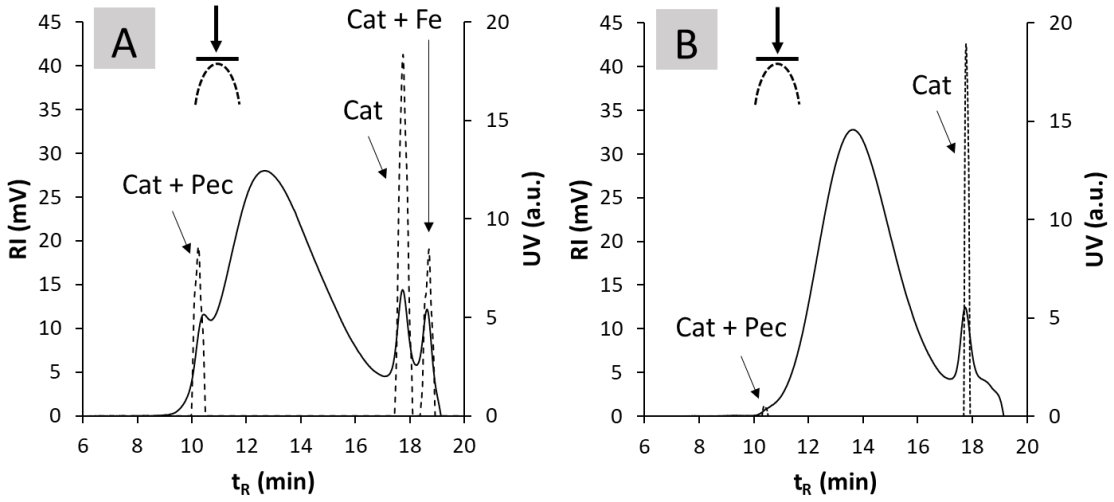

***Figure VI.43**: Size exclusion chromatograms (regular line) coupled to UV absorbance at 280 nm (dotted line) of a mixed pectin, iron, hydrogen peroxide and (+) catechin solution. Iron concentration was fixed at 300 µg g^{-1} in A/ and at 15 µg g^{-1} in B/. RI: refractive index, t_R: retention time, Arrow trace: maximum of initial pectin peak. Proposed UV peaks attribution: Cat = (+)-catechin; Pec: pectin; Fe: iron.*

The color intensity (CI) and the total polyphenol index (TPI) of model solutions were measured to assess structural change of (+)-catechin, p-coumaric acid and cyanidin alone or as pools in oxidative solutions containing Pec, H_2O_2 and 15 or 300 ppm Fe (**Figure VI.5**). The total polyphenol index (**Figure VI.5-A**) of oxidative model solutions free of phenolic compounds "1" was the lowest and close to that of solutions Cya and 1 + Cya. Solution "1" showed higher TPI at higher Fe content. The TPI was significantly higher for the other oxidative model solutions that ranked Mix PCs > Cat > pCA > Cya. No significant difference was found between the TPI of model solutions with 300 ppm and 15 ppm Fe, though a significant decrease was observed between the TPI of solutions of Mix PCs alone and in the oxidative model solution at 300 ppm Fe but not at 15 ppm Fe. In contrast, the TPI of the solution containing only Cat as phenolic component was significantly increased in the oxidative model condition, while that for solutions containing pCA or Cya did not vary significantly.

The color intensity (CI, **Figure VI.5-B**) of oxidative model solutions free of phenolic compounds "1" was the lowest and close to that of solutions containing Cat, pCA, and 1 + pCA, and particularly to 1 + Cya at 300 ppm Fe concentration. The CI was significantly higher for the model solution at 15 ppm Fe containing the mix of phenolic compounds (MixPCs) followed by that containing Cat, while those containing pCA and Cya were lower and not significantly different between them at either Fe content. However, the CI of the oxidative model solution at 300 ppm Fe containing the Mix PCs was significantly lower than that of Cat, but both were significantly higher than those containing pCA and Cya. CI was significantly higher for the model solutions containing the Mix PCs with 15 ppm Fe than 300 ppm, and was opposite to that of Cat. The CI of solution containing Cya was significantly higher than that under oxidative condition and the color intensity of the Mix PCs solution was equivalent to that of solution

of Cya. However, the CI of solution of Mix PCs was significantly lower than the solution of Mix PCs under oxidative model condition (1 + MixPCs ; **Figure VI.5-B**). A similar trend was observed between solution containing Cat or pCA alone and in oxidative condition with a more important difference for Cat. Thus, under oxidative condition, iron content together with (+)-catechin affected the most the TPI and CI of model solutions.

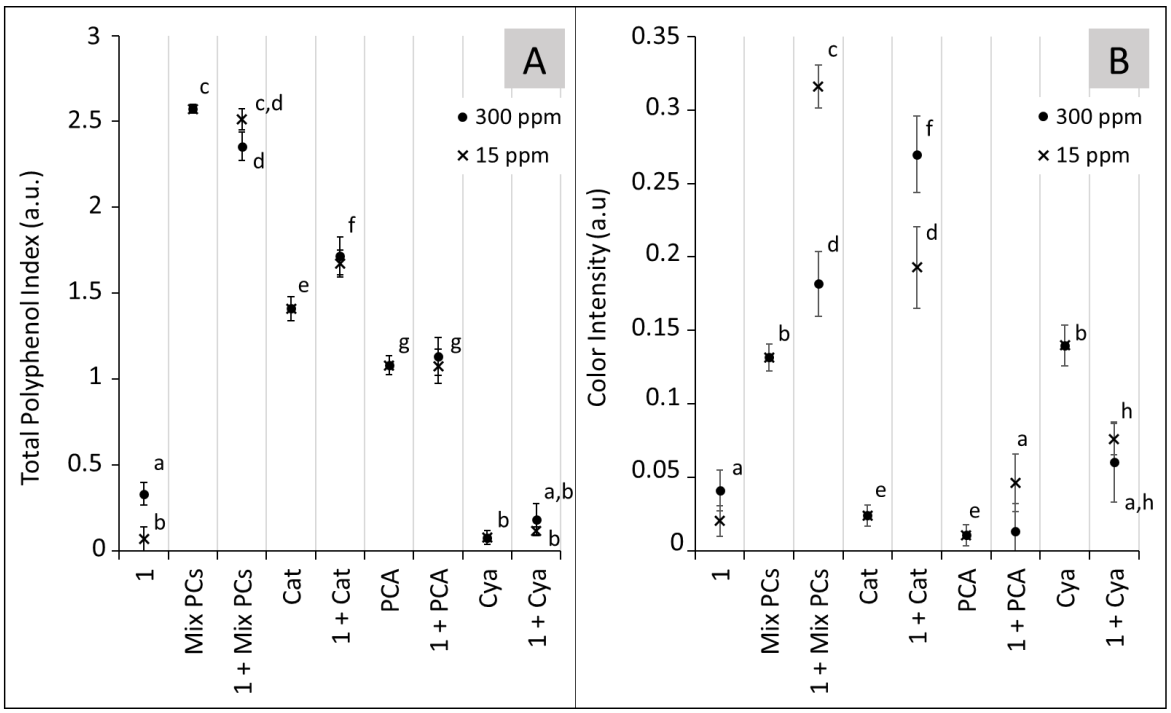

***Figure VI.44**: Effect of iron concentration on total polyphenol index (A) and color intensity (B) of different model solutions (± sd). 1: mixture of pectin, iron, hydrogen peroxide; Mix PCs: mixture of phenolic compounds ((+)-catechin, Cat; p-coumaric acid, PCA; and cyanidin, Cya). Iron concentration was fixed at 300 µg g^{-1} (dot) and at 15 µg g^{-1} (cross). Different letters are significantly different (n = 3; p value ≤ 0.05).*

VI.6. Discussion

The contribution of three families of fleshy fruit phenolic compounds in the presence of transition metal was assessed on the oxidative degradation of pectin taken as a key polysaccharide controlling texture during fruit consumption and processing. Pectin degradation has a major impact on fruit mechanical properties (Airianah, Vreeburg et al. 2016, Videcoq, Barbacci et al. 2017) and is sensitive to oxidative degradation (Fry 1998). The molecular weight of pectin was thus followed as a criterion of the impact of phenolic compounds to stop or promote Fe-H_2O_2-mediated oxidative cleavage. To that aim, model solutions were made from commercially available phenolic compounds and selected based on their presence in apple and grape. Though, some of them are minor components of their respective family in these fruit, such as cyanidin for anthocyanidins, they were included in the

model study as they might have specific reactivity toward oxidative conditions (Perron and Brumaghim 2009).

VI.6.1. Pectin susceptibility to Fe^{2+} / O_2

The oxidation degree of Fe in aqueous media is known to depend on temperature, pH and concentration (Beverskog and Puigdomenech 1996). In the model system condition with 300 ppm Fe, pH 3.0 and 25 °C, Fe was predominantly in the ferrous form Fe^{2+} as described by the Pourbaix diagram of iron. The redox potential of Fe^{3+}/Fe^{2+} (0.771 V) compared to that of O_2/H_2O_2 (0.695 V) means that the reaction promoted is the oxidation of Fe^{2+} by O_2 to produce H_2O_2 and Fe^{3+}, and this reaction is favoured by acidic media (Silberberg 2007). Then, since the ferrous cation is in excess in the model solution, oxygen from ambient air would be consumed to form hydrogen peroxide. The Fenton (**I**) and Haber-Weiss (II) reactions would then produce ROS which could degrade pectin. However, Fe^{2+} in water at pH 3.0 without addition of H_2O_2 was unable to produce ROS affecting pectin molecular weight (**Figure VI.1**)**.** Thus, the ROS production might have been inhibited by the interaction of ferrous iron with the pectin galacturonic acid sites (Mierczyńska, Cybulska et al. 2015, Maire du Poset, Lerbret et al. 2018). Even if the methyl esterification degree of the pectin used (DM = 72%) was high, the mole number of un-esterified sites remained enough close to that of Fe at 300 ppm (**Table VI.1**), and these sites would have complexed the major proportion of iron. However, with regard to the complexation of divalent cations with pectin galacturonic acid residues, one divalent cation interacts with two galacturonic acid sites (Celus, Kyomugasho et al. 2018). In that case, the pectin would complex only half of the iron content, but the remaining iron did not appear to be sufficient to affect pectin molecular weight under the experimental conditions used.

Fenton reaction: $Fe^{2+} + H_2O_2 \rightleftarrows Fe^{3+} + HO^- + HO^\bullet$ (**I**)

Haber-Weiss reaction: $(HO^\bullet + H_2O_2 \rightleftarrows H_2O + O_2^{\bullet-} + H^+)$

$O_2^{\bullet-} + H^+ + H_2O_2 \rightleftarrows O_2 + HO^\bullet + H_2O$ (**II**)

VI.6.2. Pectin degradation is boosted in oxidative conditions

Therefore, when the oxidative conditions are boosted by means of hydrogen peroxide or ascorbic acid, the ROS produced degrade the pectin as described by Fry (1998). These boosted conditions not only require an oxidant (H_2O_2) but also the transition metal (Fe) since no effect was observed when H_2O_2 was added alone with pectin (**Figure VI.1**).

Calcium was added to the model solutions as this metallic ion is present in fruit cell walls and is known to ionically cross-link pectin (Hocking, Tyerman et al. 2016). However, the calcium might not be

determinant in pectin resistance to oxidation as no effect was observed after its addition with or without oxidative condition. Furthermore, pectin gelation due to calcium cross-linking was not observed in our experiments.

VI.6.3. Phenolic compounds show anti- and pro-oxidant activities

Phenolic compounds are well known as antioxidant (Rice-Evans, Miller et al. 1996, Gülçin 2012). Indeed, the hydroxyl radicals produced through the Fenton and Haber-Weiss reactions (**I-II**), could be scavenged by the phenolic compounds present in the solution, but this was not the case, as pectin was still degraded. Moreover, considering the high kinetic constant (k_I= *53.0* (±0.7) L. mole^{-1} sec.$^{-1}$) of the Fenton reaction equilibrium (Barb, Baxendale et al. 1951), the excess of Fe^{2+} content that was twice than that of H_2O_2 (**Table VI.1**) may have induced the quasi total conversion of H_2O_2 into hydroxyl radicals. Then, the number of moles of hydroxyl radicals produced would be equivalent to that of H_2O_2, which is lower than that of total phenolic compounds (**Table VI.1**). Even in excess with regard to the hydroxyl radicals, the phenolic compounds did not inhibit fully pectin degradation. Thus, there was likely a competition between ROS scavenging by phenolics and ROS attacks of pectin. These may be closely related to the kinetic constant of such reactions.

The opposite behaviour observed with the pool of phenolic compounds in presence of the low amount of iron, may be related to a pro-oxidant activity as reported for tea polyphenols able to induce ROS production (Lambert and Elias 2010). In fact, in such condition, the mole content of Fe^{2+} was 14.5-fold less than that of H_2O_2 (**Table VI.1**). Thus, according to the above-mentioned Fenton reaction, the H_2O_2 would have produced hydroxyl radicals through the total conversion of Fe^{2+} to Fe^{3+}. The phenolic compounds present in solution would have scavenged a part of the hydroxyl radicals produced, and the large excess of phenolic compounds remaining (**Table VI.1**) may thus have reacted with Fe^{3+} to form phenoxyl radical and other ROS (Lambert and Elias 2010) that might enhanced degradation of pectin. Such results suppose that the Fenton reaction was predominant among the different possible interactions that may have occurred between the phenolic compounds, iron, pectin and hydrogen peroxide.

VI.6.4. Oxidative conditions affect structure of phenolic compounds

Both the TPI and CI of the model solutions depended on the phenolic components and their products of reaction resulting from the oxidative conditions (Wirth, Morel-Salmi et al. 2010), such as polymer of (+)-catechin or condensation products between the three phenolic components (Timberlake and Bridle 1976, Escribano-Bailón, Dangles et al. 1996, Schofield, Mbugua et al. 2001). The oxidative condition significantly decreased the TPI of the mix solution of phenolic components (Cat,

pCA and Cya) for Fe at 300 ppm, and decreased the CI as well. At high Fe concentration, the ROS level would be high and would induce structural modifications of phenolic compounds. Most polyphenol oxidation led to the browning of the solution and the decay of the colour intensity (Robards, Prenzler et al. 1999) that may explain the lower CI value at higher Fe content. ROS produced by high Fe content and H_2O_2 may have induced oxidative modifications of the chromophore structure of the phenolic compounds that resulted in the shift of the light absorption to different wavelengths and thus affecting the CI values. Such putative structural changes of phenolic compounds may have occurred without notable losses, as variation of TPI under oxidative condition was minimal.

VI.6.5. Individual contributions of Cat, pCA and Cya in model oxidative solutions

Among the three phenolic components used in the model solutions, pCA and Cya protected the least pectin from oxidative degradation by Fe and H_2O_2 compared to Cat. Such lack of protection could be due to their lower content in the model solutions (respectively, 10- and 50-times less) than Cat. Instead, if the concentrations of pCA or Cya were higher, their antioxidant effect on pectin might have been increased but the presence of Cat is known to exergue an antagonist effect on these phenolic compounds (Luís, Duarte et al. 2018). Cat is a major phenolic component in apple or grape vacuole and is the main monomer of condensed tannins (Gómez-Alonso, García-Romero et al. 2007, Kschonsek, Wolfram et al. 2018). To mimic apple or grape composition, Cat was the highest phenolic component of the model system and impacted the most pectin degradation, TPI and CI. In contrast, the Cya showed an inverse effect on CI, which was masked by the predominant effect of Cat. In addition, Cat affected the most the TPI values. This may be explained as Cat structure contains two aromatic cycles that absorbed at 280 nm (i.e. TPI value) while pCA and Cya contain only one. Thus, the more the Cat structure will be modified, the more the absorbance at 280 nm will be altered; whereas pCA and Cya structure modifications would have lesser impact on TPI.

VI.6.6. Cat interactions

The anti- and pro-oxidative behaviour of Cat according to Fe concentration remain unexplained. A hypothetic scheme of the different interactions between Cat, iron, pectin and H_2O_2 is proposed in **Figure VI.6.**

At 300 ppm Fe in the oxidative model solution, Cat would compete with pectin in the scavenging of ROS (Gülçin 2012). This would limit the polyuronan degradation and led to partial Cat structural modification (**Figure VI.4**), such as tannin a polymeric form of Cat (Schofield, Mbugua et al. 2001). In this condition, despite the probable major consumption of Fe^{2+} with H_2O_2 through Fenton reaction, the excess Fe^{2+} may have interacted with Cat to form iron-(+)-catechin complex (Perron and Brumaghim

2009). Part of these complexes (+)-catechin structures may have induced the observed co-elution with pectin (**Figure VI.4-A**) as individual entities or bonded to pectin (Renard, Watrelot et al. 2016).

However, when ROS production was from H_2O_2 and 15 ppm Fe, a pro-oxidative activity of Cat was found that may be related to Cat interaction with Fe^{3+} form. Moreover, phenoxyl radicals would induce cyclic reaction with the excess of non-radical forms of Cat which would then leave to an increase in radical production (Sakihama, Cohen et al. 2002) that have boosted the pectin degradation (**Figure VI.6**). Thus, the catechin complexes formation would be limited due to the lacking in Fe^{2+} form, which may explain the quasi-absence of Cat co-elution with pectin (**Figure 43B**).

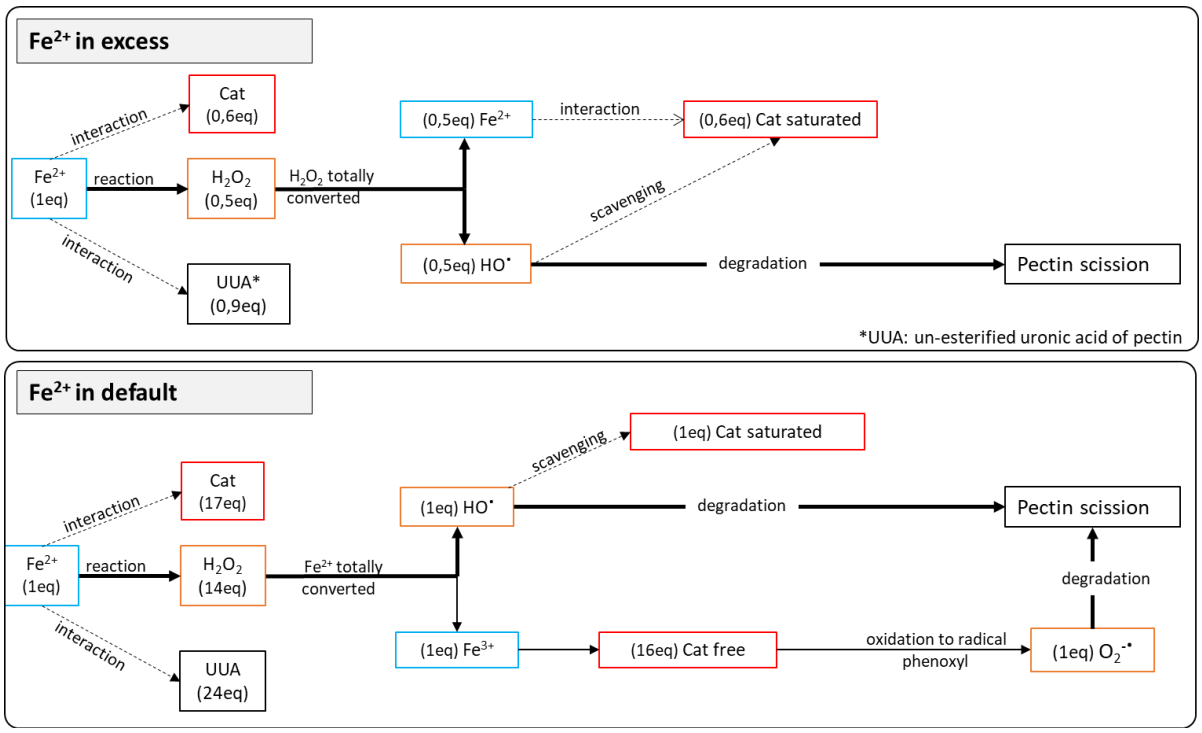

***Figure VI.45**: Hypothetic interactions between iron, Cat, pectin and H_2O_2 according to Fe content. Bold, plain and dashed arrows are higher to lower kinetic reactions, respectively.*

VI.7. Conclusion

The presence of iron alone in aerobic condition have no impact on pectin molecular weight but degrades pectin only when hydrogen peroxide is added with concomitant production of reactive oxygen species. Among the phenolic components studied, the low amounts of p-coumaric acid and cyanidin tested have an antioxidant potential limiting the oxidative degradation of pectin while (+)-catechin behaviour has both anti- and pro-oxidant activities depending on the iron and hydrogen peroxide contents. A scheme of the interactions occurring between these compounds leading to pectin degradation have been proposed as a starting point of further studies aiming at elucidating the mechanism under this behaviour and at exploring the contribution of other phenolic structures belonging to the hydroxycinnamic acids, anthocyanidins and flavanol classes.

In apple and grape, the content of these phenolic compounds together with iron and hydrogen peroxide content may be different according to cellular tissue compartment, fruit metabolism, development and environment. These model solutions studies gave clues on possible pectin degradation and phenolic compounds modification related to iron content and oxidation happening in fruit matrix that would impact organoleptic properties during consumption and processing.

VI.8. Acknowledgements

This work was supported in part by Cap Aliment Food for Tomorrow program funding by Région Pays de la Loire. The authors thank Ms M-J. Crepeau (INRA BIA) for technical assistance during HPLC-SEC measurements.

VI.9. References

Abramovič, H. (2015). Chapter 93 - Antioxidant Properties of Hydroxycinnamic Acid Derivatives: A Focus on Biochemistry, Physicochemical Parameters, Reactive Species, and Biomolecular Interactions. Coffee in Health and Disease Prevention. V. R. Preedy. San Diego, Academic Press**:** 843-852.

Airianah, O. B., R. A. M. Vreeburg and S. C. Fry (2016). "Pectic polysaccharides are attacked by hydroxyl radicals in ripening fruit: evidence from a fluorescent fingerprinting method." Annals of Botany **117**(3): 441-455.

Barb, W., J. Baxendale, P. George and K. Hargrave (1951). "Reactions of ferrous and ferric ions with hydrogen peroxide. Part I.—The ferrous ion reaction." Transactions of the Faraday Society **47**: 462-500.

Beverskog, B. and I. Puigdomenech (1996). "Revised pourbaix diagrams for iron at 25–300 °C." Corrosion Science **38**(12): 2121-2135.

Briat, J.-F. (2002). "Metal ion-activated oxidative stress and its control." Oxidative stress in plants. Taylor and Francis, New York: 171-189.

Broadley, M., P. Brown, I. Cakmak, Z. Rengel and F. Zhao (2012). Function of Nutrients: Micronutrients. Marschner's Mineral Nutrition of Higher Plants (Third Edition). P. Marschner. San Diego, Academic Press**:** 191-248.

Celus, M., C. Kyomugasho, A. M. Loey, T. Grauwet and M. E. Hendrickx (2018). "Influence of Pectin Structural Properties on Interactions with Divalent Cations and Its Associated Functionalities." Comprehensive Reviews in Food Science and Food Safety **17**(6): 1576-1594.

Chen, S. x. and P. Schopfer (1999). "Hydroxyl-radical production in physiological reactions." The FEBS Journal **260**(3): 726-735.

del Río, L. A. (2015). "ROS and RNS in plant physiology: an overview." Journal of Experimental Botany **66**(10): 2827-2837.

Di Lecce, G., S. Arranz, O. Jáuregui, A. Tresserra-Rimbau, P. Quifer-Rada and R. M. Lamuela-Raventós (2014). "Phenolic profiling of the skin, pulp and seeds of Albariño grapes using hybrid quadrupole time-of-flight and triple-quadrupole mass spectrometry." Food Chemistry **145**: 874-882.

Dumville, J. C. and S. C. Fry (2003). "Solubilisation of tomato fruit pectins by ascorbate: a possible non-enzymic mechanism of fruit softening." Planta **217**(6): 951-961.

Eghbaliferiz, S. and M. Iranshahi (2016). "Prooxidant activity of polyphenols, flavonoids, anthocyanins and carotenoids: updated review of mechanisms and catalyzing metals." Phytotherapy Research **30**(9): 1379-1391.

Escribano-Bailón, T., O. Dangles and R. Brouillard (1996). "Coupling reactions between flavylium ions and catechin." Phytochemistry **41**(6): 1583-1592.

Fry, S. (1998). "Oxidative scission of plant cell wall polysaccharides by ascorbate-induced hydroxyl radicals." Biochemical Journal **332**(Pt 2): 507.

Fry, S., J. Miller and J. Dumville (2001). Possible functions of copper ions in cell wall loosening. Plant Nutrition, Springer**:** 100-101.

Galanakis, C. M. (2018). Polyphenols: Properties, Recovery, and Applications, Woodhead Publishing.

Gómez-Alonso, S., E. García-Romero and I. Hermosín-Gutiérrez (2007). "HPLC analysis of diverse grape and wine phenolics using direct injection and multidetection by DAD and fluorescence." Journal of Food Composition and Analysis **20**(7): 618-626.

Gülçin, İ. (2012). "Antioxidant activity of food constituents: an overview." Archives of Toxicology **86**(3): 345-391.

Harnly, J. M., R. F. Doherty, G. R. Beecher, J. M. Holden, D. B. Haytowitz, S. Bhagwat and S. Gebhardt (2006). "Flavonoid Content of U.S. Fruits, Vegetables, and Nuts." Journal of Agricultural and Food Chemistry **54**(26): 9966-9977.

Hocking, B., S. D. Tyerman, R. A. Burton and M. Gilliham (2016). "Fruit calcium: transport and physiology." Frontiers in plant science **7**: 569.

Inze, D. and M. Van Montagu (2002). Oxidative Stress in Plants, London: CRC Press.

Kschonsek, J., T. Wolfram, A. Stöckl and V. Böhm (2018). "Polyphenolic Compounds Analysis of Old and New Apple Cultivars and Contribution of Polyphenolic Profile to the In Vitro Antioxidant Capacity." Antioxidants **7**(1): 20.

Lambert, J. D. and R. J. Elias (2010). "The antioxidant and pro-oxidant activities of green tea polyphenols: A role in cancer prevention." Archives of Biochemistry and Biophysics **501**(1): 65-72.

Le Bourvellec, C. and C. M. G. C. Renard (2012). "Interactions between Polyphenols and Macromolecules: Quantification Methods and Mechanisms." Critical Reviews in Food Science and Nutrition **52**(3): 213-248.

Lee, J., B. L. S. Chan and A. E. Mitchell (2017). "Identification/quantification of free and bound phenolic acids in peel and pulp of apples (Malus domestica) using high resolution mass spectrometry (HRMS)." Food Chemistry **215**: 301-310.

Luís, Â., A. P. Duarte, L. Pereira and F. Domingues (2018). "Interactions between the major bioactive polyphenols of berries: effects on antioxidant properties." European Food Research and Technology **244**(1): 175-185.

Macheix, J.-J., A. Fleuriet and J. Billot (2017). Fruit Phenolics, CRC press.

Maire du Poset, A., A. Lerbret, A. Zitolo, F. Cousin and A. Assifaoui (2018). "Design of polygalacturonate hydrogels using iron (II) as cross-linkers: A promising route to protect bioavailable iron against oxidation." Carbohydrate polymers **188**: 276-283.

Mattivi, F., R. Guzzon, U. Vrhovsek, M. Stefanini and R. Velasco (2006). "Metabolite profiling of grape: flavonols and anthocyanins." Journal of agricultural and food chemistry **54**(20): 7692-7702.

Mierczyńska, J., J. Cybulska, B. Sołowiej and A. Zdunek (2015). "Effect of Ca2+, Fe2+ and Mg2+ on rheological properties of new food matrix made of modified cell wall polysaccharides from apple." Carbohydrate polymers **133**: 547-555.

Özcan, M. M., M. Harmankaya and S. Gezgin (2012). "Mineral and heavy metal contents of the outer and inner tissues of commonly used fruits." Environmental monitoring and assessment **184**(1): 313-320.

Parr, A. J., A. Ng and K. W. Waldron (1997). "Ester-linked phenolic components of carrot cell walls." Journal of agricultural and food chemistry **45**(7): 2468-2471.

Perron, N. R. and J. L. Brumaghim (2009). "A review of the antioxidant mechanisms of polyphenol compounds related to iron binding." Cell biochemistry and biophysics **53**(2): 75-100.

Renard, C. M., A. Baron, S. Guyot and J.-F. Drilleau (2001). "Interactions between apple cell walls and native apple polyphenols: quantification and some consequences." International Journal of Biological Macromolecules **29**(2): 115-125.

Renard, C. M. G. C., A. A. Watrelot and C. Le Bourvellec (2016). "Interactions between polyphenols and polysaccharides: mechanisms and consequences in food processing and digestion." Trends in Food Science & Technology.

Rice-Evans, C. A., N. J. Miller and G. Paganga (1996). "Structure-antioxidant activity relationships of flavonoids and phenolic acids." Free Radical Biology and Medicine **20**(7): 933-956.

Robards, K., P. D. Prenzler, G. Tucker, P. Swatsitang and W. Glover (1999). "Phenolic compounds and their role in oxidative processes in fruits." Food Chemistry **66**(4): 401-436.

Sakihama, Y., M. F. Cohen, S. C. Grace and H. Yamasaki (2002). "Plant phenolic antioxidant and prooxidant activities: phenolics-induced oxidative damage mediated by metals in plants." Toxicology **177**(1): 67-80.

Saulnier, L. and J. F. Thibault (1999). "Ferulic acid and diferulic acids as components of sugar-beet pectins and maize bran heteroxylans." Journal of the Science of Food and Agriculture **79**(3): 396-402.

Schofield, P., D. M. Mbugua and A. N. Pell (2001). "Analysis of condensed tannins: a review." Animal Feed Science and Technology **91**(1): 21-40.

Sekher Pannala, A., T. S. Chan, P. J. O'Brien and C. A. Rice-Evans (2001). "Flavonoid B-Ring Chemistry and Antioxidant Activity: Fast Reaction Kinetics." Biochemical and Biophysical Research Communications **282**(5): 1161-1168.

Silberberg, M. S. (2007). Principles of general chemistry, McGraw-Hill Higher Education New York.

Sinela, A. M., C. Mertz, N. Achir, N. Rawat, K. Vidot, H. Fulcrand and M. Dornier (2017). "Exploration of reaction mechanisms of anthocyanin degradation in a roselle extract through kinetic studies on formulated model media." Food Chemistry **235**: 67-75.

Thibault, J.-F. and M.-C. Ralet (2008). "32 Pectins, their Origin, Structure and Functions." Advanced dietary fibre technology: 369-378.

Timberlake, C. and P. Bridle (1976). "Interactions between anthocyanins, phenolic compounds, and acetaldehyde and their significance in red wines." American Journal of Enology and Viticulture **27**(3): 97-105.

USDA (2018). National Nutrient Database for Standard Reference.

Videcoq, P., A. Barbacci, C. Assor, V. Magnenet, O. Arnould, S. Le Gall and M. Lahaye (2017). "Examining the contribution of cell wall polysaccharides to the mechanical properties of apple parenchyma tissue using exogenous enzymes." Journal of experimental botany **68**(18): 5137-5146.

Vidot, K., M.-F. Devaux, C. Alvarado, S. Guyot, F. Jamme, C. Gaillard, R. Siret and M. Lahaye (2019). "Phenolic distribution in apple epidermal and outer cortex tissue by multispectral deep-UV autofluorescence cryo-imaging." Plant Science.

Vidot, K., C. Rivard, G. Van Vooren, R. Siret and M. Lahaye (2019). "Metallic ions distribution in texture and phenolic content contrasted cider apples " Food Chemistry.

Wirth, J., C. Morel-Salmi, J. M. Souquet, J. B. Dieval, O. Aagaard, S. Vidal, H. Fulcrand and V. Cheynier (2010). "The impact of oxygen exposure before and after bottling on the polyphenolic composition of red wines." Food Chemistry **123**(1): 107-116.

Chapitre VII

VII. Discussion générale

Sommaire

VII.1.Sujet de recherche

Cette thèse s'est concentrée sur les fruits charnus et en particulier deux variétés de pommes à cidre, Douce Moen et Guillevic récoltées en 2017 et 2018 en Bretagne. Les expérimentations ont été étendues dans la mesure du possible aux baies de raisins de cuve, notamment les cépages Cabernet franc, Cabernet sauvignon et Grolleau. Ces variétés de fruits ont été sélectionnées pour leur importance économique dans la région Nord-Ouest de la France. Ainsi, le contrôle de leur qualité est un paramètre important qui conditionne l'organisation de la filière, du producteur au consommateur en passant par le transformateur. Les critères de qualité des fruits que sont la couleur, la saveur et la texture, sont souvent dépendants ou associés aux mécanismes faisant intervenir des composants intrinsèques (et leurs interactions potentielles) des fruits dont les ions métalliques, les composés phénoliques et les parois cellulaires. Cependant, dans ces fruits, les interactions entre les ions métalliques avec les pectines des parois cellulaires et les composés phénoliques ont été très peu décrites. Dans ce contexte, les travaux de la thèse se sont donc concentrés sur la distribution de ces composés dans les fruits *in-vivo* afin d'établir s'il existait une colocalisation dans les tissus cellulaires et évaluer la conséquence de ces localisations sur les caractéristiques organoleptiques des fruits et de leurs produits issus de la transformation technologique. Au travers de l'ensemble de ces travaux et des résultats associés, ce travail de thèse a ainsi pour but global de contribuer à l'ébauche d'un modèle conceptuel combinant le rôle des ions, la dynamique de l'eau et des polysaccharides pariétaux sur les propriétés mécaniques des tissus et la disponibilité des polyphénols lors de la consommation et transformation des fruits.

VII.2.Développement des méthodes « cryo »

Les ions métalliques au même titre que les composés phénoliques, peuvent être présents en solution dans le tissu cellulaire des fruits charnus (Macheix, Fleuriet et al. 2017). Cette propriété rend leur localisation dans le tissu natif difficile à cause de la forte mobilité que cela induit. Ainsi, des premiers travaux se sont focalisés sur la mise en place de méthodes « cryo » pour la préparation d'échantillons et ce, pour limiter la redistribution de ces composés hautement diffusibles (Moore, Lombi et al. 2012). La préparation des échantillons par le processus d'infusion, de congélation rapide « hand-freezing », de cryo-section et d'observation à froid via le système développé permettant de maintenir l'échantillon à l'état congelé, s'est avérée efficace et plus accessible que les différentes méthodes cryo existantes. Ces développements sont décrits et discutés dans le **Chapitre II**, et ont particulièrement été adaptés à l'observation des ions métalliques et des composés phénoliques par microscopie confocale à l'aide de marqueurs fluorescents. De même, le système d'observation à froid des échantillons a pu être adapté au microscope en épi-fluorescence de la ligne DISCO du synchrotron SOLEIL (Gif-sur-Yvette, Saint-Aubin, France), pour localiser les composés phénoliques en fonction de

leur autofluorescence après excitation en UV profond (**Chapitre III**). Cependant, les essais sur le tissu de raisin ont été particulièrement laborieux, nécessitant une certaine précaution et dextérité dans les processus de préparation et d'observation. En effet, ces tissus sont plus fragiles et sensibles à la décongélation que les tissus de pomme. En particulier, la température d'observation à -30°C qu'offre le montage développé n'est pas suffisamment froide pour ce type de tissu. Le maintien de l'état congelé des coupes de raisin nécessiterait donc des températures d'observation plus basses. Cette différence de maintien entre les fruits pourrait être liée à une différence au niveau des propriétés mécaniques des parois cellulaires, certainement plus fragiles chez le raisin, mais également à une richesse plus élevée en soluté du tissu de raisin par rapport au tissu de pomme (Finley, Hurst et al. 2018). Ces contraintes techniques liées à la nature et la composition du raisin expliquent que la majeure partie des développements et des études des distributions décrites dans les **Chapitres III et V** se sont concentrés par la suite sur les pommes. Néanmoins, de futurs développements seraient nécessaires pour adapter la méthodologie aux fruits plus sensibles tels que le raisin, notamment avec des méthodes de congélation plus douces comme la congélation sous micro-ondes (Xanthakis, Le-Bail et al. 2014). En effet, les résultats du **Chapitre II** ont montré que les températures et vitesses de congélation sont des paramètres clés dans la préservation de l'intégrité des tissus hydratés et nécessitent de nouvelles études notamment pour mieux contrôler les réarrangements structuraux associés aux effets osmotiques pendant la congélation. Par ailleurs, l'extension de cette approche ouvre de nouvelles opportunités pour l'étude des composés diffusibles des végétaux.

VII.3.Distribution des composés dans les fruits

Les méthodes « cryo » développées ont été appliquées en utilisant des techniques de fluorescence de marqueurs spécifiques et d'autofluorescence en UV (375 et 275 nm) et de fluorescence X via des rayonnements synchrotrons. Ces dernières ont permis la localisation des ions métalliques et des composés phénoliques dans les tissus de fruits à l'état congelé (**Chapitres II, III et V).** Les résultats de distributions des composés phénoliques et des ions métalliques ont montré qu'ils ne semblent pas être affectés par le vieillissement des fruits (**Chapitres III-V**), bien que ce résultat puisse présenter un biais du fait de la zone réduite du tissu analysé et du nombre réduit d'échantillons analysés. La peau concentre majoritairement les ions métalliques (Özcan, Harmankaya et al. 2012) et les composés phénoliques (Treutter 2001) d'où l'étude cartographique sur cette zone du fruit. Les cartographies ont mis en évidence la présence de ces composés dans toutes les régions du tissu et une représentation schématique des zones de concentrations observées peut être proposée comme dans la **Figure VII.1**.

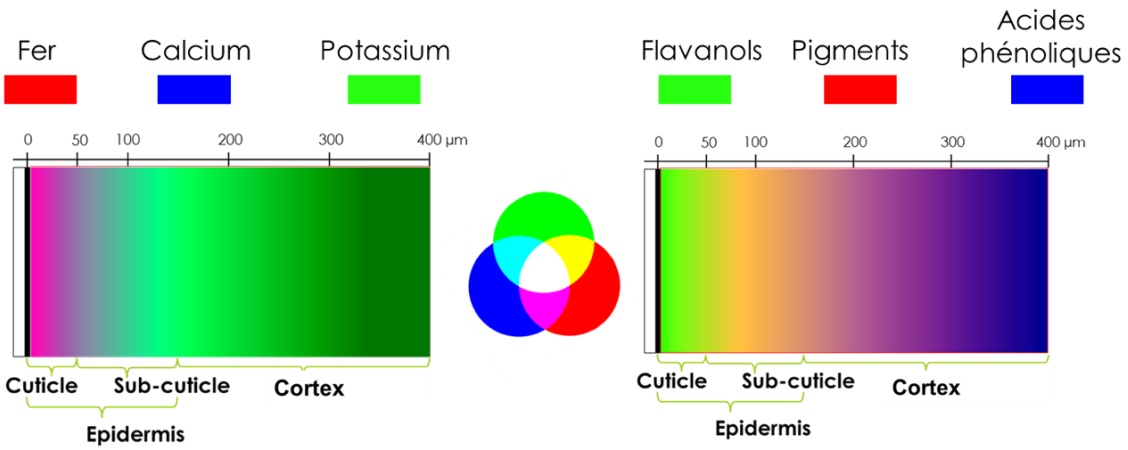

***Figure VII.46** : Représentation schématique des distributions des ions métalliques (à gauche) et des composés phénoliques (à droite) dans les premiers 400 µm du tissu de pomme.*

D'une façon générale, le calcium a surtout été localisé dans l'épiderme concentrant les couches sous cuticules (**Chapitre V**), et s'accumulerait dans des zones intracellulaires sous forme de spots alors qu'il serait présent dans les parois cellulaires de façon plus diffuse (**Chapitre II**). Le potassium, quant à lui, a été retrouvé de façon homogène au niveau cellulaire (**Chapitre II**) et tissulaire présentant toutefois une concentration moins importante dans la cuticule (**Chapitre V**). Ces localisations *in-situ* sont en accord avec leur présence rapportée par la littérature dans les compartiments intracellulaires et pariétaux, principalement décrite par des méthodes d'analyse *in-vitro* (Bush 1995, Rogiers, Coetzee et al. 2017). En ce qui concerne les ions métalliques de transition, leur cartographie a surtout montré une forte concentration dans la couche cuticulaire, en particulier pour le fer (**Chapitre V**). Leur localisation à l'échelle subcellulaire comme pour le calcium et le potassium n'a pas pu être établie notamment à cause de leurs faibles teneurs dans les fruits, le manque de marqueurs fluorescents spécifiques de ces métaux de transition, mais également du fait des cristaux de glace provenant principalement de la vacuole repoussant tous les composés cellulaires vers la paroi. Des développements sont nécessaires pour disposer de marqueurs fluorescents plus spécifiques des ions et ainsi accéder à ce niveau d'information.

En ce qui concerne les composés phénoliques, leurs distributions au niveau tissulaire ont mis en évidence la localisation des composés de la famille des acides phénoliques dans les couches cellulaires du cortex interne (**Chapitre III**). La distribution de ces acides phénoliques semble varier en fonction de la variété et s'étend légèrement dans les couches sous cuticules chez Guillevic (**Chapitre III**). Une identification de certains de ces composés, en particulier les acides hydroxycinnamiques, a révélé leur présence au niveau des parois cellulaires, bien que cette identification pose question notamment sur l'origine des acides hydroxycinnamiques dosés (**Chapitre IV**). Parmi la famille des

flavonoïdes, les flavanols sont prépondérants dans les premières couches de cellules cuticulaires, alors que les pigments phénoliques sont surtout localisés dans les couches sous cuticules de l'épiderme **(Chapitre III)**. Au niveau subcellulaire, ces flavonoïdes ont principalement été observés au niveau intracellulaire proche des parois cellulaires (**Chapitre II**), ce qui supporterait l'hypothèse de la présence de sites de synthèse de ces composés au niveau du tonoplaste vacuolaire (Brillouet, Romieu et al. 2014) repoussés vers les parois cellulaires par la turgescence.

La combinaison des techniques utilisées offre une méthodologie intéressante pour la cartographie des ions métalliques et des composés phénoliques dans les pommes à l'échelle tissulaire et cellulaire. Ces différentes distributions des ions métalliques et des composés phénoliques sur du tissu congelé se rapprochent des localisations réelles de ces composants dans les fruits, bien que la préparation par congélation induise la formation de cristaux de glace dans le tissu qui déplaceraient les composants intracellulaires vers les parois cellulaires. De plus, l'utilisation de marqueurs fluorescents modifierait la composition chimique des cellules et par conséquent, les distributions initiales des composés. Pour pallier ces problèmes, les méthodes de préparation d'échantillons doivent encore être améliorées, de même que la résolution spatiale des méthodes d'analyse des ions métalliques, ou encore la spécificité des méthodes de caractérisation *in-situ* de la nature des composés phénoliques. Une autre difficulté rencontrée dans les différentes méthodes de cartographie mises en place était le moyen de quantification des composés observés lié au manque de matrices standard présentant les mêmes propriétés physiques (distributions homogènes des composés, hétérogénéités des structures au sein de la coupe, épaisseurs) que les cryo-sections de fruits.

Quoi qu'il en soit, les distributions des ions métalliques et des composés phénoliques obtenues aux échelles tissulaire, cellulaire et subcellulaire, permettent d'entrevoir leurs contributions sur les caractéristiques organoleptiques des fruits frais et transformés.

VII.4.Contribution des composés étudiés sur les propriétés organoleptiques des fruits intacts

Les quantités et les distributions des ions métalliques et des composés phénoliques dépendent de la variété, de l'année de récolte et des régions tissulaires du fruit, ce qui semble refléter les variations dues à la génétique, au développement et aux facteurs environnementaux (**Chapitres III et V**).

VII.4.1. Le potassium un élément clé

Parmi les différents composants étudiés, le potassium présente une distribution particulière, peu affectée par les variations éco-physiologiques des fruits (**Chapitre V**) qui peut être associée au rôle de cet élément dans des mécanismes de régulation osmotique pour préserver le bon fonctionnement cellulaire sous différentes conditions environnementales. En effet, les gradients de métabolites, tels que les acides organiques ou les sucres, de même que les autres ions métalliques seraient en partie régulés par le flux de potassium afin de maintenir des pressions osmotiques cellulaires stables (Hulme 1971). Ainsi, la présence limitée de potassium dans la région cuticulaire (**Chapitre V**) serait due à la forte concentration des métabolites dans cette région du tissu. Dans cette région, ces métabolites de types cationiques pourraient interagir avec les parois cellulaires et moduler ainsi leurs propriétés mécaniques. En effet, les sites de complexations potentiels et disponibles des pectines pariétales ne seraient pas totalement occupés par les cations métalliques de par leur plus faible proportion dans l'ensemble du fruit (**Chapitre V**). D'autant plus qu'une partie de ces ions, outre leurs formes complexées aux pectines pariétales, se retrouvent aussi dans le contenu intracellulaire (Barker and Pilbeam 2015). Le potassium modulerait ainsi les interactions entre les différents constituants dans les tissus de fruits frais.

VII.4.2. Régulation des stress biotiques et abiotiques

Les couches cuticulaires et sous cuticulaires des fruits sont enrichies en composés phénoliques (**Chapitre III**) et en métaux de transition (**Chapitre V**). Etant donné que les fruits sont particulièrement exposés à une large gamme de stress biotiques et abiotiques, cette concentration de composés phénoliques pourrait être associée aux métaux de transition dans les mécanismes oxydatifs de défense, notamment pour lutter contre les agents pathogènes ou les rayonnements UV néfastes pour les tissus (Inze and Van Montagu 2002, Edreva 2005). En effet, ces couches externes sont connues pour avoir une fonction de barrière afin de limiter l'intrusion des agents pathogènes mais aussi pour réguler les échanges d'eau et de gaz avec l'environnement (Khanal and Knoche 2017). Cette barrière nécessite donc des propriétés mécaniques parmi lesquelles les complexes pectines – calcium peuvent contribuer localement, d'où le recrutement important de calcium dans les couches cellulaires et sous cuticulaires (**Chapitre V**).

VII.4.3. Rôles sur la fermeté des fruits

La fermeté des pommes est connue pour être dépendante de la composition polysaccharidique et de l'épaisseur des parois cellulaires, de la taille et distribution des cellules et espaces intercellulaires associées à la compartimentation apoplastique et cellulaire de l'eau (Lahaye, Bouin, Barbacci, Le Gall,

& Foucat, 2018; Videcoq, et al., 2017; Winisdorffer, et al., 2015). Cependant, outre ces paramètres intrinsèques, les composants étudiés pourraient aussi influencer les propriétés mécaniques du fruit. Par exemple, le potassium a été retrouvé en plus grande quantité chez Guillevic, la variété la plus ferme (**Chapitre V**). En tant que soluté majeur dans la régulation de la pression de turgescence, cet élément pourrait être un déterminant important de la fermeté des fruits en fonction de sa distribution cellulaire et apoplastique. En effet, les pectines dans les parois cellulaires de Guillevic sont plus riches en sites potentiels de complexation, le potassium pourrait avoir un rôle de contre-ions (Sentenac and Grignon 1981) et contribuer à la création de pression osmotique et au gonflement des parois cellulaires, qui associés à la turgescence expliqueraient la plus grande fermeté du fruit. De même, parmi les cations métalliques, le calcium pourrait contribuer aux propriétés mécaniques des parois cellulaires et des tissus en réticulant les pectines via leurs sites de complexation potentiels (Voragen, Coenen et al. 2009). Cependant, les résultats ont montré une corrélation inverse entre les teneurs globales de calcium, de sites de complexation et de viscoélasticité du cortex (**Chapitre V**). La quantité de cet élément ne semble donc pas être déterminante sur la texture du fruit globale. Toutefois, il n'est pas impossible que le calcium affecte les propriétés mécaniques des couches tissulaires de façon plus localisée, notamment au niveau de la couche sous cuticule qui concentre le calcium (**Chapitre V**). De même, le magnésium est aussi présent en grande quantité devant le calcium et il n'est pas impossible qu'en solution concentrée en pectine telle que dans les parois cellulaires des couches sous cuticules, le magnésium fortement présent dans cette région (**Chapitre V**) participerait à la réticulation des pectines. Ainsi, les proportions de potassium, calcium et magnésium dans la pomme associée aux caractéristiques des pectines pariétales pourraient avoir un impact sur les propriétés mécaniques et la fermeté des tissus.

Par ailleurs, la présence importante des composés phénoliques dans les couches externes du tissu (**Chapitre III**) pourrait être associée à une résistance mécanique plus ferme de la peau par rapport à la chair des fruits. La résistance mécanique des tissus est souvent liée aux parois cellulaires (Held, Jiang et al. 2015). Cependant, la présence de ces composés phénoliques dans les parois cellulaires reste assez floue. En effet, même si des traces d'acides hydroxycinnamiques ont été retrouvées dans les parois cellulaires, leur origine reste à établir (**Chapitre IV**). De plus, leurs concentrations à l'état de traces limiteraient leurs contributions dans les phénomènes de réticulation des polysaccharides pariétaux et par conséquent sur les propriétés mécaniques des tissus des fruits. Par ailleurs, dans les tissus in-vivo, la présence hypothétique des composés phénoliques dans les solutions apoplastiques (Renard, Watrelot et al. 2015) pourrait réguler l'activité des ROS et ainsi limiter les dommages que ces ROS pourraient causer au niveau de la paroi cellulaire, notamment sur la dégradation des pectines.

VII.4.4. Influence sur les couleurs et la saveur

La distribution et les proportions relatives des anthocyanidines, des flavanols et des acides phénoliques dans les couches cellulaires des fruits pourraient être liées à la distinction des couleurs et saveurs entre les variétés de fruits. En effet, cela est mis en évidence par le rapprochement des couleurs et saveurs des variétés Douce Moen et Guillevic avec la distribution de ces composés phénoliques dans les tissus **(Chapitre III)**. De même, ces propriétés organoleptiques peuvent dépendre de la distribution des métaux de transition du fait qu'ils soient potentiellement complexés aux pigments (Perron and Brumaghim 2009) tels que des anthocyanidines présentes dans les couches cellulaires sous cuticule (**Chapitres III et IV**). Ainsi, la plus faible proportion de fer et de manganèse retrouvée dans l'épiderme de Guillevic comparé à Douce Moen pourrait être liée à la différence de couleur de peau de ces variétés de pommes (**Chapitre V**). Par ailleurs, la plus grande quantité de fer et de cuivre retrouvée dans le cortex de Guillevic par rapport à Douce Moen (**Chapitre V**) indiquerait un rôle de ces métaux de transition dans les mécanismes de polymérisation des composés phénoliques étant donné que les degrés de polymérisation des tannins chez Guillevic sont plus élevés que chez Douce Moen (Sanoner, Guyot et al. 1999). Sachant que les tannins sont responsables de l'astringence des fruits (Ashok and Upadhyaya 2012), la distribution de ces métaux dans le tissu pourrait impacter indirectement leurs saveurs.

Ainsi, les différentes distributions des ions métalliques et des composés phénoliques dans le tissu des fruits restent une question ouverte d'un point de vue du métabolisme, du développement, de la physiologie et des caractéristiques organoleptiques des fruits.

VII.5.Impact sur les fruits déstructurés

Le rapprochement des distributions observées entre les familles de composés a permis d'établir lesquelles seraient susceptibles d'interagir entre eux et avec la paroi cellulaire, notamment lors de la dégradation des tissus. Toutefois, les composés étudiés présentent des gradients de distribution avec des zones de concentration spécifiques dans le tissu. Malgré leurs faibles concentrations dans certaines zones du tissu, ces éléments sont quand même présents et peuvent participer aux différentes interactions potentielles.

Par exemple, une large gamme d'interactions peut avoir lieu entre les acides hydroxycinnamiques intracellulaires et les parois cellulaires telles que discutée dans le **Chapitre IV**. Les composés phénoliques, notamment les structures tanniques, ont une forte capacité d'adsorption sur les parois

cellulaires (Le Bourvellec and Renard 2012). Cela a donc un effet limitant sur l'accessibilité des composés phénoliques dans les produits transformés.

Par ailleurs, les ions métalliques en particulier les métaux de transition pourraient interagir avec les polysaccharides pariétaux ou les composés phénoliques et induire des modifications de leurs structures. En effet, ils pourraient être à l'origine ou participer à la formation de ROS intervenant dans la déconstruction des parois cellulaires (Airianah, Vreeburg et al. 2016) ou encore la condensation/polymérisation des composés phénoliques entre eux (Guyot, Bernillon et al. 2008). Ce type de modifications structurales impacterait la couleur et la saveur du fruit déstructuré associé aux composés phénoliques, mais aussi sa texture liée à l'intégrité des parois cellulaires.

Cependant, comme schématisé dans la **Figure VII.1**, la proximité des différents composés en fonction des zones tissulaires induirait des interactions privilégiées lors de la déstructuration des tissus, par exemple entre le fer et les flavanols majoritairement retrouvés dans l'épiderme. Ces proximités entre composés ont stimulé le développement d'un système modèle in vitro pour étudier leurs interactions potentielles avec les polysaccharides pariétaux pouvant avoir des conséquences sur les propriétés organoleptiques des fruits transformés (**Chapitre VI**). Cette étude s'est notamment concentrée sur l'impact des composés phénoliques vis-à-vis de la dégradation oxydative de la pectine induite par le fer en milieu oxydant. L'inactivité du fer seul reflète la nécessité d'agent oxydant en particulier de peroxyde d'hydrogène pour initier la formation de ROS (via la réaction de Fenton (Halliwell and Gutteridge 2015)) et induire une dégradation de la pectine. Dans la matrice déstructurée de fruit, ce type d'agent oxydant serait initialement présent car ils sont issus des produits des réactions enzymatiques ayant lieu dans les compartiments cellulaires et intercellulaires (del Río 2015). De même les activités anti- et pro-oxydante retrouvées pour les composés phénoliques, en particulier de la (+)-catéchine, semblent être dépendantes des proportions de fer et de peroxyde d'hydrogène dans la matrice. De plus dans ce système, la (+)-catéchine aurait tendance à complexer le fer et à s'adsorber sur les pectines (**Chapitre VI**). Ces interactions pourraient donc avoir un impact sur les propriétés mécaniques du fruit déstructuré mais aussi sur les couleurs et saveurs liées à la modification des structures phénoliques et à la perte de leurs disponibilités dans ces matrices.

Néanmoins, comme décrites par les études de distributions (**Chapitres II-III et V**) dans les pommes et les raisins, les teneurs des composés phénoliques, du fer et certainement d'agent oxydant peuvent être différentes selon les compartiments tissulaires, le métabolisme et le stade de développement du fruit, et les facteurs environnementaux. Ainsi, en adaptant le système modèle construit en fonction de la variabilité spatiale et des concentrations des composés des fruits (agents oxydants, enzymes, métaux de transition, caractéristiques des polysaccharides pariétaux, composés phénoliques…), il

serait possible d'améliorer la compréhension des mécanismes responsables des propriétés organoleptiques des matrices de fruits lors de leur consommation ou de leur transformation. Un premier modèle conceptuel peut déjà être proposé à partir des observations de la thèse (**Figure VII.2**).

A/ Fruit intact

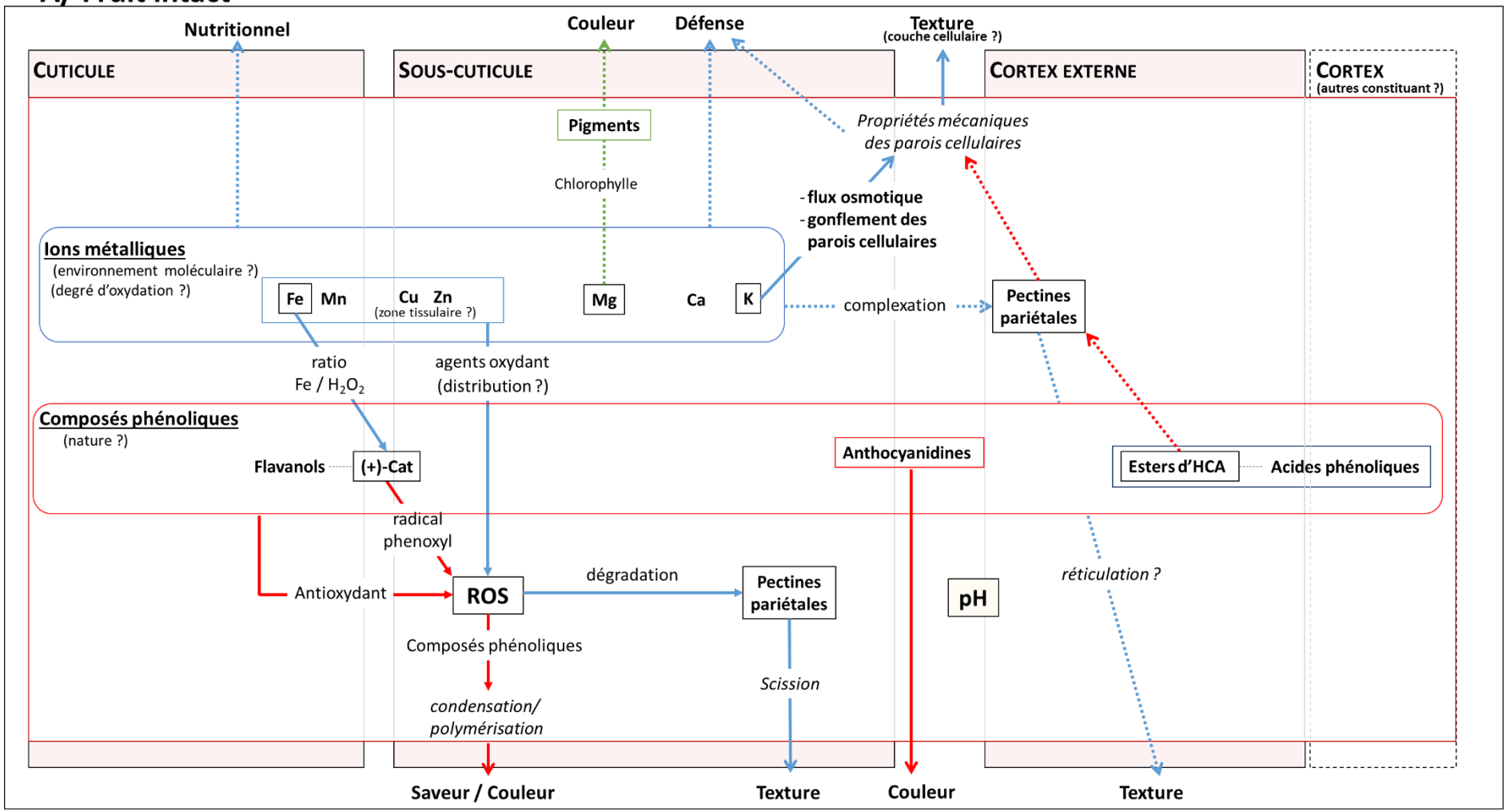

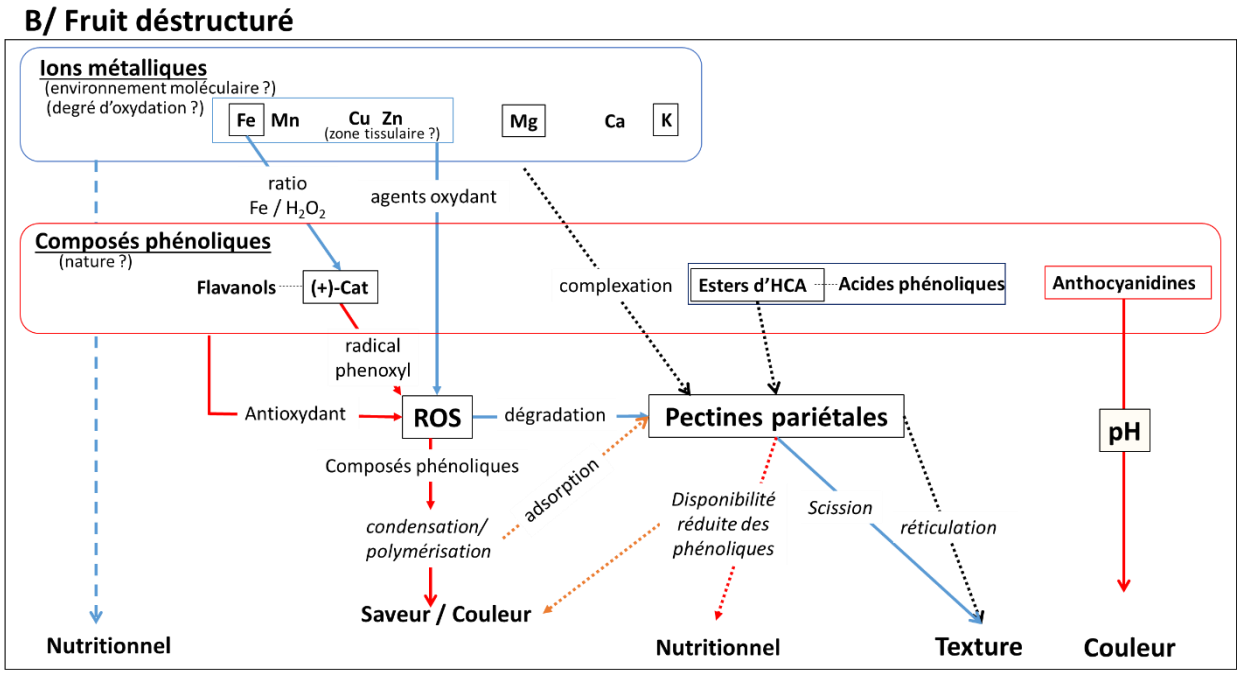

Figure VII.47 : *Modèle conceptuel basé sur les observations de la thèse et de la littérature, représentant les différentes interactions pouvant avoir lieu dans le fruit intact et dans le fruit déstructuré en fonction des zones du tissu. Cu : cuivre, Zn : zinc, Fe : fer, Mn : manganèse, Mg : magnésium, Ca : calcium, K : potassium, H_2O_2 : peroxyde d'hydrogène, (+)-Cat : (+)-catéchine, ROS : « reactive oxygen species », ligne pointillé : interaction potentielle. Trait plein : interaction validée.*

Dans le schéma A/ Fruit intact *: Les composants sont positionnés en fonction des résultats de leur cartographies dans les zones tissulaires. Par exemple, le Mg majoritairement présent au niveau sous-cuticule serait en interaction avec la chlorophylle ce qui affecterait potentiellement les pigments et donc la couleur du fruit. De même, les ions métalliques dans les zones cuticules et sous-cuticule peuvent affecter les mécanismes de défense du fruit, complexer les pectines pariétales induisant potentiellement leur réticulation affectant les propriétés mécaniques des parois cellulaires et la texture des couches cellulaires et/ou du fruit. Le K, affecterait les flux osmotiques et le gonflement des parois cellulaires modulant leurs propriétés mécaniques qui influence potentiellement la capacité de défense et la texture du fruit. Les teneurs des ions métalliques peuvent aussi être responsable des propriétés nutritionnelles du fruit. Les travaux ont montré que les métaux de transition conduisent à la formation de ROS en présence d'agents oxydants. Agents oxydants dont il faudrait déterminer la distribution dans ces zones externes du fruit. Les travaux ont aussi montré que le ratio Fe/H2O2 en présence de Cat peuvent affecter la production de ROS, en passant par les radicaux phenoxyl. L'ensemble des composés phénoliques présente un effet plutôt antioxydant sur les ROS. Les ROS produits interagissent avec les composés phénoliques pour induire leur condensation/polymérisation affectant les saveurs et couleurs du fruit. Les ROS induisent aussi la dégradation des pectines pariétales, et leurs scissions affectent les propriétés mécaniques des parois cellulaires et potentiellement la texture du fruit. Au contraire, les acides phénoliques, en particulier les esters d'HCAs potentiellement localisés sur les pectines pariétales pourrait induire leur réticulation et donc moduler les propriétés mécaniques des parois cellulaires affectant la texture du tissu et du fruit. Les anthocyanidines sont surtout dépendantes du pH affectant la couleur du tissu/fruit.*

Dans le schéma B/ fruit déstructuré : *Les potentielles interactions retrouvées sont en parti les mêmes que celles du fruit intact. Une interaction supplémentaire est la potentielle adsorption des composés phénoliques condensés/polymérisés sur les parois cellulaires/pectines, avec pour conséquence de réduire leurs disponibilités affectant les propriétés organoleptiques et nutritionnels du fruit déstructuré.*

VII.6.Modèle conceptuel des interactions impactant les propriétés organoleptiques dans les fruits intacts et déstructurés

Dans le modèle proposé **Figure VII.2**, différentes interactions avérées et potentielles dans le fruit frais et dans le fruit déstructuré sont schématisées. Les interactions supposées permettent de mettre en avant les points nécessitants des travaux complémentaires pour préciser ce modèle et avoir une meilleure visibilité des phénomènes intervenants sur les propriétés organoleptiques des fruits frais et déstructurés. Toutefois, un point non précisé dans ce modèle, mais tout aussi important, concerne les facteurs environnementaux et génétiques qui jouent des rôles prépondérants dans la distribution des ions métalliques et des autres composants des fruits.

VII.6.1. Les distributions à clarifier

En ce qui concerne les études de distributions, la méthodologie utilisant les conditions « cryo » devra être reprise pour poursuivre la cartographie des différents constituants dans les tissus des fruits. Tout d'abord, la nature des composants dans les tissus demande encore à être approfondie. Par exemple, les métaux de transition réellement localisés dans la cuticule par fluorescence X sont le fer et le manganèse (**Chapitre V**) alors que le cuivre et le zinc, dont la présence a été identifiée dans la peau **(Chapitre V)**, n'ont pas pu être cartographiés spécifiquement dans cette région cuticulaire. Le matériau du porte échantillon pour la mesure de la fluorescence X sur la ligne LUCIA de Soleil qui est fait de cuivre et la limite d'énergie d'excitation (≤ 8 keV) ne permettent pas d'exciter le cuivre et le zinc (min. : 9,6 keV). Toutefois, pour vérifier la localisation tissulaire du cuivre et du zinc, la fluorescence X reste valide mais il faudra modifier le matériau du porte-échantillon et accéder à une ligne permettant une plus forte énergie d'excitation telle que la ligne ID16 de l'ESRF (European Synchrotron Radiation Facility) pour cartographier le cuivre (Collin, Doelsch et al. 2014) et le zinc (Sarret, Willems et al. 2009). Aussi, il sera intéressant d'accéder à la distribution à l'échelle subcellulaire des ions métalliques, notamment par fluorescence X synchrotron via une nanosonde potentiellement accessible sur la ligne NANOSCOPIUM du synchrotron SOLEIL (Somogyi, Medjoubi et al. 2015). Toutefois, la mise en œuvre de cette technique risque d'être limitée par la difficulté d'obtenir des cryo-sections d'épaisseur de l'ordre du nanomètre avec des fruits charnus, mais aussi par la concentration réduite des métaux dans ces cryo-sections qui, malgré la sensibilité élevée apportée par le synchrotron, ne pourraient pas être visualisés. Pour localiser les ions métalliques, un autre moyen serait de développer des marqueurs fluorescents spécifiques de ces ions métalliques et de les mettre en œuvre avec des observations en cryo-microscopie confocale. Également, malgré quelques essais non concluants, la cartographie de ces ions métalliques par LA-ICP-MS pourrait être une méthode efficace (Becker, Zoriy et al. 2010). Elle nécessite néanmoins des développements méthodologiques quant à la préservation des tissus et la quantification liée à l'absence de matrices standard adaptées. Cette absence de matrices de référence

est une limite commune aux techniques de S-XRF ou de fluorescence en UV profond (DUV) où aucune information quantitative locale n'a pu être établie.

Pour les composés phénoliques par DUV, seule la distribution des grandes familles a été obtenue mais pas de molécules spécifiques. En effet, les caractérisations à partir des spectres d'autofluorescence des composés phénoliques étaient pertinentes pour les premières observations faites au cours de la thèse mais elles ont atteint leurs limites pour identifier leurs natures spécifiques et l'analyse à l'échelle tissulaire. L'étude des spectres *in-situ* par le montage POLYPHEME de la ligne DISCO à Soleil (Jamme, Villette et al. 2010) pourrait potentiellement permettre de distinguer plus clairement la nature des composés phénoliques au sein d'une même famille. Un autre moyen potentiel pour identifier la nature des composés phénoliques sera là aussi de développer des marqueurs fluorescents spécifiques des composés plutôt que des familles, afin d'observer leur distribution via la méthode de cryo microscopie confocale développée (**Chapitre II**). Par ailleurs, les techniques d'imagerie combinant la spectrométrie de masse sont en pleins développements et permettraient d'accéder *in-situ* à la nature de ces composés phénoliques (Franceschi, Dong et al. 2012). Cependant, cette technique présente une faible résolution de l'ordre de 100 µm et nécessite des sections lyophilisées. Des développements pour adapter les systèmes cryo et la résolution seront donc indispensables pour évaluer la distribution à l'échelle cellulaire et subcellulaire.

Outre la nature des composés phénoliques et métaux de transition dont la cartographie a été initiée, il serait intéressant d'établir la distribution des enzymes oxydatives (Jukanti 2017) et des cations organiques. Par exemple, un point à vérifier serait la corrélation de la distribution du Mg avec celle des chlorophylles, connues pour affecter la couleur des tissus (Pareek, Sagar et al. 2017). De même, un autre point à éclaircir serait la distribution et la quantification des agents oxydants dans les tissus tel que l'H_2O_2. Cela permettrait d'évaluer leur proximité avec les métaux de transition mais aussi d'établir les ratios des concentrations à mettre en œuvre dans l'étude des mécanismes à travers des solutions modèles. L'intérêt pour ces autres constituants du tissu conduira donc de futures études sur leur localisation. Grâce aux méthodes « cryo », les composés tels que les enzymes d'oxydo-réduction ou l'H_2O_2 pourront être cartographiés par le développement de marqueurs fluorescents qui leur seraient spécifiques, comme par exemple le 3,3'-diaminobenzidine (DAB) pour localiser le peroxyde d'hydrogène et l'anion superoxyde (Halbhuber, Scheven et al. 1996, Haugland, Gregory et al. 2005, Kumar, Yusuf et al. 2014). Par ailleurs, la localisation spécifique d'H_2O_2 sans les autres ROS est réalisable grâce à l'utilisation de nano-marqueurs (nanoparticule d'or couplée à l'acide 4-carboxyphenylboronique), visualisés par microscopie électronique en transmission et microscopie RAMAN (Qu, Liu et al. 2016).

Les zones internes du fruit demanderaient aussi à être étudiées, car elles pourraient présenter des compositions différentes des tissus externes (Ferguson and Watkins 1983, Treutter 2001). Ces tissus sont les plus représentés quantitativement dans le fruit et auront donc un impact important lors de la consommation du fruit frais ou lors de sa transformation.

Outre la proximité des composés dans les fruits frais, des études sont à réaliser pour identifier les cinétiques réactionnelles dans les mécanismes d'oxydo-réduction engendrés par ces proximités dans l'élaboration des caractéristiques organoleptiques des fruits lors de leur consommation ou leur transformation. De même, établir la variation de pH dans les tissus sera tout aussi intéressant car ce paramètre peut influencer directement ou indirectement les différentes interactions affectant les propriétés organoleptiques des matrices ou même la structure des composés phénoliques, tels que les anthocyanidines (Sinela, Mertz et al. 2017).

Les différentes études, qui seront menées sur les distributions des composants dans le tissu, devront aussi être corrélées à la mesure de propriétés organoleptiques spécifiques des différentes zones du tissu. En cela, le développement de microsondes mécaniques permettant d'accéder à la texture de ces zones tissulaires pourrait être imaginé. En ce qui concerne la couleur, des microdosages par colorimétrie ou spectrophotométrie pourraient être réalisables sur des volumes ou des surfaces dans des zones réduites de tissus (Matsuoka and Yoshimura 2010, Cheng, Zheng et al. 2011).

VII.6.2. Les mécanismes à élucider

En ce qui concerne les interactions et les mécanismes réactionnels d'oxydo-réduction, les premières observations effectuées au cours de cette thèse ont mis en avant certains points qui restent à élucider. Par exemple, la connaissance de l'état d'oxydation des métaux de transition serait une information clé pour la meilleure compréhension de leurs interactions potentielles dans les différentes couches cellulaires (Sarret, Willems et al. 2009, Zhao, Moore et al. 2014). Ce type d'information peut être accessible en restant à l'échelle de la micro-fluorescence X (ligne LUCIA, Soleil) via la méthode XANES (X-ray Absorption Near Edge Structure) qui permet d'accéder à la spéciation et à l'environnement chimique de ces ions métalliques dans le tissu (Sarret, Manceau et al. 1998, Isaure, Fayard et al. 2006). En effet, l'état d'oxydation associé aux concentrations conditionne notamment la réactivité des ions métalliques avec les agents oxydants, les ROS et les composés phénoliques (**Chapitre VI**) des matrices déstructurées. A partir des solutions modèles, l'exploration détaillée des mécanismes dégradant les composés phénoliques et les pectines via les ROS permettrait d'évaluer les phénomènes de dépolymérisation des pectines (Dumville and Fry 2003) et de polymérisation ou de condensation des composés phénoliques (Guyot, Bernillon et al. 2008). Les futures études en solution modèle pourraient inclure d'autres constituants de la matrice fruit ainsi que la concentration des

différents constituants mis en œuvre, en particulier les métaux de transition et des agents oxydants, et leurs cinétiques de réactions (Sinela, Mertz et al. 2017). Pour cela, en suivant les mêmes méthodes analytiques (HPLC-SEC et spectrophotométrie), les travaux devront être faits avec des gammes de concentrations variantes et des temps d'analyses contrôlés. La mesure des ROS produits dans ces matrices déstructurées sera aussi une étude intéressante qui pourrait être estimée avec les techniques chromatographiques associées aux piégeages des ROS de type HPLC-DPPH (Ishiwata, Yamaguchi et al. 2004). Ce type de technique consiste au suivi par HPLC d'une molécule réactive avec les ROS, le 1,1-diphenyl-2-picrylhydrazyl (DPPH). D'autres techniques peuvent être envisagées comme l'EPR (electron paramagnetic resonance), la technique « phare » de détections de ROS qui consiste à la mesure de l'absorption des radiations électromagnétiques d'un échantillon mis sous champs magnétiques (Davies 2016).

S'agissant des propriétés mécaniques des tissus, les cations métalliques majoritaires K, Ca et Mg de la couche sous cuticule pourraient participer à la structuration des pectines pariétales et donc avoir une influence sur les propriétés mécaniques des parois et des tissus. Là encore, les phénomènes de réticulation des pectines via la complexation des ions métalliques dans les fruits frais demandent à être approfondis, notamment sur les relations stœchiométriques entre les ions présents dans les parois et les sites acides des pectines. Toujours en solution modèle, il serait donc intéressant de développer des méthodes permettant d'évaluer le comportement des pectines vis-à-vis des interactions avec le K, Ca et Mg, en simulant les conditions physico-chimiques des parois cellulaires des fruits *in-vivo*. Associées à ces études, des mesures de texture seraient appropriées pour approfondir la compréhension de ces mécanismes d'interaction des ions métalliques avec les pectines.

Le rôle des ions métalliques et notamment du K sur les flux osmotiques et les gonflements des parois serait à explorer en particulier avec la dynamique de l'eau. Par ailleurs, la présence d'acides phénoliques avec en particulier les acides hydroxycinnamiques estérifiés dans les parois cellulaires reste à préciser au même titre que leur implication dans la réticulation des polysaccharides pariétaux qui participerait à leurs propriétés mécaniques (Christiaens, Van Buggenhout et al. 2016). Ainsi, les techniques de dosage d'acides hydroxycinnamiques estérifiés aux parois cellulaires devront être améliorées, notamment pour ôter le doute sur leur origine. Il faudrait inclure une étape éliminant les composés phénoliques intracellulaires adsorbés sur les parois cellulaires, en modifiant les conditions de lavages et les conditions d'hydrolyses par exemple. Enfin, l'adsorption fortement suggérée des composés phénoliques en particulier des polymères flavanols sur les parois cellulaires (Liu, Lopez-Sanchez et al. 2019), reste aussi un point à éclaircir étant donné l'impact sur la saveur ou l'aspect nutritionnel que pourrait induire ce type d'interaction dans les fruits déstructurés.

VII.7.Conclusions et perspectives

L'objectif initial visant à établir la cartographie des ions métalliques et des composés phénoliques pour mieux appréhender leurs rôles et leurs interactions avec les parois cellulaires a été, en partie, atteint. Ces travaux ouvrent également la voie à d'autres études complémentaires afin d'améliorer et de préciser les colocalisations de ces composants dans les tissus de fruits charnus. De même, il faudra poursuivre sur les notions proposées des rôles et des interactions de ces composants modulant les propriétés mécaniques des tissus et les disponibilités dans les matrices déstructurées. Pour l'ensemble de ces futures études, les rôles de facteurs environnementaux et génétiques des fruits seront des points déterminants à prendre en compte. D'un point de vue transfert et application, l'identification des déterminants clés, impactant les propriétés organoleptiques des matrices de fruits, issu de l'ensemble de ces travaux et synthétisé dans un modèle conceptuel devrait faciliter l'évaluation et le contrôle de la qualité des fruits. Un exemple de développement pourrait être la création de nouveaux produits à base de fruits par l'infusion de solutions combinant des très faibles concentrations de métaux de transition, d'agents oxydants et de composés phénoliques pour en modifier la texture et la couleur.

VII.8.Références

Airianah, O. B., Vreeburg, R. A. M., & Fry, S. C. (2016). Pectic polysaccharides are attacked by hydroxyl radicals in ripening fruit: evidence from a fluorescent fingerprinting method. *Annals of Botany, 117*(3), 441-455. doi:10.1093/aob/mcv192

Ashok, P. K., & Upadhyaya, K. (2012). Tannins are astringent. *Journal of Pharmacognosy and Phytochemistry, 1*(3), 45-50.

Barker, A. V., & Pilbeam, D. J. (2015). *Handbook of plant nutrition*: CRC press.

Becker, J. S., Zoriy, M., Matusch, A., Wu, B., Salber, D., Palm, C., & Becker, J. S. (2010). Bioimaging of metals by laser ablation inductively coupled plasma mass spectrometry (LA-ICP-MS). *Mass spectrometry reviews, 29*(1), 156-175.

Brillouet, J.-M., Romieu, C., Lartaud, M., Jublanc, E., Torregrosa, L., & Cazevieille, C. (2014). Formation of vacuolar tannin deposits in the chlorophyllous organs of Tracheophyta: from shuttles to accretions. *Protoplasma, 251*(6), 1387-1393.

Bush, D. S. (1995). Calcium regulation in plant cells and its role in signaling. *Annual Review of Plant Biology, 46*(1), 95-122.

Cheng, Y. S., Zheng, Y., & VanderGheynst, J. S. (2011). Rapid quantitative analysis of lipids using a colorimetric method in a microplate format. *Lipids, 46*(1), 95-103.

Christiaens, S., Van Buggenhout, S., Houben, K., Jamsazzadeh Kermani, Z., Moelants, K. R. N., Ngouémazong, E. D., . . . Hendrickx, M. E. G. (2016). Process–Structure–Function Relations of Pectin in Food. *Critical Reviews in Food Science and Nutrition, 56*(6), 1021-1042. doi:10.1080/10408398.2012.753029

Collin, B., Doelsch, E., Keller, C., Cazevieille, P., Tella, M., Chaurand, P., . . . Meunier, J.-D. (2014). Evidence of sulfur-bound reduced copper in bamboo exposed to high silicon and copper concentrations. *Environmental Pollution, 187*, 22-30. doi:https://doi.org/10.1016/j.envpol.2013.12.024

Davies, M. J. (2016). Detection and characterisation of radicals using electron paramagnetic resonance (EPR) spin trapping and related methods. *Methods, 109*, 21-30. doi:https://doi.org/10.1016/j.ymeth.2016.05.013

del Río, L. A. (2015). ROS and RNS in plant physiology: an overview. *Journal of Experimental Botany, 66*(10), 2827-2837. doi:10.1093/jxb/erv099

Dumville, J. C., & Fry, S. C. (2003). Solubilisation of tomato fruit pectins by ascorbate: a possible non-enzymic mechanism of fruit softening. *Planta, 217*(6), 951-961.

Edreva, A. (2005). The importance of non-photosynthetic pigments and cinnamic acid derivatives in photoprotection. *Agriculture, ecosystems & environment, 106*(2-3), 135-146.

Ferguson, I. B., & Watkins, C. B. (1983). Cation distribution and balance in apple fruit in relation to calcium treatments for bitter pit. *Scientia Horticulturae, 19*(3), 301-310. doi:https://doi.org/10.1016/0304-4238(83)90078-X

Finley, J. W., Hurst, W. J., & Lee, C. Y. (2018). *Principles of food chemistry*: Springer.

Franceschi, P., Dong, Y., Strupat, K., Vrhovsek, U., & Mattivi, F. (2012). Combining intensity correlation analysis and MALDI imaging to study the distribution of flavonols and dihydrochalcones in Golden Delicious apples. *Journal of Experimental Botany, 63*(3), 1123-1133.

Guyot, S., Bernillon, S., Poupard, P., & Renard, C. (2008). Multiplicity of phenolic oxidation products in apple juices and ciders, from synthetic medium to commercial products. *Recent advances in polyphenol research, 1*, 27.

Halbhuber, K.-J., Scheven, C., Jirikowski, G., Feuerstein, H., & Ott, U. (1996). Reflectance enzyme histochemistry (REH): visualization of cerium-based and DAB primary reaction products of phosphatases and oxidases in cryostat sections by confocal laser scanning microscopy. *Histochemistry and Cell Biology, 105*(3), 239-249. doi:10.1007/bf01462297

Halliwell, B., & Gutteridge, J. M. (2015). *Free radicals in biology and medicine*: Oxford University Press, USA.

Haugland, R. P., Gregory, J., Spence, M. T. Z., & Johnson, I. D. (2005). *Handbook of fluorescent probes and research products*: Molecular Probes.

Held, M. A., Jiang, N., Basu, D., Showalter, A. M., & Faik, A. (2015). Plant cell wall polysaccharides: structure and biosynthesis. *Polysaccharides: Bioactivity and Biotechnology*, 3-54.

Hulme, A. C. (1971). The biochemistry of fruits and their products. Vol. 2. *The biochemistry of fruits and their products. Vol. 2.*

Inze, D., & Van Montagu, M. (2002). *Oxidative Stress in Plants*: London: CRC Press.

Isaure, M.-P., Fayard, B., Sarret, G., Pairis, S., & Bourguignon, J. (2006). Localization and chemical forms of cadmium in plant samples by combining analytical electron microscopy and X-ray spectromicroscopy. *Spectrochimica Acta Part B: Atomic Spectroscopy, 61*(12), 1242-1252.

Ishiwata, K., Yamaguchi, T., Takamura, H., & Matoba, T. (2004). DPPH radical-scavenging activity and polyphenol content in dried fruits. *Food Science and Technology Research, 10*(2), 152-156.

Jamme, F., Villette, S., Giuliani, A., Rouam, V., Wien, F., Lagarde, B., & Réfrégiers, M. (2010). Synchrotron UV fluorescence microscopy uncovers new probes in cells and tissues. *Microscopy and microanalysis, 16*(5), 507-514.

Jukanti, A. (2017). Function (s)/Role (s) of Polyphenol Oxidases. In *Polyphenol Oxidases (PPOs) in Plants* (pp. 73-92): Springer.

Khanal, B. P., & Knoche, M. (2017). Mechanical properties of cuticles and their primary determinants. *Journal of Experimental Botany, 68*(19), 5351-5367. doi:10.1093/jxb/erx265

Kumar, D., Yusuf, M. A., Singh, P., Sardar, M., Sarin, N. B., & Biosciences, J. M. I. (2014). Histochemical detection of superoxide and H2O2 accumulation in Brassica juncea seedlings. *Bio Protoc, 4*(8), e1108.

Le Bourvellec, C., & Renard, C. M. G. C. (2012). Interactions between Polyphenols and Macromolecules: Quantification Methods and Mechanisms. *Critical Reviews in Food Science and Nutrition, 52*(3), 213-248. doi:10.1080/10408398.2010.499808

Liu, D., Lopez-Sanchez, P., Martinez-Sanz, M., Gilbert, E. P., & Gidley, M. J. (2019). Adsorption isotherm studies on the interaction between polyphenols and apple cell walls: Effects of variety, heating and drying. *Food Chemistry, 282*, 58-66.

Macheix, J.-J., Fleuriet, A., & Billot, J. (2017). *Fruit Phenolics*: CRC press.

Matsuoka, S., & Yoshimura, K. (2010). Recent trends in solid phase spectrometry: 2003–2009. A Review. *Analytica Chimica Acta, 664*(1), 1-18.

Moore, K. L., Lombi, E., Zhao, F.-J., & Grovenor, C. R. M. (2012). Elemental imaging at the nanoscale: NanoSIMS and complementary techniques for element localisation in plants. *Analytical and Bioanalytical Chemistry, 402*(10), 3263-3273. doi:10.1007/s00216-011-5484-3

Özcan, M. M., Harmankaya, M., & Gezgin, S. (2012). Mineral and heavy metal contents of the outer and inner tissues of commonly used fruits. *Environmental monitoring and assessment, 184*(1), 313-320.

Pareek, S., Sagar, N. A., Sharma, S., Kumar, V., Agarwal, T., González-Aguilar, G. A., & Yahia, E. M. (2017). Chlorophylls: Chemistry and Biological Functions. *Fruit and Vegetable Phytochemicals: Chemistry and Human Health, 2 Volumes*, 269.

Perron, N. R., & Brumaghim, J. L. (2009). A review of the antioxidant mechanisms of polyphenol compounds related to iron binding. *Cell biochemistry and biophysics, 53*(2), 75-100.

Qu, L.-L., Liu, Y.-Y., He, S.-H., Chen, J.-Q., Liang, Y., & Li, H.-T. (2016). Highly selective and sensitive surface enhanced Raman scattering nanosensors for detection of hydrogen peroxide in living cells. *Biosensors and Bioelectronics, 77*, 292-298. doi:https://doi.org/10.1016/j.bios.2015.09.039

Renard, C. M. G. C., Watrelot, A. A., & Le Bourvellec, C. (2015). Interactions between polyphenols and polysaccharides: mechanisms and consequences in food processing and digestion. *Trends in Food Science & Technology*. doi:http://dx.doi.org/10.1016/j.tifs.2016.10.022

Rogiers, S. Y., Coetzee, Z. A., Walker, R. R., Deloire, A., & Tyerman, S. D. (2017). Potassium in the Grape (Vitis vinifera L.) Berry: Transport and Function. *Frontiers in plant science, 8*, 1629.

Sanoner, P., Guyot, S., Marnet, N., Molle, D., & Drilleau, J. F. (1999). Polyphenol profiles of french cider apple varieties (Malus domestica sp.). *Journal of Agricultural and Food Chemistry, 47*(12), 4847-4853. doi:10.1021/jf990563y

Sarret, G., Manceau, A., Spadini, L., Roux, J.-C., Hazemann, J.-L., Soldo, Y., . . . Menthonnex, J.-J. (1998). Structural Determination of Zn and Pb Binding Sites in Penicillium chrysogenum Cell Walls by EXAFS Spectroscopy. *Environmental Science & Technology, 32*(11), 1648-1655. doi:10.1021/es9709684

Sarret, G., Willems, G., Isaure, M.-P., Marcus, M. A., Fakra, S. C., Frérot, H., . . . Saumitou-Laprade, P. (2009). Zinc distribution and speciation in Arabidopsis halleri × Arabidopsis lyrata progenies presenting various zinc accumulation capacities. *New Phytologist, 184*(3), 581-595. doi:10.1111/j.1469-8137.2009.02996.x

Sentenac, H., & Grignon, C. (1981). A model for predicting ionic equilibrium concentrations in cell walls. *Plant physiology, 68*(2), 415-419.

Sinela, A. M., Mertz, C., Achir, N., Rawat, N., Vidot, K., Fulcrand, H., & Dornier, M. (2017). Exploration of reaction mechanisms of anthocyanin degradation in a roselle extract through kinetic studies on formulated model media. *Food Chemistry, 235*, 67-75. doi:https://doi.org/10.1016/j.foodchem.2017.05.027

Somogyi, A., Medjoubi, K., Baranton, G., Le Roux, V., Ribbens, M., Polack, F., . . . Samama, J.-P. (2015). Optical design and multi-length-scale scanning spectro-microscopy possibilities at the Nanoscopium beamline of Synchrotron Soleil. *Journal of Synchrotron Radiation, 22*(4), 1118-1129.

Treutter, D. (2001). Biosynthesis of phenolic compounds and its regulation in apple. *Plant Growth Regulation, 34*(1), 71-89. doi:10.1023/a:1013378702940

Voragen, A. G. J., Coenen, G.-J., Verhoef, R. P., & Schols, H. A. (2009). Pectin, a versatile polysaccharide present in plant cell walls. *Structural Chemistry, 20*(2), 263. doi:10.1007/s11224-009-9442-z

Xanthakis, E., Le-Bail, A., & Ramaswamy, H. (2014). Development of an innovative microwave assisted food freezing process. *Innovative Food Science & Emerging Technologies, 26*, 176-181. doi:http://dx.doi.org/10.1016/j.ifset.2014.04.003

Zhao, F.-J., Moore, K. L., Lombi, E., & Zhu, Y.-G. (2014). Imaging element distribution and speciation in plant cells. *Trends in Plant Science, 19*(3), 183-192.

Annexes

Sommaire

Annexe 1 : Publications

A/ Cryo-laser scanning confocal microscopy of diffusible plant compounds

Vidot *et al. Plant Methods (2018) 14:89*
https://doi.org/10.1186/s13007-018-0356-x

Plant Methods

METHODOLOGY Open Access

Cryo-laser scanning confocal microscopy of diffusible plant compounds

Kevin Vidot[1,2*], Cédric Gaillard[1*], Camille Rivard[3,4], René Siret[2] and Marc Lahaye[1*]

Abstract

Background: The in vivo observation of diffusible components, such as ions and small phenolic compounds, remains a challenge in turgid plant organs. The analytical techniques used to localize such components in water-rich tissue with a large field of view are lacking. It remains an issue to limit compound diffusion during sample preparation and observation processes.

Results: An experimental setup involving the infusion staining of plant tissue and the cryo-fixation and cryo-sectioning of tissue samples followed by fluorescence cryo-observation by laser scanning confocal microscopy (LSCM) was developed. This setup was successfully applied to investigate the structure of the apple fruit cortex and table grape berry and was shown to be relevant for localizing calcium, potassium and flavonoid compounds.

Conclusion: The cryo-approach was well adapted and opens new opportunities for imaging other diffusible components in hydrated tissues.

Keywords: Cryogenic fixation, Cryo-confocal microscopy, Metallic ions, Phenolics, Apple, Grape

Background

Plant growth involves intricate relations between cell water compartmentalization and cell wall mechanical properties [1]. These relations involve cations for osmotic regulation and cell wall polysaccharide interactions, remodelling or deconstruction [2–7], but detailed knowledge on cation roles and interactions is impeded by their high mobility and/or low abundance in turgid tissue. Analytical methods for cation localization with a high spatial resolution are thus required. Due to the high water content of growing plant tissue, restraining the diffusion of mobile ions and preserving tissue integrity remain a challenge [8–10].

Specific chemical or physical fixation methods of plant tissue structures for microscopic observations exist [11]. Cryo-techniques coupled to cryo-observation in large fields of view using fluorescent techniques are particularly suited to localize metallic cations and diffusible compounds at low concentrations. The cryogenic fixation of plant tissues for light microscopy, called cryo-observation, has been described [12] but has been rarely used in the fluorescent mode [13]. This scarcity is most likely due to the difficulty in keeping the cold chain intact between sample cryo-fixation, cryo-sectioning and sample observation in frozen conditions. To that end, a method of fluorescence staining followed by cryo-fixation and cryo-observation by laser scanning confocal microscopy (LSCM) was developed and applied to the apple fruit cortex and table grape berry as models of turgid plant organs.

Results

Staining approaches

Staining of the sample with aqueous dye solutions must be completed prior to cryo-fixation. In the present case, it was achieved by the infusion or perfusion (Fig. 1) of fresh samples using acridine orange (AO), a fluorescent dye for the cell walls and anionic sites of cell organelles, DNA and RNA [14–16]. Compared to the direct staining of fresh sample sections, AO infusion was efficient, while perfusion showed limited dye diffusion in the vicinity of

*Correspondence: kevin.vidot@inra.fr; cedric.gaillard@inra.fr; marc.lahaye@inra.fr
[1] UR 1268 Biopolymères Interactions Assemblages, INRA, 44300 Nantes, France
Full list of author information is available at the end of the article

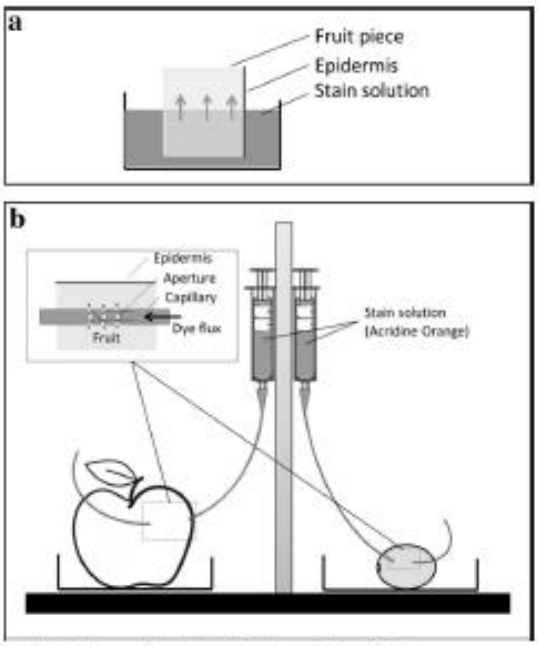

Fig. 1 Staining methods by **a** infusion and **b** perfusion

the capillary and required an increase of the laser intensity to reveal probe fluorescence. Although less efficient, the latter method may be useful to study specific tissue locations with limited operation artefacts. Due to its efficiency and simplicity, infusion staining was chosen in the following study. Such a staining method that is used prior to fixation and cutting a section has already been reported to successfully stain potassium in leaves [17].

Cryo-fixation

The freezing process impacts turgid tissue structure due to ice crystal formation. The different cryo-fixation methods of AO infused samples were compared with regard to the apparent integrity of cell walls (Fig. 2). Observations at approximately −25 °C revealed that slow freezing at −20 °C (Fig. 2a, b), fast freezing in liquid nitrogen (Fig. 2c, d), and fast freezing in cold isopentane (Fig. 2e, f) impacted the overall tissue structure from most to least. These results agree with the impact of the rate of ice nucleation: the faster the freezing technique is, the less ice nucleation is present, and the better that structures are preserved. Slow-freezing under microwaves was also tested as an alternative to fast-freezing. Applying low-power microwaves during freezing drastically reduced the growth of ice nuclei and limited cell damage due to ice expansion [18]. The fruit tissue cryo-fixed by this technique yielded remarkable results with regard to the preservation of its cell integrity (Fig. 2g, h). This was particularly the case for the grape berry, for which tissue integrity was the most difficult to preserve. However, this promising technique still needs development to optimize its parameters, such as microwave power, freezing temperature and processing time. The preservation of

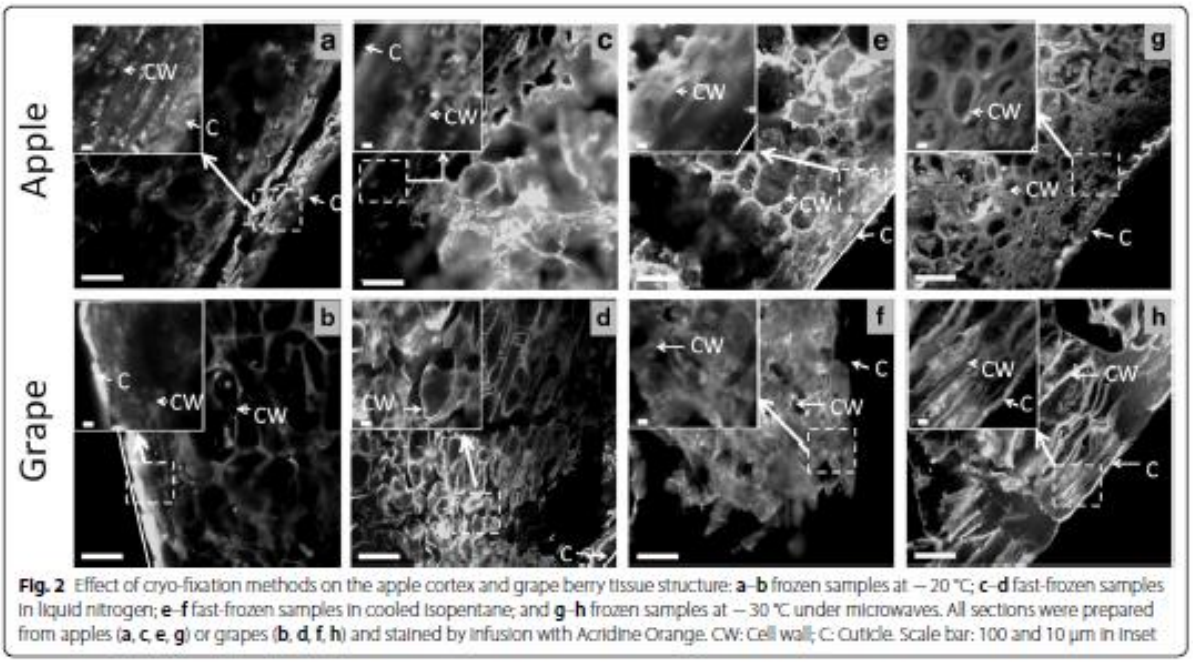

Fig. 2 Effect of cryo-fixation methods on the apple cortex and grape berry tissue structure: **a**–**b** frozen samples at −20 °C; **c**–**d** fast-frozen samples in liquid nitrogen; **e**–**f** fast-frozen samples in cooled isopentane; and **g**–**h** frozen samples at −30 °C under microwaves. All sections were prepared from apples (**a**, **c**, **e**, **g**) or grapes (**b**, **d**, **f**, **h**) and stained by infusion with Acridine Orange. CW: Cell wall; C: Cuticle. Scale bar: 100 and 10 µm in Inset

inner cells in apple and grape tissues was more efficient using cooled isopentane freezing (Fig. 2e, f) than using microwave freezing (Fig. 2g, h). This may be explained by the short processing time of isopentane freezing (60 s) compared to that of 3 h for the microwave technique due to the air blast freezer used. Furthermore, by avoiding the Leidenfrost effect, isopentane freezing was preferred over liquid nitrogen freezing. However, the measurement of cell wall thickness as a function of freezing conditions revealed an impact of the cooling rate on cell wall thickness (Fig. 3). Congo Red-stained apple cell walls at approximately 200 µm from the cuticle were 2.5-fold thicker in tissue frozen by cold isopentane than in fresh tissue (room temperature), while tissue frozen at − 20 °C or by liquid nitrogen gave an intermediate average thickness.

Observation of diffusible compounds

As an application of the entire process on turgid plant organs, calcium, potassium and flavonoid compounds were localized in apple fruit and table grape berry tissue. Samples were independently infused with the calcium probe Fluo-3, potassium probe PBFI, and flavonoid probe DPBA. The samples were then fast-frozen in cold isopentane, cryo-sectioned and observed by cryo-LCSM (Fig. 4a–f). The results showed diffuse calcium staining in the cell wall, while fluorescence spots were observed within cells (Fig. 4a, b). Potassium and flavonoids were distributed in the entire fruit tissue (Fig. 4c–f), and specific locations appeared in the cytosol next to the cell walls (Fig. 4e, f). As a comparison, the direct staining of fresh sections yielded weaker labelling mainly due to the absence of intracellular staining (Fig. 4g–l). These observations may be attributed to low compound concentrations resulting from their diffusion during staining and loss during washes as well as from the higher diffusion of quenchers inducing faster fluorescence bleaching at room temperature [19, 20].

Discussion

The experimental setup presented here was developed to image metallic cations and phenolic compound distributions in in vivo-like fleshy fruit by fluorescence confocal microscopy. Particular care was paid to the issues related to the low concentration and highly diffusible properties of these components. The fruit region of interest was established at the epidermal areas of grape and apple fruit. To allow full cell observation (range of cell diameter i.e., 10–100 µm) [21], section thicknesses needed to be adapted according to the tissue. Despite the particular physicochemical and mechanical characteristics of samples, sections with thicknesses of 100 µm were achieved but required dexterity for their handling, particularly for grape tissue. In addition, the physical state of the sample is essential when studying diffusible components [22]. For turgid plant organs such as fleshy fruit, water, which amounts to 80–85% of their weight, determines the morphological, physiological and physical properties of tissues at room temperature or in frozen solid states. Cryo-fixation limits the diffusion and redistribution of highly diffusible components [22, 23] but has several drawbacks. First, it requires that the sample be stained before freezing, and second, it faces the issue of structural damage by ice crystals [24, 25]. We found that

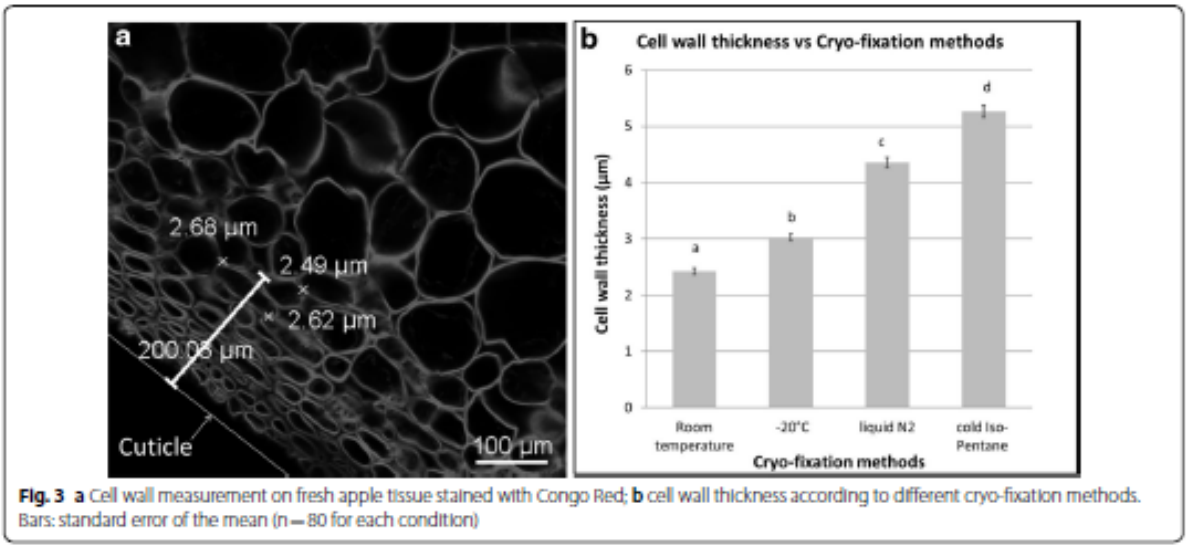

Fig. 3 **a** Cell wall measurement on fresh apple tissue stained with Congo Red; **b** cell wall thickness according to different cryo-fixation methods. Bars: standard error of the mean (n = 80 for each condition)

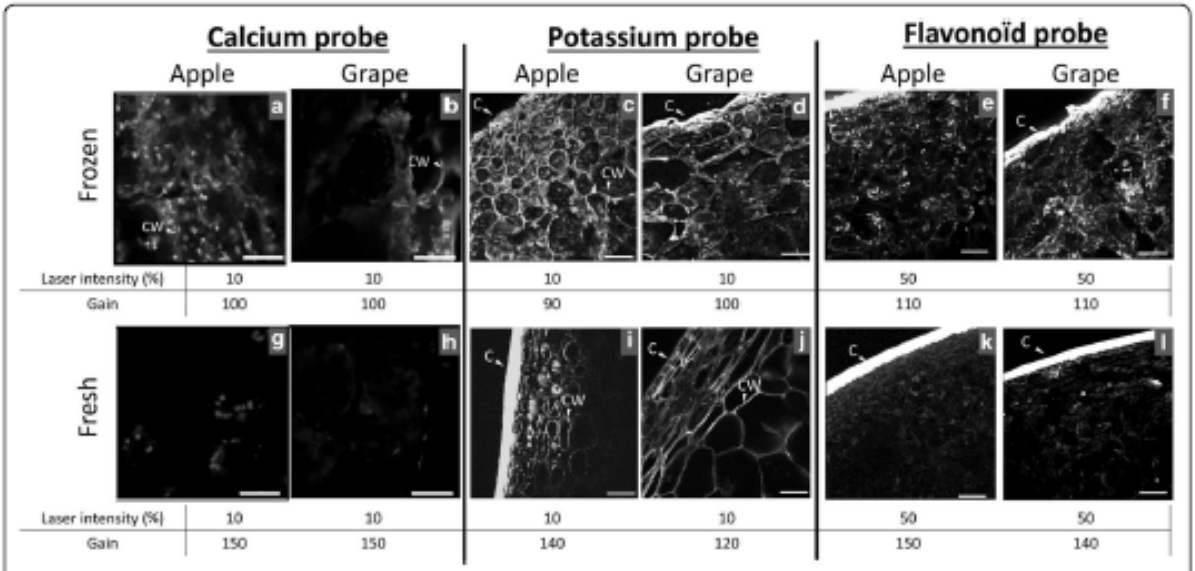

Fig. 4 Cryo-observation of apple **a**, **c**, **e** and grape **b**, **d**, **f** tissues infused by Fluo-3 (calcium), PBFI (potassium), DPBA (flavonoid) dyes and cryo-fixed in cooled isopentane. Fluorescence observations in fresh apple fruit (**g**, **i**, **k**) and grape berry (**h**, **j**, **l**) sections directly stained by Fluo-3, PBFI and DPBA. C: Cuticle, CW: Cell Wall. Scale bar: 50 µm for calcium probe and 100 µm for potassium and flavonoid probes. Laser excitation and gain are indicated to stress the difference in fluorescence intensity recovered between fresh and frozen samples. The applied fluorescence intensity of the cuticle is due in part to autofluorescence related to the presence of phenolic compounds

fresh tissue infusion remains the most efficient and user-friendly method. It is well adapted to turgid plant tissue due to its porosity and exchange properties. Applied to apple and grape tissues, labelling was observed up to the fifth or sixth cell layer from the exposed area (approximately 100 µm for each layer) after two hours of staining. To reduce tissue destruction by ice crystals, cryogenic techniques have been developed. Plunge freezing [26], jet freezing, or slam freezing in cryogenic fluid or high pressure freezing (HPF) transform liquid water to a vitreous solid phase [27]. Currently, HPF is recognized as the method of choice for cryopreservation and is well adapted for ultramicrotome sections. This fast freezing process (≈0.5 ms) allows cell preservation up to 600 µm in thickness [28] and is optimal for investigating small cells and objects by the cryo-electron microscopy of vitreous samples (CEMOVIS) [29], cryo-correlative light transmission electron microscopy (cryo-CLEM) [30] or cryo-correlative light scanning electron microscopy [31]. These techniques are suited for preparing samples for cryo-transmission electron microscopy (cryo-TEM), which has a field of view of smaller than 100 µm^2 and is thus not suitable for large sample sizes when a field of view of more than 500 µm^2 is required. In that context, hand freezing at atmospheric pressure remains the simplest, fastest and most repeatable method of cryo-fixation, as samples are dipped in a cryogen, such as cold isopentane. The hand freezing method used here was inspired by the freezing step involved in the Tokuyasu method, with no sucrose infiltration, as fruit tissues are naturally rich in osmolytes that logically act as natural cryoprotectants [32]. Cryo-observation in light microscopy has already been developed [12], but to our knowledge, only a few commercial or homemade fluorescence microscopes equipped with a cryo-chamber cooled by liquid nitrogen are available. They are specifically used to observe vitrified ultrathin sections by fluorescence microscopy as a preliminary step prior to observation by cryo-TEM. In available cryo-fluorescence microscopy setups, dry lenses with relatively long working distances (WDs) and limited numerical apertures (NAs) are used [30]. Recently, a prototype of a LSCM stage and objective lens were described for the high-resolution cryo-observation of sub-cellular localization of animal proteins [20]. In our setup, the inverted optic of the LSCM possesses a short WD that maximizes the NA. These are key factors determining the fluorescence sensitivity and spatial resolution required to localize compounds at low concentrations, such as metallic cations or phenolic compounds in fruit tissue, with a large field of view.

The freezing of water-rich biological materials has been reported to affect cell contraction and the swelling of cell walls [33]. In the present study, the cell wall thickness was observed to vary according to the apple cryo-fixation

temperature. As postulated [33], the extracellular water medium freezes first and provokes an outward water flux from the cells to osmotically equilibrate intracellular and extracellular media. Water in biomaterials is also known to expand by almost 9% during freezing and develops transient stresses when the material is frozen from all sides [34]. The cell wall swelling observed in relation to the freezing rate and temperature may be related to these mechanisms, but further studies are required to understand the water behaviour in the fruit cell wall during cryo-fixation. Although water flux and osmolyte redistribution may have occurred during sample cryo-fixation, which impacted the diffusible component distribution, these artefacts may have been limited. Indeed, the two types of calcium labelling distribution observed in both apple and grape tissues showing diffuse staining in cell walls and intense fluorescence spots in cells (Fig. 4a, b) were in agreement with their reported presence in nuclei, vesicles and plant cell walls [22, 35]. Furthermore, the observation of potassium labelling in the apoplast and cell wall of fresh tissue (Fig. 4i, j) and in cells (Fig. 4c, d) of frozen tissue was in agreement with its apoplastic, cytosolic and vacuolar location in fleshy fruit cells [36]. In the literature, calcium and potassium were measured directly on isolated cells and organelles using a fluorescent probe. Lastly, flavonoid distribution mainly observed in the cytosol close to the cell wall supports their putative sites of synthesis. Conversely, their proposed accumulation in the vacuole was not dominant in the present observations in apple and grape, but such localization remains a matter of debate (Fig. 4e, f) [37]. The cellular localization of these different diffusible compounds in the two fleshy fruit parenchymal tissues demonstrated the benefit of the cryo-method.

Conclusion

The localization of highly diffusible and low concentrated components such as metallic cations and flavonoids was achieved in fluorescence mode by LSCM. The reduction of component mobility was realized by keeping samples in a frozen state during the entire preparation process and by the design and adaptation of a cryo-LSCM setup for the observation of frozen sections. The successful localization of calcium, potassium and flavonoids in apple and grape fruits as a model of turgid tissue illustrated the benefits of the cryo-approach. The results indicated that the freezing temperature and cooling rate remain key parameters in the preservation of hydrated tissue integrity and require further studies to better control the associated osmotic-related structural rearrangements. The extension of this approach to other highly diffusible compounds will benefit from the development of specific and sensitive diffusible fluorescent markers. This approach opens new opportunities for studies of small metabolites and ions in the plant sciences.

Methods

Plant material

The fruit tissue nomenclature used in this study is shown in Fig. 5. Gala apples and Italia white table grapes were obtained from a local retail store. Regions of interest corresponding to the apple cortex and grape berry with epidermis were sampled as cubes of approximately 0.125 cm^3 using a razor blade (Fig. 1).

Sample preparation for microscopy

Samples were stained by infusion or perfusion before freezing according to different paths followed by cryo-sectioning and cryo-observation. For comparison,

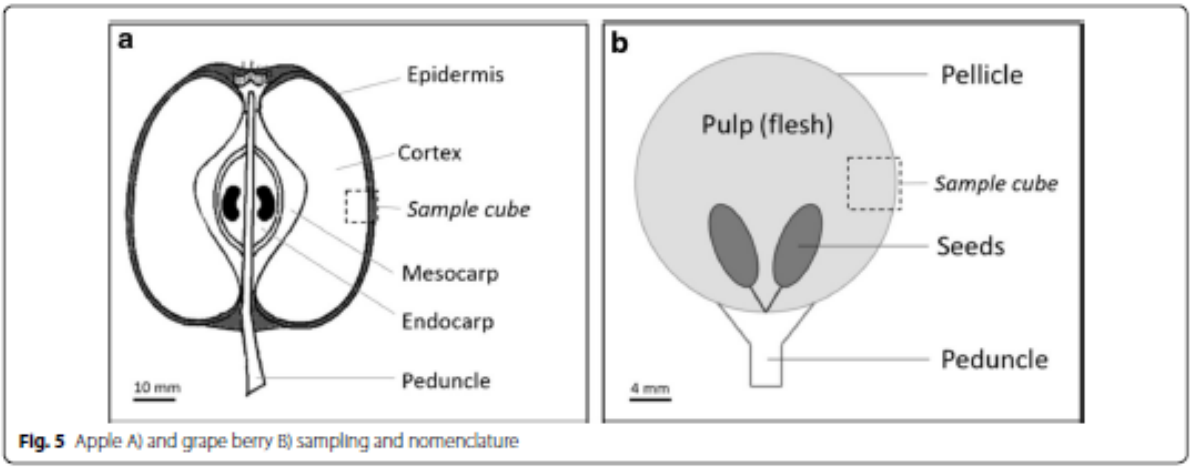

Fig. 5 Apple A) and grape berry B) sampling and nomenclature

samples were also stained by a conventional method and observed in an unfrozen state.

Staining

- *Fluorescence stains:* Acridine orange (AO hydrochloride salt; MERCK Calbiochem, France) was prepared as a *0.02% w/v solution in 0.01 M PBS buffer (pH 7).* Congo Red stain (Congo Red powder, FLUKA, Switzerland) was prepared as a 0.1 mg/mL solution in deionized water at pH 5. Fluo-3 calcium probe (Fluo-3 pentapotassium salt, Thermo Fisher Scientific, France) and PBFI potassium probe (PBFI, tetraammonium salt, Thermo Fisher Scientific, France) were prepared as a 0.1 mg/mL solution in MES (25 mM) + Tris (10 mM) buffer (pH 6.0) [17] and kept as a stock solution in an amber flask at 4 °C. The phenolic probe DPBA (2-Aminoethyl diphenylborinate, Sigma-Aldrich, UK) was prepared by dissolving 20 mg in 5 mL of ethanol and 15 ml of phosphate buffer solution 0.01 M (pH 7).
- The conventional staining of fruit sections (see below for sectioning details) was performed by applying 2 mL of staining solution onto the sections for 5–10 min at room temperature. Sections were then rinsed 3 times with buffer for approximately 5 min each.
- Staining by infusion of fruit samples: Cubes of apple and grape were bathed in staining solutions for 2 h at 5 °C (Fig. 1a).
- Staining by perfusion of entire fruit: Staining solution was introduced in specific areas of the entire fruit using a syringe (5 mL) filled with 2 mL of staining solution connected to 10 cm of capillary tubing (inner diam. 1 mm) inserted in the fruit. The tubing was perforated at the contact zone in the fruit, with a 10-mm length and a 0.8-mm pore size (approximately 10 apertures) to allow for the diffusion of the stain. To ensure the flow of the stain in the fruit, the syringe outlet was set 10 cm above the capillary outlet. The flow rate was approximately 125 µL/h. Diffusion was applied overnight at 5 °C (Fig. 1b).

Cryo-fixation

Cryo-fixation was achieved following several methods to obtain different cooling rates:

- The slow freezing of samples at −20 °C was conducted for at least 24 h in a conventional freezer.
- Two fast-freezing methods were tested using the cryogen: for the first one, the sample was directly plunged in liquid nitrogen, whereas for the second one, it was plunged in isopentane (2-methylbutan anhydrous > 99%, SIGMA) cooled by liquid nitrogen. In both cases, the freezing duration was 60 s.
- Freezing under microwave [38] was conducted with the following parameters: microwave equipment (SAIREM, France) operated at a frequency of 2450 MHz, the microwave chamber stabilization time was 30 min at 5 °C, a temperature of −30 °C was set using an air blaster (ACFRI, France), the microwave power was 5 ± 0.1 W, and the duration of freezing was 3 h.

Sectioning

- Fresh specimens were sectioned at room temperature using a vibrating blade microtome (Vibratome HM 650 V, MICROM, France), stained by a conventional method and collected between 60 × 24 mm glass cover slips (#1) (Thermo Fisher Scientific, Germany) separated by a 250-µm-thick spacer (Gene Frame, 25 µL, 1 × 1 cm^2, Thermo Fisher Scientific, UK). The sectioning parameters used were a section frequency of 60 Hz, a vibration amplitude of 1.0 mm, and a cutting speed of 1.0 mm/sec. Sections were cut to a thickness of 100 µm.
- Frozen specimens were cryo-sectioned using a cryotome (microtome cryostat HM 500 OM, MICROM, France) operated at −20 °C. The sample cube was fixed on the support section using a water droplet free of cryo-protectant. The cryotome steel blade was a type C profile (16 cm length). The cutting speed was fixed at 1 mm/sec, and the thickness of the sections was 100 µm. Sections were picked up and placed between two 22 × 22 mm #1 glass cover slips (Thermo Fisher Scientific, Germany), which were sealed by frozen water microdroplets.

In all cases, sectioning was performed on the stained sample contact area.

The transfer of cold sections within cover slips to the confocal microscope was conducted rapidly over liquid nitrogen.

Laser scanning confocal microscopy (LSCM) observations

LSCM (Eclipse Ti inverted microscope, NIKON Inc. Japan) was used both in bright field and fluorescence modes. Observations were made using a 20 × magnification objective lens and, if needed, a numerical zoom of 3x. The laser excitation and fluorescence emission wavelengths were 488 nm for acridine orange, 500–530 nm for Fluo-3 and DPBA dyes, 488 nm and 600 nm for Congo Red dye, and 375 nm and 500–530 nm for PBFI dye.

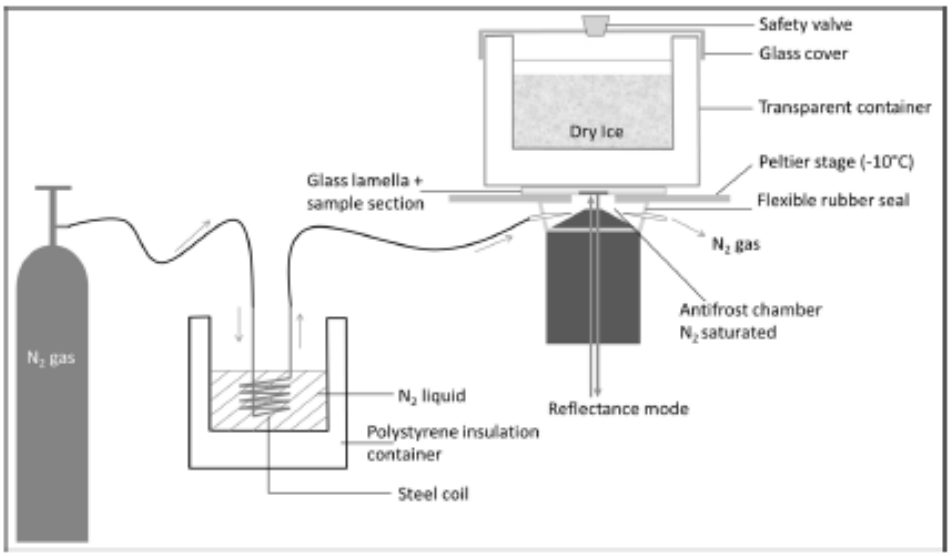

Fig. 6 Setup for LSCM cryo-observation

Laser intensity and gain were adjusted visually for sample fluorescence.

Cryo-observation by LSCM

The critical points to manage for LSCM cryo-observation were sample section warming induced by environmental factors and by the laser during observation as well as frost formation on the sample slide. The sample slide was placed onto a Peltier stage (PE100, Linkam Scientific, Epsom UK) under which an adaptable flexible rubber seal was fixed between the objective lens and the stage (Fig. 6). This closed space between the lens and the stage was flushed by a cooled nitrogen gas flux to prevent frost formation on the sample slide. A glass container filled with dry ice was placed on top of the sample slide. The measured temperature of the Peltier stage was approximately −25 °C. The container transparency allowed the microscope optical condenser to observe the sample in a bright field.

Cell wall thickness measurement

Cell wall thickness was specifically evaluated on four apple fruit samples after staining with Congo Red (a cell wall specific dye) and observed at room temperature after slow freezing at −20 °C and after fast freezing by liquid nitrogen and by isopentane. Four sections per sample were recovered, and five cell wall measurements (a total of 80 measurements) were performed on the cell layer at approximately 200 µm from the cuticle using NIS Analysis software (Nikon).

Authors' contributions
KV, ML, RS, CG designed the study. KV performed the experiments and analysed the data. KV drafted the manuscript. ML, RS, CG, CR revised the manuscript. All authors read and approved the final manuscript.

Author details
[1] UR 1268 Biopolymères Interactions Assemblages, INRA, 44300 Nantes, France. [2] USC 1422 GRAPPE, INRA, Ecole Supérieure d'Agricultures, SFR 4207 QUASAV, 55 rue Rabelais, 49100 Angers, France. [3] Synchrotron SOLEIL, L'Orme des Merisiers, Saint-Aubin, 91192 Gif-Sur-Yvette Cedex, France. [4] UAR 1008 DPT CEPIA, INRA, 44300 Nantes, France.

Acknowledgements
Prof. Alain Lebail and Piyush-Kumar Jha, Ph.D., of the GEPEA team, ONIRIS (Nantes, France), are thanked for their discussions on microwave freezing, making their microwave equipment available and helping with its operation.

Competing interests
The authors declare that they have no competing interests.

Availability of data and materials
Not applicable.

Consent for publication
All authors have given consent for the publication.

Ethics approval and consent to participate
Not applicable.

Funding
This research was sponsored in part by the Region Pays de La Loire under the program RFI Food for Tomorrow-Cap Aliment and by INRA and group ESA.

Received: 20 April 2018 Accepted: 8 October 2018
Published online: 13 October 2018

References

1. Hamant O, Traas J. The mechanics behind plant development. N Phytol. 2010;185(2):369–85.
2. Jarvis MC, Briggs SPH, Knox JP. Intercellular adhesion and cell separation in plants. Plant, Cell Environ. 2003;26:977–89.
3. White PJ, Broadley MR. Calcium in plants. Ann Bot. 2003;92(4):487–511.
4. Dumville JC, Fry SC. Solubilisation of tomato fruit pectins by ascorbate: a possible non-enzymatic mechanism of fruit softening. Planta. 2003;217:951–61.
5. Francoz E, Ranocha P, Nguyen-Kim H, Jamet E, Burlat V, Dunand C. Roles of cell wall peroxidases in plant development. Phytochemistry. 2015;112:15–21.
6. Rice RW. The physiological role of minerals in the plant. In: Datnoff LE, Elmer WH, Huber DM, editors. Mineral nutrition and plant disease. St Paul: APS Press; 2007. p. 9–29.
7. Sattelmacher B. The apoplast and its significance for plant mineral nutrition. N Phytol. 2000;149:167–92.
8. Mentré P. Preservation of the diffusible cations for SIMS microscopy. I. A problem related to the state of water in the cell. Biol Cell. 1992;74(1):19–30.
9. Chandra S, Morrison GH. Sample preparation of animal tissues and cell cultures for secondary ion mass spectrometry (SIMS) microscopy. Biol Cell. 1992;74(1):31–42.
10. Moore KL, Chen Y, van de Meene AM, Hughes L, Liu W, Geraki T, Mosselmans F, McGrath SP, Grovenor C, Zhao FJ. Combined NanoSIMS and synchrotron X-ray fluorescence reveal distinct cellular and subcellular distribution patterns of trace elements in rice tissues. N Phytol. 2014;201(1):104–15.
11. Palin R, Geitmann A. The role of pectin in plant morphogenesis. Biosystems. 2012;109(3):397–402.
12. Echlin P. Low-temperature microscopy and analysis. Berlin: Springer; 1992.
13. Kitin P, Voelker SL, Meinzer FC, Beeckman H, Strauss SH, Lachenbruch B. Tyloses and phenolic deposits in xylem vessels impede water transport in low-lignin transgenic poplars: a study by cryo-fluorescence microscopy. Plant Physiol. 2010;154(2):887–98.
14. Widholm JM. The use of fluorescein diacetate and phenosafranine for determining viability of cultured plant cells. Stain Technol. 1972;47(4):189–94.
15. Houtman CJ, Kitin P, Houtman JCD, Hammel KE, Hunt CG. Acridine orange indicates early oxidation of wood cell walls by fungi. PLoS ONE. 2016;11(7):e0159715.
16. Nafisi S, Saboury AA, Keramat N, Neault J-F, Tajmir-Riahi H-A. Stability and structural features of DNA intercalation with ethidium bromide, acridine orange and methylene blue. J Mol Struct. 2007;827(1–3):35–43.
17. Mühling KH, Sattelmacher B. Determination of apoplastic K + in intact leaves by ratio imaging of PBFI fluorescence. J Exp Bot. 1997;48(8):1609–14.
18. Xanthakis E, Le-Bail A, Ramaswamy H. Development of an innovative microwave assisted food freezing process. Innov Food Sci Emerg Technol. 2014;26:176–81.
19. Lakowicz JR. Principles of fluorescence spectroscopy. 3rd ed. New York: Springer; 2006.
20. Nahmani M, Lanahan C, DeRosier D, Turrigiano GG. High-numerical-aperture cryogenic light microscopy for increased precision of superresolution reconstructions. Proc Natl Acad Sci U S A. 2017;114(15):3832–6.
21. Bain JM, Robertson RN. The physiology of growth in apple fruits. I. Cell size, cell number, and fruit development. Aust J Sci Res B. 1951;4(2):75–107.
22. Hare DJ, New EJ, de Jonge MD, McColl G. Imaging metals in biology: balancing sensitivity, selectivity and spatial resolution. Chem Soc Rev. 2015;44(17):5941–58.
23. McRae R, Bagchi P, Sumalekshmy S, Fahrni CJ. In Situ Imaging of Metals in Cells and Tissues. Chem Rev. 2009;109(10):4780–827.
24. Moor H. Theory and practice of high pressure freezing. In: Steinbrecht RA, Zierold K, editors. Cryotechniques in biological electron microscopy. Berlin: Springer; 1987. p. 175–91.
25. Dahl R, Staehelin LA. High-pressure freezing for the preservation of biological structure: theory and practice. J Elec Mic Tech. 1989;13(3):165–74.
26. Ryan PR, Newman IA, Arif I. Rapid calcium exchange for protons and potassium in cell walls of Chara. Plant, Cell Environ. 1992;15(6):675–83.
27. Kanno H, Speedy RJ, Angell CA. Supercooling of water to −92 °C under pressure. Science. 1975;189:880–1.
28. Moore KL, Lombi E, Zhao F-J, Grovenor CRM. Elemental imaging at the nanoscale: NanoSIMS and complementary techniques for element localisation in plants. Anal Bioanal Chem. 2012;402(10):3263–73.
29. Al-Amoudi A, Chang JJ, Leforestier A, McDowall A, Salamin LM, Norlén LP, Richter K, Blanc NS, Studer D, Dubochet J. Cryo-electron microscopy of vitreous sections. The EMBO Journal. 2004;23:3583–8.
30. Schorb M, Briggs JA. Correlated cryo-fluorescence and cryo-electron microscopy with high spatial precision and improved sensitivity. Ultramicroscopy. 2014;143:24–32.
31. Strnad M, Elsterova J, Schrenkova J, Vancova M, Rego RO, Grubhoffer L, Nebesarova J. Correlative cryo-fluorescence and cryo-scanning electron microscopy as a straightforward tool to study host-pathogen interactions. Sci Rep. 2015;5:18029.
32. Tokuyasu KT. A technique for ultracryotomy of cell suspensions and tissues. The Journal of Cell Biology. 1973;57(2):551–65.
33. Floury J, Le Bail A, Pham QT. A three-dimensional numerical simulation of the osmotic dehydration of mango and effect of freezing on the mass transfer rates. J Food Engin. 2008;85(1):1–11.
34. Ishii T, Matsunaga T, Pellerin P, O'Neill MA, Darvill A, Albersheim P. The plant cell wall polysaccharide rhamnogalacturonan II self-assembles into a covalently cross-linked dimer. J Biol Chem. 1999;274(19):13098–104.
35. Bush DS. Calcium regulation in plant cells and its role in signaling. Annu Rev Plant Biol. 1995;46(1):95–122.
36. Rogiers SY, Coetzee ZA, Walker RR, Deloire A, Tyerman SD. Potassium in the Grape (Vitis vinifera L.) Berry: Transport and Function. *Front Plant Sci* 2017, 8:1629.
37. Kitamura S. Transport of flavonoids: from cytosolic synthesis to vacuolar accumulation. In: *The science of flavonoids*. Springer; 2006: 123–146.
38. Hanyu Y, Ichikawa M, Matsumoto G. An improved cryofixation method: cryoquenching of small tissue blocks during microwave irradiation. J Microsc. 1992;165(2):255–71.

C/ Benchmarking of techniques used to assess the freeze damage in potatoes

Accepted Manuscript

Benchmarking of techniques used to assess the freeze damage in potatoes

Piyush Kumar Jha, Kevin Vidot, Epameinondas Xanthakis, Xavier Falourd, Joran Fontaine, Vanessa Jury, Alain Le-Bail

PII: S0260-8774(19)30203-1

DOI: https://doi.org/10.1016/j.jfoodeng.2019.05.008

Reference: JFOE 9598

To appear in: *Journal of Food Engineering*

Received Date: 15 January 2019

Revised Date: 28 March 2019

Accepted Date: 11 May 2019

Please cite this article as: Jha, P.K., Vidot, K., Xanthakis, E., Falourd, X., Fontaine, J., Jury, V., Le-Bail, A., Benchmarking of techniques used to assess the freeze damage in potatoes, *Journal of Food Engineering* (2019), doi: https://doi.org/10.1016/j.jfoodeng.2019.05.008.

Benchmarking of techniques used to assess the freeze damage in potatoes

Piyush Kumar Jha [a, b, c], Kevin Vidot [c, d], Epameinondas Xanthakis [e], Xavier Falourd [c, d], Joran Fontaine [a, b, c], Vanessa Jury [a, b, c], Alain Le-Bail [a, b, c]

[a] ONIRIS, CS 82225, 44322 Nantes cedex 3, France
[b] UMR GEPEA CNRS 6144 - ONIRIS, 44322 Nantes cedex 3, France
[c] SFR IBSM 4204, 44316 Nantes, France
[d] UR 1268 Biopolymères Interactions Assemblages, INRA, 44316 Nantes, France
[e] RISE Research Institutes of Sweden – Agrifood and Bioscience, Gothenburg 41276, Sweden

Corresponding authors: Alain Le-Bail (alain.lebail@oniris-nantes.fr)

Abstract

In this study, benchmarking of methods used for assessing freeze damage in potatoes was carried out. Initially, the samples were frozen by subjecting them to three different temperatures (i.e. at – 18 °C, – 30 °C, and at – 74 °C). Then, different analytical techniques comprising of focused methods (i.e. cryo-SEM, confocal laser scanning microscopy-CLSM) and global methods (i.e. texture analysis, low field nuclear magnetic resonance (NMR), exudate loss and colour change) were used to assess the impact of the freezing treatment from the different point of view addressed by each method. As a result, each of these methods were able to distinguish significantly fresh samples from the frozen-thawed samples. Focused methods like cryo-SEM and CLSM methods could differentiate the impact of all three different protocols. Meanwhile, texture analysis (including conventional method and novel method based on a touchless laser puff firmness tester), NMR and exudate loss could only determine the quality difference between – 18 °C and – 74 °C freezing conditions. Colour analysis was found as an inappropriate parameter for comparing the three freezing protocols. Among all analytical techniques, cryo-SEM provides the most authentic information about the product as the analysis is performed in frozen state, while for other techniques the product is thawed prior to analysis.

1. Introduction

Freezing is a preservation technique that has been used for ages for increasing the shelf life of food products. Compared to other long-term preservation methods, freezing technique causes

less deterioration to nutrients and sensory properties in fruits and vegetables (Barbosa-Cánovas, Altunakar & Mejía-Lorío (2005). However, it can cause some irreversible damages such as texture loss, colour change, etc. Three main phenomena may describe freeze damage; the primary mechanical effect caused by the transition of water into ice, the biochemical effect caused by cryo-concentration and the secondary mechanical effect eventually caused by ice contraction after freezing (Reid, 1997; Shi, Datta, & Mukherjee, 1999, 1998; Shi, Datta, & Throop, 1998).The extent of freeze damage caused to the food products on thawing is greatly linked to the size and location of the ice crystals, which in turn is related to the applied freezing rate (Chevalier, Le Bail, & Ghoul, 2000). Freeze damage can also be linked to the cryo-concentration effect; the aqueous solution present in the cells is exposed to a progressive concentration in solute caused by ice formation. The remaining aqueous phase which tends to become more and more concentrated can cause denaturation of the proteins and other organized biopolymers (i.e. cellulose based systems for fruits and vegetables), which in turn degrade their mechanical properties and by the way the overall texture of the tissue (Gao & Critser, 2000; Lovelock, 1957; Reid, 1997). The mechanisms of freeze damage associated with cryo-concentration effect have been thoroughly discussed in a review article from Gao & Critser (2000). Rapid freezing (high freezing rate) favours the genesis of fine ice crystals distributed uniformly within the product, thus reducing the dislocation of water from intra to the extra cellular spaces, resulting in higher water holding capacity upon thawing. In addition, the time of exposure to the highly concentrated aqueous solution caused by cryo-concentration is being reduced during rapid freezing, resulting to a lesser extend of the biochemical degradations (Delgado & Sun, 2001; Fennema, 1966; Orlowska, Havet, & Le-Bail, 2009; Sadot, Curet, Rouaud, Le-bail, & Havet, 2017; Shi, Datta, & Mukherjee, 1998; Singh & Heldman, 2009). The result is reduced cell destruction and better quality attributes. However, two main disadvantages lie behind rapid freezing rates : (i) rapid freezing process requires a higher amount of energy, hence increases the consumed energy and the overall operating costs and (ii) the use of extremely high freezing rates such as cryogenic freezing, may lead to crack development in the samples and yield unexpectedly poor quality of the final product (secondary mechanical effect quoted above) (Shi, Datta, & Mukherjee, 1999, 1998; Shi, Datta, & Throop, 1998). On the contrary, at a slow freezing rate, intracellular water move to the extracellular domains (from the inside of the cell) and thus can result in greater ice crystal size (in the extracellular spaces) and also in a higher cell dehydration (Gao & Critser, 2000; Mazur, 1984). Besides, slow freezing rate will also result in a prolonged exposition of the tissue to the concentrated solution occurred from the cryo-concentration effect (Gao &

Critser, 2000; Mazur, 1977, 1984). In fact, the formation of larger ice crystals along with volume shrinkage and long-term exposure to high solute concentrations would cause a higher destruction of cellular structure (high risk of punctured cell membrane/cell wall, collapsed cell structure and cell separation) (Chassagne-Berces et al., 2009; Chassagne-berces, Fonseca, Citeau, & Marin, 2010; Gao & Critser, 2000; Mazur, 1984). As an outcome, the leakage of the fluid from the cell will be higher and a product having a water-soaked appearance and mushy texture will be obtained. The last important parameter that may be responsible for quality losses of frozen foods is the storage conditions; time-temperature parameters, as well as temperature fluctuations, are also responsible for the quality loss.

The assessment of the quality of a frozen food product is obtained via analytical methods used to quantify the freeze damage. Broadly, these methods can be categorized as global methods and focused methods. The global methods provide quality information at a macro/meso level. In other terms, the quality information obtained using such methods is the average value from a whole sample or at least from a substantial piece of sample (several grams or several cm^3). The global methods comprise of texture analysis, exudate loss measurement, solute diffusivity, impedancemetry, colour analysis, etc. While the focused methods provide quality information at a micro level (cell level or even at a lower scale such as ice crystal or water molecule scale). For instance, information about ice crystals size, cellular structure intactness, etc. can be obtained by using focused methods. Microstructures evaluation methods such as Scanning electron microscopy (SEM) (includes conventional SEM, environmental SEM (ESEM), and cryo-SEM), confocal laser scanning microscopy (CLSM), X-rays tomography, etc. fall under focused method. Low field nuclear magnetic resonance relaxometry (NMR) is at the same time a global and focused method as it embraces a sample of *circa* 1 cm^3 scale and provides info at the level of water molecules (Jha et al., 2018).

In the literature, numerous benchmarking studies are available related to freezing effects on the quality parameters of the fruits and vegetables. However, no studies are available in the literature that benchmarks the techniques used to assess the freeze damage in fruits and vegetables.

This work was framed under the following objectives

i. To introduce new freeze damage assessment methods and check their efficiency in quantifying the freeze damage.

ii. To benchmark the freeze damage methods (both conventional and novel) used for assessing the freeze damage in plant-based products with the intention to facilitate the researchers and industries to choose the appropriate method to assess the freeze damage.

The ultimate objective of this study is to provide a decision table which will allow to categorize the analytical techniques based on sensitivity, efficiency, accuracy, cost of operation, and ease of operation.

2. Materials and methods

2.1. Product properties

Potatoes (*Solanum tuberosum* L. cv. Innovator) were the food matrix chosen for this benchmarking study. McCain Foods (Harnes, France) kindly supplied us potato batch having uniform size and maturity. Two batches of potato were used for this test. The first batch of potato was used for NMR tests. In order to reduce the variability, for each freezing condition, samples intended for NMR test were taken from the same potato. Potatoes from the second batch were used for time-temperature history study and freeze damage assessment tests. The average moisture content of both batches was $75.70 \pm 1.40\%$ (wet basis) (Note: the values of moisture content are presented here as mean $\pm$ standard deviation. Similarly, the values for other parameters in the entire manuscript are expressed as mean $\pm$ standard deviation).

2.2. Sample preparations

The sample size used to study the effect of conventional freezing processes on the quality parameters depended on the freeze damage assessment methods. For instance, to study the effect of freezing rates on freezing characteristics, texture, colour and drip loss, cuboids of potato ($1.3 \times 1.3 \times 1$ cm^3 – length × height × width; weight 1.95 ± 0.5 g) were used. The potatoes were cut in cuboid shape using a dicer (Ibili Manage, Inc. Spain). The potato samples used for NMR relaxometry and cryo-SEM analysis were cylindrical in shape (Ø = 8 mm and H = 10 mm). For confocal laser scanning microscopy (CLSM) analysis, cylindrical potato samples (Ø = 8 mm and H = 5 mm) were chosen. The samples were then immediately transferred into the freezer and were cooled from the ambient temperature to the desired temperature.

It is worth mentioning that during this study, one of our aims was to analyze the samples in its original state without causing any alterations to them, thus we had to vary sample size for potato according to the freeze damage assessment methods. For instance, NMR tube has an

internal diameter of 1 cm and hence required sample having a diameter < 1 cm. Also, another requirement of NMR test is to have the NMR tube covered minimum up to 1 cm in height. The cylindrical sample with a diameter of 8 mm and height of 1cm perfectly matched both the requirements. For cryo-SEM, sample size similar as NMR facilitated easy cutting of sample in the frozen state and allowed the selection of the analyzed sample from nearly the same location for each condition. For CLSM, small sample size helped the proper and fast staining of the sample and facilitated the selection of the analyzed sample from the same location of each matrix.

2.3. Freezing apparatus and freezing conditions

Freezing of potatoes (unblanched) was performed at − 18 °C in a cold room, at − 30 °C and 0.5 m/s air velocity in an industrial batch freezer (MATAL, France), and at − 74 °C in an ultra-low temperature freezer (TSE240V, Thermo Scientific, Marietta, Georgia, USA). The three conditions will be referred to as slow freezing (SF), intermediate freezing (IF) and fast freezing (FF) in further sections of the manuscript. Once frozen, the samples were packed in the zip-lock and stored at − 40 ± 2 °C (≈ for 2-3 days) until quality evaluation tests were performed. The time-temperature profile during the freezing tests was studied by inserting a K-type thermocouple at a geometric centre of the product. The (thermocouple) was calibrated against a reference platinum probe (Comptoir Lyon Allemand – Lyon-France). During measurements the temperature of the sample was recorded every 2 s with a data logger with an accuracy of ±0.1 °C. For comparison purposes, temperature profiles from the initial temperature 18 °C to − 18 °C were considered. The characteristic freezing time and overall freezing time were determined using time-temperature data. The characteristic freezing time was the measure of local freezing rate and it was defined as the time during which the temperature at a particular point changed from the initial freezing point to a temperature at which 80% of the water (at that point) was converted into ice. The temperature range considered for the characteristic freezing time estimation was from − 1 to − 7 °C, similar temperature range was used by Li & Sun (2002) for the determination of characteristic freezing time during ultrasound assisted freezing of potatoes. The overall freezing time was the time required to lower the temperature of the geometrical centre of the product from the ambient temperature (18 °C) in the present study) to a given temperature (− 18 °C). Samples for quality analysis were frozen using the same procedure but without optical fibre inserted. Each experiment was performed at a minimum of individual triplicates.

2.4. Thawing protocol

The frozen potato samples were thawed at room temperature (20 ± 1 °C) for 2 h in a zip-lock bag ("static air thawing" method) before performing colour, drip loss, texture and solute diffusion measurements. For NMR analysis the samples were thawed at 4 °C for 4 h in the NMR tube.

2.5. Colour analysis

The colour of the potatoes was measured using a portable and handheld chroma meter CR-400 (Konica Minolta, Inc. Japan). Using this equipment, the L^*, a^*, b^* values for samples from each condition were obtained with high accuracy. The maximum value for L^* is 100 (represents a perfectly white surface or a perfectly reflecting diffuser) and its minimum value is 0 (represents perfectly black surface). The positive and negative a^* corresponds to red and green colour. Similarly, positive and negative b^* represents yellow and blue colour, respectively. A single value for the colour difference was achieved by calculating the overall colour difference (ΔE) value; it takes into account the differences between L^*, a^*, b^* of the specimen (e.g. frozen-thawed sample) and reference (fresh sample), and it was calculated by using Eq. (1) (Anon, 2018). The frozen samples were thawed before the colour measurements. At least eight measurements were recorded for each freezing protocol.

$$\Delta E = \sqrt{\Delta L^{*2} + \Delta a^{*2} + \Delta b^{*2}} \quad (1)$$

2.6. Drip loss measurement

The drip loss required great care in terms of manipulation. The mass differences that are being determined are usually small and it can be advantageous to use paper tissue to collect all the drip released by a sample. This requires the weight of the bag containing the sample, the initial mass of the tissue paper and all the final masses. There is also a risk of moisture condensation on the sample during frozen storage (if unpacked) or during the thawing process or even sample handling after thawing if their temperature is lower than the dew point temperature. The drip loss unit is very often given as g drip per g of sample. In most existing studies, drip losses are expressed as free drip; this means that drip the collected from the sample due to gravity forces and possible capillary interactions with the tissue paper. In some studies, the samples are compressed under selected stress (Jahncke, Baker, & Regenstein, 1992) or after centrifugation for selected g values under given times (Penny, 1975). In our

191 study, the drip loss was determined based on the weight difference between frozen sample
192 (W_1), and thawed sample (W_2). The drip loss (%) was calculated using Eq. (2). At least 9
193 samples were analyzed for each freezing condition.

$$\text{Drip Loss (\%)} = \frac{W_1 - W_2}{W_1} \times 100 \qquad (2)$$

194

195 **2.7. Texture analysis**

196 Texture analysis of food is often carried out using the TPA protocol (Texture Profile
197 Analysis) proposed by Bourne (Bourne, 1968). Quite often, simple compression tests are used
198 for frozen food aiming at determining the Young's Modulus (small deformation, typically
199 10% strain) and eventually the failure strain or stress. In our study, the frozen potato samples
200 were thawed and compressed in a texture analyser (AMETEK, Lloyd Instruments, France)
201 equipped with a 1000 N load cell and operating at a test speed of 50 mm/min beyond failure
202 point which was marked by a significant drop in the force reading (Figure 1). The
203 compression test was performed using a 50 mm compression plate. A similar procedure was
204 used by Khan & Vincent (1993, 1996) for determining the failure stress, Young's Modulus,
205 and failure strain of potato. Based on our preliminary trials and the results from Khan &
206 Vincent (1993) and Alvarez, et al. (2002), compression of the sample to 50% strain was found
207 more than sufficient to cause the failure of our sample (Figure 1). The maximum force exerted
208 during the compression test was recorded as the firmness/hardness (N) of the samples (Figure
209 1). Moreover, the stress vs. strain curves during compression tests were examined and
210 Young's modulus (E) (the slope of the loading curve at the point of its highest gradient) was
211 also acquired (Chassagne-Berces et al., 2009). All measurements were performed at 21 ± 2°C.
212 At least 12 samples were analyzed for each freezing condition.

213 **2.7.1. Laser-puff firmness tester**

214 A touchless laser-puff firmness tester which was designed and constructed in our lab (GEPEA
215 lab, ONIRIS) was used for non-destructive measuring of the texture of fresh and frozen-
216 thawed potatoes (Figure 2). The firmness tester consists of the following components: a mean
217 to generate impulsive jet of air; a nozzle (having a diameter of 0.004 m) to direct the air onto
218 the surface of the specimen under investigation; a deformation measurement unit containing a
219 laser source to generate coherent source of light directed on the surface of the object impacted
220 by the air jet, a detector of the light which is reflected from the specimen surface, and an

221 analyzer to estimate the amount of deformation sustained by the product surface; a control
222 panel to change the pressure value and an appropriate software (developed in our lab) to
223 execute the test. Based on the preliminary trials, for measuring the firmness of frozen-thawed
224 potatoes, the air nozzle was located at 10 mm from the food surface and an air pressure of
225 5×10^5 Pa and air jet exposure time of 100 ms were found most appropriate. The estimated
226 pressure exerted onto the food surface was in the range of 3.32×10^5 Pa assuming a surface of
227 1.256×10^{-5} m² impacted by the air jet. Prussia, Astleford, Hewlett, & Hung (1994) used
228 impact pressure of 3.10×10^5 Pa (45 psia) in order to determine the firmness of potato.
229 Similar to the authors, Hung, McWatters, & Prussia (1998) who used the same exposure time
230 to determine the firmness of peaches.

231 The sample was placed on the sample platform below the air delivery nozzle and the position
232 of sample was adjusted using a positioner in order to ensure (i) the air jet and the laser hits the
233 same point on the sample and (ii) the distance between end of the nozzle and the sample
234 surface is same for all trials. Subsequently, by using the software air jet was directed on the
235 sample and the deformation was measured. The software yielded deformation results in volts
236 (Figure 3). The maximum deformation can be referred to as the difference between the
237 highest initial value and lowest value recorded by the deformation unit during the test. The
238 conversion of volts to mm (millimeter) based unit was made by multiplying with a conversion
239 factor (in the present case, volt value was multiplied by 2 to obtain final value in mm). The
240 final deformation value was an average of sixteen measurements.

241 **2.8. Microstructure examination**

242 **2.8.1. Cryo-SEM analysis**

243 Cryo-SEM analysis is a very specific technique which requires very careful and proper
244 sample preparation. A thin specimen of slab shape was cut from a given location of the frozen
245 food using a sharp scalpel. In our case, the central section of the frozen potato samples was
246 selected for collecting the sample. Also, in the case of structured tissue, given shape must be
247 provided to the sample to identify a given orientation; for example, in the case of a muscle,
248 the longer section of sample is usually longitudinal to the fibers in order to be able to do cut
249 view either parallel or perpendicular to the fibers. In the case of a vegetal tissue has no major
250 orientation so special care was taken mainly for the location, shape and size of the sample. It
251 was fixed into the groove notched in a copper sample holder (10 mm diam. 10 mm height)
252 using an OCT (optimal cutting temperature) compound (Tissue-Tek, Sakura, Finetek, USA).

An important technical issue lies in preventing any thawing of sample when the sample is contacted onto the sample order. To overcome this difficulty, the following protocol was used. All manipulations were done in a cold box filled with CO_2 sticks (-78.5 °C) in order to condition the sample which was kept in this ambiance. The sample holder was refreshed down to around 0 °C by contacting a CO_2 stick. Then a small amount of OCT was installed in the groove of the sample holder. Then, at the same time, the sample holder was contacted onto a CO_2 stick meanwhile the frozen sample was contacted to the OCT located in the groove. Within less than a few seconds, the sample was fixed onto the sample holder thanks to the freezing of the OCT. The very high thermal diffusivity of the copper material (sample holder) compared to the frozen sample ensures that the sample will not undergo any thawing when the sample is contacted to the sample holder. The sample was left for 2 min in a box filled with dry CO_2 to harden the OCT compound. After that, the sample was loaded onto a precooled copper specimen stub (in liquid N_2) and was quickly transferred in the cryo-preparation chamber of the cryo-SEM (LS10, ZEISS EVO, Germany) maintained under vacuum at – 80 °C, where it was cryo-fractured using a precooled sharp knife mounted inside the chamber. The fractured sample was etched in the preparation chamber for about 5 to 10 min to expose the subsurface information in order to allow a partial sublimation of the ice crystals. The etching time required adjustment depending on the size of the sample, the pressure level and the type of tissue. The sample was finally coated with a thin conducting layer of gold (5 nm) in the cryo-preparation chamber and then was transferred to the cold stage in the cryo-SEM (maintained at – 80 °C) where microstructural observation was performed. The fractured surfaces of potatoes were examined with an accelerating voltage of 11 kV. An illustration of the sample preparation steps is presented in Figure 4. It is worth mentioning that all the samples prepared for cryo-SEM analysis after the different freezing conditions acquired from the same potato.

2.8.2. Confocal laser scanning microscopy (CLSM)

The confocal laser scanning microscopy was also used for potatoes samples. Figure 5 provides a brief description of the protocol followed to prepare potatoes for the CLSM observations. The CLSM was performed using an Eclipse Ti inverted microscope (Nikon Ti A1, Japan). For each freezing condition, independent experiments were performed in triplicates.

It is worth noticing that the acridine orange (used for this study) is well known to be a

metachromic dye, especially for staining DNA and RNA. Such dye is able to give fluorescence with emissions wavelength depended on its interaction with chemical functions, charge or geometry of a compound. The acridine orange was chosen here as a dye able to stain simultaneously the different cell layers of the fruits as it has been widely applied for fluorescent staining of plant tissue with a high fluorescence emission. The maximum emission wavelength of this dye is 500-530 nm and excitation occurs at about 488 nm.

2.9. NMR relaxometry

For all the freezing protocols, NMR tests were performed for samples in frozen state (at − 20 °C) and frozen-thawed state (at 4 °C). Initially, the frozen samples were placed in the NMR tube (Ø = 10 mm) precooled to − 20 °C. Then the tube was quickly placed in the spectrometer (maintained at − 20 °C) and left for 10 min to ensure that the samples were at − 20 °C at the beginning of NMR test at a negative temperature. Upon completion of NMR tests in frozen condition, the same samples were thawed (at 4 °C for 4 h) and then NMR tests on frozen-thawed samples (at 4 °C) were carried out. In order to compare the damage caused by different freezing procedures, the NMR measurements of fresh samples were performed at 4 °C and were compared with results obtained for frozen-thawed samples obtained under various freezing protocols. The Minispec mq20 spectrometer (Bruker) at 0.47 T (20 MHz proton resonance frequency) equipped with a thermostated (± 0.1 °C) ^{1}H probe was used for NMR analysis. Triplicates were performed for each freezing condition of potato.

In the present study, T_2 (transverse) relaxation time of protons and their respective population in the product were evaluated. The T_2 distributions were determined using a Carr−Purcell−Meiboom−Gill (CPMG) sequence. For the NMR test at frozen and frozen-thawed state, the 180° pulse separation was 0.04 and 0.1 ms, 2000 and 10000 even echoes were collected, and the 1024 and 256 scans were acquired with a recycle delay of 1 and 5 s resulting in a total acquisition time of about 20 and 40 min respectively.

An inverse Laplace transformation (ILT) was applied to convert the relaxation signal into a continuous distribution of T_2 relaxation components. For this purpose, a numerical optimization method was used by including non-negativity constraints and L1 regularization and by applying a convex optimization solver primal–dual interior method for convex objectives (PDCO).

2.10. Statistical analysis

One-way ANOVA (analysis of variance) was used to determine any significant difference (in terms of freezing and quality characteristics) among the freezing conditions. Duncan's multiple range test was performed to determine differences between the means ($p < 0.05$).

3. Results and discussion

3.1. Effect of different freezing rates on temperature history

The representative temperature histories of potatoes frozen under the different freezing conditions are presented in Figure 6. The SF process yielded freezing curves having three stages i.e. the supercooling, nucleation, and phase change. Meanwhile, intermediate freezing (IF) exhibited only two stages (i.e. nucleation and phase change stages) and fast freezing (FF) showed only one stage (i.e. phase change state) in Figure 6. SF condition gave a degree of supercooling of 0.15 ± 0.07 °C, while no supercooling curve was observed for the other two freezing conditions. Similar freezing curves lacking obvious supercooling at higher freezing rates (at − 80 °C and liquid nitrogen immersion freezing) were also obtained by Cao et al. (2018) during freezing of blueberries. It was inferred by them that at a faster freezing rate the supercooled state might be unstable or lack persistence. The initial freezing point for SF and IF condition was recorded as -0.3 ± 0.14 and -0.73 ± 0.06 °C (Table 1). It seems that a slight depression in freezing point happened upon increasing the freezing rate. For FF condition, it was hard to detect the initial freezing point due to a rapid decline in the temperature during the freezing process. However, more replications could be helpful to be conducted prior to the confirmation of this outcome. Recently, Cao et al. (2018) also reported slight decrease (but not significant) in the initial freezing temperature of blueberries when the freezing rate was increased from 0.023 °C/s (at − 20 °C) to 0.049 °C/s (at − 40 °C) or 0.11°C/s (at − 80 °C) or 0.76 °C/s (liquid nitrogen immersion freezing). The initial freezing point of blueberries at 0.023, 0.049, 0.11, and 0.76 °C/s rates were recorded as -2.67 ± 0.32 °C, -3.23 ± 0.12 °C, -3.53 ± 0.35 °C and -3.36 ± 0.60 °C respectively (Cao et al., 2018). Among other freezing parameters being studied, the characteristic freezing time was found to be the shortest for FF condition (8.52 ± 1.53 min), followed by IF and SF condition (17.18 ± 0.79 min and 29.12 ± 3.94 min respectively) (Table 1). The time spent in this zone is very crucial as it determines the quality of the final product. From the perspective of higher quality preservation, a shorter width of this zone is desired. Similar to characteristic freezing time, the overall freezing time and the overall freezing rate also exhibited a similar trend.

3.2. Texture analysis

348 **3.2.1. Conventional method**

349 The confined compression test was the conventional method used to determine the texture of
350 potatoes. The hardness and Young's modulus values of fresh and thawed sample (from
351 different freezing conditions) are shown in Table 2. The values of fresh samples were
352 significantly different ($p < 0.05$) compared with those of the frozen-thawed samples. FF
353 process caused less decay in hardness value (≈ 50%) than IF process (≈ 62%) or SF process
354 (≈ 74%). However, significant differences in hardness values were observed only between SF
355 and FF samples. Young's modulus values exhibit a similar tendency as hardness values in
356 Table 2.

357 Khan & Vincent (1996) reported that compressive stiffness of potato less degraded when
358 freezing was performed at a higher freezing rate (10 °C/min) compared to slow freezing rate
359 (1 °C/min). According to Mazur (1984) and Chassagne-Berces, Fonseca, et al. (2010), lower
360 dehydration associated with small ice crystals induced less breakage of cell walls, and hence,
361 better texture preservation was achieved at higher freezing rates when compared to the slow
362 freezing rate. The high freezing rates also decrease the collapse of cell walls and generate less
363 intercellular spaces, and hence result in better texture preservation (Chassagne-Berces et al.,
364 2009). Besides, Phinney, Frelka, Wickramasinghe, & Heldman (2017) reported that the
365 extent of texture loss of potato depends on the freezing time. It was found that the hardness of
366 thawed potato reached a maximum value when the freezing time decreased dramatically up to
367 1000 s. Further, increase in freezing time beyond 1000 s to around 5000 s did not cause any
368 further texture loss in their case. Van Buggenhout et al. (2006) evaluated the effect of three
369 different freezing conditions i.e. slow freezing (freezing time (f_t) = 300 min), rapid freezing (f_t
370 = 40 min)) and cryogenic freezing (f_t = 10 min)) on the hardness retention of thawed carrots.
371 They reported that rapid and cryogenic freezing condition had a higher hardness retention
372 than the slow freezing condition.

373 **3.2.2. Laser-Puff firmness tester**

374 Laser-Puff firmness tester allows rapid and non-destructive texture analysis of the food
375 products (Hung et al., 1998; McGlone & Jordan, 2000; Prussia et al., 1994). An attempt was
376 made to use this method, to the best of our knowledge for the first time, for measuring the
377 texture of frozen-thawed fruits and vegetables. In this section, the results from laser-puff
378 firmness analysis of potato will be presented and discussed. The deformation curves and
379 deformation values obtained during laser-puff firmness test of fresh and frozen-thawed

potatoes (under different freezing rates) are shown in Figure 7. The fresh samples had significantly ($p < 0.05$) lower deformation value than all frozen-thawed samples (Figure 7b). As expected, SF samples suffered the highest deformation during the tests. The deformation occurred at IF samples was less than SF samples, but greater than the FF samples. However, the deformation values of IF samples were not significantly different ($p > 0.05$) from the values of SF and FF samples. The FF sample showed lower deformation than the other conditions, and those values were found to be significantly lower than SF, but not significantly different from IF values. The obtained results (in terms of deformation) are coherent with those obtained by the classical method (discussed above). In conclusion, this method could distinguish fresh and frozen-thawed samples, but had limited capability to differentiate the tested freezing conditions.

3.3. NMR relaxometry

NMR tests were performed for the samples in frozen (at – 20 °C) and frozen-thawed states (at 4 °C) after being frozen under the different freezing conditions. Figure 8 shows the results from NMR relaxometry of potato in a frozen state (at – 20 °C). The relaxation peaks, T_2^* (including magnetic field inhomogeneities) and T_2 of frozen samples provide information about the structure of the samples and about the unfrozen water at – 20 °C (Figure 8). $T_{2\alpha}^*$ is the relaxation peak of protons associated with the macromolecules. $T_{2\beta}^*$, $T_{2\gamma}$, and $T_{2\delta}$ are the relaxation peaks associated with the protons of unfrozen water (Foucat & Lahaye, 2014; Luyts et al., 2013). Results showed that the $T_{2\alpha}^*$ values (relaxation time and proton population) for all freezing conditions were similar, which indicated that the different freezing protocols didn't influence differently the systems at a macromolecular level (Figure 8a). Similarly, $T_{2\beta}^*$ values were not significantly different among the different freezing conditions (Figure 8a). If we follow the hypothesis that the faster the freezing process is the less is the destruction it imparts, the values of relaxation peak components of non-freezable water ($T_{2\gamma}$ and $T_{2\delta}$) associated with the samples frozen quickly provide an evidence of better preservation of structures. Only samples that were frozen slowly (at – 18 °C) showed different values for these relaxation peak components (Figure 8a and b). It was observed that $T_{2\gamma}$ component values (relaxation time and proton population) for IF and FF conditions were not significantly different ($p > 0.05$) between each other, meanwhile, these values were significantly different ($p < 0.05$) with that obtained for SF condition. The lowest value of $T_{2\gamma}$ time observed for slow freezing (0.72 ms instead of around 0.80 ms for the other freezing conditions) can be

412 explained by a greater destruction followed by a diffusion of "solutes" inducing a relative
413 increase in viscosity (Lahaye, Falourd, Limami, & Foucat, 2015). The $T_{2\delta}$ component
414 relaxation times for all freezing conditions were not different from each other. But, the
415 $T_{2\delta}$ component proton population was significantly lower ($p < 0.05$) for SF compared to the
416 other conditions. This seemed to indicate the loss of fluid from the respective water
417 compartment due to greater damage occurred during SF process. No significant difference (p
418 > 0.05) (with respect to $T_{2\delta}$ component proton population) was observed among IF and FF
419 samples.

420 Figure 9 represents the T_2 peaks of fresh and frozen-thawed samples at 4 °C. With regard to
421 fresh samples, the distribution of T_2 relaxation peak has five components (T_{2a}, T_{2b}, T_{2c}, T_{2d} &
422 T_{2e}), whose values averages are in good agreement with the literature data (Rutledge, Rene,
423 Hills, & Foucat, 1994). Based on these data, an allocation of different components of T_2 have
424 been proposed: T_{2a} and T_{2b} are the relaxation peaks associated with the water present in the
425 cell walls and the vacuolar membrane. T_{2c} is the relaxation peak of water in starch grains. T_{2d}
426 and T_{2e} are the relaxation peaks of water in the non-starch vacuoles, the nucleus and the
427 cytoplasm (Rutledge et al., 1994). The measurement of the T_2 components values (relaxation
428 time and proton population) of the samples after thawing makes it possible to observe the
429 influence of different freezing protocols on the mobility of the water compared with the fresh
430 samples. It can be seen that the freezing-thawing process affects the resolution of the T_2
431 distribution peaks (Figure 9). For instance, the T_{2c} and T_{2d} components which were
432 distinctively visible in the fresh sample could no longer be differentiated in the frozen-thawed
433 sample. Apart from this, T_{2d} and T_{2e} times of fresh potato decreased upon freezing-thawing.

434 Among the different freezing conditions used in this study, only FF (at – 74 °C) preserved T_2
435 components distributions with good resolution over the entire time range studied. Four T_2
436 components were characterized for FF (against five for fresh samples), meanwhile, for IF and
437 SF conditions, three and two T_2 components could only be characterized. For all freezing
438 conditions, the mobility of water associated with non-starch vacuoles, nuclei and cytoplasm
439 (T_{2d} and T_{2e}) decreased. This reflects a reorganization of the fluids following a partial rupture
440 of the cellular structures (Lahaye et al., 2015) irrespective of the freezing speed. Compared to
441 fresh sample, the decrease in T_{2e} time was lower for FF process ($\approx$ 46%) and was followed by
442 SF ($\approx$ 53%) and IF ($\approx$ 54%) process. However, no significant difference among freezing
443 processes (in terms of T_{2e} time) was observed. T_{2e} component proton population data reveal

that FF and IF samples had similar values ($p > 0.05$) as the fresh sample, while it significantly decreased ($p < 0.05$) in the case of SF samples. This decrease was followed by an increase in proton population of the consecutive peak in the T_2 distribution curve for SF samples (Figure 9b), depicting the transfer of water between two compartments which might have probably happened due to the breakdown of vacuolar membrane. However, no such trend was observed for other freezing conditions (Figure 9c and d). The T_2 component values (relaxation time and proton proportion) adjacent to the T_{2e} for SF samples was significantly different ($p < 0.05$) from those of FF and IF conditions. The T_{2a} and T_{2b} components of FF samples had similar relaxation times as the fresh samples, illustrating the overall better preservation of membranes and walls (despite a reorganization at the level of populations). IF also fairly maintained the T_{2b} component values and they were found to be similar to the fresh sample. Due to poor resolution, it was difficult to extract T_{2a} component value for IF samples. T_{2a} and T_{2b} component values for SF sample also could not be resolved due to the poor resolution of the peak.

Cao et al. (2018) used T_2 time of water proton to differentiate fresh blueberries from frozen-thawed blueberries. They found that the freezing-thawing process caused a reduction in T_2 time of vacuole, cell wall, cytoplasm and extracellular water compared to the fresh sample. With respect to the proton population of different compartments, it was observed that freezing and thawing did not cause any alteration in the proton population of different compartments compared to a fresh samples. Moreover, they also used T_2 relaxation peak data to distinguish different freezing conditions (i.e. freezing at – 20, – 40, – 80 °C and freezing by immersing in liquid nitrogen). It was reported that among all freezing conditions, – 80 °C freezing conditions better maintained T_2 time of vacuole ($p < 0.05$) depicting better protection to the vacuole membrane. Unlike them, we did not observe any significant difference among the freezing trials with respect to the relaxation times of thawed samples frozen by different methods, however, we could observe a significant differences between FF, IF and SF conditions with respect to the proton population of T_2 peaks. The proton population data (associated with T_2 times) was used by Zhang et al. (2018) to study the effect of state/phase transition on water mobility in frozen mango during 4-week storage.

3.4. Drip loss

Drip loss is one of the commonly and widely used methods to evaluate the freeze damage in frozen products (especially in meat, fish, fruits and vegetable matrices). This method

estimates the freeze damage at a global level, or in other terms, provides an average value of freeze damage of a product. In this section the impact of the studied freezing conditions on the exudate loss from the product will be presented and discussed. Figure 10 shows the dependence of drip loss on freezing rate. The results reveal that drip loss decreased slightly when freezing rate was increased, however, significant difference was observed only between samples that were frozen under FF and SF conditions. IF samples were not significantly different ($p > 0.05$) compared to the samples of the other two freezing rates. The drip loss results exhibited similar trends to those of T_{2e} component proton population from NMR that showed that the application of − 18 °C freezing protocol maintained less the intracellular water content. This result may be attributed to a better preservation of the intracellular water and to a lower damage of the pectocellulosic walls from the faster freezing rates. As a result, this method was able to detect the differences between the selected freezing rates. The water holding capacity of the frozen sample is linked to the size and location of ice crystals as well as the thawing rate (Van Buggenhout, Messagie, et al., 2006). The formation of large ice crystals in the cellular matrix can affect the water holding capacity of a cellular matrix in two ways: (i) large ice crystals genesis during freezing can damage the cell membrane due to mechanical effects, to cryo-concentration phenomena and shrinkage effects (particularly during slow freezing rates) which in turn, will promote loss of mass during thawing (Bevilacqua, Zaritzky, & Calvelo, 1979; Delgado & Sun, 2001; Sadot et al., 2017) and (ii) higher drip loss may occur due to the formation of bigger ice crystals which correspond to smaller specific surface area. This fact is associated with water re-absorption decrease during thawing (Bevilacqua et al., 1979; Sadot et al., 2017). Charoenrein & Owcharoen (2016) and Fuchigami, Hyakumoto, & Miyazaki (1995) observed decrease in exudate loss with increasing freezing rates in frozen mangoes and carrots.

3.5. Colour

Freezing-thawing process significantly ($p < 0.05$) affected the colour parameters (L^*, a^*, and b^* values) of the unblanched potatoes Figure 11. The L^* value (or lightness) and b^* value (or yellowness) decreased, while the a^* value (redness) increased for potatoes after freezing-thawing (Figure 11a, b and c). These results are in agreement with the previously reported study on freezing-thawing of unblanched potatoes (Koch et al., 1996). The colour change during the freezing-thawing process of unblanched potato has been attributed to the browning reaction that generally happens due to enzymatic activity during thawing process (Cano, 1996; Koch et al., 1996). The freezing rates had little effect on the colour parameters of

potatoes. Interestingly, it was found that FF process increased the redness value of potatoes significantly ($p < 0.05$) than compared to SF process. Chassagne-berces, Fonseca, et al. (2010) reported that freezing at – 80 °C increased the redness value of Golden Delicious apple compared to the one frozen at – 20 °C. The redness value of IF samples was not significantly different compared with those frozen under FF and SF conditions. No significant differences for rest of the colour parameters (L^* value, b^* value and ΔE) were observed among the freezing protocols.

3.6. Microstructure analysis

3.6.1. Cryo-SEM analysis

Scanning electron microscopy permits to obtain very high-quality images of a food matrix microstructure. With respect to the frozen cellular matrices, micrographs acquired using SEM (especially the cryo-SEM) provide important details about ice and cell morphology (shape of the cell and the integrity of pectocellulosic walls). To the best of our knowledge, for the first time, cryo-SEM was used to compare the changes occurring to the microstructure of potato at different freezing rates. Figure 12 illustrates the SEM images of fresh and frozen potatoes. The images of fresh and frozen potato were obtained using an environmental SEM (E-SEM) and cryo-SEM, respectively. It can be seen in the figure that the fresh potato has polyhedral shape cells with starch embedded in it. The microstructure morphology upon freezing depended highly on the freezing rate being applied. The SF process not only created bigger ice crystals in the cells but also caused the highest damage to the cellular structure. The cells were highly distorted (deformed cells with broken and irregular cell wall structure) under SF conditions. The IF process produced smaller ice crystals and maintained the cell wall integrity better than the SF conditions. However, some cells lost their polyhedral shape and turned almost into round shape when freezing was performed at IF conditions (cells pointed by the orange arrow in Figure 12e and Figure 12f). The FF process yielded smallest ice crystals compared to other freezing processes. Moreover, it can also be observed that the cellular structure (in terms of cell shape i.e. polyhedral shape and cell wall integrity) was maintained well. Similar to the authors, Bomben & King (1982), Chassagne-Berces et al. (2009) and Chassagne-Berces, Fonseca, et al. (2010) cryo-SEM imaging could differentiate the apples frozen by different freezing conditions based on microstructure. Moreover, they also observed that slow freezing process (e.g. freezing at – 20 °C or 0.4 K/min) altered the shape of the cell more than the fast freezing processes (e.g. freezing at – 80 °C or 450 K/min or by liquid nitrogen immersion freezing). The calculations for ice crystals size were not made as it was

542 difficult to locate the boundary of the ice crystals. Moreover, the ice crystals had a 3D
543 structure and if the calculation were made, we could get only 2D information, this would have
544 led to an inaccurate estimation of the size of the ice crystals. Chassagne-Berces et al. (2009)
545 quantified the size of ice crystals formed at different freezing protocols (at – 20 °C, – 80 °C
546 and by immersion in liquid nitrogen) from the cryo-SEM images using gray level
547 granulometry based on mathematical morphology. They reported that the size of ice crystals
548 was between 10 and 30 μm after freezing at – 20 °C and below 5 μm for faster freezing at
549 – 80 °C and by immersion in liquid nitrogen conditions. Since we were not able to quantify
550 the size of ice crystals, a direct comparison with their results remained difficult.

551 **3.6.2. CLSM analysis**

552 CLSM images of fresh and frozen-thawed potatoes are presented in Figure 13. This method
553 provides information about the status of the cell such as the shape of cells and integrity of the
554 cell wall. Compared to the fresh sample, the cells were highly disorganised and distorted in
555 SF samples. The altered shape of the cells and damaged cell wall structures in the slowly
556 frozen sample can be observed in the CLSM images (Figure 13). The buckled and folded cell
557 wall structure in SF samples indicated a major dehydration related damage that generally
558 happens at lower freezing rates (Chassagne-Berces et al., 2009; Gao & Critser, 2000; Mazur,
559 1977, 1984). IF process affected the cell shape as cell walls were found slightly distorted,
560 while IF seemed to have fairly preserved the integrity of the cellular structure and avoid cell
561 wall rupture as observed by SF. Moreover, extracellular spaces that can be generated due to
562 the freezing-thawing process were observed in IF samples (Figure 13c), while it was missing
563 in FF samples (Figure 13d). It can be seen (Figure 13c and Figure 14c) that these gaps were
564 adjacent to the shrunk cells, which clearly indicates the dislocation of water from the inner of
565 the cell to the extracellular space. It was difficult to distinguish freezing-thawing induced gaps
566 between the cells in SF sample as the structure was completely destroyed. FF condition
567 helped to preserve the original shape and integrity of the cellular structure. The results from
568 CLSM (in terms of cell morphology) were coherent with the results from cryo-SEM.
569 Charoenrein & Owcharoen (2016) used CLSM to study the effect of freezing rates and freeze-
570 thaw cycles on the cellular structure of mangoes. Using this method, they were able to
571 observe the freezing-thawing related degradation of cellular structure. Moreover, based on
572 CLSM images, they were able to discriminate the different freezing protocols (i.e. freezing at
573 – 80, – 40 and – 20 °C). For instance, CLSM micrographs depicted that cells observed after

fast freezing (at − 80 °C) and thawing suffered a minimal amount of degradation; the cells were still round and similar to cells from fresh tissues. The IF frozen (at − 40 °C)-thawed sample showed a slightly flat cellular structure, while the slow frozen (at − 20 °C)-thawed mangoes exhibited larger changes. The cells of the slowly frozen samples lacked uniformity and some intercellular spaces were also observed in slowly frozen tissues. Sirijariyawat, Charoenrein, & Barrett (2012) used CLSM to study the change in cellular morphology in mangoes upon freezing-thawing. They reported that freezing (at − 50 °C) followed by storage (at − 20 °C chest freezer for 14 days) and thawing (at 4 °C for 2 h and kept at 25 °C for 30 min prior to analysis) of mango samples transformed the well-defined circular to elliptical regular cells of fresh sample to irregular shaped cells with disintegrated cell wall.

4. Conclusions

In this study, potato samples were frozen under different freezing regimes and their quality were evaluated using different techniques. The slowly frozen (− 18 °C) potatoes exhibited supercooling during freezing while no supercooling was noticed for other freezing conditions (i.e. − 30 °C- intermediate freezing process and − 74 °C- fast freezing process). The initial freezing point (initial freezing temperature) could be detected for slow freezing and intermediate freezing conditions, while it was hard to detect the initial freezing point for the fast freezing condition. The initial freezing point temperature data for slow freezing and intermediate freezing conditions revealed that a depression in freezing point occurred when freezing rate was increased. The slow freezing process resulted in coarser ice crystals and also caused the highest damage to the cellular structure. The cells were highly distorted (deformed cells with buckled and folded cell wall structure) when the slow freezing condition was used. Intermediate freezing rate process led to relatively fine ice crystals compared to slow freezing process. Although IF process led to greater cell wall structure integrity, however, it was not able to preserve the cell shape. The fast freezing process not only promoted the formation of very fine ice crystals but also preserved the morphology of the cells. The NMR analytical parameters, texture and drip loss showed limitations to differentiate the different freezing protocols. . None of the freezing protocols preserved the colour parameters of the fresh potato.

Benchmarking of freeze damage assessment methods for vegetables on the basis of efficiency, accuracy, cost-of operation, and ease of operation

In this section, freeze damage assessment methods used during this study were evaluated based on various benchmarking parameters and a decision table (dedicated to benchmarking

study) was proposed. Table 3 summarizes the results obtained within this study. Pros and cons related to the different methods considered in this study for assessing the freeze damage in potato were discussed.. These observations would provide useful information about the analytical techniques that can be used to estimate freeze damage efficiently.

The focused freeze damage assessment technologies like CLSM, and global freeze damage assessment techniques like texture analysis (also includes laser-puff texture analysis), low field NMR relaxometry, and colour analysis tests used in this study was found to be relevant methods to distinguish the fresh samples from frozen/thawed sample.

The acquired results suggest that cryo-SEM and CLSM are suitable for validating minor quality changes among the different freezing protocols. Meanwhile, the global methods such as texture, NMR, and drip loss can only reflect larger quality changes.

In order to compare freezing protocols, colour analysis was found to be an unsuitable parameter.

Efficiency and accuracy wise, cryo-SEM and CLSM can be termed as best methods to analyze the freezing injuries.

NMR, cryo-SEM and CLSM techniques are expensive techniques, whereas texture analysis, drip loss measurements, colour analysis are cost-effective technologies. The analyses time for NMR is long, while other methods take substantially less time.

From a global point of view, a debate could be opened on which is the most relevant technique to assess freeze damage. Two key parameters can be tackled, (i) the size of the field that is embraced by the technique and (ii) the representative size of the technique. For example, NMR will tackle a sample of ca 1 cm and will provide information at the level of a water molecule (2.75 Å). Cryo-SEM will look at field of ca 100 µm with information at nanometer scale, even though in this case the freeze damage is observed at the scale of an ice crystal (*circa* 10 µm). The ratio between the size of field and the representative size of technique could be considered as a kind of "freeze damage assessment index" (FDA Index) to assess the relevance of each technique. The higher the FDA index will be, the useful will be (*a priori*) the technique. From such point of view NMR looks like the best candidate, even though the interpretation and quantification of the freeze damage based on T_1 and T_2 values are not very well documented in the literature and still remain quite subjective. The major concerns relates to the size of the field. Observation of the freeze damage on a single cell can

637 be very informative and detailed, but ca a hundred of cell should be analyzed to obtain an
638 averaged information, which is out of reach for time reasons. Another aspect relies on the
639 possibility to repeat the analysis and on the time needed for a single measurement. CLSM and
640 Cryo-SEM bring informative images that can help to visualize the defaults and that can
641 support observations done with other techniques at a broader field like NMR, texture, drip
642 losses. The precision of the analytical method is one of the most important factors when choosing the
643 methods for freeze damage assessment. A method that imparts minimum error to the measured result
644 will help in better understanding of the impact of process conditions on the sample. Based on the error
645 calculations made for the quantitative methods (Table 3), the drip loss measurement seemed to be
646 more satisfactory , followed by colour analysis, hardness analysis, deformation analysis by the laser-
647 puff tester, NMR analysis and Young's Modulus analysis. Overall, the error imparted by the
648 analytical techniques were quite low in values.

649 The proper assessment of freeze damage remains a challenge and requires a mass of
650 experimental work before drawing any conclusion. However, this comparative study is maybe
651 the first one that proposes a benchmarking of so many different analytical techniques often
652 considered to assess the freeze damage.

653 **Acknowledgements:**

654 This work received financial support from the French National Research Agency (ANR) and
655 the Swedish Research Council FORMAS under the FREEZEWAVE project (SUSFOOD–
656 ERANET, FR: ANR-14-SUSF-0001, SE: 2014-1925). We would like to thank Anthony Ogé
657 (ONIRIS) for designing the laser-puff firmness tester. A special thanks to McCain food for
658 supplying potatoes required for the experimentation. The authors would also like to thank
659 Romain Mallet (Univ-Angers - SCIAM) for their assistance in cryo-SEM imaging
660 respectively.

661

662 **References**

663 Alvarez, M. D., Canet, W., & López, M. E. (2002). Influence of deformation rate and degree
664 of compression on textural parameters of potato and apple tissues in texture profile
665 analysis. *European Food Research and Technology*, *215*, 13–20.
666 Anon (2018). http://cobra.rdsor.ro/cursuri/cielab.pdf. Retrieved on 3rd July 2018.
667 Barbosa-Cánovas, G. V., Altunakar, B., & Mejía-Lorío, D. J. (2005). Introduction to freezing.
668 *Freezing of fruits and vegetables: An agribusiness alternative for rural and semi-rural*
669 *areas* (Vol. 158, pp. 1-36). Rome: Food & Agriculture Organization.
670 Bevilacqua, A., Zaritzky, N. E., & Calvelo, A. (1979). Histological measurements of ice in
671 frozen beef. *Journal of Food Technology*, *14*, 237–251.
672 Bomben, J. L., & King, C. J. (1982). Heat and mass transport in the freezing of apple tissue. *J.*
673 *Fd Technol.*, *17*, 615–632.
674 Bourne, M. C. (1968). Texture Profile of Ripening Pears. *Journal of Food Science*, *33*, 223–
675 226.
676 Cano, M. P. (1996). Vegetables. In L. E. Jeremiah (Ed.), *Freezing effects on food quality* (pp.
677 247–298). New York: Marcel Dekker.Inc.
678 Cao, X., Zhang, F., Zhao, D., Zhu, D., & Li, J. (2018). Effects of freezing conditions on
679 quality changes in blueberries. *Journal of the Science of Food and Agriculture*, 98, 4673-
680 4679.
681 Charoenrein, S., & Owcharoen, K. (2016). Effect of freezing rates and freeze-thaw cycles on
682 the texture, microstructure and pectic substances of mango. *International Food Research*
683 *Journal*, *23*, 613–620.
684 Chassagne-berces, S., Fonseca, F., Citeau, M., & Marin, M. (2010). Freezing protocol effect
685 on quality properties of fruit tissue according to the fruit , the variety and the stage of
686 maturity. *LWT - Food Science and Technology*, *43*, 1441–1449.
687 Chassagne-Berces, S., Poirier, C., Devaux, M. F., Fonseca, F., Lahaye, M., Pigorini, G.,
688 Girault, C., Marin, M., & Guillon, F. (2009). Changes in texture, cellular structure and
689 cell wall composition in apple tissue as a result of freezing. *Food Research International*,
690 *42*, 788–797.
691 Chevalier, D., Le Bail, a., & Ghoul, M. (2000). Freezing and ice crystals formed in a
692 cylindrical food model: Part II. Comparison between freezing at atmospheric pressure
693 and pressure-shift freezing. *Journal of Food Engineering*, *46*, 287–293.
694 Delgado, A. E., & Sun, D. W. (2001). Heat and mass transfer models for predicting freezing
695 processes – a review. *Journal of Food Engineering*, *47*, 157–174.
696 Fennema, O. (1966). An over-all view of low temperature food preservation. *Cryobiology*,
697 *3*(3), 197–213.
698 Foucat, L., & Lahaye, M. (2014). Short communication A subzero ^{1}H NMR relaxation
699 investigation of water dynamics in tomato pericarp. *Food Chemistry Journal*, *158*, 278–
700 282.
701 Fuchigami, M., Hyakumoto, N., & Miyazaki, K. (1995). Programmed Freezing Affects
702 Texture, Pectic Composition and Electron Microscopic Structures of Carrots. *Journal of*
703 *Food Science*, *60*, 137–141.
704 Gao, D., & Critser, J. K. (2000). Mechanisms of Cryoinjury in Living Cells. *ILAR Journal*,
705 *41*, 187–196.
706 Hung, Y. C., McWatters, K. H., & Prussia, S. E. (1998). Peach Sorting Performance of
707 Anondestructive Laser Air-Puff Firmness Detector. *Applied Engineering in Agriculture*,
708 *14*, 513–516.
709 Jahncke, M., Baker, R. C., & Regenstein, J. M. (1992). Frozen storage of unwashed cod
710 (Gadus morhua) frame mince with and without kidney tissue. *Journal of Food Science*,

711 *57*, 575–580.
712 Jha, P. K., Xanthakis, E., Chevallier, S., Jury, V., & Le-Bail, A. (2018). Assessment of freeze
713 damage in fruits and vegetables. *Food Research International*. In press, accepted article.
714 Khan, A. A., & Vincent, J. F. V. (1993). Compressive Stiffness and Fracture Properties of
715 Apple and Potato Parenchyma. *Journal of Texture Studies*, *24*, 423–435.
716 Khan, A. A., & Vincent, J. F. V. (1996). Mechanical damage induced by controlled freezing
717 in apple and potato. *Journal of Texture Studies*, *27*, 143–157.
718 Koch, H., Seyderhelm, I., Wille, P., Kalichevsky, M. T., & Knorr, D. (1996). Pressure-shift
719 freezing and its influence on texture, colour, microstructure and rehydration behaviour of
720 potato cubes. *Nahrung*, *40*, 125–131.
721 Lahaye, M., Falourd, X., Limami, A. M., & Foucat, L. (2015). Water mobility and
722 microstructure evolution in the germinating medicago truncatula seed studied by NMR
723 relaxometry. A revisited interpretation of multicomponent relaxation. *Journal of*
724 *Agricultural and Food Chemistry*, *63*, 1698–1710.
725 Li, B., & Sun, D. W. (2002). Effect of power ultrasound on freezing rate during immersion
726 freezing of potatoes. *Journal of Food Engineering*, *55*, 277–282.
727 Lovelock, J. E. (1957). The denaturation of lipid-protein complexes as a cause of damage by
728 freezing. *Proceedings of the Royal Society of London. Series B, Biological Sciences*, *147*,
729 427–433.
730 Luyts, A., Wilderjans, E., Waterschoot, J., Haesendonck, I. Van, Brijs, K., Courtin, C. M.,
731 Hills, B., & Delcour, J. A. (2013). Low resolution 1H NMR assignment of proton
732 populations in pound cake and its polymeric ingredients. *Food Chemistry*, *139*, 120–128.
733 Mazur, P. (1977). The role of intracellular freezing in the death of cells cooled at
734 supraoptimal rates. *Cryobiology*, *14*, 251–272.
735 Mazur, P. (1984). Freezing of living cells: mechanisms and implications. *American Journal of*
736 *Physiology–Cell Physiology*, *247*, C125–142.
737 McGlone, V. A., & Jordan, R. B. (2000). Kiwifruit and apricot firmness measurement by the
738 non-contact laser air-puff method. *Postharvest Biology and Technology*, *19*, 47–54.
739 Orlowska, M., Havet, M., & Le-Bail, A. (2009). Controlled ice nucleation under high voltage
740 DC electrostatic field conditions. *Food Research International*, *42*, 879–884.
741 Penny, I. F. (1975). Use of a centrifuging method to measure the drip of pork Longissimus
742 dorsi slices before and after freezing and thawing. *Journal of the Science of Food and*
743 *Agriculture*, *26*, 1593–1602.
744 Phinney, D. M., Frelka, J. C., Wickramasinghe, A., & Heldman, D. R. (2017). Effect of
745 Freezing Rate and Microwave Thawing on Texture and Microstructural Properties of
746 Potato (Solanum tuberosum). *Journal of Food Science*, *82*, 933–938.
747 Prussia, S. E., Astleford, J. J., Hewlett, B., & Hung, Y. C. (1994). *5,372,030*. U.S. Patent and
748 Trademark Office.
749 Reid, D. S. (1997). Overview of physical/chemical aspects of freezing. In M. C. Erickson &
750 Y.-C. Hung (Eds.), *Quality in frozen food* (pp. 10–28). Dordrecht: Springer
751 Science+Business Media.
752 Rutledge, D. N., Rene, F., Hills, B. P., & Foucat, L. (1994). Magnetic resonance imaging
753 studies of the freeze□drying kinetics of potato. *Journal of Food Process Engineering*,
754 *17*, 325–352.
755 Sadot, M., Curet, S., Rouaud, O., Le-bail, A., & Havet, M. (2017). Numerical modelling of an
756 innovative microwave assisted freezing process. *International Journal of Refrigeration*,
757 *80*, 66–76.
758 Shi, X., Datta, A. K., & Mukherjee, Y. (1998). Thermal Stresses From Large Volumetric
759 Expansion During Freezing of Biomaterials. *Transactions of the ASME*, *120*, 720–726.
760 Shi, X., Datta, A. K., & Mukherjee, Y. (1999). Thermal fracture in a biomaterial during rapid

761 freezing. *Journal of Thermal Stresses*, *22*, 275–292.
762 Shi, X., Datta, A. K., & Throop, J. A. (1998). Mechanical Property Changes during Freezing
763 of a Biomaterial. *Transactions of the ASAE*, *41*, 1407–1414.
764 Singh, R. P., & Heldman, D. R. (2009). Food Engineering. In S. L. Taylor (Ed.), *Introduction*
765 *to Food Engineering* (4th ed., pp. 501–541). San Diego: Academic Press publications.
766 Sirijariyawat, A., Charoenrein, S., & Barrett, D. M. (2012). Texture improvement of fresh and
767 frozen mangoes with pectin methylesterase and calcium infusion. *Journal of the Science*
768 *of Food and Agriculture*, *92*, 2581–2586.
769 Van Buggenhout, S., Lille, M., Messagie, I., Von Loey, A., Autio, K., & Hendrickx, M.
770 (2006). Impact of pretreatment and freezing conditions on the microstructure of frozen
771 carrots: Quantification and relation to texture loss. *European Food Research and*
772 *Technology*, *222*, 543–553.
773 Van Buggenhout, S., Messagie, I., Maes, V., Duvetter, T., Loey, A. Van, & Hendrickx, M.
774 (2006). Minimizing texture loss of frozen strawberries : effect of infusion with
775 pectinmethylesterase and calcium combined with different freezing conditions and effect
776 of subsequent storage / thawing conditions. *European Food Research and Technology*,
777 *223*, 395–404.
778 Zhang, Y., Zhao, J. H., Ding, Y., Xiao, H. W., Sablani, S. S., Nie, Y., Wu, S.-J., & Tang, X.
779 M. (2018). Changes in the vitamin C content of mango with water state and ice crystals
780 under state/phase transitions during frozen storage. *Journal of Food Engineering*, *222*,
781 49–53.

782

783

Captions for the Figures

Figure 1: Load-strain curve providing detail about the firmness of the potato during the compression tests.

Figure 2: Laser-puff firmness testing prototype.

Figure 3: A representative deformation curve obtained while performing the laser puff test. Conversion of volts to mm: 1 V = 2 mm.

Figure 4: Illustration of sample preparation step prior to imaging in cryo-SEM.

Figure 5: Protocol followed for CLSM imaging of unblanched potato.

Figure 6: Representative freezing curves of potatoes under different freezing methods.

Figure 7: (a) Deformation curve obtained for fresh and frozen-thawed samples (conversion of volts to mm: 1 V = 2 mm) and (b) deformation values (in mm) for fresh and frozen-thawed potatoes (under different freezing rates) acquired using laser-puff firmness tester. SF (slow freezing at − 18 °C), IF (intermediate freezing at − 30 °C) and FF (fast freezing at − 74 °C).

Figure 8: Distributions of relaxation peak components ((a) T_2^* and (b) T_2) at − 20 °C of potato samples frozen by various freezing protocols: slow freezing at − 18 °C (red lines), intermediate freezing at − 30 °C (blue lines), and fast freezing at − 74 °C (black lines). (The x-axis correspond to the relaxation times expressed in ms (milliseconds).

Figure 9: T_2 relaxation peak data of frozen-thawed potatoes at 4 °C: (a) fresh sample, (b) after freezing at − 18 °C (c) after freezing at − 30 °C and (d) after freezing at − 74 °C.

Figure 10: Effect of different freezing conditions on the drip loss of potato.

Figure 11: Effect of freezing protocols on color parameters (a - L^* value or Lightness, b - a^* value or Redness, c - b^* value or Yellowness and d - ΔE) of potato. Mean values of 9 repetitions are represented with confidence interval.

Figure 12: Microstructure of potato before and after freezing under the different freezing protocols. (a, b) environmental SEM images of the fresh cell showing the cellular structure and starch granules imbedded into it. Cryo-SEM after freezing at − 18 °C-SF (c, d), at − 30 °C-IF (e, f) and at − 74 °C-FF (g, h), respectively. White colored arrows in images are pointing the cells containing ice crystals. Red arrow showing the area where the breakdown of cell structure happened. Orange arrows indicate the cells that might have transformed from polyhedral to almost round shape. Other abbreviations in the picture are A: air space; S: starch granule; W: cell wall structure.

Figure 13: Microstructure evaluation using CLSM: (a) fresh potato, (b) frozen-thawed after freezing at − 18 °C-SF, (c) at − 30 °C-IF and (d) at − 74 °C-FF. Other abbreviations in the picture are S: starch granule, W: cell wall, S_p is probably the gap created when of cell moved apart from each other as a consequence of freezing-thawing. The red arrows indicating the deformed, distorted and shrunk cells. Orange arrows indicating loss of regularity of the cell

walls compared to fresh and FF samples. Yellow arrows showing the folded and buckled cell wall structure formed due to SF process.

Figure 14: Microstructure evaluation using CLSM: (a) single cell of fresh potato, (b) single potato cell (imaged in frozen state) after freezing at − 18 °C (SF), (c) frozen-thawed potato structure after frozen at − 30 °C (IF) and (d) frozen-thawed potato structure after frozen at − 74 °C(FF) (d). S_p is probably the gap between the cells created due to freezing-thawing process. Black arrow showing a part of broken cell wall. White arrow indicating discontinuity in the cell wall structure. Red arrow evince the deformed cell with irregular cell wall structure (orange arrows).

850 **Captions for Tables**

851 Table 1. Effects of different freezing protocols on the freezing properties of potatoes.

852 Table 2. Textural parameters measured for potatoes under different freezing conditions.

853 Table 3. Benchmarking study on freeze damage assessment methods.

879 Table 1. Effects of different freezing protocols on the freezing properties of potatoes.

Freezing condition	Initial freezing point (°C)	Characteristic freezing time (min)	Overall freezing time (min)	Overall freezing rate (°C/min)
− 18 °C (SF)	− 0.3 ± 0.14	29.12 ± 3.94	72.30 ± 0.14	0.48 ± 0.00
− 30 °C (IF)	− 0.73 ± 0.06	17.18 ± 0.79	26.31 ± 0.62	1.36 ± 0.05
− 74 °C (FF)	n.d.	8.52 ± 1.53	14.51 ± 1.49	2.51 ± 0.25

880

882 Table 2. Textural parameters measured for potatoes under different freezing conditions.

Parameters	Hardness (N)	Young's modulus (MPa)
Fresh	190 ± 19^{a}	5.46 ± 0.44^{a}
SF (at − 18 °C)	47 ± 11^{c}	1.37 ± 0.33^{c}
IF (at − 30 °C)	$68 \pm 16^{b, c}$	$2.09 \pm 0.41^{b, c}$
FF (at − 74 °C)	90 ± 8^{b}	2.60 ± 0.45^{b}

883

Table 3. Benchmarking study on freeze damage assessment methods.

Freeze damage assessment methods for	Focused Methods		Global methods				
fruits and vegetables	Cryo-SEM	CLSM	Texture Analysis		NMR	Drip loss	Colour
			Conventional	Laser-Puff			
Sample preparation	Difficult	Difficult	Easy	Easy	Easy	Easy	Easy
Ability to detect differences between fresh and frozen/thawed sample	×	++++	++++	++++	++++	++++	++++
Ability to distinguish different freezing protocols	++++	++++	++	++	+	++	-
Analysis time (sample preparations + data acquisition and treatment)	+	+	+	+	+++	+	+
Interpretation of measured analytical parameters	Easy	Easy	Easy	Easy	Difficult	Easy	Easy
Nature of sample	F	F/T	F/T	F/T	F & F/T	F/T	F/T
Cost of operation	High	High	Low cost	Low cost	High	Low cost	Low cost
Status of method	OU	NUO	VC	NM	NUO	VC	VC
Error (%)	×	×	Hardness = ±0.5 YM = ±3.2	±0.90	<±1	±0.0016	L = ±0.02 a = ±0.21 b = ±0.15

+ = Lowest value; ++++ = Highest value; × = Not applicable; - = No effect.
Abbreviations of the words: F = Frozen; F/T = Frozen/Thawed; FD = Freeze dried; OU = Often used; NUO = Not used often; VC = Very common; NM = New method; YM = Young's Modulus.
L, a, b are different colour parameters.

- Benchmarking of methods for accessing freeze damage in potatoes was carried out
- Three different freezing protocols have been compared
- Focused methods could differentiate the impact of all different freezing protocols
- Texture, NMR and exudate loss had limitations to differentiate freezing conditions

B/ Phenolic distribution in apple epidermal and outer cortex tissue by multispectral deep-UV autofluorescence cryo-imaging

Contents lists available at ScienceDirect

Plant Science

journal homepage: www.elsevier.com

Technical perspectives

Phenolic distribution in apple epidermal and outer cortex tissue by multispectral deep-UV autofluorescence cryo-imaging

Kevin Vidot [a, b], Marie-Françoise Devaux [a], Camille Alvarado [a], Sylvain Guyot [c], Frederic Jamme [d], Cédric Gaillard [a], René Siret [b], Marc Lahaye [a, *]

[a] UR 1268 Biopolymères Interactions Assemblages, équipe Paroi Végétale et Polysaccharides Pariétaux (PVPP), INRA, 44300, Nantes, France
[b] USC 1422 GRAPPE, INRA, Ecole Supérieure d'Agricultures, SFR 4207 QUASAV, 49100, Angers, France
[c] UR 1268 Biopolymères Interactions Assemblages, équipe Polyphénols, Réactivité, Procédés (PRP), INRA, 35653, Le Rheu, France
[d] Synchrotron SOLEIL, L'Orme des Merisiers, Saint-Aubin, 91192 Gif-sur-Yvette Cedex, France

ARTICLE INFO

Keywords:
Malus domestica
Phenolic compounds
Autofluorescence
Multispectral imaging
Deep-UV synchrotron light
Cryo-microscopy

ABSTRACT

Phenolic compounds in fruit are involved in responses to biotic and abiotic stresses and are responsible for organoleptic properties. To establish the distribution of these secondary metabolites at the tissue and sub-cellular scales, mapping of fluorescence in apple epidermis and outer cortex tissue in cryogenic condition was performed after deep-UV excitation at 275 nm. Douce Moën and Guillevic cider apple varieties were sampled and frozen after harvest, after 30 days at 4 °C and after 20 days at room temperature. Image analysis of fluorescence emission images acquired between 300 and 650 nm allowed the assignment of fluorescence signals to phenolic compound families based on reference molecules. Emission attributed to monomeric and/or condensed flavanol was localized in whole tissue with major fluorescence in the cuticle region. Hydroxycinnamic acids were found predominantly in the outer cortex and appeared in the cell wall. Fluorescent pigments were mostly found in the epidermis. The distribution of flavanols in the sub-cuticle and phenolic acids in the outer cortex distinguished apple varieties. Storage conditions had no impact on phenolic distribution. The proposed fluorescent imaging and analysis approach enables studies on phenolic distribution in relation to fruit development, biotic/abiotic stress resistance and quality.

1. Introduction

Phenolic compounds are common plant secondary metabolites that have been grouped into three classes: flavonoids, phenolic acids and stilbenes [1]. The flavonoids encompass flavanols that are also found as oligomers and polymers (i.e., proanthocyanidins and condensed tannins), anthocyanins and flavonols, while phenolic acids comprise hydroxybenzoic acids and hydroxycinnamic acids (Fig. 1). Except for flavanols and hydroxybenzoic acids, which are mainly present in their free form, most phenolic compounds are glycosylated and/or acylated derivatives. Their ultraviolet absorption capacity limits light- induced damage to tissues while they are part of plant defence mechanisms against external biotic stresses [2,3]. In fleshy fruit, phenolic compounds are known for their antioxidant contribution to foods and organoleptic properties, such as colour, astringency or bitterness [4–6]. Various studies in apple and grape have shown important differences in phenolic content between varieties according to fruit development and tissue [7]. Phenolic compounds are commonly characterized by biochemical techniques on whole fruit, skin, flesh, seed or juice extracts. However, there are few reports on the distribution of specific phenolic compounds at the tissue and sub-cellular scales under *in-vivo-like* conditions. Flavanols and condensed tannins were determined to be localized in the epidermis, parenchyma and seeds by microscopy of fresh or chemically fixed apple [8], grape [9,10] and other fruits [11–14]. Flavanols were localized by DMACA staining (4-dimethylaminocinnamaldehyde) [14–16] while flavonols were highlighted by fluorescence microscopy using the specific dye DPBA (diphenylboric acid-2-aminoethyl ester) [17,18]. However, chemical preparation damage to fleshy fruit tissue integrity affects the cellular localization of diffusible compounds [19], and dyes are limited by their specificities.

* Corresponding author.
Email addresses: kevin.vidot@inra.fr (K. Vidot); mailto.marie-francoise.devaux@inra.fr (M-F Devaux); camille.alvarado@inra.fr (C. Alvarado); sylvain.guyot@inra.fr (S. Guyot); frederic.jamme@synchrotron-soleil.fr (F. Jamme); cedric.gaillard@inra.fr (C. Gaillard); r.siret@groupe-esa.com (R. Siret); marc.lahaye@inra.fr (M. Lahaye)

https://doi.org/10.1016/j.plantsci.2019.02.003
Received 13 December 2018; Received in revised form 29 January 2019; Accepted 1 February 2019
Available online xxx
0168-9452/

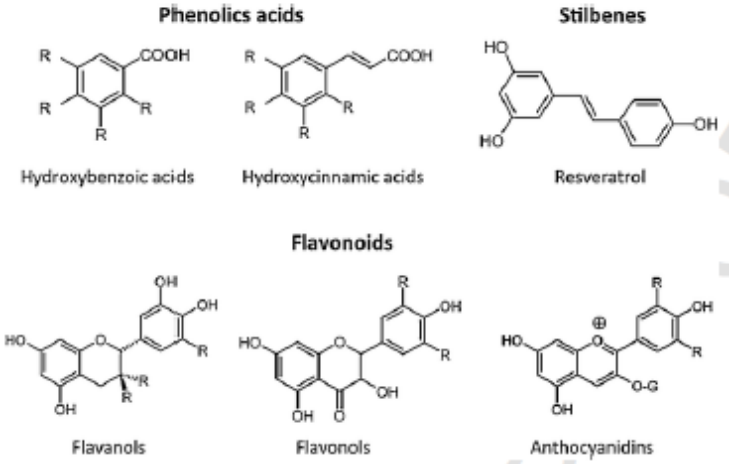

Fig. 1. Generic phenolic compound structures. -R may correspond to -H, –OH or $–OCH_3$ and –X may correspond to –H in monomeric form or other flavanol units in polymeric form (Vermerris and Nicholson 2006).

To address these issues, mapping phenolic compounds through their autofluorescence characteristics appears to be a good alternative as no specific stain is required. Hydroxycinnamic acids express a blue fluorescence when excited at the UV wavelength of approximately 350 nm [20,21] while anthocyanins and flavonols are autofluorescent at visible wavelengths [22]. Monomeric and condensed tannin ((+)catechin, (-)epi-catechin, procyanidins) fluorescence requires deep-UV wavelength excitation at approximately 280 nm [23,24]. The use of different bandpass filters to select specific ranges of fluorescence emissions offers the opportunity to localize different compounds within the same sample through a multispectral approach [25]. However, data on the fluorescence emission of specific phenolic compounds are scarce due to the high number of entities that constitute this metabolite family and because access to pure reference phenolic compounds is limited.

To avoid artefacts related to small compound diffusion and loss during sample preparation, cryo-fixation, cryo-microtomy and fluorescence cryo-observation of biological samples have seen recent developments. Cryo-confocal observations at high resolutions were introduced with the realization of specific microscope stages and immersion objective lens prototypes [26,27]. A simpler and readily accessible setup was developed to observe fleshy fruit tissue by cryo-laser scanning confocal microscopy (LSCM) [18]. Among the advantages of cryo-observations is the lower fluorescence bleaching compared to that during room temperature observations and thus the recovery of higher fluorescence intensity [26,28].

Preliminary tests of fresh fruit auto-fluorescence responses after excitation at 375 nm were performed on apple and grape. The latter revealed promising autofluorescence signals, while a lower excitation wavelength was found necessary to assess flavanol localization. The objective of the present work was to map phenolic compounds in cryo-fixed outer tissues of apple. The mapping was performed at a large field of view by multispectral autofluorescence imaging after deep-UV excitation at 275 nm using the setup developed for fleshy fruit cryo-observation. Two cider apple varieties stored in three different conditions were studied to evaluate the genetic and physiological impacts on phenolic compound distribution. Fluorescence excitation and emission characteristics of reference phenolic compounds were recorded to help identify fruit tissue phenolics.

2. Materials and methods

2.1. Materials

2.1.1. Chemicals

Phenolic compounds used for reference fluorescence spectra were from the laboratory collections of BSA-ORAPPE (Angers, France) and BIA-PRP (Rennes, France). Formic acid was purchased from Sigma-Aldrich (UK) and methanol was purchased from CarloErba (Italy).

2.1.2. Fruits

Apple (*Malus domestica*, Royal Gala) and grape (*Vitis vinifera*, Red Italian) for preliminary fluorescence analysis after 375 nm UV excitation were from a local retail store. These fruits were used without further storage. For the fluorescence mapping following excitation at 275 nm, two cider apple varieties, Douce Moën (*M. domestica*, Douce Moën) and Guillevic (*M. domestica*, Guillevic), were provided by IFPC (Le Rheu, France). Fruits were harvested on October 2017 in orchards at Surzur (Morbihan, France). Nine fruits of each variety were subjected to three different storage conditions: three were immediately sampled, three were stored at 4 °C for 30 days and three were stored at room temperature for 20 days before sampling.

2.2. Methods

2.2.1. Spectrofluorometry

Phenolic references were dissolved at 2 mg mL^{-1} in 2 mL of H_2O:MeOH (1:1 in volume) + 1% formic acid (in volume). Quartz cuvettes (10 x 4 mm, 114F-QS, Suprasil HELLMA Analytics, France) were filled with 500 µL of standard solution and observed by spectrofluorimetry (F-4500, HITACHI, Japan). Emission and excitation spectra for each compound were recorded between 200 nm and 600 nm.

2.2.2. Laser scanning confocal microscopy (LSCM)

Cubes of 5 × 5 × 5 mm^3 were sampled from the epidermal region of equatorial fruit slices of commercial apple and grape. Sections of 100 µm thickness were cut from fresh cubes with a vibrating blade microtome (HM 650 V, MICROM, France) and immediately observed or dipped in standard buffer solution pH 10 (HI 70010C, NIST standard, HANNA INSTRUMENTS, Hungary) followed by H_2O milliQ wash prior to LSCM observations at room temperature. LSCM (A1 Eclipse Ti in-

verted microscope, NIKON Inc., Japan) was configured with laser diode excitation at 375 nm. Fluorescence emission was acquired at 20× magnification with a resolution of 0.63 µm pixel^{-1} and image size of 512 × 512 pixels^2 (16-bit). Four bandpass emission filters were used to map fluorescence: 400–450 nm, 500–530 nm, 560–600 nm and 630–700 nm. These form sets of multispectral images of four channels with spectral controlled excitation and emission parameters.

2.2.3. Synchrotron deep-UV wide-field fluorescence microscopy (DUV)

One 5 × 5 × 5 mm^3 cube was randomly sampled from the epidermal region of a cider apple fruit equatorial slice. The cube was frozen in liquid nitrogen-cooled isopentane and stored at −20 °C prior to analysis. Sections (60 µm thick) were cut from frozen cubes using a cryostat microtome (HM 500 OM, MICROM, France) at −20 °C. The section was placed between quartz lamella (R52-5000, ESCO Optics, USA) glued together by frozen water droplets. Synchrotron UV microscopy was performed at the DISCO (Dichroism, Imaging, mass Spectrometry for Chemistry and biOlogy) beamline at the SOLEIL (Source Optimisée de Lumière à Energie Intermédiaire du LURE (Laboratoire à Utilisation du Rayonnement Electromagnétique)) synchrotron radiation facility [29] (Gif-sur-Yvette, Saint-Aubin, France) on the inverted epi-fluorescence TELEMOS microscope [30]. Observation was realized under cryogenic conditions using a handmade setup composed of a Peltier stage (PE100, LINKAM Scientifics, UK) cooled by dry ice as described in [18]. The wide-field microscope TELEMOS modified by the DISCO beamline staff was a Zeiss Axio Observer Z-1 designed to observe samples after deep-UV (DUV) excitation. The microscope was equipped with a motorized sample plate (MS-2000 XY, Applied Scientific Instrument, USA) to move the sample along the X and Y axes. Sample movement along the Z axis was controlled by the inverted microscope. The setup used the 10× magnification Zeiss Ultrafluar lens (N.A 0.2, WD 7.4) and a sharp 300 nm dichroic mirror "DM" (Omega Optical), which reflected the 280 nm excitation and transmitted emission light above 300 nm. Multispectral fluorescence emission was recorded using six different emission bandpass filters: 300–306 nm, 327–353 nm, 352–388 nm, 412–438 nm, 420–460 nm and 600–650 nm (Semrock, Rochester, USA). In the text, filters are referred to by their low wavelength limit. A back-illuminated CCD camera (Pixis BUV, Princeton Instrument, USA) recorded the images (1024 × 1024 pixels; 1 x 1 µm^2 per pixel; grey level coded in 16 bit). Acquisition times were 12.5 s for the 300 nm filter, 5 s for the 327, 352, 412 and 420 nm filters, and 7.5 s for the 600 nm filter. Acquisition was performed from the sample cuticle to approximately one mm inside the tissue. With three biological repetitions and three different storage modalities, a total of nine images were registered per variety.

The beamline intensity, which was focused at the centre of the observation field, led to raw images that required corrections to homogenize illumination. In addition, the camera provided a non-null background without illumination. Both inhomogeneous illumination and background corrections were realized according to the following formula:

$$Ic = \frac{I - Dark}{White - Dark}$$

where Ic is the corrected image; I is the raw image; Dark is the background and White is the flat field

For this purpose, nine different "dark" images were recorded without sample and without any illumination, one for each of the six emission filters. The "White" images were acquired using a frame (1.0 × 1.0 cm^2, AB-0576, Gene Frame, THERMOSCIENTIFIC, UK) displaying a homogeneous autofluorescent signal. Thresholding was also required to define the sample image from the camera noise. Image pretreatments were performed using MATLAB® 2017b.

The corrected images were cropped to 300 x 400 µm^2 size to fit within a pertinent sample image area. To take into account out-of-plane sample sections, several acquisitions were recorded for the same sample area with a maximum of six focal planes. As this method was not confocal imaging, a clear image was reconstructed by combining the different focal plane views with the extended focus software HeliconFocus6® (version 6.3.0) using the pyramidal method.

2.2.3.1. Multispectral analysis of DUV fluorescence images DUV fluorescence emission was valued based on the grey scale intensity of pixels in cropped images. Principal component analysis was applied separately on each multispectral image, and fluorescence profiles were extracted from selected emission filters.

2.2.3.2. Image analysis Individual emission images were unfolded to form one vector [31]. The image vectors were combined into one table per sample containing six columns corresponding to the six filters and n rows corresponding to the n pixels of the image. Principal component analysis (PCA) was applied to the resulting data table, and correlation circles were drawn from the PCA loadings. Principal component images were obtained by refolding scores [31]. Component images were filtered to keep 99% of pixels closer to the median value and to remove eventual aberrant pixel values prior to normalization of grey levels between 0 and 255. PCA reconstructed colour images were created from components 1, 2 and 3 identified in the blue, red and green channels, respectively.

Localization of phenolic compounds in samples was also analysed by computing fluorescence intensity profiles from the cuticle to the inner tissue. This "image distance" analysis was realized using FIJI/ImageJ® software [32] and the mathematical morphology plugin process/erode (3D) [33]. Thresholding was first applied to create a binary mask of the sample. Distance from the cuticle was obtained by the following procedure: one-pixel erosion (pixel size = 1 x 1 µm^2) was applied to the sample mask and the resulting binary image was subtracted from the initial sample binary image. This step was iteratively applied until the last image column was reached. The mean profile was smoothed to reduce intensity variations due to the presence of cell lumens with low fluorescence and cell walls with high fluorescence. This was realized by applying local regression (LOESS) with a degree of smoothing of 0.4. Normalization between 0 and 1 was realized on the maximum smoothed mean value to allow profiles comparison between samples. Examples of raw and smoothed profiles are shown for Douce Moën at harvest in Supplementary Figs. 1 and 2. The smoothed profiles from the three biological replicates per storage modality were averaged and the mean profile per modality was plotted with its 95% confident interval (Supplementary Fig. 3).

2.2.3.3. Statistical analyses The effect of storage was evaluated by Student's t-tests of the smoothed mean pixel values of three biological replicates per pixel distance. As no significant differences were found between storage modalities, Student's t-test for variety effect was performed on the nine replicates.

Principal component analysis, LOESS smoothing and Student's t-tests were performed in R [34].

3. Results

3.1. Fluorescence properties of reference phenolic compound

Excitation and emission fluorescence spectra were registered from standard phenolic compounds (Supplementary Fig. 4) and the maximum wavelength responses recorded (Table 1). If associating specific compounds with peculiar emission wavelengths is difficult due to the width of spectra with large overlaps, distinguishing families of compounds, such as flavanols (including condensed tannins), phenolic acids, anthocyanins and flavonols remains possible. For example, phenolic acids, such as p-coumaric acid, ferulic acid and caffeic acid have

Table 1
Fluorescence excitation/emission maxima of phenolic compounds registered by spectrofluorometry: regular case: literature, bold case: this study.

Compounds	$\lambda_{max\ excitation}$ (nm)	$\lambda_{max\ emission}$ (nm)
Emission range (< 350 nm)		
Protein group		
Phenylalanin [70]	258	285
Tyrosin [70]	276	302
Emission range (300-400 nm)		
Flavanols group		
(-) Epicatechin	290	320
(+) Catechin	290	320
Procyanidin B1	285	320
Procyanidin B2	295	320
Epigallocatechin	275	320
Others compounds		
Tryptophan [22]	280	357
2,5-Dihydroxybenzaldehyde [21]	278	360
Syringic acid	310	360
Vanillic acid [21]	278	360
Gallic acid	320	370
Myricetin [21]	268	370
Resveratrol	310/360	390
Emission range (400-500 nm)		
Phenolic acids group		
Ferulic acid	310/370	420
p-Coumaric acid	350	420
Caffeic acid	270/360	440
Chlorogenic acid	360	460
Others compounds		
Kaempferol [21]	268	422
Rutin	300	460
Emission range (500-600 nm)		
Flavonols group		
Anthocyanins [22]	300/410	360/420/530
Cyanidin hydrate	278	550
Quercetin-3-O-glucoside	260/410	510
Quercetin	420	520
Quercetin galactoside	295	600
Others compounds		
Arbutin	420	530
Phloridzin	250/330	540
Chlorophyll/chloroplast [37]	360	680

a maximum emission at approximately 420 nm, while flavanols such as (+) catechin, (-) epi-catechin and procyanidin share maximum emission at approximately 320 nm. In fact, due to their large excitation spectra, most phenolic compounds will fluoresce under excitation at 275 nm. Among the tested reference compounds, only phloridzin, rutin and arbutin will not fluoresce after deep-UV excitation.

3.2. Preliminary analysis of autofluorescence observed after excitation at 375 nm

In a preliminary study, autofluorescence observations of fleshy fruit were realized with a laboratory confocal laser scanning microscope using a UV diode laser at 375 nm. This test was performed to check the pertinence of autofluorescence analysis on two types of fleshy fruits: Royal Gala apple and Italian Red grape. In all cases, the cuticle presented bright and intense fluorescence as previously observed [35]. Red spots were observed within the cells of both fruit but particularly in grape, while light yellow fluorescence was observed in vacuole-like compartments only in apple. Red fluorescence could correspond to chlorophyll residues while yellow emission could be related to compounds of the flavonol class, such as quercetin derivatives [36,37]. A weak blue emission was also observed in the cell wall at native pH and was found to increase at pH 10, as reported for ferulic or coumaric acids [20]. These emission variations after UV excitation at 375 nm provided support for the mapping of phenolic compounds using multispectral autofluorescence imaging. However, a lower excitation wavelength was sought to access compounds in the flavanol family.

3.3. Autofluorescence after excitation at 275 nm

The autofluorescence of flavanols in fleshy fruit tissue requires excitation at a low UV wavelength, which is yet inaccessible with a common microscopy laser beam. The synchrotron beamline at DISCO allows for exciting samples in the 200–350 nm range. To limit the diffusion of phenolic compounds, apple tissue was first cryo-fixed prior to cryo-observation of multispectral fluorescence from 300 nm to 650 nm (Fig. 3). Outer-cortex parenchyma fluorescence was distinguished from that of epidermal tissue, which encompasses cuticle and sub-cuticular cell layers (Fig. 3). Between 327 and 388 nm, sub-cuticular cell layer fluorescence was more intense and disappeared at higher bandpass wavelength filters except, for the 600 nm filter. Intense fluorescent spots were observed inside the cell mainly with 300 and 327 nm filters, but in all cases, cells walls showed a more intense signal than cells.

To better distinguish differences in sample fluorescence, principal component analysis was applied to the collection of images obtained with the different bandpass filters. All principal component analyses performed on the three modalities presented similar loadings. For example, the loading and component images are shown in Fig. 4 for representative samples of Douce Moën and Guillevic apple varieties at harvest. Fluorescence through 300, 327, 352, 412, 420 and 600 nm filters contributed mainly to components 1 and 2 and fluorescence at 300, 327 and 600 nm contributed more weakly to components 3 and 4. Most filters contributed to component 1, which corresponded to the general variations of fluorescence intensity and explained 65.8% and 61.7% of the total variance for Douce Moën and Guillevic, respectively. The component images showed that the highest overall fluorescence intensity was mainly localized in the walls of outer-cortical cells. The second component, expressing the contribution of the 300 and 327 nm filters (positive side) in opposition to the emission filters 412 and 420 nm (negative side), contrasted the sub-cuticular cell layers. Filters 352 and 600 nm were inversely related to this second component for the two varieties. The third component pointed out the cuticle region with a relatively higher fluorescence measured using the 327 nm emission filter (in red) compared to the 300 and 600 nm filters (in blue), showing the rest of the sample. The fourth component showed a higher level of noise and a relatively higher fluorescence level associated with the 300 nm filter (in blue) in the epidermal region as well as in the cell walls of sub-cuticular cells and outer cortical cells. Thus, fluorescence distinguished three areas: the cuticle region with a relatively higher fluorescence emission using the 327 nm filter, the sub-cuticular cell layers with the 300 nm and 600 nm filters, and the walls of outer-cortical cells with the 352, 412 and 420 nm filters. The three first component images of the representative samples were combined in an ROB image to better visualize the tissue regions according to fluorescence (Fig. 4). To objectivize differences observed in fluorescence distribution, normalized intensity profiles for all images of the two varieties at the different storage conditions were measured.

Intensity profiles from the cuticular to the outer cortical tissue were obtained for the four bandpass filters discriminating the most apple tissues: 300, 327, 420 and 600 nm. As cell lumen and cell walls showed marked differences in fluorescence intensities, smoothing of each profile was realized by local regression (LOESS) at the expense of fine structures contributing to fluorescence (cells, cell walls, sub-cellular structures). The smoothed and normalized curves allowed comparison of trends in fluorescence variations along the first 400 µm under the cuticle. Examples of raw and smoothed profiles are shown for the Douce Moën variety at harvest in Supplementary Figs. 1 and 2. Considering close fruit calibres within varieties, Student's *t*-test at each distance point per filter showed that storage modalities had no effect on

fluorescence profiles (p-value > 0.05; Supplementary Fig. 3). Thus, all biological replicates (n = 9) were used to evaluate the effect of apple varieties on fluorescence intensity profiles. Significant differences were particularly noted with the 327 nm and 420 nm filters (Fig. 5). For the 327 filter, an inverse gradient was observed between the two varieties with a rupture point at approximately 100 µm from the cuticle. Douce Moën showed higher fluorescence intensity than Ouillevic, particularly in the first 10 µm under the cuticle but was lower than that of Ouillevic 60 µm away from the cuticle. The 420 nm filter also presented two significantly different areas, first in the epidermis where the Ouillevic signal was higher than that of Douce Moën and opposite to the 327 nm filter profile and second in the outer cortex (300 to the 400 µm limit of the images) where Ouillevic fluorescence was lower. A maximum was observed at approximately 100 µm for Ouillevic, while for Douce Moën, it was at approximately 330 µm from the cuticle. Weak significant differences were observed between Ouillevic and Douce Moën in the sub-cuticular cell layers for the 300 nm filter and in the outer cortex for the 600 nm filter. These two profiles also showed similar ruptures at approximately 75–100 µm from the cuticle. The mean smoothed plot profiles (Fig. 6) showed good agreement with the fluorescence distribution observed in the representative PCA reconstructed images (Fig. 4). The three regions observed may be approximately delimited from these results (Fig. 6) for Douce Moën to range from approximately 0 to 50 µm, 50 to 200 µm and 200 µm to 400 µm while for Ouillevic, to range from approximately 0 to 60 µm, 60 to 150 µm and 150 to 400 µm. These regions may correspond to the cuticle and the sub-cuticle forming the epidermis and the outer cortex as depicted in Fig. 3.

The fluorescence emission of reference phenolic compounds allowed us to propose the possible nature of chemicals in the different tissues (Table 1). Fluorescence observed with the 300 nm filter was more likely due to proteins as this range of emission is related to the amino-acids tyrosine and phenylalanine [38]. Fluorescence through the 327 nm filter may have corresponded to the tryptophan and most likely to catechins that are predominant in apple fruit tissue. Since these compounds are flavanol monomers and oligomers, by extension such fluorescence would also reveal condensed tannins. Likewise, fluorescence at 420 nm would represent the phenolic acid family, such as hydroxycinnamic acids, while the fluorescence at 600 nm would be pigments, such as anthocyanin or chlorophyll. According to these propositions, pigments would be particularly localized in the sub-cuticular cell layers of both varieties, while flavanols including condensed tannins would be present in the epidermis and outer cortex of both varieties, though with higher intensity in the sub-cuticular cell layers of Ouillevic. The distribution of phenolic acids differed markedly between the two varieties. In Douce Moën, they were present mainly in the outer cortex, while in Ouillevic they were also present in the sub-cuticular cell layers. Storage conditions did not appear to affect these distributions.

4. Discussion

The results showed that multispectral observation of auto-fluorescence provides a convenient alternative for localizing phenolic compound families in fleshy fruit tissue with limited sample preparation and artefact introduction compared to classical resin embedding and staining methods. Adaptation of the cryogenic procedures developed for cryo-LSCM [18] to the wide-field TELEMOS microscope of the DISCO beamline at the SOLEIL synchrotron facility allowed observation of fluorescence from 275 nm, which excited flavanols and condensed tannins together with other phenolic compounds in well-preserved apple tissue with limited metabolite diffusion. The obtained images confirmed the efficiency of the cryogenic process as intracellular content appeared filled, though of lower fluorescence intensity compared to cell walls. Cryo-observation also improved fluorescence intensity [26], likely by reducing fluorescent bleaching due to the temperature dependency of quencher diffusion [28]. This phenomenon was particularly helpful in establishing the qualitative distribution of fluorescent compounds in fruit tissue.

Fluorescence tended to indicate phenolic compounds within cell walls. However, most phenolics are localized within cell organelles, vacuoles or the cytoplasm [39,40] with fewer in cell walls. In apple, phenolic compounds have not been described as part of the cell wall polysaccharide composition [41,42]. Some authors [43] suggested that tannin accumulation takes place in the vacuole, but their polymerization appeared near the cell walls. As apple fruit cells are highly hydrated, ice crystals formed during cryo-fixation of the water-filled vacuoles [44] may have pushed fluorescent organelles and cytoplasmic materials close to the cell walls. As a consequence, part of the cell wall fluorescence observed with the 10× magnification lens (resolution: 1.24 µm / pixel) may have resulted from nearby intracellular fluorescent compounds/organelles. However, the blue emission observed by LSCM in the cell wall of fresh apple and grape tissue and its increased fluorescence at basic pH supported the presence of hydroxycinnamic acids in cell walls. This observation was realized at higher magnification (20×, resolution of 0.63 µm / pixel) than that of the TELEMOS setup and excluded the potential of ice crystal effects on cell wall fluorescence. Hydroxycinnamic acids have already been reported in apple fruit mostly in vacuoles due to their characterization in the juice [45] [46,47], but they are also known to be present in plant cell walls [48]. Their low concentration in apple cell walls likely prevented their detection by classic analytical techniques. However, further work is needed to assess the nature of these compounds and whether they are esters of cell wall polysaccharides, as reported for other plants [20,49,50].

The cuticle was the most fluorescent zone of apple and grape fruit tissues observed by LSCM (Fig. 2). The observation of cuticle autofluorescence was already reported in several fruits, including apples and grapes and may be related to high concentrations of proteins and phenolic acids [35,51]. Though anthocyanins, flavonols, flavanols (including condensed tannins), hydroxycinnamic acids and proteins were essentially reported in the epidermis region [52–54], they were more

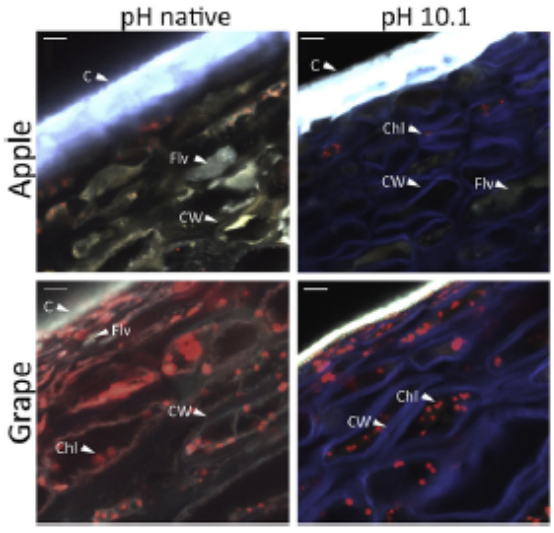

Fig. 2. Local retail store fresh apple and grape autofluorescence at natural pH and at pH = 10.1 after excitation at 375 nm. The fluorescence emissions recorded are 400–450 nm (blue), 500–530 nm (green), 560–600 nm (yellow), and 630–700 nm (red). C: cuticle, CW: cell wall, Chl: chlorophyll residues, Flv: flavonols. Scale bar: 20 µm.

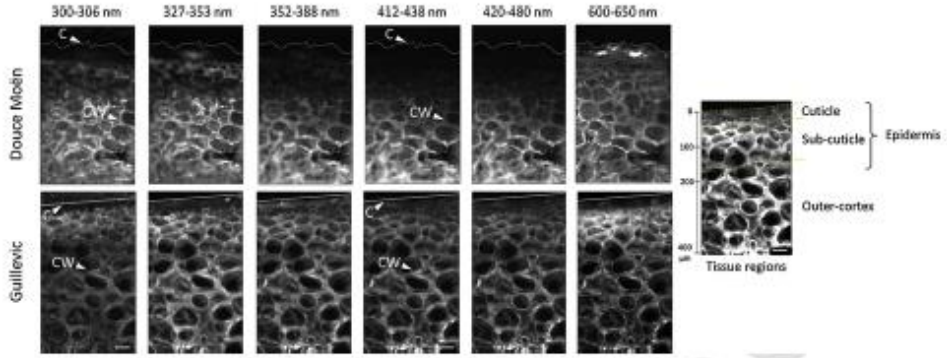

Fig. 3. Frozen apple autofluorescence for one replicate of Douce Moën and Guillevic at harvest after excitation at 275 nm. Tissue regions are drawn on the right image resulting from a combination of whole Guillevic filter emission images. C: cuticle, CW: cell wall, Scale bar: 40 µm.

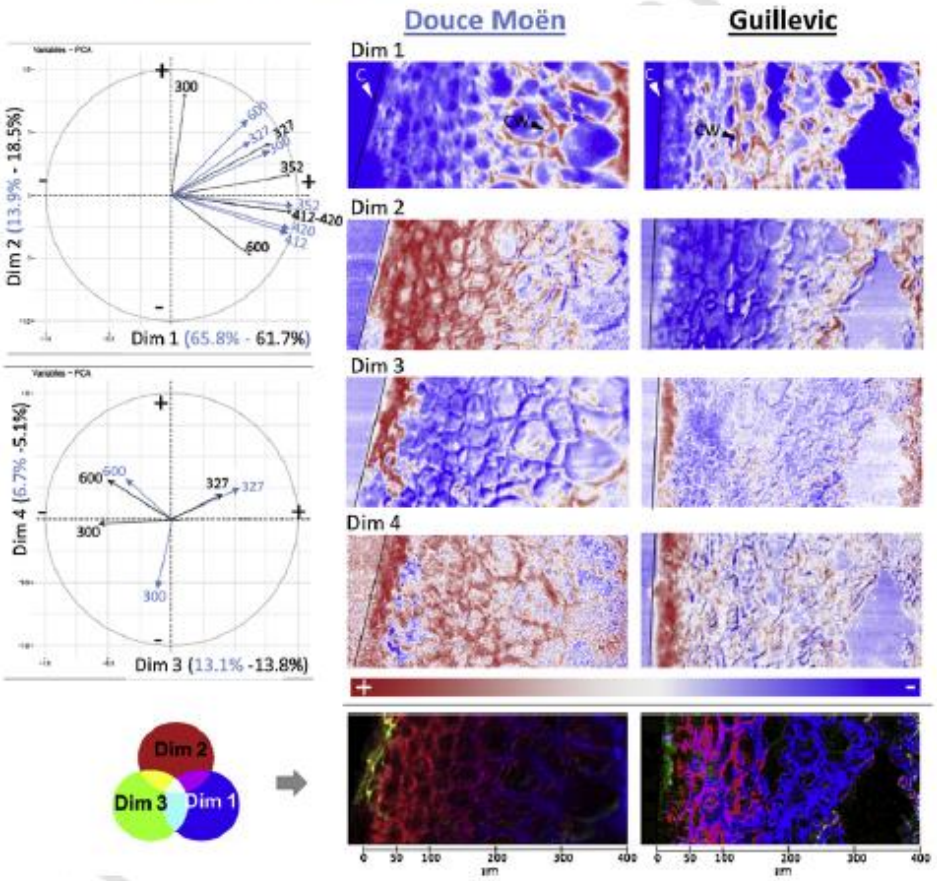

Fig. 4. Principal component analysis on the six emission filter images for one replicate of Douce Moën (blue character and arrows) and Guillevic (black character and arrows) at harvest and the PCA images of the four components. On the component images, blue and red pixels represent negative and positive contributions of the emission filters to the component. RGB reconstructed images from PCA components were built from dimension 1 (blue), dimension 2 (red) and dimension 3 (green). C: cuticle, CW: cell wall.

rarely localized in sub-cuticular cell layers [8,10,14]. The high concentration of phenolic compounds in the sub-cuticular cell layers is probably related to defence against pathogens [55] or light damage to tissues. The firmer mechanical resistance of grape and apple skins compared to their flesh [56,57] may also be associated to the important presence of phenolic compounds in the skin. Indeed, phenolic compounds and, in particular, flavonoids were proposed to increase the rigidity of the cutin matrix in the cuticle of ripe tomato [58]. Comparatively, excitation with DUV at 275 nm revealed a lower cuticle autofluorescence. Although flavonoids and phenolic acids, the main cuticle

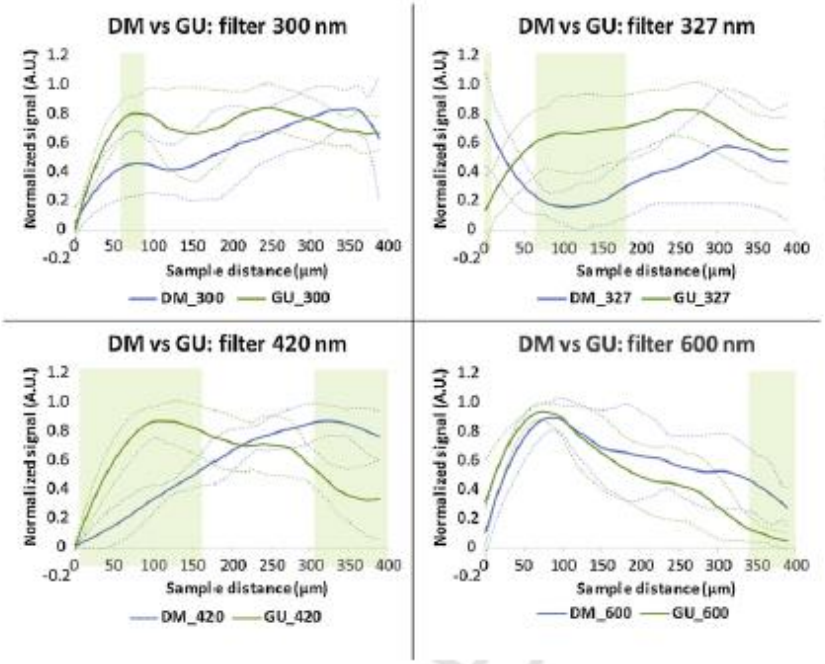

Fig. 5. Smoothed (LOESS method: α = 0.4) and normalized average plot profiles of Douce Moën (DM) and Guillevic (GU) signal acquisition for emission filters 300 nm, 327 nm, 420 nm and 600 nm after excitation at 275 nm. The dotted lines represent the 95% confidence interval. The coloured areas correspond to significant differences between DM and GU with a p-value < 0.01 by Student's test (n = 9).

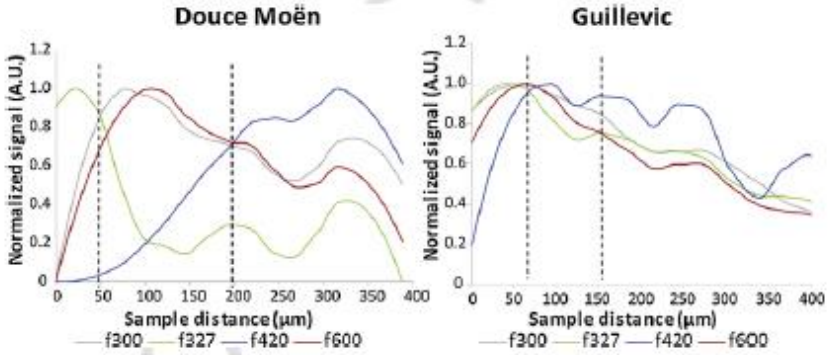

Fig. 6. Superposed smoothed (LOESS method: α = 0.4) and normalized average plot profiles of Douce Moën and Guillevic signal acquisition for emission filters 300 nm (grey line), 327 nm (green line), 420 nm (blue line) and 600 nm (red line) after excitation at 275 nm. The profiles were plotted along the sample section distance from the outer cuticle to 400 µm deep inside the tissue.

phenolic compounds, have large excitation and emission spectra (Supplementary Fig. 4), 275 nm excitation was not optimal to yield high autofluorescence intensities. Though such a wavelength was beneficial for exciting flavanols and proteins fluorescence, it appears that flavanols are in low concentration - if any- within the cuticle but are present in the first cell layers underneath (Fig. 3).

The red-skinned Douce Moën and the yellow-skinned Guillevic cider apples were used as model fruits to help distinguish phenolic compound locations by their autofluorescence. Douce Moën is known to be richer in hydroxycinnamic acids and in monomeric tannins, such as (+) catechin, (-) epicatechin and procyanidin with lower tannin degrees of polymerization compared to Guillevic [59]. Anthocyanins were not characterized in the two varieties, but the more colourful Douce Moën skin evidenced higher anthocyanin and/or pigment contents than that of Guillevic. Based on distinct fluorescent emissions of reference compounds after 275 nm excitation, autofluorescence in Douce Moën and Guillevic cryo-sections allowed the detection of pigments in the sub-cuticular cell layers in agreement with the known flavanols, anthocyanins and chlorophyll concentrations in apple skin [60,61]. The main distribution of tannins in the sub-cuticular area together with that of phenolic acids in the outer cortex parenchyma may be related to the ratio reported for procyanidin (PC) and hydroxycinnamic acid (HC) concentrations in the fresh peel (HC/PC: 0.63) and parenchyma (HC/PC: 1.29) [62]. This different distribution was not reported in the literature for grape in which flavanols were mainly localized in the epidermis and in the seeds although hydroxycinnamic acid content was higher in skin than in pulp [16,54,63].

Changes in phenolic compounds distribution were not observed with storage modalities that were aimed at impacting apple ripening. This result is at odds with studies showing phenolic compound variations during ripening of fruit [7], such as apple [52,64] and grape [10,65]. The lack of autofluorescence discrimination between ripening stages may be related to the small tissue area observed. Instead, the present study evidenced a variation in phenolic distribution between apple varieties. This may be related to different tissue thicknesses as for both varieties, different rupture points in phenolic distributions were observed along distance profiles from the cuticle. These ruptures could correspond to different cell layers in the epidermis and the outer cortex. In particular, a rupture was discernible in fluorescence profiles at an approximately 100 µm depth from the skin samples. Apple histology studies have shown changes from smaller cells in the epidermis to larger cells in the outer cortex parenchyma tissue at an approximately 100-µm depth from the surface of mature fruit [66–68]. Thus, differences in phenolic compound distribution between the two varieties could reveal genetically distinct thicknesses of epidermal cell layers as well as different secondary metabolism in these tissues.

5. Conclusion

The cryo-method used here could benefit from further developments in sample preparation and means of cryo-multispectral fluorescence observations. Applying microwaves during cryo-fixation [69] to avoid ice crystal growth combined with the use of confocal microscope stages and lenses for high-resolution cryo-observations [26,27] is expected to improve the localization of phenolic compounds in the cell and cell wall. Nevertheless, multispectral fluorescence cryo-imaging at 275 nm excitation allowed the distinction of three major classes of phenolic compounds in tissue under *in-vivo-like* conditions without any specific dyes. The detection of hydroxycinnamic acids in apple and grape cell walls requires their identification and linkage in the walls. Coupling multispectral analysis based on LSCM observations in the UV–vis wavelength and synchrotron deep-UV analysis could provide a convenient way to extend the range of accessible autofluorescent phenolic compound distributions in the same sample tissue section. These observations will enable other studies on the mechanical behaviour resulting from the presence of these compounds in fruit tissues in the context of fruit development, quality and processing.

Acknowledgements

Part of this work was realized and supported under the proposal number 20,170,043 at synchrotron SOLEIL. This work was also supported in part by the Food for Tomorrow programme from the Region Pays de la Loire.

Appendix A. Supplementary data

Supplementary material related to this article can be found, in the online version, at doi:https://doi.org/10.1016/j.plantsci.2019.02.003.

References

[1] W. Vermerris, R. Nicholson, Phenolic Compound Biochemistry, Springer, Dordrecht, The Netherlands, 2006.
[2] A. Solovchenko, M. Merzlyak, Optical properties and contribution of cuticle to UV protection in plants: experiments with apple fruit, Photochem. Photobiol. Sci. 2 (2003) 861–866.
[3] A. Edreva, The importance of non-photosynthetic pigments and cinnamic acid derivatives in photoprotection, Agric. Ecosyst. Environ. 106 (2005) 135–146.
[4] G. Williamson, The role of polyphenols in modern nutrition, Nutr. Bull. 42 (2017) 226–235.
[5] J.W. Finley, W.J. Hurst, C.Y. Lee, Principles of Food Chemistry, 4th edition, Springer, 2018.
[6] J. Kschonsek, T. Wolfram, A. Stöckl, V. Böhm, Polyphenolic compounds analysis of old and new apple cultivars and contribution of polyphenolic profile to the in vitro antioxidant capacity, Antioxidants Basel (Basel) 7 (2018).
[7] J.-J. Macheix, Fruit Phenolics, CRC press, 2018.
[8] G.L. Lees, N.H. Suttill, K.M. Wall, T.H. Beveridge, Localization of condensed tannins in apple fruit peel, pulp, and seeds, Can. J. Bot. 73 (1995) 1897–1904.
[9] K. Amrani Joutei, Y. Glories, M. Mercier, Localisation des tanins dans la pellicule de baie de raisin, VITIS 33 (1994) 133–138.
[10] Y. Cadot, M. Chevalier, G. Barbeau, Evolution of the localisation and composition of phenolics in grape skin between veraison and maturity in relation to water availability and some climatic conditions, J. Sci. Food Agric. 91 (2011) 1963–1976.
[11] F.B. Essig, A Systematic histological study of palm fruits. I. The Ptychosperma Alliance, Syst. Bot. 2 (1977) 151–168.
[12] K. Yonemori, M. Oshida, A. Sugiura, Fine structure of tannin cells in fruit and callus tissues of persimmon, Acta Hortic. 436 (1997) 403–416.
[13] L. Raymond, B. Schaffer, J.K. Brecht, J.H. Crane, Internal breakdown in mango fruit: symptomology and histology of jelly seed, soft nose and stem-end cavity, Postharvest Biol. Technol. 13 (1998) 59–70.
[14] H. Hammouda, C. Alvarado, B. Bouchet, J. Kalthoum-Chérif, M. Trabelsi-Ayadi, S. Guyot, Tissue and cellular localization of tannins in tunisian dates (Phoenix dactylifera l.) by light and transmission electron microscopy, J. Agric. Food Chem. 62 (2014) 6650–6654.
[15] U. Mayr, S. Michalek, D. Treutter, W. Feucht, Phenolic compounds of apple and their relationship to scab resistance, J. Phytopathol. 145 (1997) 69–75.
[16] Y. Cadot, M.T. Miñana Castelló, M. Chevalier, Flavan-3-ol compositional changes in grape berries (Vitis vinifera L. cv Cabernet Franc) before veraison, using two complementary analytical approaches, HPLC reversed phase and histochemistry, Anal. Chim. Acta 563 (2006) 65–75.
[17] W.A. Peer, D.E. Brown, B.W. Tague, G.K. Muday, I. Taiz, A.S. Murphy, Flavonoid accumulation patterns of transparent testa mutants of Arabidopsis, Plant Physiol. 126 (2001) 536–548.
[18] K. Vidot, C. Gaillard, C. Rivard, R. Siret, M. Lahaye, Cryo-laser scanning confocal microscopy of diffusible plant compounds, Plant Methods 14 (2018) 89.
[19] K.L. Moore, Y. Chen, A.M. van de Meene, L. Hughes, W. Liu, T. Geraki, F. Mosselmans, S.P. McGrath, C. Grovenor, F.J. Zhao, Combined NanoSIMS and synchrotron X-ray fluorescence reveal distinct cellular and subcellular distribution patterns of trace elements in rice tissues, New Phytol. 201 (2014) 104–115.
[20] P.J. Harris, R.D. Hartley, Detection of bound ferulic acid in cell walls of the Gramineae by ultraviolet fluorescence microscopy, Nature 259 (1976) 508.
[21] M.A. Rodríguez-Delgado, S. Malovaná, J.P. Pérez, T. Borges, F.J. García Montelongo, Separation of phenolic compounds by high-performance liquid chromatography with absorbance and fluorimetric detection, J. Chromato. A 912 (2001) 249–257.
[22] R. Drabent, B. Pliszka, T. Olsznewska, Fluorescence properties of plant anthocyanin pigments. I. Fluorescence of anthocyanins in Brassica oleracea L. extracts, J. Photochem. Photobiol. B, Biol. 50 (1999) 53–58.
[23] S. Gómez-Alonso, E. García-Romero, I. Hermosín-Gutiérrez, HPLC analysis of diverse grape and wine phenolics using direct injection and multidetection by DAD and fluorescence, J. Food Compos. Anal. 20 (2007) 618–626.
[24] D. Airado-Rodríguez, I. Durán-Merás, T. Galeano-Díaz, J.P. Wold, Front-face fluorescence spectroscopy: a new tool for control in the wine industry, J. Food Compos. Anal. 24 (2011) 257–264.
[25] M. Correel, M.-F. Devaux, F. Guillon, C. Barron, Comparison of UV and visible autofluorescence of wheat grain tissues in macroscopic images of cross-sections and particles, Comput. Electron. Agric. 127 (2016) 281–288.
[26] M. Nahmani, C. Lanahan, D. DeRosier, G.G. Turrigiano, High-numerical-aperture cryogenic light microscopy for increased precision of superresolution reconstructions, Proc Natl Acad Sci U S A 114 (2017) 3832–3836.
[27] R. Faoro, M. Bassu, Y.X. Mejia, T. Stephan, N. Dudani, C. Boeker, S. Jakobs, T.P. Burg, Aberration-corrected cryoimmersion light microscopy, Proc. Natl. Acad. Sci. U. S. A. 115 (2018) 1204–1209.
[28] J.R. Lakowicz, Principles of Fluorescence Spectroscopy, 3rd edition, Springer, New York, 2006.
[29] A. Giuliani, F. Jamme, V. Rouam, F. Wien, J.-L. Giorgetta, B. Lagarde, O. Chubar, S. Bac, I. Yao, S. Rey, DISCO: a low-energy multipurpose beamline at synchrotron SOLEIL, J. Synchrotron Radiat. 16 (2009) 835–841.
[30] F. Jamme, S. Kascakova, S. Villette, F. Allouche, S. Pallu, V. Rouam, M. Refregiers, Deep UV autofluorescence microscopy for cell biology and tissue histology, Biol. Cell 105 (2013) 277–288.
[31] H. Grahn, P. Geladi, K. Esbensen, Multivariate and Hyperspectral Image Analysis, in: Encyclopedia of Analytical Chemistry, John Willey & Sons, 2016.
[32] C.A. Schneider, W.S. Rasband, K.W. Eliceiri, NIH image to ImageJ: 25 years of image analysis, Nat. Methods 9 (2012) 671–675.
[33] A.A. Neves, E.J. Silva, J.M. Roter, F.G. Belladona, H.D. Alves, R.T. Lopes, S. Paciornik, G.A. De-Deus, Exploiting the potential of free software to evaluate root canal biomechanical preparation outcomes through micro-CT images, Int. Endod. J. 48 (2015) 1033–1042.
[34] R Core Team, R: a Language and Environment for Statistical Computing, R Foundation for Statistical Computing, Vienna, Austria, in: http://www.R-project.org, 2014.
[35] J.A. Considine, R.B. Knox, Development and histochemistry of the cells, cell-walls, and cuticle of the dermal system of fruit of the grape, Vitis-vinifera L., Protoplasma 99 (1979) 347–365.

[36] P. Hutzler, R. Fischbach, W. Heller, T.P. Jungblut, S. Reuber, R. Schmitz, M. Veit, G. Weissenböck, J.-P. Schnitzler, Tissue localization of phenolic compounds in plants by confocal laser scanning microscopy, J. Exp. Bot. 49 (1998) 953–965.
[37] J.I. García-Plazaola, B. Fernández-Marín, S.O. Duke, A. Hernández, F. López-Arbeloa, J.M. Becerril, Autofluorescence: Biological functions and technical applications, Plant Sci. 236 (2015) 136–145.
[38] F.W.J. Teale, G. Weber, Ultraviolet fluorescence of the aromatic amino acids, Biochem. J. 65 (1957) 476–482.
[39] A.H. Moskowitz, G. Hrazdina, Vacuolar contents of fruit subepidermal cells from Vitis species, Plant Physiol. 68 (1981) 686–692.
[40] S. Kitamura, Transport of flavonoids: from cytosolic synthesis to vacuolar accumulation, in: E. Grotewold (Ed.), The Science of Flavonoids, Springer, 2006, pp. 123–146.
[41] C. Le Bourvellec, K. Bouzerzour, C. Ginies, S. Regis, Y. Plé, C.M.G.C. Renard, Phenolic and polysaccharidic composition of applesauce is close to that of apple flesh, J. Food Compos. Anal. 24 (2011) 537–547.
[42] C.M.G.C. Renard, A.A. Watrelot, C. Le Bourvellec, Interactions between polyphenols and polysaccharides: mechanisms and consequences in food processing and digestion, Trends Food Sci. Technol. 60 (2017) 43–51.
[43] S. Gagné, C. Saucier, L. Gény, Composition and cellular localization of tannins in cabernet sauvignon skins during growth, J. Agric. Food Chem. 54 (2006) 9465–9471.
[44] S. Chassagne-Berces, C. Poirier, M.F. Devaux, C. Fonseca, M. Lahaye, G. Pigorini, C. Girault, M. Marin, F. Guillon, Changes in texture, cellular structure and cell wall composition in apple tissue as a result of freezing, Food Res. Int. 42 (2009) 788–797.
[45] S. Guyot, N. Marnet, P. Sanoner, J. Drilleau, Variability of the polyphenolic composition of cider apple (Malus domestica) fruits and juices, J. Agric. Food Chem. 51 (2003) 6240–6247.
[46] P. Mattila, J. Hellström, R. Törrönen, Phenolic acids in berries, fruits, and beverages, J. Agric. Food Chem. 54 (2006) 7193–7199.
[47] J. Lee, B.L. Chan, A.E. Mitchell, Identification/quantification of free and bound phenolic acids in peel and pulp of apples (Malus domestica) using high resolution mass spectrometry (HRMS), Food Chem. 215 (2017) 301–310.
[48] P. Albersheim, A. Darvill, K. Roberts, R. Sederoff, A. Staehelin, Plant Cell Walls, Garland Sciences, New York, 2011.
[49] S.C. Fry, Phenolic components of the primary cell wall. Feruloylated disaccharides of D-galactose and L-arabinose from spinach polysaccharides, Biochem. J. 203 (1982) 493–504.
[50] L. Saulnier, J.F. Thibault, Ferulic acid and diferulic acids as components of sugar-beet pectins and maize bran heteroxylans, J. Sci. Food Agric. 79 (1999) 396–402.
[51] S. Fernández, S. Osorio, A. Heredia, Monitoring and visualising plant cuticles by confocal laser scanning microscopy, Plant Physiol. Biochem. 37 (1999) 789–794.
[52] M. Awad, A. de Jager, L. van der Plas, A. van der Krol, Flavonoid and chlorogenic acid changes in skin of Elstar and Jonagold apples during development and ripening, Acta Sci. Pol. Hortorum Cultus 90 (2001) 69–83.
[53] S. Khanizadeh, R. Tsao, D. Rekika, R. Yang, M.T. Charles, H.P. Vasantha Rupasinghe, Polyphenol composition and total antioxidant capacity of selected apple genotypes for processing, J. Food Compos. Anal. 21 (2008) 396–401.
[54] G. Di Lecce, S. Arranz, O. Jáuregui, A. Tresserra-Rimbau, P. Quifer-Rada, R.M. Lamuela-Raventós, Phenolic profiling of the skin, pulp and seeds of Albariño grapes using hybrid quadrupole time-of-flight and triple-quadrupole mass spectrometry, Food Chem. 145 (2014) 874–882.
[55] R.M. Bostock, S.M. Wilcox, G. Wang, J.E. Adaskaveg, Suppression of Monilinia fructicola cutinase production by peach fruit surface phenolic acids, Physiol. Mol. Plant Pathol. 54 (1999) 37–50.
[56] M. Grotte, F. Duprat, D. Loonis, E. Pietri, Mechanical properties of the skin and the flesh of apples, Int. J. Food Prop. 4 (2001) 149–161.
[57] H. Bargel, K. Koch, Z. Cerman, C. Neinhuis, Evans Review No. 3: Structure-function relationships of the plant cuticle and cuticular waxes — a smart material?, Funct. Plant Biol. 33 (2006) 893.
[58] B.P. Khanal, M. Knoche, Mechanical properties of cuticles and their primary determinants, J. Exp. Bot. 68 (2017) 5351–5367.
[59] P. Sanoner, S. Guyot, N. Marnet, D. Molle, J.F. Drilleau, Polyphenol profiles of french cider apple varieties (Malus domestica sp.), J. Agric. Food Chem. 47 (1999) 4847–4853.
[60] E.A. Veraverbeke, N. Van Bruaene, P. Van Oostveldt, B.M. Nicolai, Non destructive analysis of the wax layer of apple (Malus domestica Borkh.) by means of confocal laser scanning microscopy, Planta 213 (2001) 525–533.
[61] R.-N. Bae, K.-W. Kim, T.-C. Kim, S.-K. Lee, Anatomical observations of anthocyanin rich cells in apple skins, Hortscience 41 (2006) 733–736.
[62] S. Guyot, N. Marnet, D. Laraba, P. Sanoner, J.-F. Drilleau, Reversed-Phase HPLC following thiolysis for quantitative estimation and characterization of the four main classes of phenolic compounds in different tissue zones of a french cider apple variety (Malus domestica Var. Kermerrien), J. Agric. Food Chem. 46 (1998) 1698–1705.
[63] Y. Cadot, M.T. Miñana-Castelló, M. Chevalier, Anatomical, histological, and histochemical changes in grape seeds from Vitis vinifera L. Cv cabernet franc during fruit development, J. Agric. Food Chem. 54 (2006) 9206–9215.
[64] M. Murata, M. Tsurutani, M. Tomita, S. Homma, K. Kaneko, Relationship between apple ripening and browning: changes in polyphenol content and polyphenol oxidase, J. Agric. Food Chem. 43 (1995) 1115–1121.
[65] R. Delgado, P. Martín, M. del Álamo, M.R. González, Changes in the phenolic composition of grape berries during ripening in relation to vineyard nitrogen and potassium fertilisation rates, J. Sci. Food Agric. 84 (2004) 623–630.
[66] H.P. Bell, The protective layers of the apple, Can. J. Res. 15c (1937) 391–402.
[67] H.B. Tukey, J.O. Young, Gross morphology and histology of developing fruit of the apple, Bot. Gaz. 104 (1942) 3–25.
[68] B.P. Khanal, M. Knoche, Mechanical properties of apple skin are determined by epidermis and hypodermis, J. Am. Soc. Hortic. Sci. 139 (2014) 139–147.
[69] E. Xanthakis, A. Le-Bail, H. Ramaswamy, Development of an innovative microwave assisted food freezing process, Innov. Food Sci. Emerg. Technol. 26 (2014) 176–181.
[70] J. Christensen, L. Nørgaard, R. Bro, S.B. Engelsen, Multivariate autofluorescence of intact food systems, Chem. Rev. 106 (2006) 1979–1994.

Annexe 2 : Script MatLab de corrections et prétraitement des images DUV (TELEMOS sur ligne DISCO)

correctIntensities

```
%% description
% correct each recoreded images for dark background and white illumination
% inhomogeneities

%% input

%  nothing : interactive function

%% output
%   nothing

%% principe
% all images acquired  in the root Folder will be processed
% they are found in roi sub-directories
%
% the user is asked for the dark and white images adapated to the series.
%
% correction is the following : Imc = (Imraw-dark)/(white-dark)normalised
%
% after correction, a median filtering of size 3x3 is applied to remove
% white noise due to low signal on the edge of the images
%
% corrected images are saved in a subfolder 'corrigees' and the hieracrrchy
% of sub-folders created by micromanager is reformed for the corrected
% images
%
% metadata are copied together with the corection of the vsiible image
% see function corrigerWhiteVis
%
% expected input folder hierarchy:
%
%     >sampleFolder
%         > PosFolders or RoiFolders
%         > SampleWhiteImage
%         > White
%               > white after offset
%      >darkFolder
%      >darkFolder.smooth
%      >whiteFolder
%         > darkFolderforWhite
%         > darkFolderforWhite.smooth
%      >whiteFolder.smooth
%
%
% expected output folder hierarchy:
%
%     >sampleFolder
```

```
%         > IntensityCorrected
%               > PosFolders or RoiFolders
%         > PosFolders or RoiFolders
%         > SampleWhiteImage
%         > White
%               > white after offset
%      >darkFolder
%      >darkFolder.smooth
%      >whiteFolder
%         > darkFolderforWhite
%         > darkFolderforWhite.smooth
%      >whiteFolder.smooth

%% use
% corrigerWhite

%% Comments
%   written for  Joel Passicousset PhD. IFPEN. proposal 20161050
% adapted for kevin Vidot (PhD PVPP INRA BIA) proposal 20170043

%% Author
% MF Devaux
% INRA BIA
% PVPP

%% date
% 5 octobre 2017:
% 2 mars 2018

%% context variables
orig=pwd;          % returns the current directory

%% start

if nargin ~=0
   error('use:  corrigerWhite');
end

%% input
%[rootFolder]=uigetdir(orig,'Root folder to process');

 [nameFolder,rootFolder,listDir,listChannel]=getInfoTelemos('root folder of TELEMOS images to process')

cd(rootFolder)

cd ..
cd ..

[rdarkFolder]=uigetdir('.','dark Images folder (preferably smoothed) ');
cd(rdarkFolder)
if ~exist('Pos0','dir')
```

```
   error('folder %s does not seem to be a TELEMOS folder')
end

cd(rootFolder)
if ~exist('intensityCorrected','dir')
   mkdir('intensityCorrected')
end
cd('intensityCorrected')
sfolder=pwd;

cd(rootFolder)
[fileWhite,rwhiteFolder]=uigetfile({'*.tif'},'white image','*.tif');

%% treatment
cd(rootFolder)

listdir=dir('roi*');
if isempty(listdir)
   listdir=dir('pos*');
   froi=0;
   fpos=1;
else
   froi=1;
   fpos=0;
end

if froi
   gsf='roi';
else  if fpos
   gsf='pos';
   else
      error('not micromanager structure of subfolder')
   end
end

info=readDIV([nameFolder '.' gsf '.metadata.txt']);
ntime=unique(info.d(:,1));
if length(ntime)~=1
   error('check number of time for each pos');
end
nz=unique(info.d(:,3));
if length(nz)~=1
   error('check number of z for each pos');
end

%read position of roi in white image
pos=readDIV([nameFolder '.pos.roi.txt']);
yl=pos.d(1,2);
xc=pos.d(1,1);

% read dark image
cd(rdarkFolder)
```

```
cd('Pos0')
listDark=dir('*.tif');
nbdark=length(listDark);

for i=1:nbdark
   dark(:,:,i)=imread(listDark(i).name);
end

% read white image
cd(rwhiteFolder)
imw=imread(fileWhite);

% determine size of images to be processed
cd(rootFolder)
cd(listdir(1).name);
list=dir('*.tif');
imetesdt=imread(list(1).name);

% compute dark and white adapted to the images to be processed
for i=1:nbdark
   darkc(:,:,i)=dark(yl:(yl+size(imetesdt,1)-1),xc:(xc+size(imetesdt,2)-1),i);
end

%white=imw;
white=imw(yl:(yl+size(imetesdt,1)-1),xc:(xc+size(imetesdt,2)-1));
%white=white-darkc;
wh=double(white)/max(double(white(:)));

% remove low values of white image
seuil=0.2;
wh(wh<seuil)=seuil;

% correct images
for i=1:length(listdir)
   display(listdir(i).name)
   cd(rootFolder);
   cd(listdir(i).name)
   %  list=dir('*_fluo_*.tif');
   list=dir('*.tif');

   rf=pwd;

   % create hireacrchy of sub-folders
   cd(sfolder)
   if ~exist(listdir(i).name,'dir')
      mkdir(listdir(i).name)
   end
   cd(listdir(i).name)
   sf=pwd;

   % for each file
   cpt=0;
```

```
   for t=1:ntime
      for z=1:nz
         for c=1:size(listChannel,1)       % for j=1:length(list)
            cpt=cpt+1;
            %read
            cd(rf)
            ime=imread(list(cpt).name);

            % subtract background
            imb=ime-darkc(:,:,c);
            % divide by white
            imc=uint16(double(imb)./wh);

            % filter noise due to low signal on the edge of the images
            imc=medfilt2(imc,[3 3 ],'symmetric');

            % save
            cd(sf)
            imwrite(imc,list(cpt).name);
         end
      end
   end

   cd(rf)
   copyfile('metadata.txt',sf)
end

cd(rootFolder)
copyfile('display_and_comments.txt',sfolder)

%% matlab function tracking
cd(sfolder)
fid=fopen('corrigerDarkAndWhite.track.txt','w');

if fid==0
   errordlg('enable to open track file');
end;

fprintf(fid,'\r\n%s\t',datestr(now,0));
fprintf(fid,'TELEMOS:  correction of images for intensity: subtract backgournd and divide by white
illumination to \r\n');
fprintf(fid,'_____
_____\r\n');

fprintf(fid,'\r\nProcessed root folder : %s\r\n',rootFolder);

fprintf(fid,'\r\nDark images found in folder:%s\r\n',rdarkFolder);
for i=1:length(listDark)
   fprintf(fid,'\t -  %s\r\n',listDark(i).name);
end
```

```
fprintf(fid,'\r\nWhite image:%s\r\n',fileWhite);
fprintf(fid,'Folder : %s\r\n',rwhiteFolder);
fprintf(fid,' White image is supposed to be preprocessed : smoothed and offseted for its own dark background: \r\n');
fprintf(fid,' White image is normalised so : smoothed and that its maximum is 1\r\n');
fprintf(fid,' Values of white image below %3.1f are set to %3.1f\r\n',seuil,seuil);

fprintf(fid,' Rois position in white and dardk images: \r\n')
fprintf(fid,'\t-Row position: %d\r\n\t-Col Position:%d\r\n',yl,xc);

fprintf(fid,'\r\n \r\n');
fprintf(fid,'Corrected images saved in folder: %s\r\n',sfolder);

fprintf(fid,'\r\n \r\n');
fprintf(fid,'Images were corrected as follow: \r\n');
fprintf(fid,'\t\tt (ImRaw(filter)-Dark(filter)) \r\n');
fprintf(fid,'\tImCorr = ----------------------------------\r\n');
fprintf(fid,'\t\t (ImWhiteSmoothOffsettedNormalisedTO1) \r\n');

fprintf(fid,'\r\n \r\n');
fprintf(fid,'Images were filtered to remove white for noise due to low signal: \r\n');
fprintf(fid,'\t- Median filtering of size 3x3: \r\n');

% save of function used
fprintf(fid,'_____
_\r\n');
info=which (mfilename);
os=computer;       % return the type of computer used : windows, mac...
switch os(1)
   case 'P'                    % for windows
      ind=strfind(info,'\');
   case 'M'                     % for Mac
      ind=strfind(info,'/');
   otherwise
      ind=strfind(info,'/');     % for UNIX, Linux (to be checked)
end;

repprog=info(1:(ind(length(ind))-1));
fprintf(fid,'function name: %s ',mfilename);
res=dir(info);
fprintf(fid,'on %s \r\n',res.date);
fprintf(fid,'function folder: %s \r\n',repprog);
%fprintf(fid,'_____
__\r\n');

fclose(fid);

%% end

cd (orig)
```

findWhiteImageTelemos

```
function [zmax]=findWhiteImageTelemos

%% description
% find the best z plane of white reference for a serie of acquisition and
% the position of the selected roi

%% input

%  nothing : interactive function

%% output
%    zmax : focal plane
%    yr: row position of the roi
%    xc : colum position of the roi

%% principe
% images were acquired for a given roi which position is found in metadata
% file
% white and dark  images were recorded for the full field of view of the DISCO
% TELEMOS carema
%
% correlation between a estimated sample white fluorescence image estalished from
% actual acquisitions and all z plane acquired for the reference TELEMOS white
% image (Matthieu slide or anay fluorescent homogeneous image) :

% used function estimateSampleWhiteImage to compute
% this estimated sample white fluorescence image
%
%   or choose any image that can roughly show the shape of illumination
%
% the z plane for which the maximum correlation is observed is retained.
% the white image is then offsetted and copied in a subfolder of the sample
% folder to show that it has been specifically selected for the sample
%
% correlation coefficients are saved in a file called
% 'corr.txt' in the subfolder 'whiteImageTelemos'
%
% expected input folder hierarchy:
%
%     >sampleFolder
%         > PosFolders or RoiFolders
%         > SampleWhiteImage
%      >darkFolder
%      >darkFolder.smooth
%      >whiteFolder
%         > darkFolderforWhite
%         > darkFolderforWhite.smooth
%      >whiteFolder.smooth
%
% expected output folder hierarchy:
%
```

```
%     >sampleFolder
%         > IntensityCorrected
%               > PosFolders or RoiFolders
%         > PosFolders or RoiFolders
%         > SampleWhiteImage
%         > White
%               > white after offset
%      >darkFolder
%      >darkFolder.smooth
%      >whiteFolder
%         > darkFolderforWhite
%         > darkFolderforWhite.smooth
%      >whiteFolder.smooth

%% use
% [zmax]=findWhiteImageTelemos

%% Comments
%   written for  Joel Passicousset PhD. IFPEN. proposal 20161050
%   adapted for Kevin Vidot PhD (INRA PVPP) proposal 20170043

%% Author
% MF Devaux
% INRA BIA
% PVPP

%% date
% 5 octobre 2017:
% 15 decembre 2017 : adapted to take into account the roi known from
% metadata
% 27 fevrier 2018 : comments details

%% context variables
orig=pwd;          % returns the current directory

%% start

if nargin ~=0
   error('use:  [zmax]=findWhiteImageTelemos');
end

%% input
[genName,rootFolder,~,~]=metadataTelemos('root folder of TELEMOS images to process');
cd(rootFolder)

[filename,rreffluoEchfolder]=uigetfile({'*.tif'},'reference fluorescence image of sample','*.tif');

cd ..
cd ..

[rfolderWhite]=uigetdir('.','Root folder of white images (preferably smoothed)');
cd(rfolderWhite)
```

```
if ~exist('Pos0','dir')
   error('folder %s does not seem to be a TELEMOS folder')
end

cd ..

[rfolderDarkforWhite]=uigetdir('.','Root folder of dark image for white images (preferably smoothed)
- one image expected in the Pos0 subfolder');
cd(rfolderDarkforWhite)
if ~exist('Pos0','dir')
   error('folder %s does not seem to be a TELEMOS folder')
end

cd(rreffluoEchfolder)
sfolder=pwd;

%% treatment
% read 'reference fluorescence image of sample
cd(rreffluoEchfolder)
imetesdt=imread(filename);
nl=size(imetesdt,1);
nc=size(imetesdt,2);

% read ROI position
cd(rootFolder)
roiPos=readDIV([genName '.pos.roi.txt']);
dl=roiPos.d(1,2);              % move in lines
dc=roiPos.d(1,1);            % move in column
if dl==0
   dl=1;
end
if dc==0
   dc=1;
end

% consider each possible white image
cd(rfolderWhite)
cd('Pos0');
% list of possible white images
list=dir('*.tif');

cc=zeros(length(list),1);

for i=1:length(list)
   display(list(i).name)

   % read image
   imw=imread(list(i).name);
   imw=imw(dl:(dl+nl-1),dc:(dc+nc-1));
  % correlation
 C=corrcoef(double(imetesdt(:)),double(imw(:)));
```

```
  cc(i)=C(1,2);
end

% find z plane of maximal correlation coefficcient
zmax=find(cc==max(cc));
% figure of correlation coefficient according to z plane
figure
plot(cc,'linewidth',2);
xlabel('z plane','fontsize',18)
ylabel('correlation coeffcient','fontsize',18)
title('correlation coefficients','fontsize',18)

% read reference white image
imw=imread(list(zmax).name);

% read dark image to offset white image
cd(rfolderDarkforWhite)
cd('Pos0');
listdark=dir('*.tif');
if length(listdark)>1
   warning('more than one dark image found for white, first image considered');
end
if isempty(listdark)
   error('dark image for white is missing');
end

dark=imread(listdark(1).name);

% offsetted white
imwo=imsubtract(imw,dark);

% profile of offsetted white image
co=improfile(imwo(dl:(dl+nl-1),dc:(dc+nc-1)),[1 nc],[1 nl]);
c=improfile(imw(dl:(dl+nl-1),dc:(dc+nc-1)),[1 nc],[1 nl]);
p=improfile(imetesdt,[1 nc],[1 nl]);
po=improfile(imsubtract(imetesdt,dark(dl:(dl+nl-1),dc:(dc+nc-1))),[1 nc],[1 nl]);

co=double(co)/double(max(co));
seuil=0.2;
co(co<seuil)=seuil;
poc=double(po)./co;

%% save
cd(sfolder);
% selected white image
sname=[strrep(filename,'.tif','') '.WhiteIMage' num2str(zmax-1) '.tif'];
imwrite(imw,sname,'tif','compression','none');

%figure
saveas(gcf,[sname '.corr.png']);

% cross correlation results
```

```
ccr.d=cc;
ccr.v=char('corrcoeff');
ccr.i=(1:length(list))';

writeDIV(ccr,[sname 'corr.txt']);

% fusion of the two images
tmp=double(imw)/double(max(imw(:)));
voir=tmp;
tmp=zeros(size(tmp));
tmp(dl:(dl+nl-1),dc:(dc+nc-1))=double(imetesdt)/double(max(imetesdt(:)));
voir(:,:,2)=tmp;
voir(:,:,3)=tmp;

figure
imshow(voir,[])
hold on
plot([dc dc+nc-1 dc+nc-1 dc dc],[dl dl dl+nl-1 dl+nl-1 dl],'r','linewidth',2);

% save offsetted white image if <white folder>
cd(rootFolder)
if ~exist('white','dir')
   mkdir('white')
end

cd('white')
sfoldero=pwd;
% selected white image
snameo=strrep(sname,'.tif','.offset.tif');
imwrite(imwo,snameo,'tif','compression','none');

figure
plot(co/max(co)*max(p),'m','linewidth',1.5)
hold on
plot(po,'k','linewidth',1.5)
ho=legend('offsetted white','offsetted sample image');

xlabel('pixel','fontsize',18)
ylabel('intensité','fontsize',18)

set(ho,'location','eastoutside')
title('profil diagonal','fontsize',18)
saveas(gcf,'profilDiagonal.png')

figure
plot(co/max(co)*max(p),'m','linewidth',1.5)
hold on
plot(poc,'r','linewidth',1.5)
plot(po,'k','linewidth',1.5)
ho=legend('offsetted white','corrected image','offsetted sample image');

xlabel('pixel','fontsize',18)
```

```
ylabel('intensité','fontsize',18)

set(ho,'location','eastoutside')
title('profil diagonal','fontsize',18)
saveas(gcf,'profilDiagonal.png')

figure
imshow(imetesdt,[])
hold on
plot([1 nc],[1 nl],'r','linewidth',2)
saveas(gcf,'profilDiagonal.locate.png')

%% matlab function tracking

fid=fopen(strrep(sname,'.tif','.track.txt'),'w');

if fid==0
   errordlg('enable to open track file');
end

fprintf(fid,'\r\n%s\t',datestr(now,0));
fprintf(fid,'TELEMOS:  Find white reference image from cross correlation with reference fluorescence
image of sample to \r\n');
fprintf(fid,'_____
_____\r\n');

fprintf(fid,'\r\nReference fluorescence image of sample:%s\r\n',filename);
fprintf(fid,'Folder : %s\r\n',rreffluoEchfolder);

fprintf(fid,'\r\nWhite Images searched in folder: % s\r\n',rfolderWhite);

fprintf(fid,'\r\n \r\n');
fprintf(fid,'Maximum correlation coefficient:%f5:2\r\n',cc(zmax));
fprintf(fid,'white image:%s\r\n',list(zmax).name);

fprintf(fid,'\r\n');
fprintf(fid,'Saved as :%s\r\n', sname);
fprintf(fid,'\t- In folder: %s\r\n',sfolder);

fprintf(fid,'\r\n\r\n \r\n');
fprintf(fid,'White image after offset:\r\n');
fprintf(fid,'\t-using dark image for White:%s\r\n',listdark(1).name);
fprintf(fid,'\t\t- read in folder : %s\\Pos0\r\n\r\n',rfolderDarkforWhite);
fprintf(fid,'Offsetted White image:%s\r\n', snameo);
fprintf(fid,'\t- Saved in folder: %s\r\n',sfoldero);


% save of function used
fprintf(fid,'_____
_\r\n');
info=which (mfilename);
os=computer;       % return the type of computer used : windows, mac...
```

```
switch os(1)
   case 'P'                    % for windows
      ind=strfind(info,'\');
   case 'M'                     % for Mac
      ind=strfind(info,'/');
   otherwise
      ind=strfind(info,'/');      % for UNIX, Linux (to be checked)
end

repprog=info(1:(ind(length(ind))-1));
fprintf(fid,'function name: %s ',mfilename);
res=dir(info);
fprintf(fid,'on %s \r\n',res.date);
fprintf(fid,'function folder: %s \r\n',repprog);
%fprintf(fid,'_____________________________________________________________________________
__\r\n');

fclose(fid);

%% end

cd (orig)
```

function smoothImageTelemos

```
 %% description
   % smooth the Telemos White or Dark images

%% input

   %  nothing interactive fonction
%% output

   %   nothing smoothed images are saved on disk

%% principe
   % Images are recorded using Telemos microscope and  MicroManager
   % raw images are search in the PosO folder in the root directory
   % all images (filters, t, z)  in the PosO are processed
   %
   % images are filtered : median filtering to remove spikes
   %                  average filtering to remoce noise
   % dead pixels (three lines and columns around the image) are not taken
   % in filtering and replaced by line and column number 4 and end-3
   %
   % images are saved on disk on Pos0smooth folder

%% use
   % smoothImageTelemos

%% Comments
   %   adatped from function developped for experiment proposal 20140308

%% Author
   % MF Devaux & FJamme
   % INRA BIA
   % PVPP

%% date
   % 5 janvier 2017
   % 2 octobre 2017: adapted for Joel Passicousset PhD. IFPEN. proposal 20161050
   % 21 November 2017
   % 15 decembre 2017 : folder name smoothPos0

%% context variables
orig=pwd;         % returns the current directory
% size of median filtering
sizeMedFilt=9;
% size of average filtering
sizeAverageFilt=25;

%% start

if nargin >0
   error('use: smoothImageTelemos');
```

```
end

%% input
[rootFolder]=uigetdir('MicroManager Root folder of image to smooth');
cd(rootFolder)
if  ~exist('Pos0','dir')
   error('no PosO folder in %s root Folder',rootFolder);
end

cd ..

% for saving smoothed images
if ~exist([rootFolder '.smooth'],'dir')
   mkdir([rootFolder '.smooth'])
end
cd([rootFolder '.smooth']);
sfolderRoot=pwd;
if ~exist('Pos0','dir')
   mkdir('Pos0');
end
cd('Pos0');
sfolder=pwd;

%% treatement

cd(rootFolder)
cd ('Pos0')
list=dir('*.tif');
nb=length(list);
for i=1:nb
   fprintf('%d: %s\r\n',i,list(i).name)
   im=imread(list(i).name);
   imtmp=im;

   % crop to remove dead pixels
   im=im(4:(end-3),4:(end-3));

   % median filtering
   imf=medfilt2(im,[sizeMedFilt sizeMedFilt],'symmetric');

   % average filtering
   f=fspecial('average',sizeAverageFilt);
   imf=imfilter(imf,f,'symmetric');

   % manage dead pixels

   imtmp(4:(end-3),4:(end-3))=imf;
   imtmp(1:3,4:(end-3))=repmat(imf(1,:),3,1);
   imtmp((end-2):end,4:(end-3))=repmat(imf(end,:),3,1);
   imtmp(:,1:3)=repmat(imtmp(:,4),1,3);
   imtmp(:,(end-2):end)=repmat(imtmp(:,end-3),1,3);
   imf=imtmp;
```

```
   % save
   cd(sfolder);
   imwrite(imf,list(i).name);

   cd(rootFolder);
   cd('Pos0')
end

copyfile('metadata.txt',sfolder);
cd ..

listtxt=dir('*.txt');
for i=1:length(listtxt)
   copyfile(listtxt(i).name,sfolderRoot);
end

%% matlab function tracking
cd(sfolder);
cd ..;
nomtrack='smoothPos0';
fid=fopen(strcat(nomtrack,'.track.txt'),'w');

if fid==0
   errordlg('enable to open track file');
end

fprintf(fid,'\r\n%s\t',datestr(now,0));
fprintf(fid,'TELEMOS: smooth image to generate dark and white images \r\n');
fprintf(fid,'_____
_\r\n');

fprintf(fid,'\r\nRaw files found in folder: %s\\Pos0\r\n',rootFolder);

fprintf(fid,'\r\n Images are filtered: median filtering of size %dX%d to remove spikes\r\n',sizeMedFilt,
sizeMedFilt);
fprintf(fid,'\r\n                                    : average filtering of size %dX%d    for
smoothing\r\n',sizeAverageFilt,sizeAverageFilt);
fprintf(fid,'\r\n dead pixels (three lines and columns around the image) are not taken in filtering and
replaced by line and column number 4 and end-3 \r\n');
fprintf(fid,'\r\n \r\n');
fprintf(fid,'smoothed images saved in folder: %s\\Pos0smooth\r\n',rootFolder);

% save of function used
fprintf(fid,'_____
_\r\n');
info=which (mfilename);
os=computer;       % return the type of computer used : windows, mac...
switch os(1)
   case 'P'                  % for windows
      ind=strfind(info,'\');
   case 'M'                   % for Mac
      ind=strfind(info,'/');
```

```
   otherwise
      ind=strfind(info,'/');      % for UNIX, Linux (to be checked)
end

repprog=info(1:(ind(length(ind))-1));
fprintf(fid,'function name: %s ',mfilename);
res=dir(info);
fprintf(fid,'on %s \r\n',res.date);
fprintf(fid,'function folder: %s \r\n',repprog);
%fprintf(fid,'_____
__\r\n');

fclose(fid);

%% end

cd (orig)
```

Annexe 3 : Script R pour l'ACP distinguant les filtres d'émissions sur les images DUV

```
#pca_image_disco
############
rm(list=(ls()))
setwd(getwd())
############
library(tiff)
library(raster)
library(FactoMineR)
library(factoextra)
###########
#reptertoires

# remplace/crée un répertoire pour recevoir les données traitées
contdir<-dir()
testdir<-match("images_RES",contdir) # test la présence du directory de résultat, si présent, l'elimine
if(is.na(testdir)==FALSE) unlink("images_RES", recursive=TRUE)

dir.create(paste(getwd(),"/images_RES",sep="")) # cree le repertoire de destination des fichiers
############
depli<-function(image){
        dim1<-dim(image)
        depli1<-c()
        for(i in 1:dim1[2]){depli1<-c(depli1,image[,i])}
        return(depli1)
}

repli<-function(vector,ligne){
        temp1<-seq(1,length(vector),ligne)
        repli1<-c()
        for(i in 1:length(temp1)){repli1<-cbind(repli1,vector[temp1[i]:c(temp1[i]+c(ligne-1))])}
        return(repli1)
}
#############
d<-dir()
e<-d[grep(".tif",d)]
im<-c()
for(i in 1: length(e)){im<-cbind(im,depli(readTIFF(e[i])))}
colnames(im)<-sub(".tif","",e)

#supprime le filtre 307
im<-im[,-grep("307",colnames(im))]
#supprime filtre 370
im<-im[,-grep("370",colnames(im))]
#supprime filtre 370
im<-im[,-grep("435",colnames(im))]

a_im<-PCA(im, graph=FALSE)
```

```
pdf(paste(getwd(),"/images_RES/acp_var.pdf",sep=""))
fviz_screeplot(a_im, addlabels = TRUE, ylim = c(0, 80))
fviz_pca_var(a_im, geom=c("arrow","text"), axes=c(1,2),select.var=list(cos2=0.2))
fviz_pca_var(a_im, geom=c("arrow","text"), axes=c(3,4),select.var=list(cos2=0.1))
fviz_pca_var(a_im, geom=c("arrow","text"), axes=c(4,5),select.var=list(cos2=0.1))
dev.off()

loads<-sweep(a_im$var$coord,2,sqrt(a_im$eig[1:ncol(a_im$var$coord),1]),FUN="/")
f4<-repli(a_im$ind$coord[,4],500)
f1<-repli(a_im$ind$coord[,1],500)
f2<-repli(a_im$ind$coord[,2],500)
f3<-repli(a_im$ind$coord[,3],500)
f5<-repli(a_im$ind$coord[,5],500)

colfunc<-colorRampPalette(c("blue","white","red"))

tiff(paste(getwd(),"/images_RES/images_pca_dim4.tiff",sep=""),width=500,                height=250,
compression=c("none"))
image(scale(f4),col=colfunc(50), main="dim4", yaxt="n", xaxt="n")
dev.off()

tiff(paste(getwd(),"/images_RES/images_pca_dim1.tiff",sep=""),width=500,                height=250,
compression=c("none"))
image(scale(f1),col=colfunc(50), main="dim1", yaxt="n", xaxt="n")
dev.off()

tiff(paste(getwd(),"/images_RES/images_pca_dim2.tiff",sep=""),width=500,                height=250,
compression=c("none"))
image(scale(f2),col=colfunc(50), main="dim2", yaxt="n", xaxt="n")
dev.off()

tiff(paste(getwd(),"/images_RES/images_pca_dim3.tiff",sep=""),width=500,                height=250,
compression=c("none"))
image(scale(f3),col=colfunc(50), main="dim3", yaxt="n", xaxt="n")
dev.off()

tiff(paste(getwd(),"/images_RES/images_pca_dim5.tiff",sep=""),width=500,                height=250,
compression=c("none"))
image(scale(f5),col=colfunc(50), main="dim5", yaxt="n", xaxt="n")
dev.off()


#jpeg 75%
jpeg(paste(getwd(),"/images_RES/images_pca_dim4.jpeg",sep=""),width=500, height=250)
image(scale(f4),col=colfunc(50), main="dim4", yaxt="n", xaxt="n")
dev.off()

jpeg(paste(getwd(),"/images_RES/images_pca_dim1.jpeg",sep=""),width=500, height=250)
image(scale(f1),col=colfunc(50), main="dim1", yaxt="n", xaxt="n")
dev.off()

jpeg(paste(getwd(),"/images_RES/images_pca_dim2.jpeg",sep=""),width=500, height=250)
```

```
image(scale(f2),col=colfunc(50), main="dim2", yaxt="n", xaxt="n")
dev.off()

jpeg(paste(getwd(),"/images_RES/images_pca_dim3.jpeg",sep=""),width=500, height=250)
image(scale(f3),col=colfunc(50), main="dim3", yaxt="n", xaxt="n")
dev.off()

jpeg(paste(getwd(),"/images_RES/images_pca_dim5.jpeg",sep=""),width=500, height=250)
image(scale(f5),col=colfunc(50), main="dim5", yaxt="n", xaxt="n")
dev.off()

################
#save.image("pca_image.Rdata")
```

Annexe 4 : Script ImageJ permettant d'accéder aux valeurs de lignes de pixels par image distance sur les images DUV

```
///Sur les images "rognées" de 250x500µm de chaque échantillon

//ouvrir le filtre de échantillon avec "le plus" de fluorescence pour crée un masque avec la forme de l'échantillon (généralement celui à 420nm)
//garder le masque ouvert et lancer le script en suivant les indications

/////////création dossier de sauvegarde des masques après chaque érosion d'un pixel
dir1="C:\\Users\\kvidot\\Desktop\\DISCO 12-2017\\image destack pre-traite\\D01\\"
myDir = dir1+"mask"+File.separator;
	File.makeDirectory(myDir);
	print("");
	print(myDir);

//récupération des masques après chaque érosion;
for (i=0; i<500; i++) {
	run("Erode (3D)", "iso=255");
	names = myDir + i+1000;
	saveAs ("Tiff", names);
}
close();

/////////création dossier de sauvegarde des masques de ligne de pixels
myDir2 = dir1+"mask_pxl"+File.separator;
	File.makeDirectory(myDir2);
	print("");
	print(myDir2);

// Soustrait les masques 1 à 1 successifs pour obtenir les masques de ligne de pixels
dir2="C:\\Users\\kvidot\\Desktop\\DISCO 12-2017\\image destack pre-traite\\D01\\mask\\"
list = getFileList(dir2);
for (i=0; i<list.length; i++) {
  a= dir2+list[i];
  open(a);
  a1= getTitle();
  b= dir2+list[i+1];
  open(b);
  b1= getTitle();
  imageCalculator("Subtract create", a1, b1);
  names2 = myDir2 + i+1000;
  saveAs ("Tiff", names2);
  run("Close All");
}
close()
//affichage msg d'erreur, "image 500 non trouvé" cliquer sur ok///


//!!!!!!!!!!!Lancer la suite du script ci-dessous manuellement!!!!!!!!!!!!!!
run("Close All");
```

```
/////////création dossier de sauvegarde des masques de ligne de pixels binarisées/////
dir1="C:\\Users\\kvidot\\Desktop\\DISCO 12-2017\\image destack pre-traite\\D01\\"
myDir3 = dir1+"mask_pxl_bin"+File.separator;
        File.makeDirectory(myDir3);
        print("");
        print(myDir3);

// on binarise 0 et 1
dir2="C:\\Users\\kvidot\\Desktop\\DISCO 12-2017\\image destack pre-traite\\D01\\mask_pxl\\"
list = getFileList(dir2);
for (i=0; i<list.length; i++) {
 a= dir2+list[i];
 open(a);
 run("Macro...", "code=[if (v==255) v=1]");
 names3 = myDir3 + i+1000;
 saveAs ("Tiff", names3);
 run("Close All");
}
```

//!!!!!!!!!!!Lancer la 3e parti du script ci-dessous manuellement!!!!!!!!!!!!!!

```
run("Close All");
// Application des masques de ligne de pixels sur l'image natif
dir1="C:\\Users\\kvidot\\Desktop\\DISCO 12-2017\\image destack pre-traite\\D01\\Crop"  ///dossier
contenant les images rognées 250x600 µm
list = getFileList(dir1);
dir2 ="C:\\Users\\kvidot\\Desktop\\DISCO 12-2017\\image destack pre-
traite\\D01\\mask_pxl_bin\\"
list2= getFileList(dir2);
for (i=0; i<list.length; i++) {
 a= dir1+list[i];
 open(a);
 a1= getTitle();
 myDir4 = dir1+"result"+getTitle+File.separator;
        File.makeDirectory(myDir4);
        print("");
        print(myDir4);
 for (j=0; j<list2.length; j++) {
        b= dir2+list2[j];
        open(b);
        b1= getTitle();
 imageCalculator("Multiply create", a1, b1);
 names4 = myDir4 +a1+j+1000;
 saveAs ("Tiff", names4);
 close();
}
run("Close All");
}
/////////création dossier de sauvegarde des fichiers Excels/////
dir1="C:\\Users\\kvidot\\Desktop\\DISCO 12-2017\\image destack pre-traite\\D01\\Crop\\"
list = getFileList(dir1);
```

```
myDir = dir1+"data_csv"+File.separator;
        File.makeDirectory(myDir);
        print("");
        print(myDir);

////// on recupère la moyenne d'intensité de gris par ligne de pixel !!!!!
run("Set Measurements...", "mean redirect=None decimal=3");
dir2="C:\\Users\\kvidot\\Desktop\\DISCO 12-2017\\image destack pre-
traite\\D01\\Crop\\result_278.tif\\"          ///changer de dossier "result_(n°filtre)
list = getFileList(dir2);
for (i=0; i<list.length; i++) {
  a= dir2+list[i];
  open(a);
  run("Macro...", "code=[if (v==0) v=NaN]");
  run("Measure");
  run("Close All");
}
saveAs("Results", myDir+"278.csv");          ///changer le nom du fichier "n°filtre correspondant"
run("Clear Results");
```

Annexe 5: Script R permettant d'accéder aux profils de distribution lissés à partir des valeurs de lignes de pixels récupéré sur ImageJ (images DUV et Fluo X)

###Les valeurs des lignes de pixels sont moyennées puis la régression linéaire par la méthode LOESS (coeff. α = 0.3) y est appliquée avant de tracer les profils.

```
rm(list=(ls()))
d<-dir(pattern="7p2keV.csv")              ###dossier de fichiers contenant les valeurs moyennes

for (i in 1:length(d)){

 filename <- d[i]
 temp=unlist(strsplit(filename,"_7p2keV.csv"))
 name=paste("plot", temp, ".pdf")
 pdf(name)                                ##### récupération du nom du graphique
 r<-read.csv(d[i], sep=";" , header=TRUE)
 Count<-c(r[1:202,5])                     #####récupération des valeur + écart-type
 plus<-c(r[1:202,7])
 moins<-c(r[1:202,8])
 µm<-c(r[1:202,1])

 mod=loess(Count~µm,span=0.3)             #####application du LOESS
 yfit=predict(mod, newdata=µm)
 modplus=loess(plus~µm,span=0.3)
 yfitplus=predict(modplus, newdata=µm)
 modmoins=loess(moins~µm,span=0.3)
 yfitmoins=predict(modmoins, newdata=µm)

####plot des profils moyens avec écart-types

 plot(µm,Count, type="l", lwd=2, xlim=c(0,550), main=temp, cex.main=2, cex.lab=1.5)
 lines(µm,plus, type="l", lty="dashed", xlim=c(0,550))
 lines(µm,moins, type="l", lty="dashed", xlim=c(0,550))

 plot(µm,yfit, type="l", lwd=2, xlim=c(0,550), main=temp, cex.main=2, cex.lab=1.5)
 lines(µm,yfitplus, type="l", lty="dashed", xlim=c(0,550))
 lines(µm,yfitmoins, type="l", lty="dashed", xlim=c(0,550))

 plot(µm,Count, type="l", lty="dashed", lwd=2, xlim=c(0,550), main=temp, cex.main=2, cex.lab=1.5)
 lines(µm,plus, type="l", lty="dashed", xlim=c(0,550))
 lines(µm,moins, type="l", lty="dashed", xlim=c(0,550))
 lines(µm,yfit, type="l", col="blue", lwd=3, xlim=c(0,550))

 dev.off()
}
```

Annexe 6 : Images brutes de fluorescence X sur l'épiderme de DM et GU (récolte 2017)

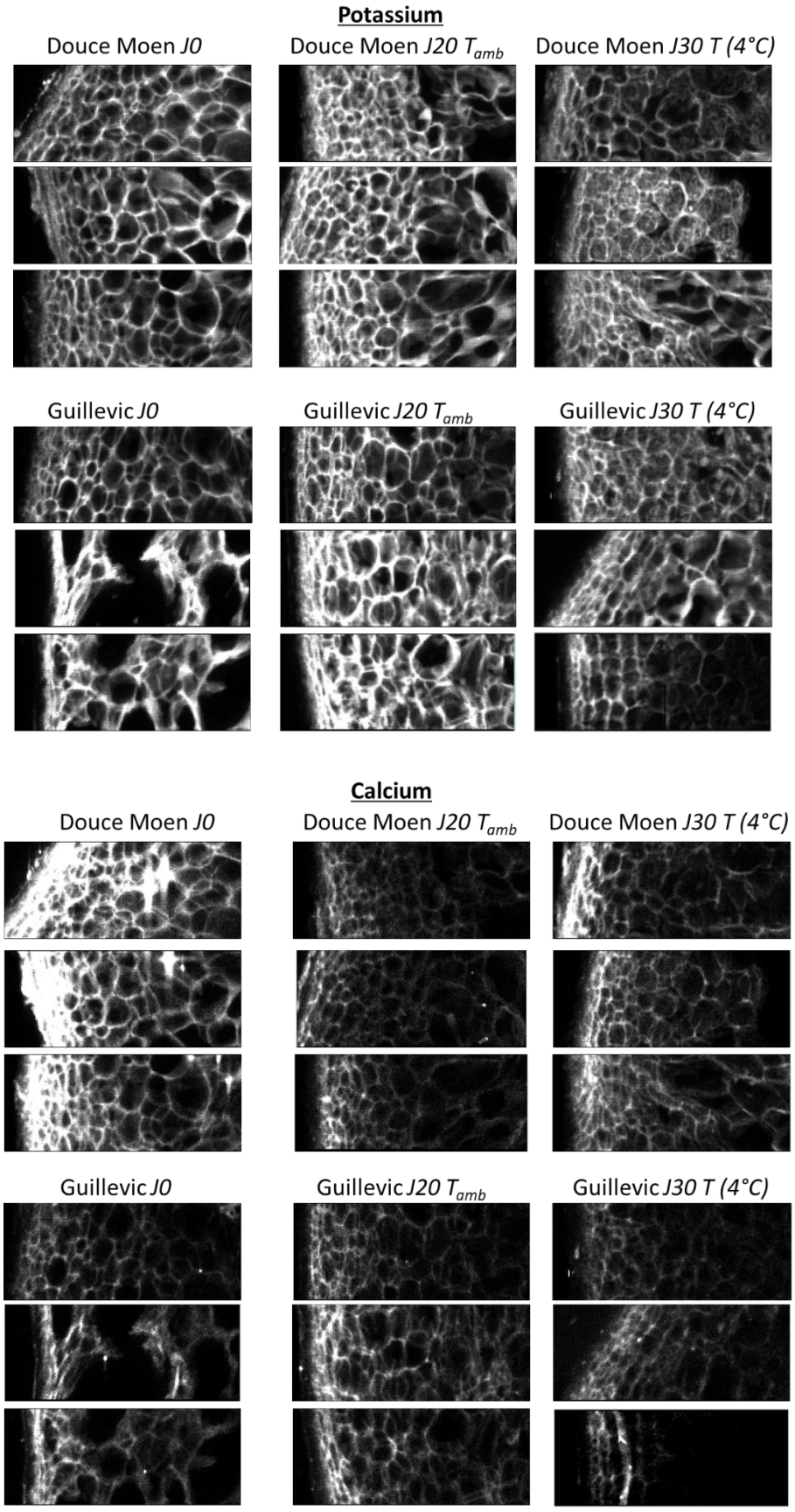

Magnesium

Douce Moen *J0*

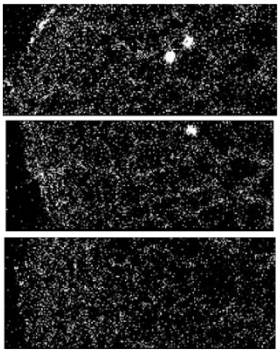

Douce Moen *J20* T_{amb}

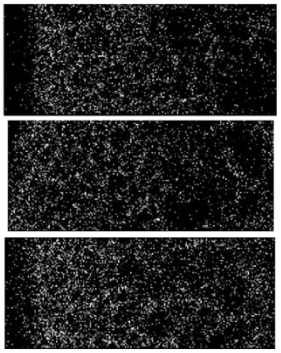

Douce Moen *J30 T (4°C)*

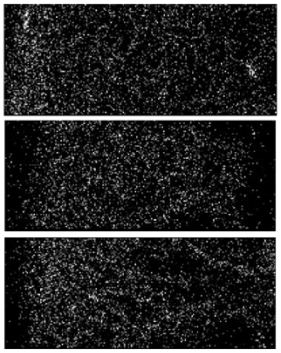

Guillevic *J0*

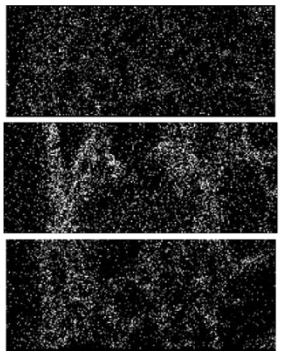

Guillevic *J20* T_{amb}

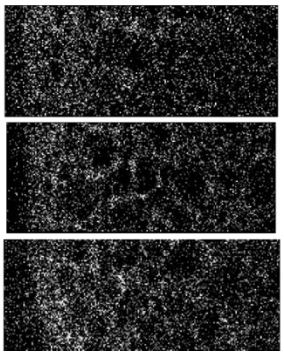

Guillevic *J30 T (4°C)*

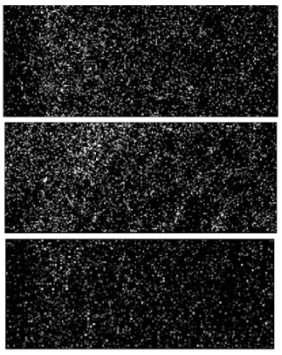

Iron

Douce Moen *J0*

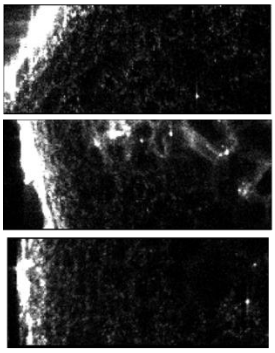

Douce Moen *J20* T_{amb}

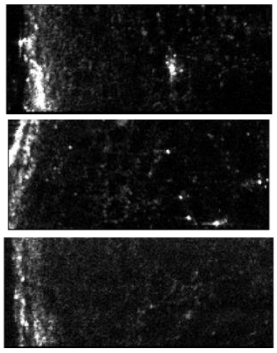

Douce Moen *J30 T (4°C)*

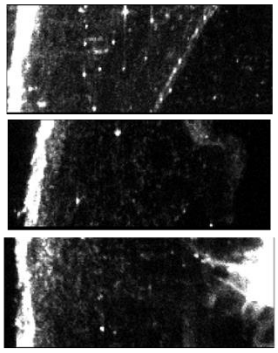

Guillevic *J0*

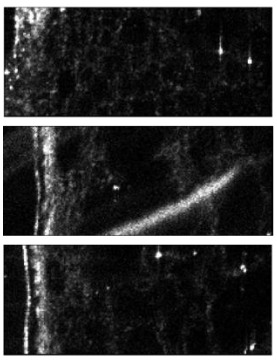

Guillevic *J20* T_{amb}

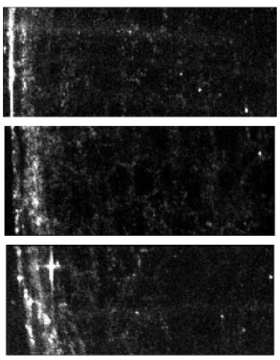

Guillevic *J30 T (4°C)*

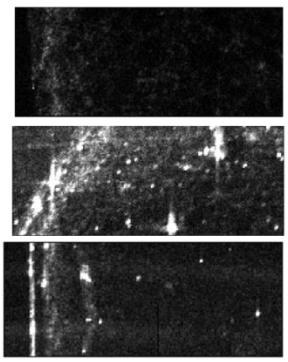

Manganese

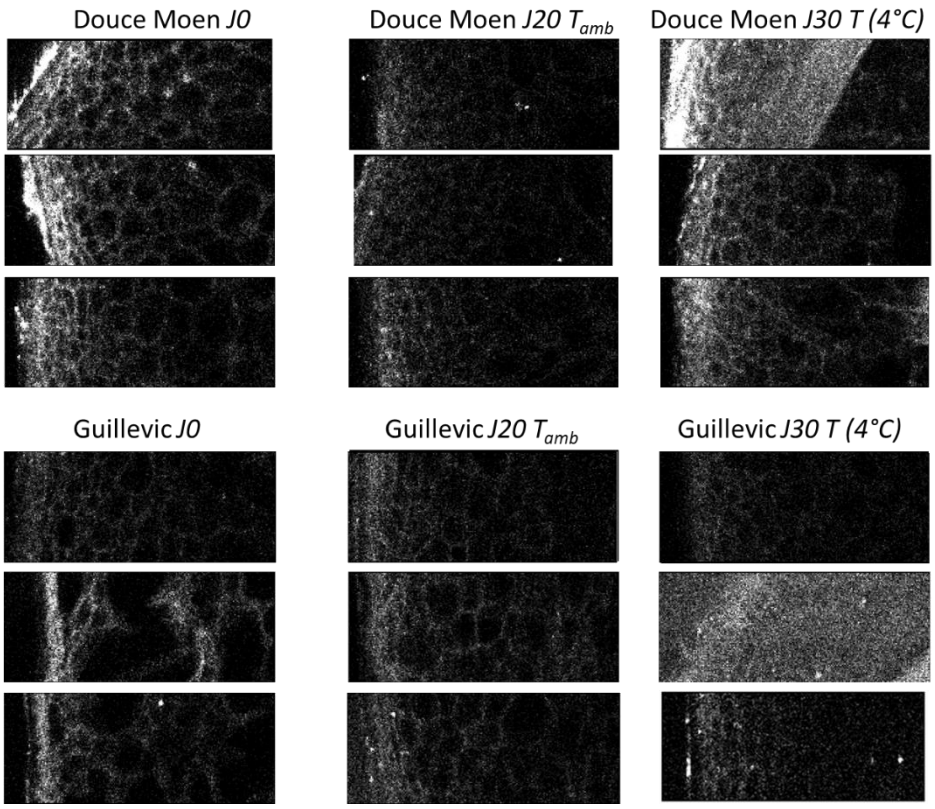
Douce Moen *J0*
Douce Moen *J20* T_{amb}
Douce Moen *J30 T (4°C)*
Guillevic *J0*
Guillevic *J20* T_{amb}
Guillevic *J30 T (4°C)*

Annexe 7 : Image RGB reconstruite à partir de la fluorescence X du tissu de GU et DM (récolte 2018)

⇨ Visualisation du K, Ca, Fe. Résolution 25 µm et 3 µm

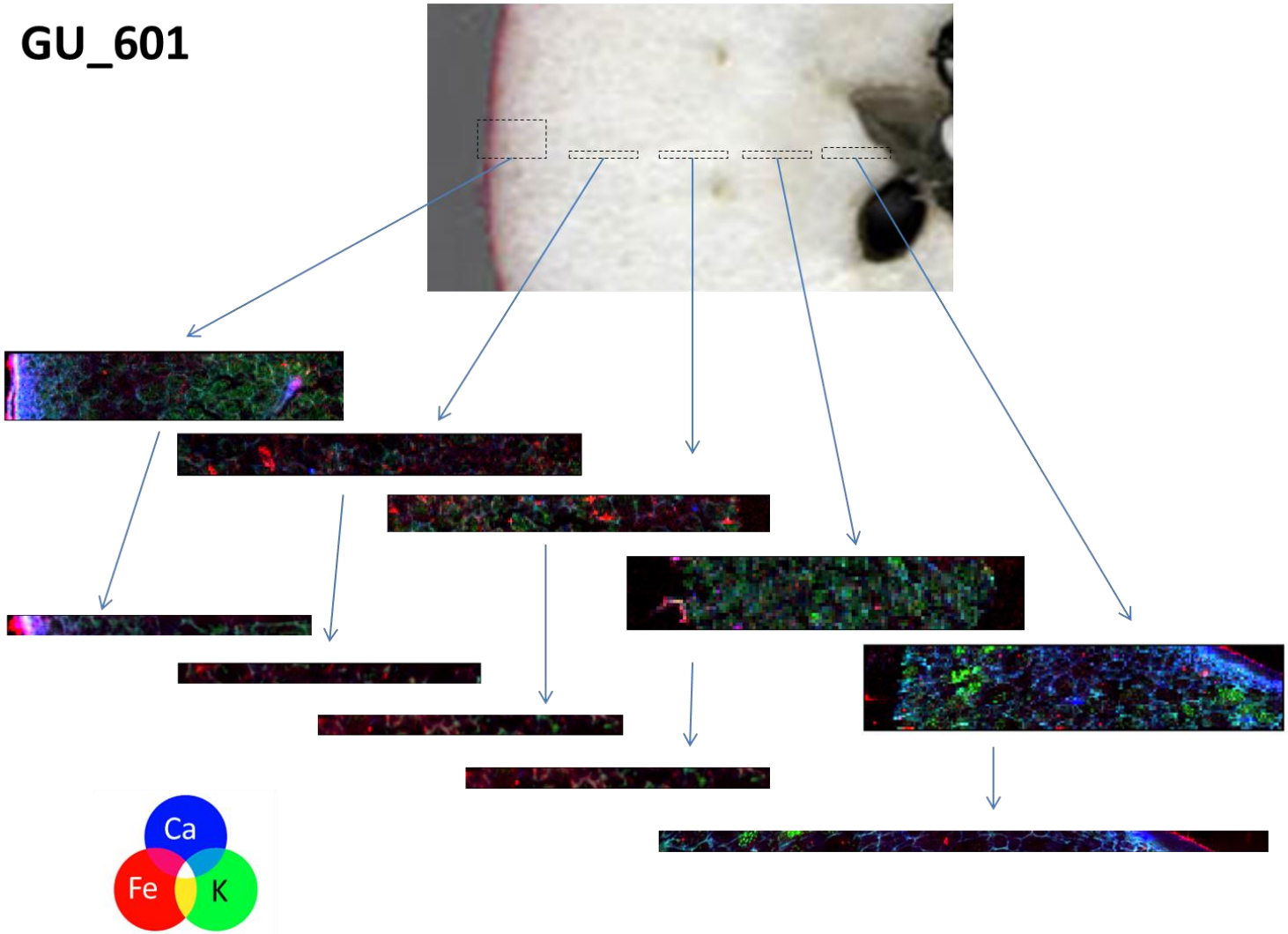

DM450

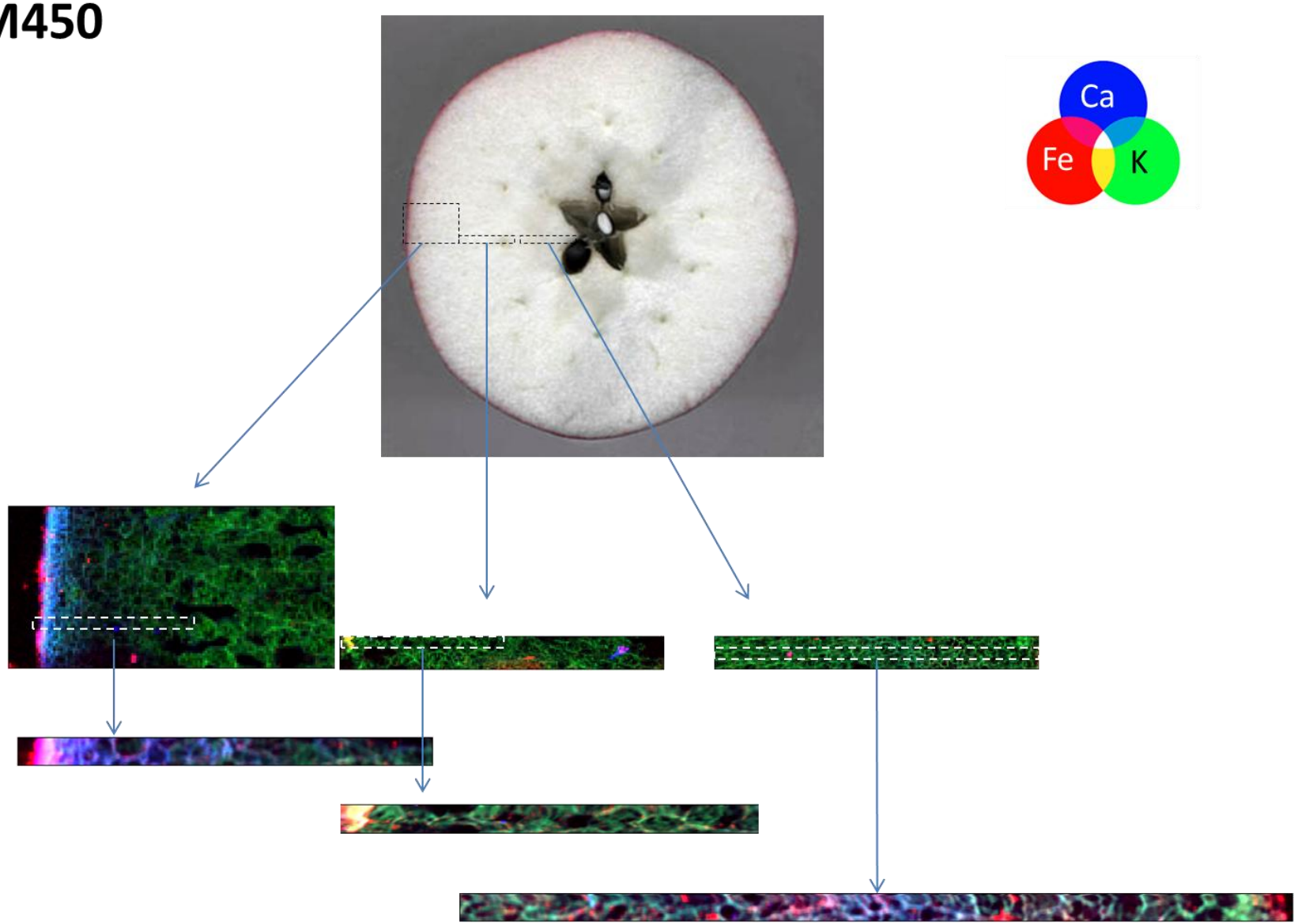

Annexe 8 : Script ImageJ permettant d'accéder aux valeurs de lignes de pixels par image distance sur les images de fluo X

```
//ouvrir l'image du potassium et faire un masque avec la fonction threshold
//garder le masque ouvert et lancer le script en suivant les indications

/////////création dossier de sauvegarde des masques/////
dir1="C:\\Users\\kvidot\\Desktop\\LUCIA\\"                    //choisir un dossier de travail
myDir = dir1+"mask"+File.separator;
        File.makeDirectory(myDir);
        print("");
        print(myDir);

//récupération des masques entier et après chaque érosion d'un pixel;
for (i=0; i<510; i++) {
        run("Erode (3D)", "iso=255");
        names = myDir + i+1000;
        saveAs ("Tiff", names);
}
close();

/////////création dossier de sauvegarde des masques de ligne de pixels/////
dir1="C:\\Users\\kvidot\\Desktop\\LUCIA\\"
list = getFileList(dir1);
myDir = dir1+"mask_pxl"+File.separator;
        File.makeDirectory(myDir);
        print("");
        print(myDir);

// Soustrait les masques 1 à 1 successifs pour obtenir les masques par ligne de pixels
dir2="C:\\Users\\kvidot\\Desktop\\LUCIA\\mask\\"
list = getFileList(dir2);
for (i=0; i<list.length; i++) {
  a= dir2+list[i];
  open(a);
  a1= getTitle();
  b= dir2+list[i+1];
  open(b);
  b1= getTitle();
  imageCalculator("Subtract create", a1, b1);
  names2 = myDir + i+1000;
  saveAs ("Tiff", names2);
  run("Close All");
}
close()
//affichage msg d'erreur///
```

//!!!!!!!!!!!Lancer la 2e parti du script manuellement!!!!!!!!!!!!!!

```
run("Close All");
/////////création dossier de sauvegarde des masques de ligne de pixels binarisées/////
dir1="C:\\Users\\kvidot\\Desktop\\LUCIA\\
list = getFileList(dir1);
myDir = dir1+"mask_pxl_bin"+File.separator;
        File.makeDirectory(myDir);
        print("");
        print(myDir);

// on binarise 0 et 1
dir2="C:\\Users\\kvidot\\Desktop\\LUCIA\\mask_pxl\\"
list = getFileList(dir2);
for (i=0; i<list.length; i++) {
 a= dir2+list[i];
 open(a);
 run("Macro...", "code=[if (v==255) v=1]");
 names3 = myDir + i+1000;
 saveAs ("Tiff", names3);
 run("Close All");
}
```

Etape de normalisation par l'image du Scatter_compton

- Les valeurs d'intensités de l'image du scatter inférieur à 0,1 sont éliminé (fonction threshold) et enregistrer : Scatter_cor (corrigé)
- Les images pour chaque élément sont alors normalisées par l'image du scatter corrigé avec le script ci-dessous

```
/////////création dossier de sauvegarde des images normalisées /////
dir1="C:\\Users\\kvidot\\Desktop\\LUCIA\\"
list = getFileList(dir1);
myDir = dir1+"Norm_scatter"+File.separator;
        File.makeDirectory(myDir);
        print("");
        print(myDir);

///////////////Normalisation //////
dir1="C:\\Users\\kvidot\\Desktop\\LUCIA\\"
list = getFileList(dir1);
for (i=0; i<list.length; i++) {
 a= dir1+list[i];
open(a);
 a1= getTitle();
open("C:\\Users\\kvidot\\Desktop\\LUCIA\\CF_2b_00310_Scatter-Compton000_Cor.tiff");
 b1= getTitle();
 imageCalculator("Divide create", a1, b1);
 names4 = myDir +a1;
 saveAs ("Tiff", names4);
run("Close All");
}
```

```
//!!!!!!!!!!!Lancer la 3e parti du script manuellement!!!!!!!!!!!!!!!
run("Close All");
// Application des masques pixels sur l'image natif
dir1="C:\\Users\\kvidot\\Desktop\\LUCIA\\Norm_scatter\\"
list = getFileList(dir1);
dir2="C:\\Users\\kvidot\\Desktop\\LUCIA\\mask_pxl_bin\\"
list2= getFileList(dir2);
dir3="C:\\Users\\kvidot\\Desktop\\LUCIA\\"
for (i=0; i<list.length; i++) {
 a= dir1+list[i];
 open(a);
 a1= getTitle();
 myDir = dir3+"result"+getTitle+File.separator;
        File.makeDirectory(myDir);
        print("");
        print(myDir);
 for (j=0; j<list2.length; j++) {
        b= dir2+list2[j];
        open(b);
        b1= getTitle();
 imageCalculator("Multiply create", a1, b1);
 names4 = myDir +a1+j+1000;
 saveAs ("Tiff", names4);
 close();
}
run("Close All");
}

/////////création dossier de sauvegarde des fichiers Excels/////
dir1="C:\\Users\\kvidot\\Desktop\\LUCIA\\"
list = getFileList(dir1);
myDir = dir1+"Data"+File.separator;
        File.makeDirectory(myDir);
        print("");
        print(myDir);

// on recupère la moyenne d'intensité de gris par ligne de pixel
run("Set Measurements...", "mean redirect=None decimal=3");
dir2="C:\\Users\\kvidot\\Desktop\\LUCIA\\"
dir3= dir2 + "resultCF_2b_00310_Mn-K_Cor.tiff\\"      ///changer le nom du dossier « élément »
list = getFileList(dir3);
for (i=0; i<list.length; i++) {
 a= dir3+list[i];
 open(a);
 run("Macro...", "code=[if (v==0) v=NaN]");
 run("Measure");
 run("Close All");
}
myDir="C:\\Users\\kvidot\\Desktop\\LUCIA_Nov_2018\\Dt_Io_Cor\\Dt_Io_Cor\\Energie_7p2keV\\h
aute_resolution\\CF_2b_00310_Cor\\Data\\"
saveAs("Results", myDir+"Mn.csv");
run("Clear Results");
```

```
run("Set Measurements...", "mean redirect=None decimal=3");
dir2="C:\\Users\\kvidot\\Desktop\\LUCIA_Nov_2018\\Dt_Io_Cor\\Dt_Io_Cor\\Energie_7p2keV\\haute_resolution\\CF_2b_00310_Cor\\"
dir3= dir2 + "resultCF_2b_00310_K-K_Cor.tiff\\"          ///changer le nom du dossier « élément »
list = getFileList(dir3);
for (i=0; i<list.length; i++) {
  a= dir3+list[i];
  open(a);
  run("Macro...", "code=[if (v==0) v=NaN]");
  run("Measure");
  run("Close All");
}
myDir="C:\\Users\\kvidot\\Desktop\\LUCIA_Nov_2018\\Dt_Io_Cor\\Dt_Io_Cor\\Energie_7p2keV\\haute_resolution\\CF_2b_00310_Cor\\Data\\"
saveAs("Results", myDir+"K.csv");
run("Clear Results");

run("Set Measurements...", "mean redirect=None decimal=3");
dir2="C:\\Users\\kvidot\\Desktop\\LUCIA_Nov_2018\\Dt_Io_Cor\\Dt_Io_Cor\\Energie_7p2keV\\haute_resolution\\CF_2b_00310_Cor\\"
dir3= dir2 + "resultCF_2b_00310_Fe-K_Cor.tiff\\"          ///changer le nom du dossier « élément »
list = getFileList(dir3);
for (i=0; i<list.length; i++) {
  a= dir3+list[i];
  open(a);
  run("Macro...", "code=[if (v==0) v=NaN]");
  run("Measure");
  run("Close All");
}
myDir="C:\\Users\\kvidot\\Desktop\\LUCIA_Nov_2018\\Dt_Io_Cor\\Dt_Io_Cor\\Energie_7p2keV\\haute_resolution\\CF_2b_00310_Cor\\Data\\"
saveAs("Results", myDir+"Fe.csv");
run("Clear Results");

run("Set Measurements...", "mean redirect=None decimal=3");
dir2="C:\\Users\\kvidot\\Desktop\\LUCIA_Nov_2018\\Dt_Io_Cor\\Dt_Io_Cor\\Energie_7p2keV\\haute_resolution\\CF_2b_00310_Cor\\"
dir3= dir2 + "resultCF_2b_00310_Ca-K_Cor.tiff\\"          ///changer le nom du dossier « élément »
list = getFileList(dir3);
for (i=0; i<list.length; i++) {
  a= dir3+list[i];
  open(a);
  run("Macro...", "code=[if (v==0) v=NaN]");
  run("Measure");
  run("Close All");
}
myDir="C:\\Users\\kvidot\\Desktop\\LUCIA_Nov_2018\\Dt_Io_Cor\\Dt_Io_Cor\\Energie_7p2keV\\haute_resolution\\CF_2b_00310_Cor\\Data\\"
saveAs("Results", myDir+"Ca.csv");
run("Clear Results");
```

Annexe 9 : Composition osidique des parois cellulaires de Douce Moen et Guillevic

Les variétés Douce Moen et Guillevic ont été récoltées en Bretagne en 2017 et 2018.

Méthode

Sur les pommes Douce Moen et Guillevic récoltées en Bretagne en 2017, les parois cellulaires du cortex externe ont été préparées par un extracteur à solvant sous pression automatisé, puis la composition en oses a été déterminés après hydrolyse acide de ces parois extraites. L'ensemble de la méthode est décrite dans Winisdorffer, Musse et al. (2015). Brièvement, environ 500 mg de chair congelé de pomme sont lyophilisés puis séchés sous vide à 40 °C. La matière sèche récupérée est alors broyée avec un broyeur à bille (FastPrep-24, MP Biochemicals, CA) à une vitesse de 6,5 $m.s^{-1}$ pendant 60 sec. La préparation des parois à partir de poudre de cortex lyophilisée est réalisée avec un extracteur à solvants sous pression automatisé ASE1 350 (DIONEX, CA, USA). La poudre (environ exactement 1 g) dans des cellules de 22 mL est extraite par de l'éthanol à 80% à 100 °C avec un flux de 2 $mL.min^{-1}$. Le temps de flux utilisé est de 6 min, suivit par un rinçage avec un volume de 150%, et un temps de purge à l'azote de 30 sec. Le matériel pariétal (AIM) est alors séché sous vide à 40 °C. L'AIM est d'abord dispersé dans de l'acide sulfurique (13 M) pendant 30 min à 30 °C et ensuite hydrolysé dans de l'acide sulfurique (1 M, 2 h à 100 °C). Après conversion des oses en acétate d'alditole, la quantification des sucres est réalisée par chromatographie en phase gazeuse (Trace GC Ultra, Thermofisher; colonne : silice greffé phase type OV-225 (BP-225 ; 25 cm x 0,32 mm ; épaisseur de phase 0,25 µm ; SGE, Australie), température 205°C, gaz vecteur : H_2 ; détection : FID).

Les analyses ont été réalisé sur quatre répétitions et la significativité déterminée par test de Student's.

Résultats

Les résultats obtenus (**Table A.1)** montrent que les seules différences significatives entre les deux variétés de pommes portent sur les quantités en mannose et en acide uronique. En effet, la variété Douce Moen était légèrement plus riche même si les valeurs retrouvées restent très proches. Ainsi, pour les deux variétés, le glucose est retrouvé en plus grande quantité suivit des acides uroniques (env. 26-30%) et de l'arabinose (env. 12-14%). Ces mesures mettent surtout en évidence la différence en terme de composition en acide uroniques, issue des acides galacturoniques des pectines. Cette donnée est intéressante notamment pour accéder à la quantité de pectines non estérifié en lien avec leur capacité d'interaction avec les cations, telle que décrit dans le **Chapitre V**.

Table A.10 : Teneur en oses en % de matière sèches de parois cellulaires.

Fruit	***Rha***	***Fuc****	***Ara***	***Xyl****	***Man****	***Gal***	***Glc***	***AU****
GU	1,1 ±0	0,9 *±0,1*	12,5 *±0,7*	5,5 *±0,3*	2,2 *±0,3*	5,5 *±0,5*	30,3 *±1,6*	26,0 *±0,5*
DM	1,2 *±0*	0,7 *±0*	13,1 *±0,5*	6,3 *±0,3*	2,7 *±0,2*	6,0 *±0,4*	30,1 *±0,7*	27,9 *±1,1*

*Rha : Rhamnose, Fuc : Fucose, Ara : Arabinose, Xyl : Xylose, Man : Mannose, Galactose, Glc : Glucose, AU : Acide Uronique, GU : Guillevic, DM : Douce Moen., * : différences significatives (n = 3 ; p-value < 0,05).*

Annexe 10 : Histologie des tissus cellulaires de Douce Moen et Guillevic

Méthode

Sur les pommes Douce Moen et Guillevic récoltées en Bretagne en 2017, deux coupes effectuées au vibratome d'une épaisseur de 150 µm, ont été sectionnées sur quatre cylindres prélevés au niveau du cortex externe à partir d'une tranche équatoriale de quatre fruits. Les coupes ont alors été imagées par la Blue Box (Devaux, Bouchet et al. 2008). Une analyse de texture d'image en niveaux de gris a été réalisée sur chacune des images en utilisant le plugin « Granulometry » en batch d'ImageJ (Legland, Arganda-Carreras et al. 2016). La taille du pixel données par la prise d'image « Blue Box » était de 3.6 sur 3.6 µm. L'analyse d'image a été réalisée jusqu'à un diamètre de 150 pixels avec un pas de 1 pixel. L'ensemble de la méthodologie utilisée est décrite dans (Devaux, Bouchet et al. 2008). Ensuite, les courbes granulométriques ont été analysées par analyse en composante principale. Les coordonnées des courbes par individus sur les deux premiers axes ont été testées par analyse de variance sur la base des modalités variétales.

Résultat

Les résultats (**Figure A.1**) indiquent une différence significative entre les deux variétés et sur les deux axes de l'ACP (axe 1, p = 0,0001 ; axe 2, p = 0,0009). Les courbes des loadings indiquent la contribution des tailles des objets noirs (cellules + méats) qui contribuent aux axes. L'axe 1 distingue les « petits « objets (en abscisses négatifs) des « gros » objets (abscisses positifs). L'axe 2 distingue des « gros » objets de valeurs intermédiaires en négatif. Cela se traduit par Douce Moen avec de plus petites « cellules » alors que Guillevic à plus de grosses « cellules » et de taille intermédiaire. La différence entre les deux variétés reste cependant peu marquée, au vue de la distribution granulométrique et position des barycentres sur l'ACP, et provient probablement de la différence de calibre des pommes.

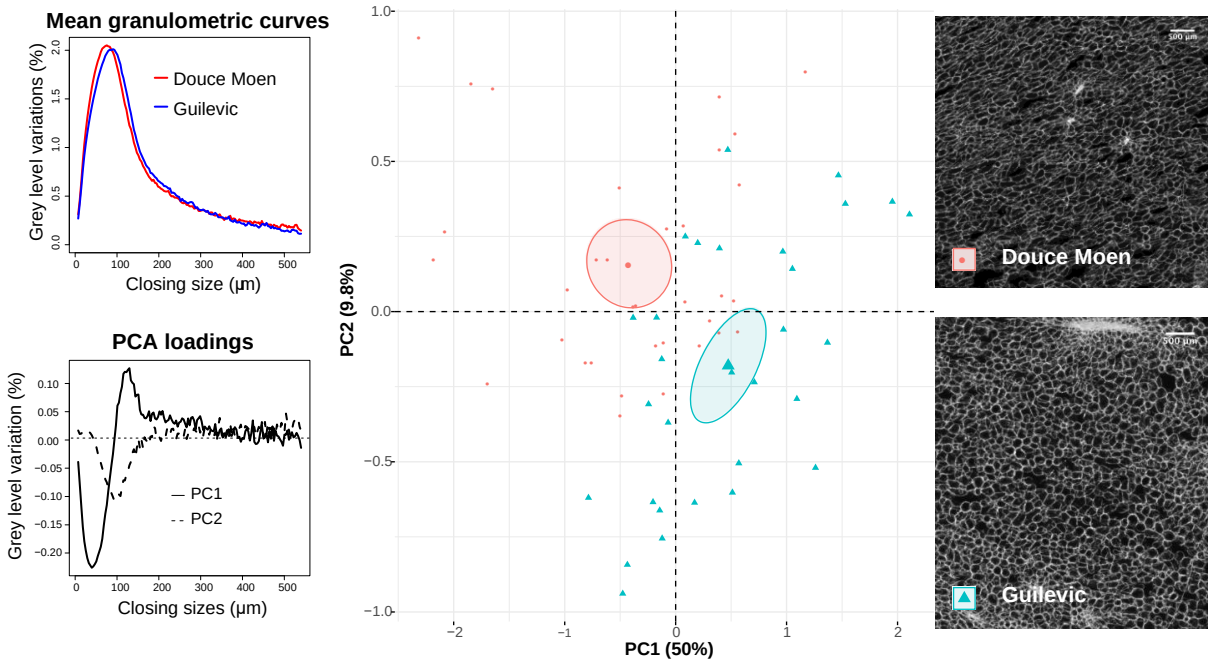

Figure A.48 *: A gauche sont représentées les courbes granulométriques moyennes et les courbes correspondantes des loadings selon les deux premières composantes. Au centre, l'ACP avec des ellipses de confiance à 0.95. A droite, sont montrées des images de coupes représentatives des deux variétés.*

Annexe 11 : Teneurs en ions métalliques dans le Cabernet sauvignon

Sur le cépage Cabernet sauvignon récolté en 2016 en région Val de Loire, une mesure de la composition en ions métalliques a été réalisé par le laboratoire départementale d'analyse INOVALYS. Les teneurs obtenues sont présentées dans le **Table A.2**.

Table A.11 : Teneur en ions métalliques en µg/g de baies sèches de Cabernet-Sauvignon récolte 2016

K	Ca	Mg	Fe	Mn	Cu	Zn
12100	500	400	15,4	2,9	1,8	2,1

Annexe 12 : Fermeté et indices de maturité des cépages Cabernet franc, Cabernet sauvignon et Grolleau

Le degré de maturité est un paramètre important pour étudier des différences entre cépages. En effet pour que les résultats soient pertinents, il faut que les degrés de maturité des fruits récoltés soient proches. Ces degrés de maturité ont donc été déterminés pour les trois cépages récoltés en 2017. Les différentes variations physiologiques et compositionnelle peuvent être associé au propriétés mécaniques des fruits. Ainsi, des mesures de compression sur les baies de raisins ont aussi été réalisées.

Méthodes

Indice de maturité

Une grappe de chaque variété est écrasée à la main puis le jus récupéré est filtré. Pour chaque variété, le filtrat est réparti en trois échantillons afin d'avoir trois réplicas. La mesure du °Brix associé à la teneur en sucres se fait directement sur le jus. L'acidité totale est mesurée par dosage acido-basique avec une solution de NaOH (0,1M) sur un titrateur puis converti en g/L H_2SO_4. Le volume de jus prélevé est de 10 mL auquel sont ajoutés 30 mL d'H_2O MilliQ avant dosage. L'indice de maturité calculé correspond au ratio °Brix sur l'acidité totale, tel que décrit par Zouid, Siret et al. (2013).

Fermeté

La méthode employée est celle décrites par Doumouya (2014). Pour chaque cépage, les baies sont collectées en fonction des trois zones de prélèvements H, M et B pour Haut, Milieu et Bas, respectivement (**Figure A.2**).

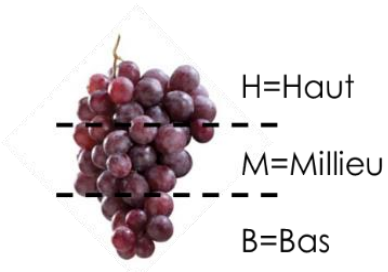

***Figure A.49** : Schéma des zones de prélèvement des baies de raisin*

Pour chaque variété, la mesure a été faite sur 10 baies par zones H, M, B et sur 10 grappes. Soit un total de 100 baies par zones et par cépage. L'analyse est réalisée avec une machine de traction universelle (MTS Universal, modèle Synergie 200H) possédant une sonde cylindrique à extrémité plane de 15 mm de diamètre et un capteur de force de 50 Newton. La baie est placée en position équatoriale.

Elle est comprimée à 20% de sa hauteur à une vitesse de 50 mm/min. Les paramètres suivants sont mesurés (**Figure A.3**):

- La force maximale de compression F1 mesurée en (N) ;
- L'énergie lié à la compression W1 mesurée en (mJ) ;
- La pente de compression Grad 1 mesurée en (N/mm) ;
- La hauteur de la baie (mm)

A partir des courbes de compression obtenues, il est possible de calculer le « module de Young » (module d'élasticité) qui correspond à la pente à l'origine de la courbe :

- Pente = dF/dd (dF étant la différence de force mesurée en fonction de la déformation: dd)

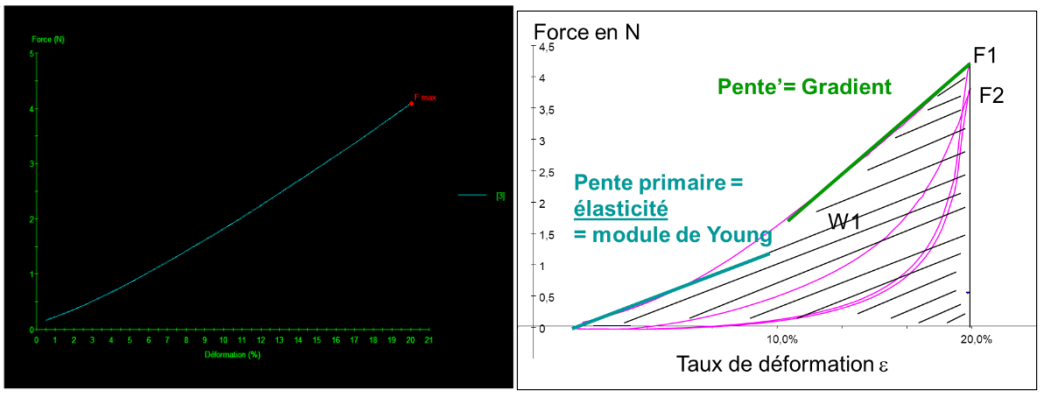

Figure A.50: *Un exemple de courbe expérimentale obtenu (à gauche). Un schéma explicatif des paramètres calculés à partir de la courbe (à droite) (Maury 2007)*

Le module de Young a été calculé à différent % de déformation : 1%, 3%, 5%, 10% et 20%, respectivement E1, E3, E5, E10 et E20.

Résultats

Les résultats **(Figure A.4)** montrent que les indices de maturité des trois cépages sont proches. Cela indique que les compositions en sucres et en acides sont relativement similaires traduisant un stade de développement proche pour ces trois variétés.

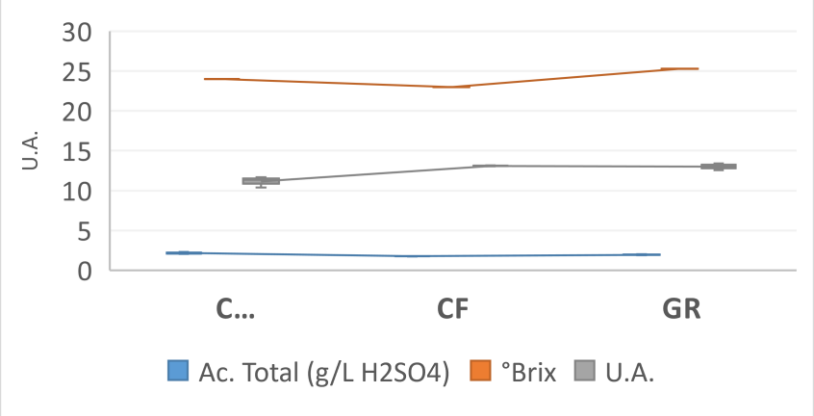

Figure A.51 : *Acidité totale, °Brix et indice de maturité des cépages Cabernet sauvignon (CS), Cabernet franc (CF) et Grolleau (GR) récoltés en 2017.*

Les résultats des mesures de compressions sont présentés dans le **Table A.3** pour la force, la hauteur et le travail à 20% de compression.

Table A12 : Moyennes *(±écart-types)* des mesures de force (F) et l'énergie (W) pour une compression de 20%, et la hauteur (H) des baies pour chaque échantillon (n=100).

	n	Moyennes		
		F (N)	**H (mm)**	**W (mJ)**
CFH	100	2,63 *±0,40*	11,32 *±0,97*	0,00 *±0,00*
CFM	100	2,72 *±0,33*	11,47 *±0,95*	0,00 *±0,00*
CFB	100	2,81 *±0,41*	11,85 *±1,08*	0,00 *±0,00*
CSH	100	3,98 *±0,96*	12,65 *±1,09*	0,00 *±0,00*
CSM	100	4,32 *±0,79*	12,95 *±0,92*	0,01 *±0,00*
CSB	100	3,78 *±1,08*	12,59 *±1,11*	0,00 *±0,00*
GRH	100	3,45 *±0,86*	14,90 *±1,36*	0,00 *±0,00*
GRM	100	3,38 *±0,87*	14,34 *±1,40*	0,00 *±0,00*
GRB	100	2,91 *±0,92*	14,01 *±1,65*	0,00 *±0,00*

Les paramètres mesurés (force maximum, travail et hauteur de baie) sur les 100 baies par zones et par variétés montrent une différence significative ($p<0,05$) inter-variétés mais pas entre les zones H, M et B. Cabernet sauvignon est le plus ferme. Le cépage Grolleau a un diamètre plus élevé.

On peut classer les trois variétés comme suit :

- Force : CS > GR > CF
- Diamètre de baies : GR > CS > CF

Les résultats du calcul des modules de Young sont présentés dans le **Table A.4** et ne montrent pas de différence clairement marquées entre les zones H, M et B et entre les variétés. Même si le cépage Grolleau semble se distinguer légèrement, les écart-types sont trop important pour pouvoir émettre une telle conclusion. Cependant, une anova réalisée pour la pente calculée avec une déformation de 20%, permet de montrer que les variétés se distinguent significativement les unes des autres avec une p value < 0,05 (cf. **figure A.5**). L'élasticité mesurée à partir des pentes pour le plus faible % de déformation (1% dans notre cas) est la valeur se rapprochant le plus du module d'Young. L'anova réalisée sur ces mesures (**Figure A.5)** montre aussi une différence significative entre les variétés. On en conclue donc que : CS > CF > GR.

De manière générale, les baies ne se distinguent pas en fonction de leur position sur la grappe mais les cépages présentent des propriétés physiques différentes :

- Force : CS ≥ GR > CF
- Elasticité (20% de déformation) : CS ≥ CF > GR
- Diamètre de baies : GR > CS ≥ CF

Pour les trois cépages, les valeurs à 1% de déformation sont comprises entre 1,31 et 2,29 MPa. Ces mesures sont proche de 1,46 - 1,63 MPa obtenue par Zouid, Siret et al. (2013) sur le Cabernet Franc. A une déformation de 20% l'élasticité mesurée à partir de la pente de la courbe est nettement inférieure qu'à 1% de déformation. Cela met en évidence une modification de la structure de l'échantillon et que cette déformation bouleverse son état physique initial. Les différences entre les cépages à ce % de déformation serait peut-être liées à des structures physiques différentes entre les cépages. Comme décrit par Yakushiji, Sakurai et al. (2001) qui met en évidence une corrélation inverse entre le poids de la baie et sa fermeté, un lien peut être fait avec la diamètre des baies dans la mesure où les deux cépages de Cabernet sont plus petits et donc moins riches en chair que Grolleau et donc une proportion relative plus importante de peau et de pépin. Il a aussi été montré que le volume de péricarpe de la baie de raisin est proportionnel à la taille de la baie alors que le nombre de cellules reste stable (Harris, Kriedemann et al. 1968). Ainsi, si les cellules et notamment les parois cellulaires qui les constituent n'évoluent pas dans le même sens que le volume de la baie, la perte de fermeté pour les baies de taille plus importante s'explique partiellement. Contrairement aux travaux de Stéphanie Doumouya (2014) (Doumouya 2014), aucune variation claire n'a pu être mise en évidence entre les propriétés mécaniques des baies et leur position dans la grappe. Il est possible que dans notre cas, le nombre et la variété de mesures n'aient pas été suffisants ou alors aux différences de cépages et/ou leurs conditions de croissance.

Table A.13 : Moyennes *(±écart-types)* de l'élasticité à différents taux de déformation 1, 5 et 20% pour chaque cépage et position dans la grappe.

	MOYENNES		
	E1	**E5**	**E20**
CFH	2,09 *±0,33*	0,87 *±0,14*	0,11 *±0,02*
CFM	2,07 *±0,38*	0,87 *±0,17*	0,11 *±0,02*
CFB	2,02 *±0,36*	0,86 *±0,16*	0,11 *±0,02*
CSH	2,26 *±0,46*	1,03 *±0,23*	0,13 *±0,03*
CSM	2,29 *±0,45*	1,07 *±0,22*	0,13 *±0,03*
CSB	2,16 *±0,49*	0,97 *±0,27*	0,12 *±0,03*
GRH	1,32 *±0,28*	0,58 *±0,16*	0,07 *±0,02*
GRM	1,39 *±0,40*	0,61 *±0,22*	0,08 *±0,03*
GRB	1,31 *±0,38*	0,55 *±0,23*	0,07 *±0,03*

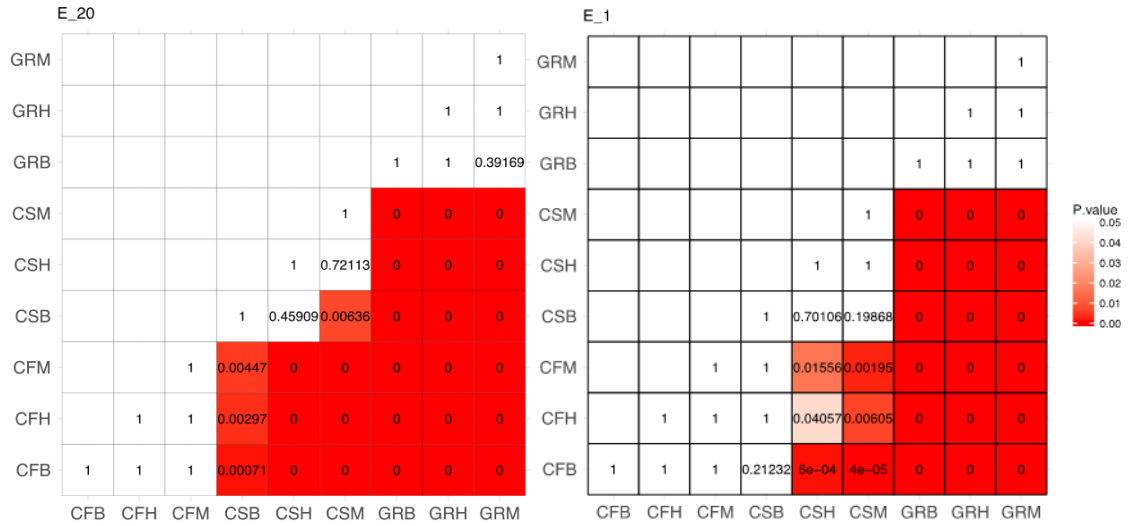

***Figure A.52** : Tableau de corrélation entre échantillon pour l'élasticité mesuré à 20% (gauche) et 1% (droite) de déformation*

Annexe 13 : Image RGB reconstruite à partir de la fluorescence X du tissu de raisin (Cabernet F. 2018)

⇨ Visualisation du K, Ca, Fe et S. Résolution 25 µm et 3 µm

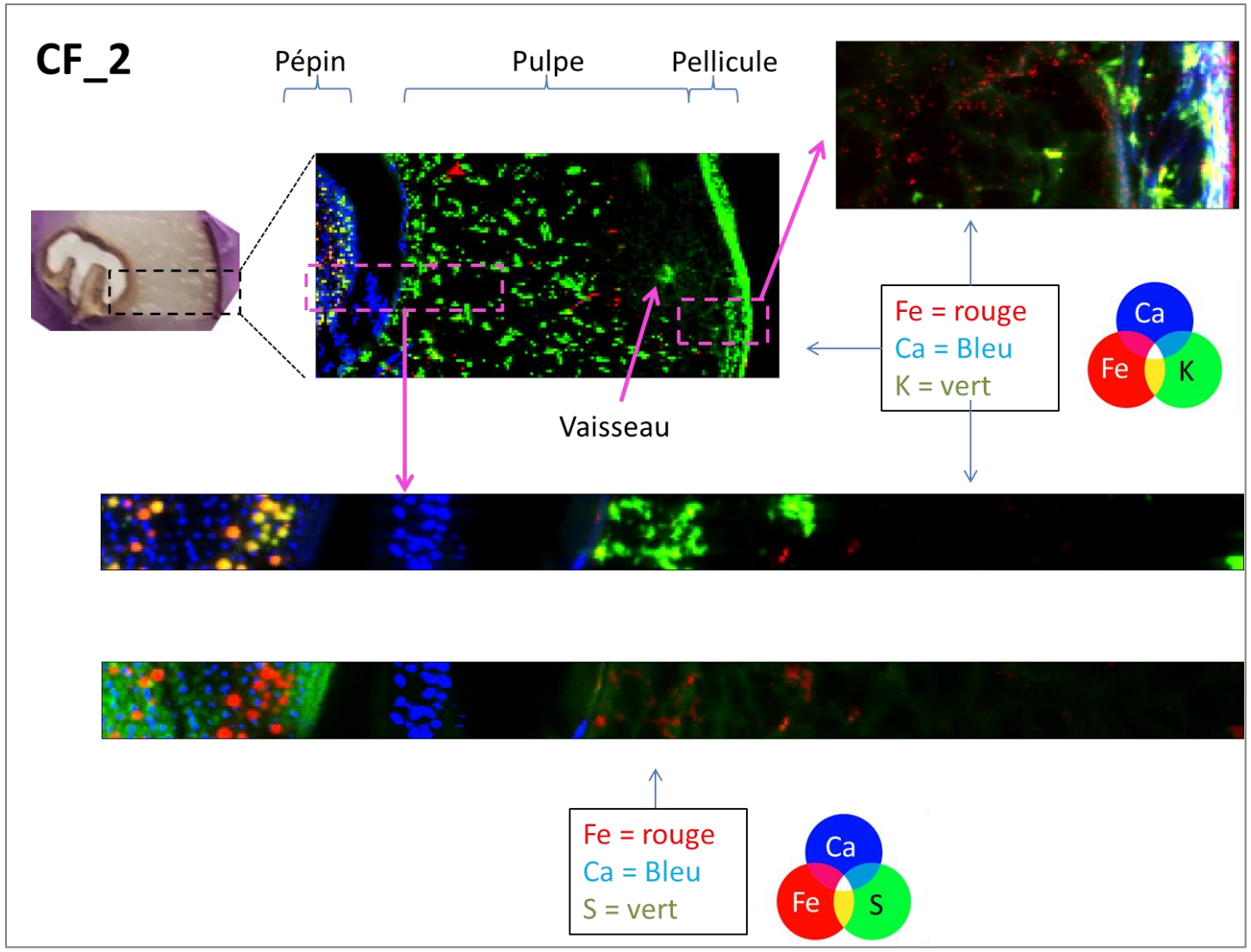

Références des annexes (9-12)

Devaux, M.-F., Bouchet, B., Legland, D., Guillon, F., & Lahaye, M. (2008). Macro-vision and grey level granulometry for quantification of tomato pericarp structure. *Postharvest Biology and Technology, 47*(2), 199-209. doi:https://doi.org/10.1016/j.postharvbio.2007.06.017

Legland, D., Arganda-Carreras, I., & Andrey, P. (2016). MorphoLibJ: integrated library and plugins for mathematical morphology with ImageJ. *Bioinformatics, 32*(22), 3532-3534. doi:10.1093/bioinformatics/btw413

Maury, C. (2007). *Détermination des paramètres de texture pour l'analyse du raisin*.

Winisdorffer, G., Musse, M., Quellec, S., Barbacci, A., Le Gall, S., Mariette, F., & Lahaye, M. (2015). Analysis of the dynamic mechanical properties of apple tissue and relationships with the intracellular water status, gas distribution, histological properties and chemical composition. *Postharvest Biology and Technology, 104*, 1-16.

Zouid, I., Siret, R., Jourjon, F., Mehinagic, E., & Rolle, L. (2013). Impact of grapes heterogeneity according to sugar level on both physical and mechanical berries properties and their anthocyanins extractability at harvest. *Journal of Texture Studies, 44*(2), 95-103.

UNIVERSITE BRETAGNE LOIRE / ECOLOGIE GEOSCIENCES AGRONOMIE ALIMENTATION

UNIVERSITÉ DE NANTES

Titre : Distribution et fonction des ions métalliques et des composés phénoliques dans les parois de fruits charnus.

Mots clés : Ions métalliques, pectine, composés phénoliques, pomme, raisin, cartographie

Résumé : La couleur, la fermeté, la saveur, ou l'aptitude à la conservation, sont les principaux critères de qualité qui déterminent le choix du consommateur, les procédés de transformation et la stabilité des fruits charnus. Ces critères dépendent des mécanismes déterminants la qualité des productions, faisant intervenir les ions métalliques, les composés phénoliques et les parois cellulaires. Pour appréhender ces mécanismes, les travaux ont été réalisés sur deux variétés de pommes à cidre et étendus aux variétés de raisins de cuve. Le développement de méthodes de cryo-microscopie associées à la fluorescence X et UV a permis l'identification et la distribution tissulaire des ions métalliques et des composés phénoliques. Les métaux de transition et les flavanols sont retrouvés majoritairement dans la cuticule alors que le calcium, le magnésium et les pigments phénoliques sont co-localisés dans les couches sous-cuticulaires. Une distribution homogène du potassium est observée de la couche sous-cuticulaire au cortex externe, zones riches en acides phénoliques. Parmi ces acides, les acides hydroxycinnamiques sont potentiellement estérifiés dans les parois cellulaires. L'impact de ces composés sur la qualité des fruits lors de leur consommation ou transformation a été abordé par l'étude des interactions entre les ions métalliques, la pectine des parois cellulaires et les composés phénoliques en présence de peroxyde d'hydrogène. L'ensemble des résultats : distribution des ions métalliques et composés phénoliques, ainsi que les interactions et les mécanismes réactionnels possibles est résumé dans un modèle conceptuel qui servira de base pour de futurs travaux visant à un meilleur contrôle des propriétés organoleptiques des fruits frais et transformés.

Title: Metallic ions and phenolic compounds distributions and functions in fleshy fruit cell wall.

Keywords : Metallic ions, pectin, phenolic compounds, apple, grape, mapping

Abstract: Colour, firmness, taste and long storage ability, are the main quality parameters that define consumer choice, processing and shelf-life of fleshy fruits. These quality criteria rely on physiological and physicochemical mechanisms that involve metallic ions, phenolic compounds and cell wall. To better understand these mechanisms, the thesis study was realised on two cider apples varieties and extended to wine grapes. The development of cryo-microscopy methods associated to X-ray and deep UV fluorescence highlighted the identification and distribution at the tissue scale of metallic ions and phenolic compounds. Transition metals and flavanols were mostly found in the cuticle while calcium, magnesium and phenolic pigments were co-localised in the sub-cuticle tissue layers. A homogeneous distribution of potassium was observed from the sub-cuticle to the outer cortex cell layers, a region that is rich in phenolic acids. Among these acids, hydroxycinnamic acids were found to be potentially esterified within cell wall. The impact of these compounds on the quality of fruit during consumption or processing was considered by studying the interactions between metal ions, cell wall pectin and phenolic compounds in the presence of hydrogen peroxide. All results: distribution of metal ions and phenolic compounds, as well as possible interactions and mechanisms of reaction, are summarized in a conceptual model that will serve as a basis for future work aiming at better controlling the organoleptic properties of fresh and processed fruit.